MINITIMECUBE:
BUILDING THE WORLD'S SMALLEST NEUTRINO DETECTOR

A DISSERTATION SUBMITTED TO THE GRADUATE DIVISION
OF THE UNIVERSITY OF HAWAIʻI AT MĀNOA IN PARTIAL
FULFILLMENT OF THE REQUIREMENTS FOR THE DEGREE OF

DOCTOR OF PHILOSOPHY
IN
PHYSICS

APRIL 2018

By
Viacheslav A. Li

Dissertation Committee:
John G. Learned, chairperson
Sandip S. Pakvasa
Jelena Maricic
Thomas E. Browder
Marcus A. Tius

In memory of John Madey ...

Abstract

The goal of this thesis is to describe the creation and testing of the world's smallest antineutrino detector, which was designed and built at the University of Hawai'i at Mānoa, and was deployed at the NIST research nuclear reactor facilities in Maryland during 2014–2016. First, we review relevant theoretical aspects of neutrino physics: sources of neutrinos and reactor antineutrinos in particular, and give a comparison between description of neutrino oscillations in quantum mechanics and quantum field theory. Second, we focus on the main components of this new-generation detector, as well as the data taking, analysis, and conclusions we drew from the project.

The novelty was in having a very small volume (2 liters) compared to all other neutrino detectors, with fast-timing electronics and photodetectors in a very confined space. The idea was to reconstruct the direction of particles propagating inside the scintillator using information from the first arrival of both Cherenkov and scintillation photons. While the project did not succeed in detecting neutrinos in its first outing, many important lessons were learned which we take to the next-generation NuLat instrument, under construction at present.

Acknowledgements

> Science is not the experience of just one scientist but of the whole community extending back to antiquity
>
> Weinberg

Without the work done by my colleagues this thesis wouldn't be possible. I am in debt to my advisor, Prof. John Learned. Most of the major ideas and decisions which led to the mTC detector as we built it are his.

I am thankful to Steve Dye and John Learned for their promotions of the Hanohano detector. I first heard about it at the International Neutrino Summer School 2010, held in Yokohama and Tokai. I was fascinated by the idea.

Later that year, as I was applying for grad schools, I sent John a message asking for more details on Hanohano and other neutrino research opportunities at the University of Hawai'i. His reply was:

```
From: John G. Learned
Date: Fri, Dec 17, 2010
...
I have a small project building a very nice
2 liter neutrino detector for use near reactors....
it hopefully opens the door to a new type of anti-electron neutrino
detection (including directionality).
...
```

Two liters, huh?! In August 2011 I saw the cubic chunk of plastic myself, and we started frantically building the detector's full assembly.

That was also exactly what I wanted: a small team, and being involved in the all stages of a neutrino experiment. Here I would like to acknowledge the team's work. Glenn Jocher who did most of the simulations and data analysis, and who is the fastest coder I have ever seen, some plots presented in this work are a collaborative effort and were often made by Glenn; Michinari Sakai — GEANT4 simulations, and using the CRY package to simulate the cosmogenic backgrounds; Ryan Dorrill — concise python scripts to initialize the detector, triggering GUI, operation shift; Mark Duvall — early electronics analysis and tests, creating the mTC logo, shift work; Bronson Edralin — calibration of electronics during the upgrade; John Koblanski — analysis of data, shift work; Kurtis Nishimura — firmware, electronics, GUI to monitor and slow control the detector, trigger scheme implementation, transition to a faster Ethernet network, interlock scheme; Gary Varner — electronics, without his IDLab and Belle involvement we wouldn't have the tools to begin with; Luca Macchiarulo — electronics, bash scripts for early electronics tests; Sergey Negrashov — slow control design, electronics development, clock board design and implementation, writing extremely fast event viewer that works with raw binary data; Joshua Murillo — design of high voltage divider, pilot interconnect board, and power supply original control together with Serge; Shige Matsuno — the very first ROOT-based event viewer, providing new ideas for young

folks to explore, initial laser calibration system; Marc Rosen — designing most of mechanical parts; Andrew Carpenter — for helping with the first shipment and assembly of the mTC at NIST.

I would like to thank Pieter Mumm and his colleagues at NIST for welcoming us in Maryland, and helping with all the logistics, and assembling the cave; University of Maryland team: William McDonough, Kristi Engel and Scott Wipperfurth for designing the mTC shielding cave, and doing the background simulations using SWORD package. Our project manager Andrew Druetzler for making shift schedules, and being on top of organizational matters.

This project wouldn't have happened without the funding provided by the U.S. National Geospatial-Intelligence Agency. I would like to thank Shawn Usman for playing one of the key roles in the project.

I am grateful for faculty and machine-shop staff of the UH Manoa physics department, and in particular to my dissertation committee members: Sandip Pakvasa, Jelena Maricic, Thomas Browder, and Marcus Tius (chemistry department). Art McDonald, who is a visiting faculty at our department, deserves a special attention. Having him at our group meetings, although a rare occasion after winning the Nobel Prize, was a great inspiration for our team. Unfortunately, John Madey, one of my original committee members and my former professor, could not see the completion of this project. His thoughts on near-field effects deeply influenced me, along with the following of his perspective.

You have a lot of fun if you understand both:

- engineering, have strong commitment to some particular issue (how to improve some device, technique)
- fundamentals of physics

and you might see how different (unrelated at first glance) things come together.

Contents

List of Figures

List of Tables

Chapter 1

The Flavor-changing Neutrino

> In a scientific pursuit there is continual food for discovery and wonder
>
> Frankenstein

Some eighty years before John sent the aforementioned message, Pauli sent an open letter [1] essentially introducing the existence of a new particle, or of what we now know as the neutrino,

```
From: W. Pauli
To: L. Meitner
Date: Thu, Dec 4, 1930
...
considering the 'false' statistics of N-14 and Li-6 nuclei,
as well as the continuous beta-spectrum, I have hit upon
a desperate remedy to save the "exchange theorem" and the
energy theorem. Namely the possibility that there could
exist in the nuclei electrically neutral particles that
I wish to call neutrons,
which have spin 1/2 and obey the exclusion principle,
and additionally differ from light quanta in that they
do not travel with the velocity of light.
...
```

In other words, the 1930 hypothesis made by Pauli stated that in order to save the concept of momentum conservation, one needs to introduce a new particle emitted along a β-ray in a β-decay of a nucleus X into Y.

$$ {}^{A}_{Z}X \rightarrow {}^{A-1}_{Z+1}Y + e^{-} + \nu \tag{1.1} $$

In the reaction (1.1), A is a number of nucleons, and Z is a number of protons, or charge. On a more fundamental level, it is a neutron inside the beta-unstable nucleus that decays into a proton, an electron, and an antineutrino. In 1930, the neutron was not yet discovered, and people didn't distinguish between antineutrinos and neutrinos. In fact, even the word "neutrino" was not yet introduced into the physicist vocabulary. It was not until a few years later when a neutron was discovered, and Fermi proposed

the first consistent theory of β-decay [2]. Fermi named the particle proposed by Pauli a neutrino, meaning a small neutral particle. It became clear to Fermi that a neutron inside a nucleus is converting into a proton with emission of an electron and a neutrino. So, the reaction of β-decay became known as,

$$n \to p + e^- + \nu \tag{1.2}$$

with a possible inverse process, or an an inverse β-decay:

$$\nu + A_Z \to \begin{cases} A_{Z+1} + e^- \\ A_{Z-1} + e^+ \end{cases} \tag{1.3}$$

Fermi has shown that if a neutrino has an energy of several MeV, then the cross section of the inverse β-decay process in Eq. (1.3) is on the order of 10^{-44} cm^2. This cross section is smaller than the cross sections of electromagnetic and nuclear scattering processes known at that time by more than a dozen orders of magnitude. It was assumed that neutrinos could not be detected experimentally. Knowing the scattering cross section, it is easy to make an estimate of the effective neutrino mean free-path in a substance of a given density. For example, let us set a number of scatterers being $\sim 10^{23}/\text{cm}^3$, a number of atoms in a cubic centimeter of water, then the effective mean free path is:

$$l_{eff} = \left(\frac{10^{23}}{\text{cm}^3} \times 10^{-44}\ \text{cm}^2 \right)^{-1} = 10^{19}\ \text{m} \tag{1.4}$$

Taking into account that one light-year is equal to $\sim 0.95 \times 10^{16}$ m, the mean free path is approximately 1000 light-years. How hard is it to imagine a million Solar systems filled with water, or a billion Suns, stacked next to each other? This was the main reason why the neutrino had the status of a poltergeist particle for more than 20 years from the moment of its theoretical prediction.

In Fig. 1.1 a Google search activity for the word "neutrino" is shown, since the statistics became available. It is important to point out the two noticeable spikes. The first one is due to the 2011 controversial OPERA result that neutrinos travel faster than light [3] — later, it was found that it was all due to a not fully connected cable in the experiment. The second much smaller spike is due to the 2015 Physics Nobel Prize shared by T. Kajita and A. McDonald, which also has its own controversy. The Nobel Committee's statement erroneously reads "for the discovery of neutrino oscillations, which shows that neutrinos have mass," while McDonald's achievement in the SNO project was to correctly identify the full solar neutrino flux changing its composition on its way through dense parts of the Sun, a so-called MSW-effect [4, 5] which is not neutrino oscillations. The long tail on the left is very likely due to the decaying interest in neutrinos after another potential spike — 2002 Nobel Prize in physics, half of which was awarded to R. Davis [6] and M. Koshiba [7] "for pioneering contributions to astrophysics, in particular for the detection of cosmic neutrinos," essentially for detecting neutrinos produced in the Sun, but mostly due to the 1987 discovery of supernova neutrinos by Kamiokande and the 1998 discovery of neutrino oscillations by SuperK, with the latter highlighted by the 2015 Nobel Prize.

Several good textbooks on neutrino physics have been published [8–10], and provide a decent overview of the subject. For more fresh results, one may consult with arXiv,

Figure 1.1: The Google trend of the word *neutrino* shows two noticeable spikes — one in 2011 due to the OPERA reporting that the neutrino speed is greater than the speed of light in vacuum [3], and another in 2015 when the Nobel Physics prize was awarded to T. Kajita (SuperK) and A. McDonald (SNO).

INSPIRE HEP, or Neutrino Unbound, which are all great online systems for neutrino physicists to stay updated.

The Standard Model of electroweak and strong interactions (SM), which started as quantum electrodynamics, nowadays also incorporates quantum chromodynamics. In Fig. 1.2 a simplified version of the modern paradigm shows major connections between different types of particles. The complete version of the SM Lagrangian, and experimental source references can be found in the Particle Data Group biennial particle physics review [11]. It is worth noting that there is not much information about neutrinos, unlike charged leptons, neutron, and hundreds of different hadrons, most of which were discovered later than the neutrino. Even the Higgs boson now, discovered only in 2012, has a better defined mass than the neutrino.

In the SM, it is assumed that neutrinos do not decay, i.e., they are stable. Beyond the SM, neutrino decay is possible, and one can find multiple papers discussing different scenarios [12, 13]. Neutrinos are massive, have three flavors, and their flavor states oscillate. We understand them enough to use them for some limited number of applications. Their nature is still unclear as to whether they are Dirac or Majorana particles [14], along with the full picture of the neutrino oscillation phenomenon, and the lack of right handed neutrinos.

Here we just briefly mention that neutrinos, like quarks, mix. Neutrinos interact only weakly, which means only two types of interaction vertices are permitted in the SM, shown in Fig. 1.3. Historically, a composition of mixed mass-state neutrinos at an interaction point is called a flavor state. Unlike quarks, neutrinos don't have a confinement constraint, and can propagate through long distances. Pontecorvo was the first to highlight the possibility of neutrino-antineutrino oscillations similar to those known for kaons [15], and Sakata was among the first to consider flavor neutrino oscillations. Maki, Nakagawa, and Sakata were the first to propose two-flavor neutrino oscillations [16]; the three-flavor mixing and oscillations were first considered in [17], which subsequently led to the neutrino mass hierarchy question.

The nature of neutrino mass minuteness compared to electrons is still not very clear. The so-called see-saw mechanism [18] is the most popular theoretical means to generate small neutrino mass. There has been a huge effort to measure an absolute value of neutrino mass, yet only upper limits have been set. Similarly, the absolute value of the neutrino magnetic moment hasn't been measured either yet, though definitely small.

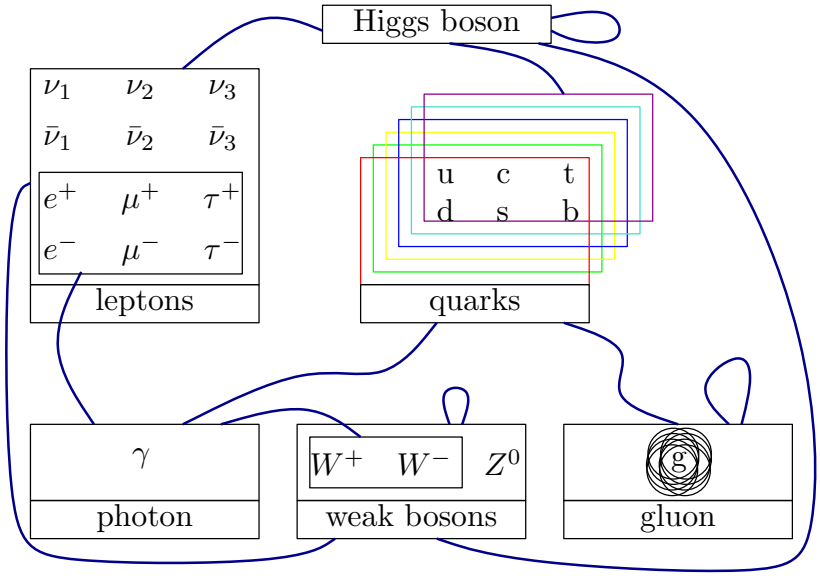

Figure 1.2: Schematic diagram of fundamental Standard Model interactions among elementary particles.

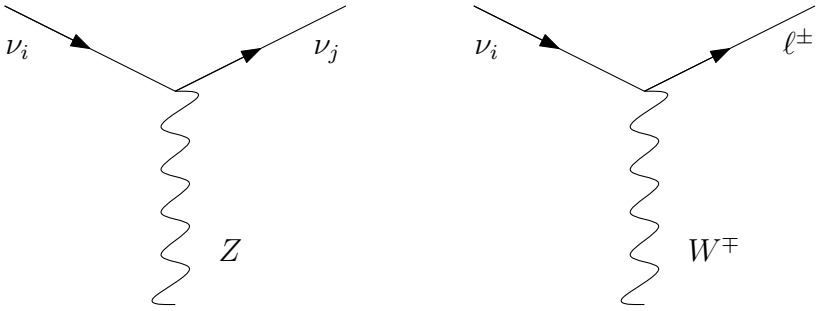

Figure 1.3: Vertices of Neutral and Charged current interaction for neutrinos.

Over the course of the last 60 years, since the experimental discovery of neutrinos [19], there have been a handful of anomalies and problems associated with them. Table 1.1 is a list with references, where a reader can find more details.

Some scientists, including those in our group, like to consider the possibility that there is another fourth type of neutrino that doesn't interact with other leptons. It is called "sterile." Lately, since the reactor antineutrino anomaly [34], as it has turned out, seems likely due to a not well-known reactor antineutrino flux [35], it appears *less* likely that there is a fourth type of neutrino. Nevertheless, the possibility is not completely ruled out.

The plot of neutron lifetime value versus publication date, shown in Fig. 1.4, is another relevant piece of information from the PDG review. The value affects the reactor antineutrino anomaly. Which value would you use? Experimental physics is very different from theoretical physics, and experimental errors are frustrating.

Parametrization of the mixing matrix for neutrinos in the SM is analogous to the one for quarks:

$$V = \begin{pmatrix} c_{12}c_{13} & c_{13}s_{12} & s_{13}\ \mathrm{e}^{-i\delta} \\ -c_{23}s_{12} - c_{12}s_{13}s_{23}\ \mathrm{e}^{i\delta} & c_{12}c_{23} - s_{12}s_{13}s_{23}\ \mathrm{e}^{i\delta} & c_{13}s_{23} \\ s_{12}s_{23} - c_{12}s_{13}c_{23}\ \mathrm{e}^{i\delta} & -c_{12}s_{23} - c_{23}s_{13}s_{12}\ \mathrm{e}^{i\delta} & c_{13}c_{23} \end{pmatrix} \tag{1.5}$$

Problem	Solution/cause	References
Majorana neutrino 1937–	not known yet	[14]
Neutrino mass hierarchy	not known yet	[20]
Solar neutrino problem 1967–2001	MSW effect	[21, 22]
Atmospheric neutrino anomaly 1983–1998	Neutrino oscillations	[23–31]
LSND anomaly 1997–	Likely cross section	[32]
GSI anomaly 2008–	not known yet	[33]
Reactor antineutrino anomaly 2011–2017	^{235}U spectrum	[34, 35]

Table 1.1: A variety of neutrino anomalies.

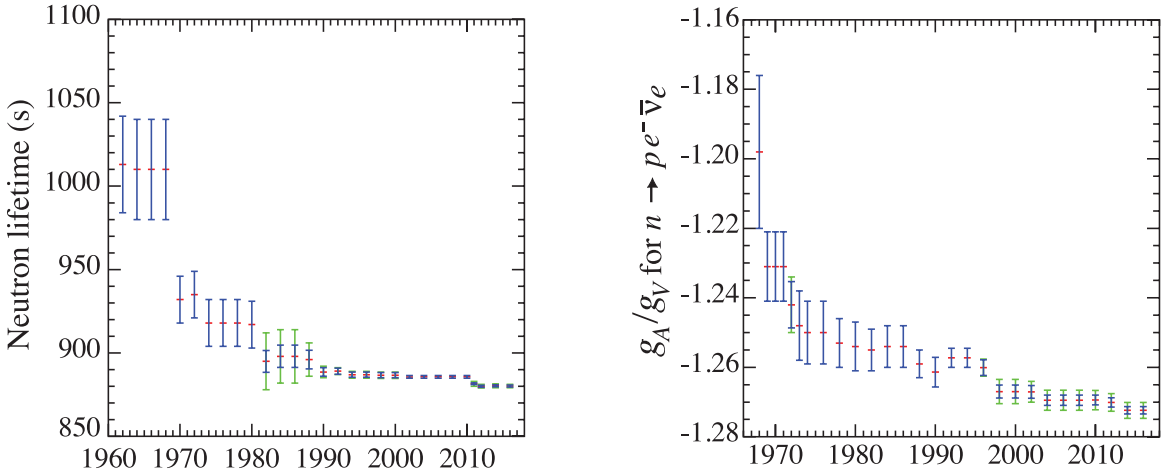

Figure 1.4: Left: neutron lifetime history plot. Right: ratio between g_A and g_V, essentially showing difference in axial and vector interactions. Figures are taken from [11].

$c_{ij} = \cos\theta_{ij}$, $s_{ij} = \sin\theta_{ij}$, with four mixing parameters — 3 angles θ_{12}, θ_{13}, θ_{23} and phase δ, which violates charge and parity symmetry. For mixing of d, s, b quarks it is called Cabibbo-Kobayashi-Maskava (CKM); for mixing of uncharged leptons ν_1, ν_2, ν_3 it is called Pontecorvo-Maki-Nakagawa-Sakata (PMNS).

The CKM matrix mixes quarks d, s, b from different generations; the PMNS matrix mixes neutrinos ν_1, ν_2, and ν_3.

$$\text{quarks: } \begin{pmatrix} u \\ d \end{pmatrix} \quad \begin{pmatrix} c \\ s \end{pmatrix} \quad \begin{pmatrix} t \\ b \end{pmatrix}, \qquad \text{leptons: } \begin{pmatrix} e \\ \nu_1 \end{pmatrix} \quad \begin{pmatrix} \mu \\ \nu_2 \end{pmatrix} \quad \begin{pmatrix} \tau \\ \nu_3 \end{pmatrix}. \tag{1.6}$$

The neutrino mixing matrix is far from the identity matrix:

$$V_{PMNS} = \begin{pmatrix} 0.693 & 0.707 & 0.145\ \mathrm{e}^{-i\delta} \\ -0.595 - 0.056\ \mathrm{e}^{i\delta} & 0.583 - 0.0573\ \mathrm{e}^{i\delta} & 0.548 \\ 0.396 - 0.085\ \mathrm{e}^{i\delta} & -0.388 - 0.086\ \mathrm{e}^{i\delta} & 0.824 \end{pmatrix} \tag{1.7}$$

In contrast to the neutrino mixing matrix, the quark mixing close to the identity matrix:

$$V_{CKM} = \begin{pmatrix} |V_{ud}| & |V_{us}| & |V_{ub}| \\ |V_{cd}| & |V_{cs}| & |V_{cb}| \\ |V_{td}| & |V_{ts}| & |V_{tb}| \end{pmatrix} \approx \begin{pmatrix} 1 & 0 & 0 \\ 0 & 1 & 0 \\ 0 & 0 & 1 \end{pmatrix} \tag{1.8}$$

Angle	Value	$\sin\theta$	$\sin^2\theta$	$\sin^2 2\theta$	Experiment type
θ_{12}	$\sim 33.0^\circ$	.545	.297	.835	solar
θ^n_{23}	$\sim 41.3^\circ$	.661	.437	.984	atmospheric and accelerator
θ^i_{23}	$\sim 49.0^\circ$	.754	.569	.981	
θ^n_{13}	$\sim 8.41^\circ$	.1463	.0214	.0838	reactor
θ^i_{13}	$\sim 8.49^\circ$	.1477	.0218	.0853	

Table 1.2: Mean values of the neutrino mixing angles and the corresponding type of experiments. The superscripts of θ_{23} and θ_{13} correspond to the neutrino mass hierarchy: n — normal, $m_3 \gg m_2 > m_1$, and i — inverted, $m_2 > m_1 \gg m_3$.

$$V_{CKM} = \begin{pmatrix} 0.97427 \pm 0.00015 & 0.22534 \pm 0.00065 & 0.00351^{+0.00015}_{-0.00014} \\ 0.22520 \pm 0.00065 & 0.97344 \pm 0.00016 & 0.0412^{+0.0011}_{-0.0005} \\ 0.00867^{+0.00029}_{-0.00031} & 0.0404^{+0.0011}_{-0.0005} & 0.999146^{+0.000021}_{-0.000046} \end{pmatrix} \tag{1.9}$$

Mixing values have been measured in multiple neutrino experiments, and their present-day values [11] are given in the Table 1.2. The values in Eq. 1.8 as well as in Table 1.2 were obtained using the standard non-relativistic quantum mechanics model, which is discussed in the next section.

1.1 In non-relativistic quantum mechanics

In quantum mechanics, a statement that something doesn't have mass and that something has zero mass are not equivalent. In the former case, it is not a mass eigenvector; in the latter, its mass eigenvalue is equal to zero. Let us consider a "standard" treatment of neutrino oscillations based on the non-relativistic quantum mechanics. We can further re-write the neutrino mixing as:

$$\begin{pmatrix} \nu_e \\ \nu_\mu \\ \nu_\tau \end{pmatrix} = \begin{pmatrix} 1 & 0 & 0 \\ 0 & c_{23} & s_{23} \\ 0 & -s_{23} & c_{23} \end{pmatrix} \begin{pmatrix} c_{13} & 0 & \mathrm{e}^{i\delta} s_{13} \\ 0 & 1 & 0 \\ \mathrm{e}^{-i\delta} s_{13} & 0 & c_{13} \end{pmatrix} \begin{pmatrix} c_{12} & s_{12} & 0 \\ -s_{12} & c_{12} & 0 \\ 0 & 0 & 1 \end{pmatrix} \begin{pmatrix} \nu_1 \\ \nu_2 \\ \nu_3 \end{pmatrix} \tag{1.10}$$

1.1.1 Two-neutrino oscillations

Consider a neutrino state $|\nu_\alpha(t)\rangle$ with a defined flavor $\alpha = e$, μ, or τ. We'll use numbers to indicate mass eigenstate ($i = 1, 2, 3$), and Greek letters α and β — for flavors. Writing it in terms of basis states $|\nu_i(t)\rangle$ with a defined mass, which satisfy Schrödinger's equation:

$$i\hbar \frac{\partial}{\partial t} |\nu_i(t)\rangle = \mathrm{H}_i |\nu_i(t)\rangle, \qquad |\nu_\alpha(t)\rangle = \sum_i V_{\alpha i} |\nu_i(t)\rangle \tag{1.11}$$

where H_i is a Hamiltonian of a i-th mass-eigenstate neutrino. It is easy to show that flavor states $|\nu_\alpha(t)\rangle$ do not satisfy Schrödinger's equation:

$$i\hbar \frac{\partial}{\partial t} |\nu_\alpha(t)\rangle = i\hbar \sum_i V_{\alpha i} \left(\frac{\partial}{\partial t} |\nu_i(t)\rangle \right) = \sum_i V_{\alpha i} \mathrm{H}_i |\nu_i(t)\rangle = \sum_i V_{\alpha i} \mathrm{H}_i \sum_\beta V^{-1}_{i\beta} |\nu_\beta(t)\rangle$$

Flavor neutrino is not a compound state of mass neutrinos but only a superposition of the latter. Therefore, mass-eigenstate neutrinos are also fermions like flavor states.

In the case when the Hamiltonian H_i doesn't depend on time it could be written

$$|\nu_i(t)\rangle = \mathrm{e}^{-\frac{i}{\hbar}\mathrm{H}_i t}\,|\nu_i(0)\rangle, \tag{1.12}$$

Let's call $|\nu_i(0)\rangle \to |\nu_i\rangle$. Stationary states satisfy

$$\mathrm{H}_i\,|\nu_i\rangle = E_i\,|\nu_i\rangle \tag{1.13}$$

Therefore, $|\nu_i(t)\rangle = \mathrm{e}^{-\frac{i}{\hbar}\mathrm{H}_i t}\,|\nu_i\rangle$, using the basis in Eq. (1.11), we get

$$|\nu_\alpha(t)\rangle = \sum_i V_{\alpha i}\,\mathrm{e}^{-\frac{i}{\hbar}\mathrm{H}_i t}\,|\nu_i\rangle \tag{1.14}$$

In the two-neutrino case, the mixing matrix V can be written as follows:

$$V = \begin{pmatrix} \cos\theta & \sin\theta \\ -\sin\theta & \cos\theta \end{pmatrix} \tag{1.15}$$

where θ is a mixing angle.

$$\begin{cases} |\nu_e(t)\rangle = \cos\theta\,|\nu_1(t)\rangle + \sin\theta\,|\nu_2(t)\rangle \\ |\nu_\mu(t)\rangle = -\sin\theta\,|\nu_1(t)\rangle + \cos\theta\,|\nu_2(t)\rangle \end{cases} \tag{1.16}$$

States $|\nu_i(t)\rangle$ are orthonormal — $\langle\nu_i|\nu_j\rangle = \delta_{ij}$. The transition amplitude for the $\nu_e \to \nu_\mu$ process is

$$\begin{aligned} A_{\nu_e\to\nu_\mu} = \langle\nu_\mu(t)|\nu_e\rangle = \left(-\langle\nu_1|\sin\theta\,\mathrm{e}^{-iE_1t} + \langle\nu_2|\cos\theta\,\mathrm{e}^{-iE_2t}\right)(\cos\theta\,|\nu_1\rangle + \sin\theta\,|\nu_2\rangle) = \\ = \cos\theta\,\sin\theta\,\left(-\mathrm{e}^{-iE_1t} + \mathrm{e}^{-iE_2t}\right) \end{aligned} \tag{1.17}$$

The modulus squared of the amplitude is the probability for the transition $\nu_e \to \nu_\mu$

$$\begin{aligned} P_{\nu_e\to\nu_\mu} = |A_{\nu_e\to\nu_\mu}|^2 = \cos^2\theta\sin^2\theta\,\left(-\mathrm{e}^{-iE_1t} + \mathrm{e}^{-iE_2t}\right)\left(-\mathrm{e}^{iE_1t} + \mathrm{e}^{iE_2t}\right) = \\ = \frac{1}{4}\sin^2 2\theta\,\left(2 - \mathrm{e}^{-i(E_1-E_2)t} - \mathrm{e}^{-i(E_2-E_1)t}\right) = \frac{1}{4}\sin^2 2\theta\,\left(2 - 2\cos(E_2-E_1)t\right) \end{aligned} \tag{1.18}$$

$$P_{\nu_e\to\nu_\mu} = \sin^2 2\theta\,\sin^2\frac{(E_2-E_1)t}{2} \tag{1.19}$$

In the ultra-relativistic limit (true for most neutrino sources, $m_i \ll E_i$)[1], using the natural system of units where $\hbar = c = 1$, the energy-momenta relations are then:

$$\begin{aligned} E_i &\approx p_i + \frac{m_i^2}{2p_i}\,, & E_2 - E_1 &= \frac{1}{2p}(m_2^2 - m_1^2) = \frac{\Delta m_{21}^2}{2p} \\ L &\approx ct, & p_1 &\approx p_2 = p \approx E\,c^{-1} \end{aligned}$$

Then the probability $P_{\nu_e\to\nu_\mu}$ looks like this

$$\boxed{P_{\nu_e\to\nu_\mu} = \sin^2 2\theta\,\sin^2\frac{\Delta m_{21}^2\,L}{4E}} \tag{1.20}$$

[1]The reader should ask here — *why did we start with non-relativistic equation in the first place?*

Switching to SI units using Planck constant value of $\hbar = 6.58 \times 10^{-22}$ MeV s, and value for the speed of light $c = 3 \times 10^8$ m s^{-1},

$$\frac{\Delta m^2_{12}\, L}{4E} \to \hbar^{-1} c^3 \frac{\Delta m^2_{21}\, L}{4E} \approx 1.27 \left(\frac{\Delta m^2_{21} c^4}{\mathrm{eV}^2}\right) \left(\frac{\mathrm{MeV}}{E}\right) \left(\frac{L}{\mathrm{km}}\right) \tag{1.21}$$

Introducing oscillation length,

$$L_{osc} = \frac{4\pi E}{\Delta m^2_{12}} \tag{1.22}$$

Eq. (1.20) can be written as

$$P_{\nu_e \to \nu_\mu} = \sin^2 2\theta \, \sin^2 \frac{\pi L}{L_{osc}} \tag{1.23}$$

In Fig. 1.5 there are two probabilities shown — transition $P_{\alpha\beta}$ from one flavor into the other, and the survival probability of the original flavor $P_{\alpha\alpha} = 1 - P_{\alpha\beta}$, as functions of baseline L measured in oscillation lengths L_{osc}, at mixing angle value $\sin^2 2\theta_{12} = 0.84$, [11]. If a detector is located from the neutrino source at length L equal to an integer number of oscillation lengths $n \times L_{osc}$ the transition probability $P_{\nu_e \to \nu_\mu}$ is equal to 0. When the baseline is $L = n \times L_{osc}/2$, then the transition probability $P_{\nu_e \to \nu_\mu} = \sin^2 2\theta$, in the two-neutrino approach. Fig. 1.6 shows the survival probability for an electron neutrino as a function of both energy and distance.

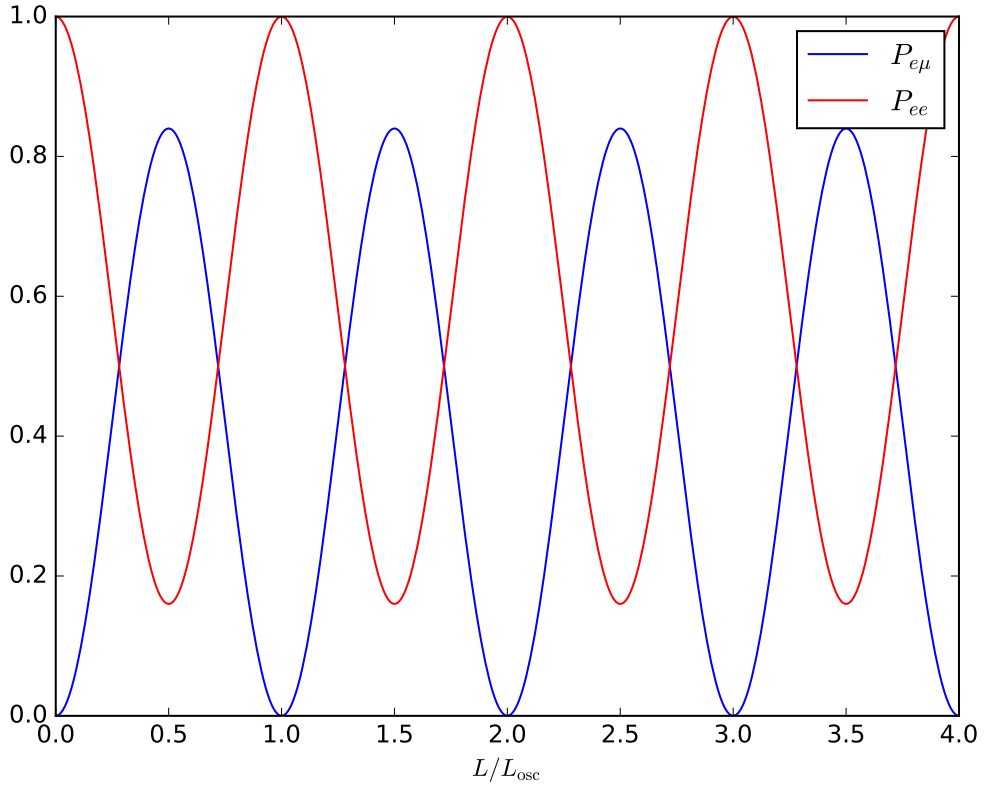

Figure 1.5: Probability of $\nu_e \to \nu_\mu$ transition, and survival probability for ν_e, according to the Eq. (1.20) with $\sin^2 2\theta_{12} = 0.84$.

It is worth noting that, although the differences between neutrino masses are likely small compared to their energies, strictly speaking the equations above simply ignore this fact, being a very crude estimation. In the derivation

$$E_2 - E_1 = p_2 - p_1 + \frac{1}{2}\frac{m_2^2}{p_2} - \frac{1}{2}\frac{m_1^2}{p_1} + \dots \tag{1.24}$$

we ignored the term $p_2 - p_1$ which is on the same order of magnitude as the term $m_2^2/p_2 - m_1^2/p_1$. We are going to be doing the same mathematical mistake to obtain three-neutrino oscillation probability, along with the incorrect starting point of applying Schrödinger's equation for non-relativistic systems to ultra-relativistic neutrinos. A much more proper derivation will be discussed in the section 1.2.

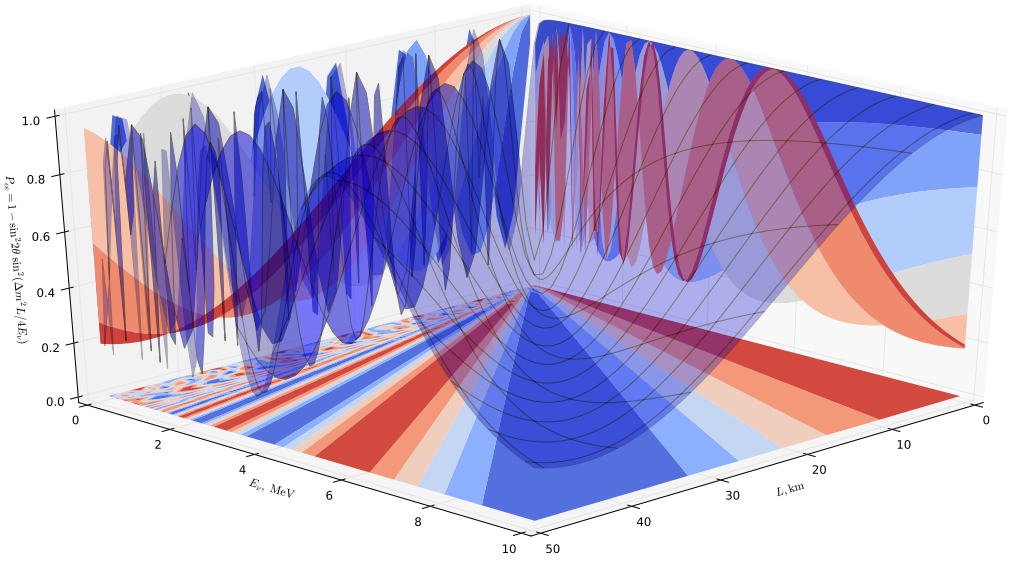

Figure 1.6: Survival probability of electron antineutrinos as a function of their energy and baseline.

1.1.2 Three-neutrino oscillations

Using the expansion in Eq. (1.11), we find formulae for the amplitude and probability of transition between different types (flavors) of neutrinos

$$\begin{aligned} A_{\nu_\alpha \to \nu_\beta} &= \langle \nu_\beta(t) | \nu_\alpha \rangle = \\ &= \left(\langle \nu_1 | V_{\beta 1}\, \mathrm{e}^{-iE_1 t} + \langle \nu_2 | V_{\beta 2}\, \mathrm{e}^{-iE_2 t} + \langle \nu_3 | V_{\beta 3}\, \mathrm{e}^{-iE_3 t} \right) \left(V_{\alpha 1}\, |\nu_1\rangle + V_{\alpha 2}\, |\nu_2\rangle + V_{\alpha 3}\, |\nu_3\rangle \right) = \\ &= V_{\alpha 1} V_{\beta 1} \mathrm{e}^{-iE_1 t} + V_{\alpha 2} V_{\beta 2} \mathrm{e}^{-iE_2 t} + V_{\alpha 3} V_{\beta 3} \mathrm{e}^{-iE_3 t} = \sum_i \mathrm{e}^{-iE_i t} V_{\alpha i} V_{\beta i} \end{aligned} \tag{1.25}$$

$$A_{\nu_\alpha \to \nu_\beta} = \sum_i \mathrm{e}^{-iE_i t} V_{\alpha i} V_{\beta i} \tag{1.26}$$

Transition probability for $\nu_e \to \nu_\mu$

$$P_{\nu_e\to\nu_\mu} = |A_{\nu_e\to\nu_\mu}|^2 = \sum_i \mathrm{e}^{-iE_it} V_{\alpha i} V_{\beta i} \sum_j \mathrm{e}^{iE_jt} V^*_{\alpha j} V^*_{\beta j} =$$

$$= \sum_i |V_{\alpha i}|^2 |V_{\beta i}|^2 + 2\mathrm{Re}\left[\sum_{i>j} \mathrm{e}^{-i(E_j-E_i)t} V_{\alpha j} V_{\beta j} V^*_{\alpha i} V^*_{\beta i}\right] \quad (1.27)$$

In the case when the CP-symmetry is not violated, phase δ is equal to 0, and the mixing matrix in Eq. (1.8) is real. Thus, we can write the expression for $P_{\nu_e\to\nu_\mu}$ as follows:

$$P_{\nu_\alpha\to\nu_\beta} = \sum_i V^2_{\alpha i} V^2_{\beta i} + 2\sum_{i>j} V_{\alpha j} V_{\beta j} V_{\alpha i} V_{\beta i} \cos(E_j - E_i)t \quad (1.28)$$

Using the unitarity condition on the mixing matrix $VV^\dagger = I, \quad \sum V_{\alpha i} V^*_{\beta i} = \delta_{\alpha\beta}$, where we call $V_{\alpha i} = V_{i\alpha}$, the following can be shown

$$\sum_i |V_{\alpha i}|^2 |V_{\beta i}|^2 + 2\mathrm{Re}\left[\sum_{i>j} V_{\alpha i} V_{\beta j} V^*_{\alpha i} V^*_{\beta i}\right] = \delta_{\alpha\beta} \quad (1.29)$$

After doing some algebra, and using Eq. (1.29) we get

$$P_{\nu_\alpha\to\nu_\beta} = \delta_{\alpha\beta} - 2\sum_{i>j} V_{\alpha j} V_{\beta j} V_{\alpha i} V_{\beta i} (1 - \cos(E_i - E_j)t) \quad (1.30)$$

$$\boxed{P_{\nu_\alpha\to\nu_\beta} = \delta_{\alpha\beta} - 4\sum_{i>j} V_{\alpha i} V_{\alpha j} V_{\beta i} V_{\beta j} \sin^2 \frac{\Delta m^2_{ij} L}{4E}} \quad (1.31)$$

Eq. (1.31) is the probability formula for the transition $\nu_\alpha \to \nu_\beta$, using the full 3×3 mixing matrix. Fig. 1.7 shows the probabilities of an electron neutrino (ν_e) to become a ν_μ, a ν_τ, or to remain the same.

1.1.3 Obtaining two-neutrino formulae from three-neutrino oscillations

If we neglect the θ_{13} ($\theta_{13} \approx 8.3°$, $\sin\theta_{13} \sim 0.145$), in this approximation

$$V = \begin{pmatrix} c_{12} & s_{12} & 0 \\ -s_{12}c_{23} & c_{12}c_{23} & s_{23} \\ s_{12}s_{23} & -c_{12}s_{23} & c_{23} \end{pmatrix} \quad (1.32)$$

Since $V_{e1} = 0$, the most simple equations are for the transitions $\nu_e \to \nu_\mu,\ \nu_\tau$. Substituting mixing matrix elements from Eq. (1.32) to the Eq. (1.31), we get

$$P_{\nu_e\to\nu_\mu} = c^2_{23} \sin^2 2\theta_{12} \sin^2 \frac{\Delta m^2_{12} L}{4E} \quad (1.33)$$

$$P_{\nu_e\to\nu_\tau} = s^2_{23} \sin^2 2\theta_{12} \sin^2 \frac{\Delta m^2_{12} L}{4E} \quad (1.34)$$

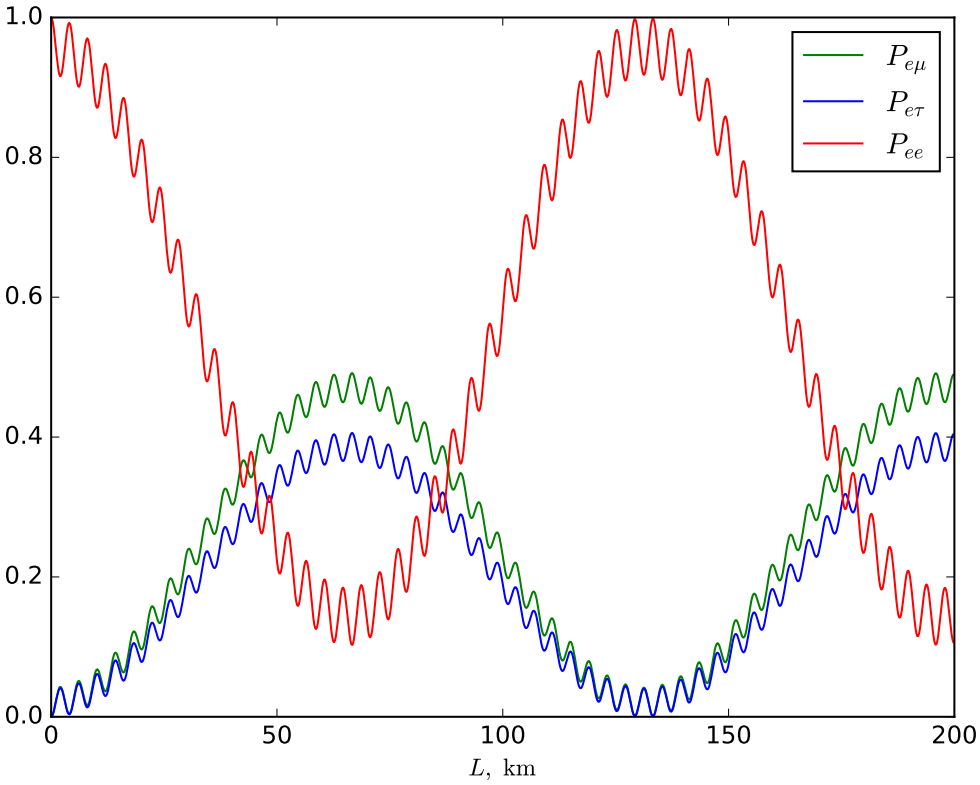

Figure 1.7: Probability as a function of baseline for $\nu_e \to \nu_\mu$ and $\nu_e \to \nu_\tau$ transitions, and survival probability for ν_e, according to the Eq. (1.31) with $\sin^2\theta_{12} = .51$, $\sin^2\theta_{23} = .307$, $\sin^2\theta_{13} = .021$, $\delta = 0$, $\Delta m^2_{21} = 7.53\times10^{-5}$ eV^2, $\Delta m^2_{31} \approx \Delta m^2_{32} = 2.45\times10^{-3}$ eV^2, $E = 4$ MeV (average reactor antineutrino energy).

Survival probability for ν_e (neglecting θ_{13}):

$$P_{\nu_e\to\nu_e} = 1 - P_{\nu_e\to\nu_\mu} - P_{\nu_e\to\nu_\tau} = 1 - \sin^2 2\theta_{12}\sin^2\frac{\Delta m^2_{12}L}{4E} \tag{1.35}$$

There is a correspondence between measured values Δm^2 with solar and atmospheric experiments $\Delta m^2_{12} \Leftarrow \Delta m^2_{\text{sol}}$, $\Delta m^2_{23} \Leftarrow \Delta m^2_{\text{atm}}$, $\frac{\Delta m^2_{12}}{\Delta m^2_{23}} \ll 1$.

If we consider such L/E that $\frac{\Delta m^2_{12}L}{4E} \ll 1$ (meaning large compared to the oscillation length, ignoring dimension here) the probability formula for $\nu_\mu \to \nu_\tau$ becomes

$$P_{\nu_\mu\to\nu_\tau} = \sin^2 2\theta_{23}\ \sin^2\frac{\Delta m^2_{23}\,L}{4E} \tag{1.36}$$

At the same time, equations for electron neutrino ν_e:

$$P_{\nu_e\to\nu_\mu} \approx P_{\nu_e\to\nu_\tau} \approx 0, \qquad P_{\nu_e\to\nu_e} \approx 1 \tag{1.37}$$

1.1.4 Sterile neutrino

It is still unclear whether there is a fourth neutrino, so called sterile, although recent data from Daya Bay experiment [35] suggest the it is less likely (at least in their

region of neutrino parameters). There are different models on how to include the fourth neutrino.

The simplest way is to add *sterile* flavor along the fourth mass eigenstate:

$$\begin{pmatrix}\nu_e\\ \nu_\mu\\ \nu_\tau\\ \nu_s\end{pmatrix} = \begin{pmatrix}V_{e1} & V_{e2} & V_{e3} & V_{e4}\\ V_{\mu1} & V_{\mu2} & V_{\mu3} & V_{\mu4}\\ V_{\tau1} & V_{\tau2} & V_{\tau3} & V_{\tau4}\\ V_{s1} & V_{s2} & V_{s3} & V_{s4}\end{pmatrix}\begin{pmatrix}\nu_1\\ \nu_2\\ \nu_3\\ \nu_4\end{pmatrix} \tag{1.38}$$

In the case with this 4th type of neutrino, the oscillation probability would have the form in the simple 2ν model [34]:

$$P^{2\nu}(\bar{\nu}_e \to \bar{\nu}_s) = \sin^2 2\theta_{new} \sin^2 \frac{1.27\Delta m^2_{new}\left[\mathrm{eV}^2\right] L\,[\mathrm{m}]}{E_{\bar{\nu}_e}\,[\mathrm{MeV}]} \tag{1.39}$$

For new oscillation/mixing parameters [36] $\sin^2 2\theta_{new} \approx 0.115$ and $\Delta m^2_{new} \approx 1\ \mathrm{eV}^2$, the oscillation probability Eq. (1.39) of an electron antineutrino to the sterile $P(\bar{\nu}_e \to \bar{\nu}_s)$ is shown in Fig. 1.8 at the region of antineutrino energy $E_{\bar{\nu}_e} \gtrsim 1.8$ MeV and baseline $L \approx 4 - 8$ m, accessible to study in mTC. As one can see, there are two particularly interesting regions: the "valley" at $E_{\bar{\nu}_e} \sim 2$ MeV and baseline $L \sim 4.5 - 5.5$ m, and the "peak" around $E_{\bar{\nu}_e} \sim 4$ MeV (mean energy of observed antineutrino).

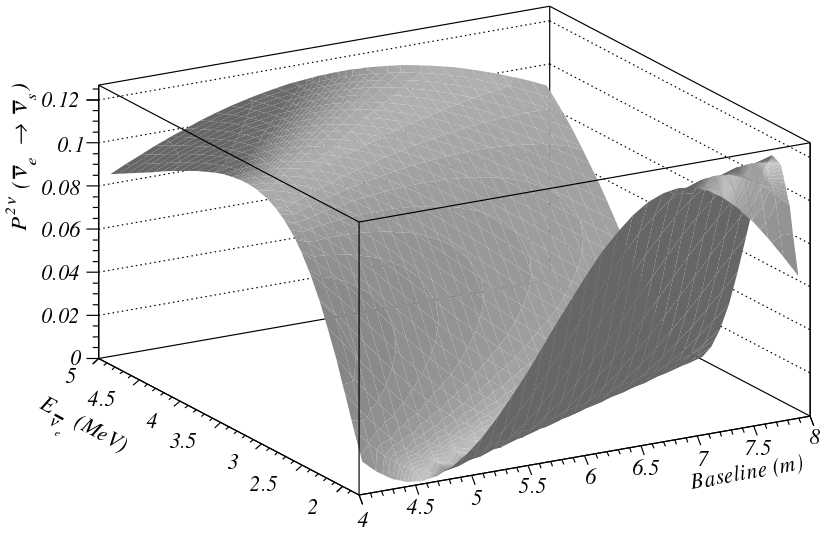

Figure 1.8: Oscillation probability of electron antineutrino into a new type of neutrino (region accessible to study in the mTC at NIST reactor confinement building).

1.1.5 Neutrino oscillations in matter

Let's define the following state in flavor neutrino basis

$$\Psi_{(f)} = \begin{pmatrix}\nu_e\\ \nu_\mu\\ \nu_\tau\end{pmatrix} = V_{PMNS}\Psi_{(m)}, \qquad \Psi_{(m)} = \begin{pmatrix}\nu_1\\ \nu_2\\ \nu_3\end{pmatrix} \tag{1.40}$$

index (f) corresponds to flavor basis, index (m) — mass basis; with normalization condition $\int d\mathbf{x}|\nu_i|^2 = 1$. Schrödinger equation for the state $\Psi_{(f)}$:

$$i\begin{pmatrix}\dot{\nu}_e\\ \dot{\nu}_\mu\\ \dot{\nu}_\tau\end{pmatrix} = \hat{E}\begin{pmatrix}\nu_e\\ \nu_\mu\\ \nu_\tau\end{pmatrix} + \hat{W}\begin{pmatrix}\nu_e\\ \nu_\mu\\ \nu_\tau\end{pmatrix} \tag{1.41}$$

$$V^+\hat{E}V = \mathrm{diag}(E_1, E_2, E_3), \qquad \hat{W} = \mathrm{diag}(W, 0, 0) \tag{1.42}$$

The interaction matrix $\hat{W}$ in Eq. (1.42) takes into account that muon and tau neutrinos cannot scatter off an electron via W-boson exchange.

$$\nu_e e \to \nu_e e\ (CC + NC), \qquad \nu_\mu e \nrightarrow \nu_\mu e\ (CC), \qquad \nu_\tau e \nrightarrow \nu_\tau e\ (CC) \tag{1.43}$$

System of Schrödinger equations on state $\Psi_{(m)}$:

$$i\begin{pmatrix}\dot{\nu}_1\\ \dot{\nu}_2\\ \dot{\nu}_3\end{pmatrix} = \begin{pmatrix}E_1 & & \\ & E_2 & \\ & & E_3\end{pmatrix}\begin{pmatrix}\nu_1\\ \nu_2\\ \nu_3\end{pmatrix} + V^+\hat{W}V\begin{pmatrix}\nu_1\\ \nu_2\\ \nu_3\end{pmatrix} \tag{1.44}$$

$$T^+\left(V^+\hat{E}V + V^+\hat{W}V\right)T = T^+V^+\left(\hat{E} + \hat{W}\right)VT = \mathrm{diag}((H_M)_1, (H_M)_2, (H_M)_3) \tag{1.45}$$

$$iT^+\dot{\Psi}_{(m)} = (H_M)T^+\Psi_{(m)}, \qquad i\dot{\Psi}_{(M)} = (H_M)\Psi_{(M)} \tag{1.46}$$

$$\Psi_{(M)} = T^+\Psi_{(m)} = T^+V^+\Psi_{(f)}, \qquad i\dot{\Psi}_{(M)} = (H_M)\Psi_{(M)} \tag{1.47}$$

In two-neutrino case

$$\begin{pmatrix}H_1 & 0\\ 0 & H_2\end{pmatrix} = \begin{pmatrix}\mathrm{c}_m & -\mathrm{s}_m\\ \mathrm{s}_m & \mathrm{c}_m\end{pmatrix}\begin{pmatrix}E_1 - W\mathrm{c}^2 & -W\mathrm{cs}\\ -W\mathrm{cs} & E_2 - W\mathrm{s}^2\end{pmatrix}\begin{pmatrix}\mathrm{c}_m & \mathrm{s}_m\\ -\mathrm{s}_m & \mathrm{c}_m\end{pmatrix} \tag{1.48}$$

$$T^+V^+ = (VT)^+ = \begin{pmatrix}\cos(\theta+\theta_m) & -\sin(\theta+\theta_m)\\ \sin(\theta+\theta_m) & \cos(\theta+\theta_m)\end{pmatrix} \tag{1.49}$$

where $T, V = g(\theta_m), g(\theta) \in SO(2)$, $g(\theta)g(\theta_m) = g(\theta+\theta_m) \in SO(2)$.

In Eq. (1.23) making the following change of variables, to get probability of two neutrino oscillations in matter

$$L_{osc}^{-1} = \frac{1}{2\pi}(E_1 - E_2) \to L_m^{-1} = \frac{1}{2\pi}(H_1 - H_2) \tag{1.50}$$

$$\theta \to \theta + \theta_m \tag{1.51}$$

Probability of two-neutrino oscillation in Eq. (1.23) when there is a medium with electrons is the following

$$P_{\nu_\alpha\to\nu_\beta} = \sin^2 2(\theta+\theta_m)\ \sin^2\frac{\pi L}{L_m} \tag{1.52}$$

In the absence of a medium (i.e. electrons) $\theta_m = 0, H_{1,2} = E_{1,2}$, and Eq. (1.52) is becoming Eq. (1.23), probability without matter, which we already obtained previously.

$H_1,\ H_2,\ \theta_m$ can be found from Eq. (1.48):

$$\mathrm{s}_m\left[(E_1 - W\mathrm{c}^2)\mathrm{c}_m + (W\mathrm{cs})\mathrm{s}_m\right] + \mathrm{c}_m\left[(-W\mathrm{cs})\mathrm{c}_m + (E_2 - W\mathrm{s}^2)(-\mathrm{s}_m)\right] = 0 \quad (1.53)$$

$$H_1 = \mathrm{c}_m\left[(E_1 - W\mathrm{c}^2)\mathrm{c}_m + (W\mathrm{cs})\mathrm{s}_m\right] - \mathrm{s}_m\left[(-W\mathrm{cs})\mathrm{c}_m + (E_2 - W\mathrm{s}^2)(-\mathrm{s}_m)\right] \quad (1.54)$$

$$H_2 = \mathrm{s}_m\left[(E_1 - W\mathrm{c}^2)\mathrm{s}_m - (W\mathrm{cs})\mathrm{c}_m\right] + \mathrm{c}_m\left[(-W\mathrm{cs})\mathrm{s}_m + (E_2 - W\mathrm{s}^2)\mathrm{c}_m\right] \quad (1.55)$$

From Eq. (1.53) it can be shown:

$$\sin 2\theta_m\left((E_1 - E_2) - W\cos 2\theta\right) = W\sin 2\theta\cos 2\theta_m \quad (1.56)$$

$$\sin^2 2\theta_m = \frac{W^2\sin^2 2\theta}{(E_1 - E_2 - W\cos 2\theta)^2 + W^2\sin^2 2\theta} = \frac{\sin^2 2\theta}{(l_\nu^{-1}l_0 - \cos 2\theta)^2 + \sin^2 2\theta} \quad (1.57)$$

where $l_0 = 2\pi W^{-1} \propto \pi A/G_F N_A Z\rho$ makes the scale at which the *matter* effect *matters* [37], A — atomic mass number, Z — atomic number (charge), N_A — Avogadro constant, ρ — matter density, l_ν — vacuum oscillation length as in Eq. (1.22):

$$l_\nu = 2\pi(E_1 - E_2)^{-1} = -4\pi\frac{E}{\Delta m^2_{12}} \quad (1.58)$$

Using Eqs. (1.56) and (1.57) we obtain, for calculating the probability in Eq. (1.52)

$$\sin^2 2(\theta + \theta_m) = \frac{\sin^2 2\theta}{(l_\nu l_0^{-1})^2 - 2l_\nu l_0^{-1}\cos 2\theta + 1} = R\sin^2 2\theta \quad (1.59)$$

$$L_m = 2\pi(H_1 - H_2)^{-1} = \frac{l_\nu}{\sqrt{(l_\nu l_0^{-1})^2 - 2l_\nu l_0^{-1}\cos 2\theta + 1}} = l_\nu\sqrt{R}, \quad (1.60)$$

where the resonance parameter R is introduced as follows:

$$R = R(l_\nu l_0^{-1}, \cos 2\theta) = \frac{1}{(l_\nu l_0^{-1})^2 - 2l_\nu l_0^{-1}\cos 2\theta + 1} \quad (1.61)$$

Therefore, the two-neutrino oscillation probability in matter from Eq. (1.52), using values for angle and length from Eqs. (1.59) and (1.60), has become

$$\boxed{P_{\nu_\alpha\to\nu_\beta} = R\sin^2 2\theta\ \sin^2\frac{\pi L}{l_\nu\sqrt{R}}} \quad (1.62)$$

A formula, analogous to Eq. (1.62), was first obtained by Mikheev and Smirnov [38, 39]. Resonance behavior of neutrino oscillation probability in the presence of matter, Eq. (1.61), is known as the MSW–effect (Mikheev, Smirnov, Wolfenstein [38, 40]). Fig. 1.9 illustrates the behavior.

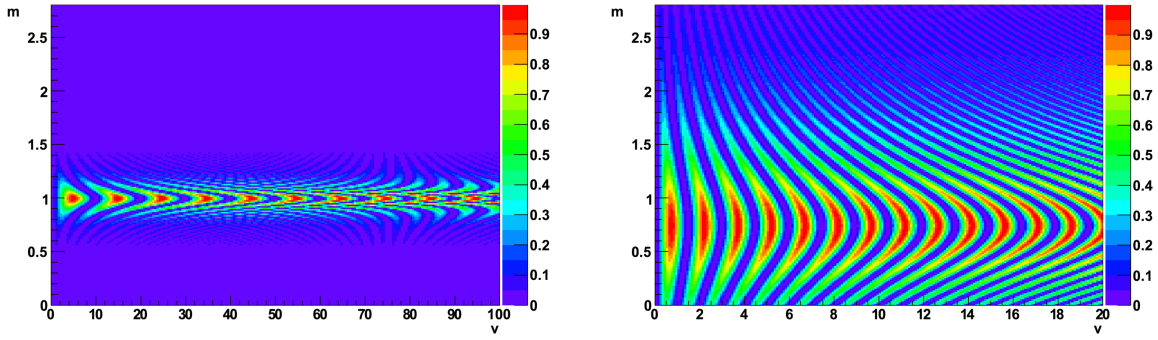

(a) $\sin^2 2\theta = 0.01$ (b) $\sin^2 2\theta = 0.45$

Figure 1.9: Neutrino oscillation probability in matter for different values of the mixing angle in matter. $m = l_\nu/l_0$, $v = L/l_\nu$, figure is adapted from [41] with the author's permission.

1.2 In quantum field theory

Let us discuss general definitions used in quantum field theory (QFT). Lagrange's function $L(t)$ and Lagrange's density (Lagrangian) $\mathscr{L}(\mathbf{x},\ t)$:

$$L(t) = \int d\mathbf{x}\ \mathscr{L}(\mathbf{x},\ t), \qquad \mathscr{L} = \mathscr{L}_0 + \mathscr{L}_{int} \tag{1.63}$$

$\mathscr{L}_0$ — Lagrangian of free fields, $\mathscr{L}_{int}$ — Lagrangian describing interaction between the fields.

To calculate probability of a scattering process it would be good to know the S–matrix (scattering matrix). The action $\mathscr{A}$ and S–matrix have the following relation:

$$\mathscr{A} = \int dt\ L(t) = \int dx\ \mathscr{L}(x), \qquad S = T\ e^{i\mathscr{A}_{int}} \tag{1.64}$$

$\mathscr{A}_{int}$ — action of interaction, T — time-ordering

$$\mathscr{A}_{int} = \int dx\ \mathscr{L}_{int}(x), \qquad T(\psi(x)\bar{\psi}(y)) = \begin{cases} \psi(x)\overline{\psi}(y), & x^0 > y^0 \\ \pm\overline{\psi}(y)\psi(x), & x^0 < y^0 \end{cases} \tag{1.65}$$

The sign + in Eq. (1.65) is chosen if field ψ describes bosons; − sign is for fermionic fields. The axiomatic S–matrix for plane waves has the following form [42]:

$$S(p) - 1 = (2\pi)^4\ \delta^4\left(\sum_{in} p_i - \sum_{out} p_f\right)\ i\mathscr{M}(p), \tag{1.66}$$

where $\{p_i\}$, $\{p_f\}$ are momentum sets of initial and final particles. Matrix element $\mathscr{M}$ can be calculated using Feynman diagrams. In general interpretation of Feynmnan diagrams, we can think of a diagram as an elementary process — an elementary scattering or decay process, which takes place in an infinitely small volume of space-time, i.e. point interaction.

The main question is how to consider such a process on a macro-level — with finite time and space of process localization. There are two approaches; both include an introduction of wave packets (as a consequence of the space-time constraint):

- *Non-local quantum field theory* [43], based on modified commutation relations among creation and annihilation operators, where wave packets are introduced in the Lagrangian. In this approach, wave packets automatically satisfy the equation of motion, the Dirac equation. This approach allows one to work with space regions smaller than the Compton wavelength of a corresponding particle. The scale is neither macroscopic nor infinitely small.
- *Introducing densities of initial and final particles* at the source and detector location, which are finite in space-time. In this approach, fields in Lagrangian don't contain any spread (either momentum or space-time) and commutation relations for creation/annihilation operators are kept canonical. Wave packets are built as a superposition of plane waves and don't contain anti-particles, which constrains the region of spacial localization of a wave packet — not smaller than a Compton wavelength.

We consider the latter for introducing wave packets and the process of their localization.

1.2.1 Wave-packets

Fields in the Lagrangian could be expressed in terms of creation/annihilation operators in momentum space

$$\Psi(x) = \int \frac{d^3p}{(2\pi)^3} \frac{1}{\sqrt{2\,E_{\mathbf{p}}}} \sum_s \left[a^s_{\mathbf{p}}\, e^{-i\,px}\; u^s(\mathbf{p}) + b^s_{\mathbf{p}}\, e^{i\,px}\; v^s(\mathbf{p}) \right] \tag{1.67}$$

$$\bar{\Psi}(x) = \int \frac{d^3p}{(2\pi)^3} \frac{1}{\sqrt{2\,E_{\mathbf{p}}}} \sum_s \left[a^{s\,+}_{\mathbf{p}}\, e^{i\,px}\; u^{s\,+}(\mathbf{p}) + b^{s\,+}_{\mathbf{p}}\, e^{-i\,px}\; v^{s\,+}(\mathbf{p}) \right] \tag{1.68}$$

Let's define $|\mathbf{p}\rangle$ as a one-particle state with defined momentum p, on mass-shell

$$|\mathbf{p}\rangle = \sqrt{2\,E_{\mathbf{p}}} a^+_p |0\rangle \tag{1.69}$$

with energy

$$E_{\mathbf{p}} = \sqrt{\mathbf{p}^2 + m^2}. \tag{1.70}$$

Writing a relationship that we would further need for calculating the amplitude $\langle \text{out}|(S-1)|\text{in}\rangle$; if the field $\Psi^+(x)$ and the state $|\mathbf{p}\rangle$ correspond to the same particle, the following is correct $[a_{\mathbf{k}},\ a^+_{\mathbf{p}}]_\pm = \delta(\mathbf{k}-\mathbf{p})$:

$$\begin{aligned} \Psi^+(x)|\mathbf{p}\rangle = \int \frac{d^3k}{(2\pi)^3} \frac{1}{\sqrt{2\,E_{\mathbf{k}}}} a_{\mathbf{k}}\, e^{-i\,kx}\; v^+(\mathbf{k})\; \sqrt{2\,E_{\mathbf{p}}} a^+_{\mathbf{p}} |0\rangle = \\ = \int \frac{d^3k}{(2\pi)^3} \frac{1}{\sqrt{2\,E_{\mathbf{k}}}}\, e^{-i\,kx}\; v^+(\mathbf{k})\; \sqrt{2\,E_{\mathbf{p}}} \delta(\mathbf{k}-\mathbf{p}) |0\rangle \end{aligned} \tag{1.71}$$

$$\Psi^+(x)|\mathbf{p}\rangle = e^{-i\,px}\; v^+(\mathbf{p})\; |0\rangle \tag{1.72}$$

We can make a one-particle state as a superposition of one-particle states $|\mathbf{k}\rangle$, as in Eq. (1.69), with defined momenta k, which we would call a *wave packet*

$$|\varphi\rangle = \int \frac{d^3k}{(2\pi)^3} \frac{1}{\sqrt{2\,E_k}} \varphi(\mathbf{k}) |\mathbf{k}\rangle \tag{1.73}$$

where $\varphi(\mathbf{k})$ — Fourier transform of coordinate-space field. State $|\varphi\rangle$ does not have a defined exact mass (analogous to a particle with a fixed life time which has a width in mass spectrum). Normalization:

$$\int \frac{d^3k}{(2\pi)^3}|\varphi(\mathbf{k})|^2 = 1 \qquad \Rightarrow \qquad \langle\varphi|\varphi\rangle = 1. \tag{1.74}$$

We can consider an example where the initial state is a two-particle state (two wave packets) and the final state is a multi-particle state (several wave packets). The transition probability would look like this:

$$\mathcal{P} = |\langle\varphi_1\varphi_2\ldots|S-1|\varphi_{\mathcal{A}}\varphi_{\mathcal{B}}\rangle|^2 \tag{1.75}$$

Assuming collinearity of wave functions, a factor $\exp(-i\mathbf{b}\mathbf{k}_{\mathcal{B}})$ appears, where $\mathbf{b}$ is an impact parameter. Thus, the initial state can be written as [44]

$$|\text{in}\rangle = |\varphi_{\mathcal{A}}\varphi_{\mathcal{B}}\rangle = \int \frac{d^3k_{\mathcal{A}}}{(2\pi)^3}\int \frac{d^3k_{\mathcal{B}}}{(2\pi)^3}\,\frac{\varphi_{\mathcal{A}}(\mathbf{k}_{\mathcal{A}})\varphi_{\mathcal{B}}(\mathbf{k}_{\mathcal{B}})e^{-i\mathbf{b}\mathbf{k}_{\mathcal{B}}}}{\sqrt{2E_{\mathcal{A}}2E_{\mathcal{B}}}}\,|\mathbf{k}_{\mathcal{A}}\mathbf{k}_{\mathcal{B}}\rangle \tag{1.76}$$

and for the final state we have

$$\langle\text{out}| = \langle\varphi_1\varphi_2\ldots| = \left(\prod_f \int \frac{d^3p_f}{(2\pi)^3}\,\frac{\varphi_f(\mathbf{p}_f)}{\sqrt{2\,E_f}}\right)\,\langle\mathbf{p}_1\mathbf{p}_2\ldots| \tag{1.77}$$

Initial and final states are the direct product of one-particle states, as long as measurements have taken place respectively at the infinite long past $t\to-\infty$ and at the infinite long future $t\to+\infty$, [45].

1.2.2 Interaction Lagrangian

It is highly interesting to describe the process of neutrino production, its propagation and subsequent detection in a detector located at some distance L from production point, as a whole one process, as schematically shown in Fig. 1.10.

It is important to note that in this approach neutrinos are neither in initial $|\text{in}\rangle$ nor final $|\text{out}\rangle$ states. It is in contrast to the usual treatment of such reactions as separate: production reaction in the source where neutrinos are in $|\text{in}\rangle$ state, and detection reaction in the detector where neutrinos are in $|\text{out}\rangle$ — calculating amplitudes separately for each process.

This approach with a virtual neutrino and macroscopic distances doesn't contradict the cluster-decomposition principle [45]. The interaction Lagrangian

$$\mathscr{L}(x) = \mathscr{L}_s(x) + \mathscr{L}_d(x) \tag{1.78}$$

$\mathscr{L}_s(x)$ — interaction Lagrangian for the source reaction, $\mathscr{L}_d(x)$ — interaction Lagrangian for the detector reaction.

In order to describe the process of β–decay, Fermi was first to introduce an effective interaction Hamiltonian [9], which can be written as a product *current* $\times$ *current*

$$\mathscr{H}_{int} = \frac{G_F}{\sqrt{2}}\,\bar{p}\gamma_\mu(1-\lambda\gamma_5)n\;\bar{e}\gamma^\mu(1-\gamma_5)\nu, \qquad \mathscr{H}_{int} = \frac{G_F}{\sqrt{2}}J^\dagger_\mu J^\mu + \text{h.c.} \tag{1.79}$$

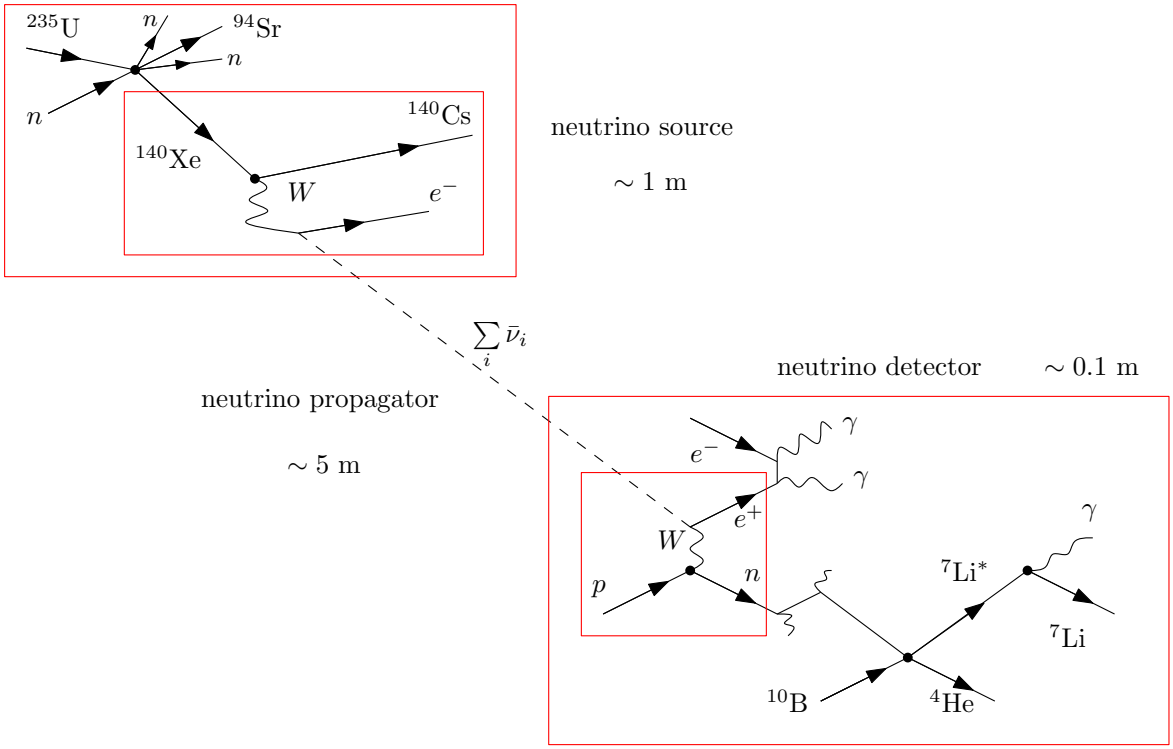

Figure 1.10: Neutrino production, propagation, and detection as one process, for a reactor antineutrino (one of the thousands of different nuclear reactions in the source shown). Macroscopic tree-level Feynman diagram. Linear dimensions are also shown for the case of the mTC setup at NIST. Of course, we cannot know for sure which particular β-decay branch took place, nor fission process in the reactor.

Later, Sudarshan and Marshak, and independently Feynman and Gell-Mann, introduced a concept of weak current for the β–decay, or the $V-A$ theory [46–48]:

$$J_\mu = J^\ell_\mu + J^h_\mu = \bar{\psi}_e \gamma_\mu (1-\gamma_5)\psi_\nu + \bar{\psi}_n \gamma_\mu (1-\lambda\gamma_5)\psi_p \tag{1.80}$$

J^h_μ — hadronic current, J^ℓ_μ — leptonic charged current:

$$J^\ell_\mu = \frac{G_F}{\sqrt{2}} \bar{\ell}_\alpha \gamma_\mu (1-\gamma_5)\nu_\alpha, \text{ where } \ell_\alpha = e,\mu,\tau, \ \nu_\alpha = \sum_{i=1}^{3} V_{\alpha i}\nu_i \tag{1.81}$$

For clarity in future derivation of neutrino propagator, we write the following interaction Lagrangian in source and detector as

$$\mathscr{L}_s = \bar{\mathsf{C}}_s(x)\,\nu_\alpha(x) + \overline{\nu}_\alpha(x)\mathsf{C}_s(x) \tag{1.82}$$
$$\mathscr{L}_d = \bar{\mathsf{C}}_d(x)\,\nu_\beta(x) + \overline{\nu}_\beta(x)\mathsf{C}_d(x) \tag{1.83}$$

For example, for the process in Fig. 1.10, the quantity $\bar{\mathsf{C}}$ (a row-vector in spinor space) is

$$\bar{\mathsf{C}}_s(x) = \frac{G_F}{\sqrt{2}} J^s_\mu(x)\bar{\ell}_\alpha(x)\gamma^\mu(1-\gamma^5) \tag{1.84}$$
$$\bar{\mathsf{C}}_d(x) = \frac{G_F}{\sqrt{2}} J^d_\mu(x)\bar{\ell}_\beta(x)\gamma^\mu(1-\gamma^5) \tag{1.85}$$

while for other reactions they might have a different form. The recipe is always — write down a proper Lagrangian, along with initial and final states first.

Constructing initial $|\text{in}\rangle$ and final $|\text{out}\rangle$ states as direct products

$$|\text{in}\rangle = |\text{in (source)}\rangle \otimes |\text{in (detector)}\rangle \tag{1.86}$$

$$|\text{out}\rangle = |\text{out (source)}\rangle \otimes |\text{out (detector)}\rangle \tag{1.87}$$

If the one-particle states are described via wave-packets, we should think of initial $|\text{in}\rangle$ and final $|\text{out}\rangle$ states as follows:

$$|\text{in}\rangle = |\phi_1\ \phi_2 \dots\rangle = \left(\prod_{i=1}^{N_{\text{in}}} \int \frac{d^3k_i}{(2\pi)^3\ \sqrt{2\,E_{\mathbf{k}_i}}}\,\phi_i(k_i)\right)|\mathbf{k}_1\mathbf{k}_2\dots\rangle \tag{1.88}$$

$$|\text{out}\rangle = |\varphi_1\ \varphi_2 \dots\rangle = \left(\prod_{j=1}^{N_{\text{out}}} \int \frac{d^3p_j}{(2\pi)^3\ \sqrt{2\,E_{\mathbf{p}_j}}}\,\varphi_j(p_j)\right)|\mathbf{p}_1\mathbf{p}_2\dots\rangle \tag{1.89}$$

where $|\mathbf{k}\rangle$ — a one-particle state with a fixed momentum on a mass-shell $k_0^2 - \mathbf{k}^2 = m^2$; N_{in} — number of particles in initial $|\text{in}\rangle$ state; $\phi_i(k_i)$ — characterizes i-th particle wave packet, k_i is a momentum in a corresponding wave packet decomposition. N_{out} — number of particles in the final state $|\text{out}\rangle$; $\varphi_j(p_j)$ — wave packet of j-th particle in the final state.

Indices in functions $\phi_i(k_i)$ and $\varphi_j(p_j)$, along with different characters ϕ and φ, simply means that all the wave packets have generally different forms.

Another thing to keep in mind is the Heisenberg uncertainty principle, Eq. 1.90. Using wave-packets, it is clear that all particles have some localization, which in turn gives us spread in both momentum and space-time.

$$\Delta p_x \Delta x \geq \hbar/2 \tag{1.90}$$

1.2.3 Neutrino oscillations in vacuum

Amplitude of transition from initial state $|\text{in}\rangle$ to final state $|\text{out}\rangle$ is given by

$$\mathscr{A} \equiv \langle\text{out}|(S-1)|\text{in}\rangle = \\ = \left(\prod_{j=1} \int \frac{d^3p_j}{(2\pi)^3\ \sqrt{2\,E_{\mathbf{p}_j}}}\,\varphi_j(p_j)\right)\left(\prod_{i=1} \int \frac{d^3k_i}{(2\pi)^3\ \sqrt{2\,E_{\mathbf{k}_i}}}\,\phi_i(k_i)\right)\langle\mathbf{p}_1\mathbf{p}_2\dots|(S-1)|\mathbf{k}_1\mathbf{k}_2\dots\rangle \tag{1.91}$$

$$\text{in}: \qquad \phi_i(k_i) = \phi_i(k_i,\ \bar{\mathbf{k}}_i) = a(\mathbf{k}_i - \bar{\mathbf{k}}_i)e^{+ik_i x_{s,\,d}} \tag{1.92}$$

$$\text{out}: \qquad \varphi_j(p_j) = \varphi_j(p_j,\ \bar{\mathbf{p}}_j) = \tilde{a}(\mathbf{p}_j - \bar{\mathbf{p}}_j)e^{-ip_j x_{s,\,d}}, \tag{1.93}$$

where $x_{i_s} \approx x_s$, $x_{j_d} \equiv y_{j_d} \approx y_d$. Sign "$-$" in the exponent is for outgoing particles; sign "$+$" is for incoming particles; $x_{i_{s,\,d}}$ is coordinate of i-th particle in the source (s) or inside the detector (d) depending whether the particle is in source or detector; a_i ($\tilde{a}_j$) are real functions with sharp maximum around $\mathbf{k}_i = \bar{\mathbf{k}}_i$ ($\mathbf{p}_j = \bar{\mathbf{p}}_j$); $\bar{\mathbf{k}}_i$ ($\bar{\mathbf{p}}_j$)

is mean momentum of i-th (j-th) particle. To go back to plane waves, one can put $a(\mathbf{k}_i - \bar{\mathbf{k}}_i) = \delta(\mathbf{k}_i - \bar{\mathbf{k}}_i)$.

All momenta in sets $\{k\}$ and $\{p\}$ are for the fields in the Lagrangian which don't have any spreading. Calculating the probability, the following structures will arise, Eq. (1.72)

$$\Psi^+(x)|\mathbf{p}\rangle = e^{-i\,p\,x}\; v^+(\mathbf{p})\;|0\rangle$$

After skipping several pages of mathematical derivations (see Appendix A.9 for a full derivation) we can write the following for the number of events

$$dN = \prod_{j=1}^{F_s} \frac{d^3\bar{p}_j}{(2\pi)^3 2E_{\bar{\mathbf{p}}_j}} \prod_{i=1}^{I_s} \frac{f_i(\bar{\mathbf{k}}_i,\ \mathbf{x}_s,\ x_s^0)d^3\bar{k}_i}{(2\pi)^3 2E_{\bar{\mathbf{k}}_i}} \prod_{j=F-F_s}^{F} \frac{d^3\bar{p}_j}{(2\pi)^3 2E_{\bar{\mathbf{p}}_j}} \prod_{i=I-I_s}^{I} \frac{f_i(\bar{\mathbf{k}}_i,\ \mathbf{y}_d,\ y_d^0)d^3\bar{k}_i}{(2\pi)^3 2E_{\bar{\mathbf{k}}_i}} \cdot$$
$$\cdot\, d\mathbf{x}_s dy_d^0 d\mathbf{y}_d \sqrt{2\pi\sigma^2}\frac{4}{\pi^3 L^2}\; 2\left(\sqrt{\frac{\pi}{2\sigma^2}}\right)^{-1} \cdot$$
$$\cdot\,(\pi)^8 \frac{1}{\sigma^2}\left(\sum_{i,\,j} V_{\alpha i}^* V_{\beta i} V_{\alpha j} V_{\beta j}^*\; e^{-\frac{1}{2\sigma^2}\frac{1}{4}\left(m_i^2 - m_j^2\right)^2 \frac{1}{4\lambda^4}L^2} e^{-i\frac{1}{2\lambda}\left(m_i^2 - m_j^2\right)L}\right) \cdot$$
$$\cdot\,\delta^4(\bar{p}_s - \bar{k}_s + q(\lambda))\delta^4(\bar{p}_d - \bar{k}_d - q(\lambda)) \sum_{\text{spins}} |\mathscr{M}_s|^2 \sum_{\text{spins}} |\mathscr{M}_d|^2 \quad (1.94)$$

$$|\mathscr{M}_d|^2 = |\bar{\mathsf{C}}_d^p \nu|^2 = |\bar{\mathsf{C}}_d^p(\{\bar{k}_i\}_d,\ \{\bar{p}_j\}_d)\nu(q)|^2 \quad (1.95)$$
$$|\mathscr{M}_s|^2 = |\bar{\nu}\mathsf{C}_s^p|^2 = |\bar{\nu}(q)\mathsf{C}_s^p(\{\bar{k}_i\}_s,\ \{\bar{p}_j\}_s)|^2 \quad (1.96)$$

And finally, the differential event rate is

$$d\Gamma = \frac{dN}{dy_d^0} = \int \prod_{j=1}^{F_s} \frac{d^3\bar{p}_j}{(2\pi)^3 2E_{\bar{\mathbf{p}}_j}} \int \prod_{i=1}^{I_s} \frac{f_i(\bar{\mathbf{k}}_i,\ \mathbf{x}_s,\ x_s^0)d^3\bar{k}_i}{(2\pi)^3 2E_{\bar{\mathbf{k}}_i}} \prod_{j=F-F_s}^{F} \frac{d^3\bar{p}_j}{(2\pi)^3 2E_{\bar{\mathbf{p}}_j}} \cdot$$
$$\cdot \int \prod_{i=I-I_s}^{I} \frac{f_i(\bar{\mathbf{k}}_i,\ \mathbf{y}_d,\ y_d^0)d^3\bar{k}_i}{(2\pi)^3 2E_{\bar{\mathbf{k}}_i}} \int d\mathbf{x}_s \int d\mathbf{y}_d \frac{4}{\pi^3 L^2}\; 4\cdot$$
$$\cdot\,(\pi)^8 \mathscr{P}_{\text{mix}}(\sigma(\lambda),\ L)\delta^4(\bar{p}_s - \bar{k}_s + q(\lambda))\delta^4(\bar{p}_d - \bar{k}_d - q(\lambda)) \cdot \sum_{\text{spins}} |\mathscr{M}_s|^2 \sum_{\text{spins}} |\mathscr{M}_d|^2 \quad (1.97)$$

Mixing probability (compare with Eq. (1.31) which was found using non-relativistic quantum mechanics)

$$\boxed{\mathscr{P}_{\text{mix}}(\sigma(\lambda),\ L) = \sum_{i,\,j} V_{\alpha i}^* V_{\beta i} V_{\alpha j} V_{\beta j}^*\; e^{-\frac{1}{2\sigma^2}\frac{1}{4}\left(m_i^2 - m_j^2\right)^2 \frac{1}{4\lambda^4}L^2} e^{-i\frac{1}{2\lambda}\left(m_i^2 - m_j^2\right)L}} \quad (1.98)$$

$$\boxed{P_{\nu_\alpha \to \nu_\beta} = \delta_{\alpha\beta} - 4\sum_{i>j} V_{\alpha i} V_{\alpha j} V_{\beta i} V_{\beta j} \sin^2 \frac{\Delta m_{ij}^2 L}{4E}} \quad (1.31)$$

Note, that unlike in the QM-approach along with the oscillatory factor, we get some new features which can only be obtained in the QFT-approach with wave packets. The following factor, in Eq. 1.99, is the suppression factor at long distances (in analogy to difference in near-field and far-field behavior for electromagnetic radiation). Unlike in

QM, in QFT the oscillatory behavior won't go on forever, which is more realistic. A good example would be that relic neutrinos from the Big Bang are all in their certain "flavor." If in the future those neutrinos are detected and there is a discrepancy in their flavor, this potentially might lead to an explanation.

$$\exp\left[-\frac{\Delta m_{ij}^4 L^2}{32\sigma^2\lambda^4}\right] \tag{1.99}$$

The real challenge is to know the proper form and spreads of the wave packets of all the initial and final particles, which are the arguments of λ and σ, momentum- and space-time-like coefficients. These derivations were shown in [41]. Latest results from Neutrino-4 [49] might turn out to be an experimental verification of this new effect (or indication in favor for sterile neutrino hypothesis). It is clear that improved statistics and more experiments are needed, especially in the region of the very short baselines. mTC-like experiments with fast-timing electronics along with fast-response photodetectors, are ideal not only to probe this theory, but also to shed some light on the proper shape of the wave packets. Having multiple identical detectors, as shown in Fig. 1.11, and being able to swap them also helps to reduce accidental backgrounds substantially [50].

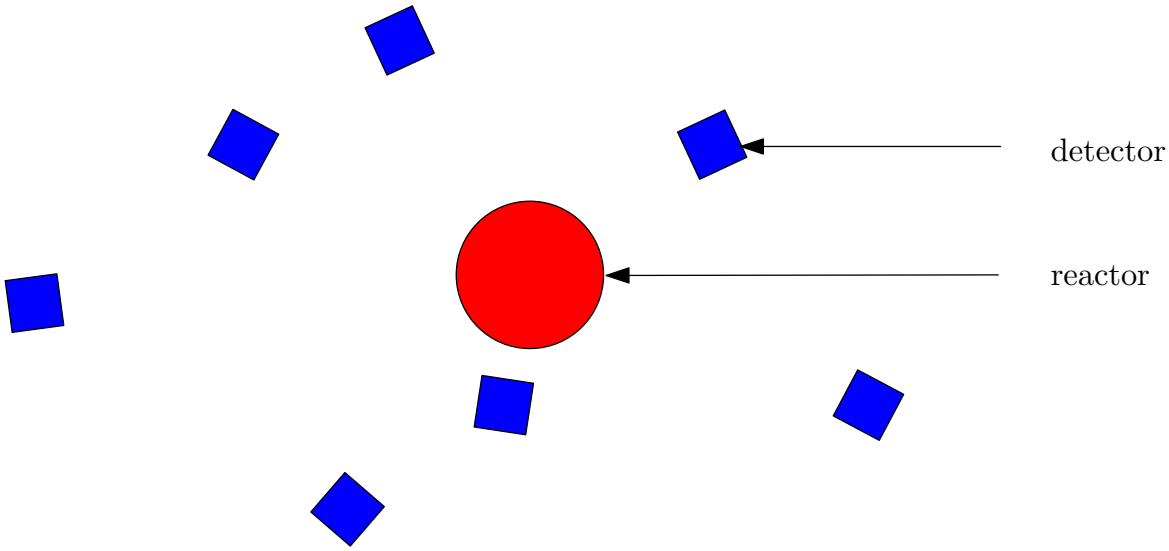

Figure 1.11: An ideal experiment to study reactor neutrinos, several mTC-like detectors surrounding a nuclear reactor.

1.3 Sources

We know quite a few sources of neutrinos. Fig. 1.12 represents average energy range and distance between neutrinos of different origins and types, and a potential detector. In Figs. 1.13–1.14 neutrino flux as measured at an average location on the Earth surface, along with typical cross section range for neutrinos of different energies. The dominant are relic and Solar neutrinos.

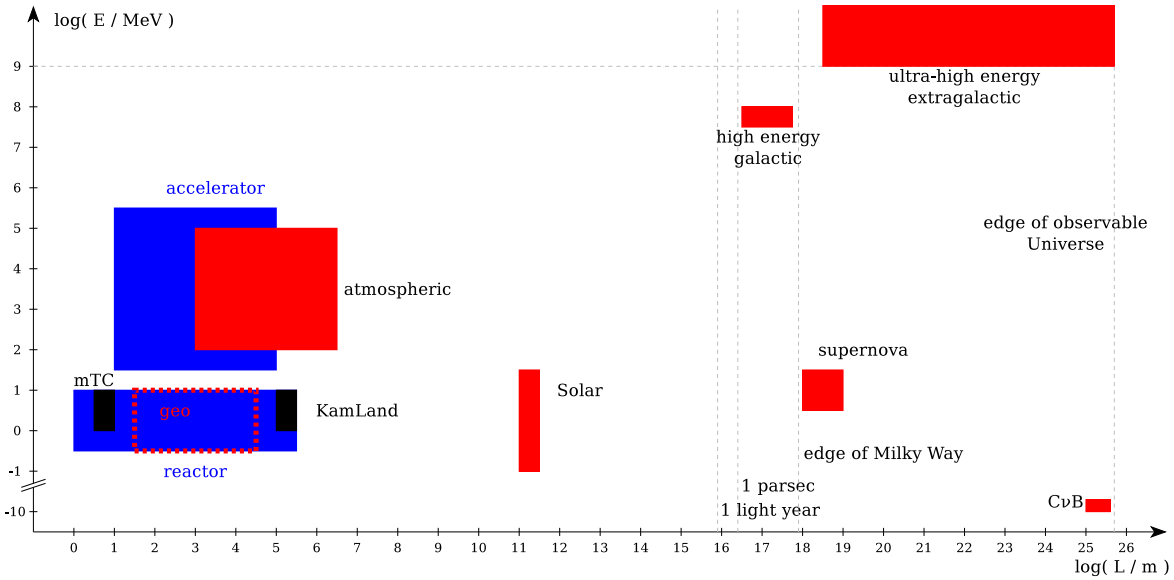

Figure 1.12: Sources of neutrinos with corresponding neutrino energy and typical propagation length.

The neutrinos which have not been detected yet are those neutrinos emitted shortly after the Big Bang (cosmic neutrino background, CνB) and diffuse neutrinos from supernovae. Detecting the Big Bang neutrinos would unveil a further past of the Universe, as they decoupled before the relic cosmic microwave photons. Although the flux is high, they are of extremely low energy. Thus, no experiment has detected them so far. Supernovae and diffuse (relic) supernovae neutrinos, neutrinos coming from within our Milky Way Galaxy and of extragalactic origins are the ultimate messengers of the Universe, which unlike photons can propagate unobscured for much longer distances (excluding ultra-high energies). Supernova type I core collapse produces an enormous amount of neutrinos. We have only one data point of such an event happening. Back in 1987, the light and neutrinos from the supernova exploding in the Large Magellanic Cloud reached Earth and the latter were recorded in IMB [54], Kamiokande [55], and Baksan [56]. The upcoming Gd-doped SuperKamiokande project [57, 58] is aimed to detect the supernova relic neutrinos.

The Earth's interior provides us with the so-called *geo-neutrinos*. Geo-neutrinos are similar to reactor ones due mostly to ^{40}K, ^{232}Th and ^{238}U. It is worth pointing out here that we know more about the Sun's interior than we know about Earth's. Most of the radiogenic heat production is due to the decay of those three. The Hanohano (Hawaii Neutrino Observatory) would be a unique laboratory to study geo-neutrinos [59]. First observation of geo-neutrinos was made by KamLAND [60], and subsequently by Borexino experiment [61].

The Earth's atmosphere provides us with the so-called *atmospheric neutrinos*,

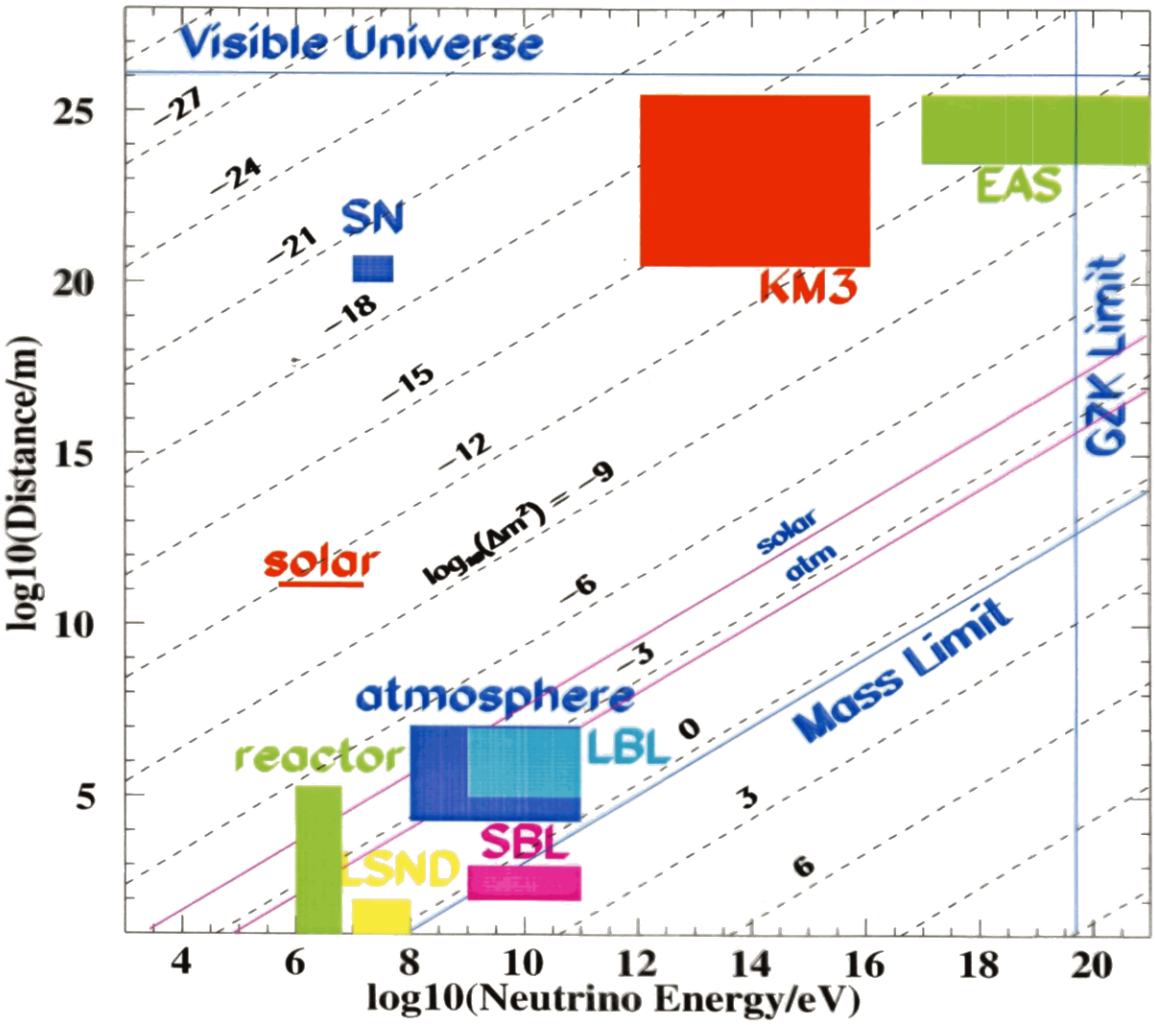

Figure 1.13: Sources of neutrinos with corresponding neutrino energy and typical propagation length, with oscillation parameters added. So-called Learned plot. Figure is taken from [51].

which are of the cosmic-ray origin — when a high energetic nucleus (usually a proton) strikes an air molecule, there is a cascade of particles, similar to what's happening in the accelerator neutrino experiments. The secondary particles are mostly pions (and kaons) which then decay according to the following branches producing neutrinos

$$\begin{aligned} \pi^+ &\to \mu^+ + \nu_\mu & \pi^- &\to \mu^- + \bar{\nu}_\mu \\ &\hookrightarrow e^+ + \nu_e + \bar{\nu}_\mu & &\hookrightarrow e^- + \bar{\nu}_e + \nu_\mu \end{aligned} \tag{1.100}$$

Human-made sources of neutrinos include accelerator and reactor neutrinos. To produce accelerator neutrinos, usually a proton beam is aimed at a beryllium target. Such collision produces a lot of short-lived mesons, mostly pions and kaons, which decay in a similar way as in Eq. 1.100. The energy range of such neutrinos is on the order of a few GeV. Furthermore, such neutrinos as detected in accelerator neutrino experiments can produce several of secondary particles, primarily pions, if scattered off nuclei, as illustrated in Fig. 1.15.

I will now go into exploring reactor antineutrinos.

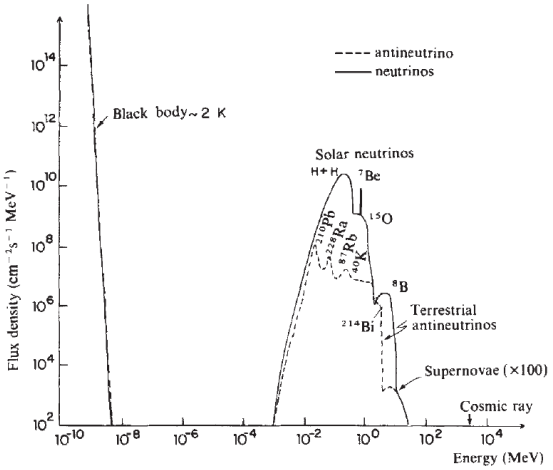

(a) Flux (in $\mathrm{cm}^{-2}\mathrm{s}^{-1}$ for line sources) at the Earth's surface due to natural sources of neutrinos and antineutrinos. Figure is taken from [52].

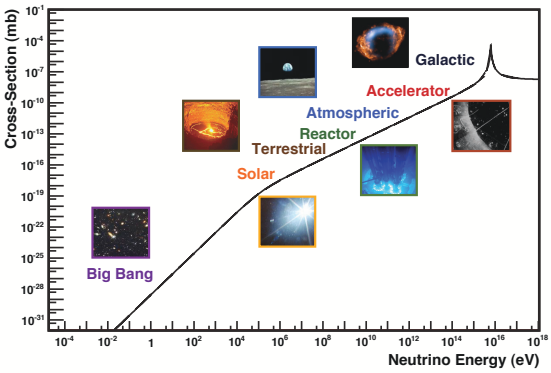

(b) Typical cross sections for different neutrino sources with corresponding neutrino energy and for a typical detection reaction. Figure is taken from [53].

Figure 1.14: Neutrino sources.

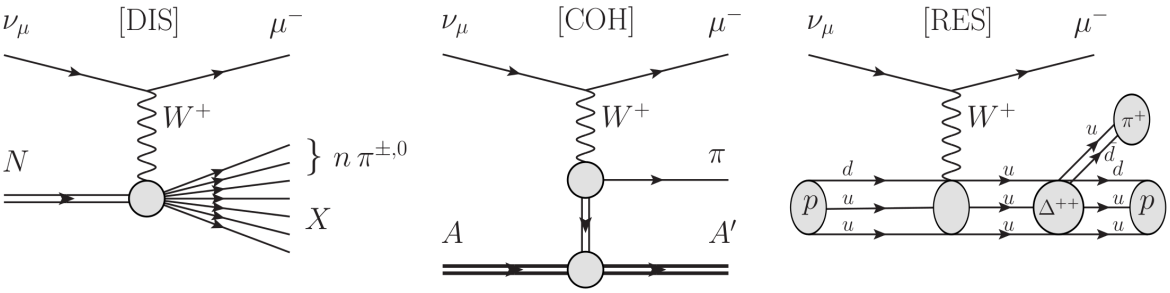

Figure 1.15: The main types of charged current muon neutrino scattering on a free nucleon/nucleus that produce pions directly. From left to right are: Deep Inelastic Scattering (DIS), Coherent pion production (COH), and Resonance production (RES). In the figure N is a nucleon, A is a nucleus and X represents the hadronic system excluding pions [62].

1.3.1 Fission reactors, and neutrino directionality

Fission was accidentally discovered in the 1930s, in the experiments of bombarding heavy elements (uranium) with neutrons [63]. One of the possible reactions is production of two lighter nuclei with a couple of free neutrons released. First, there was a confusion by the Fermi group [64] that the reaction was β-decay. What was really β-decaying were the fission products. Once it was also realized that those neutrons could be used in a chain reaction, the idea of a first nuclear fission reactor and atomic bomb were conceived. An example of a ^{235}U–fission reaction

$$\mathrm{n} + {}^{235}\mathrm{U} \rightarrow {}^{236}\mathrm{U} \rightarrow {}^{92}\mathrm{Kr} + {}^{141}\mathrm{Ba} + 3\mathrm{n} \tag{1.101}$$

The electron antineutrino, emitted from one of thousands β-decay chains of the fission products, interacts with a proton via the weak interaction producing a positron and neutron which may be detected in most IBD detectors[2] via a delayed-coincidence

[2]Note there are detectors, like Rovno, which only detect neutrons (see Section A.10).

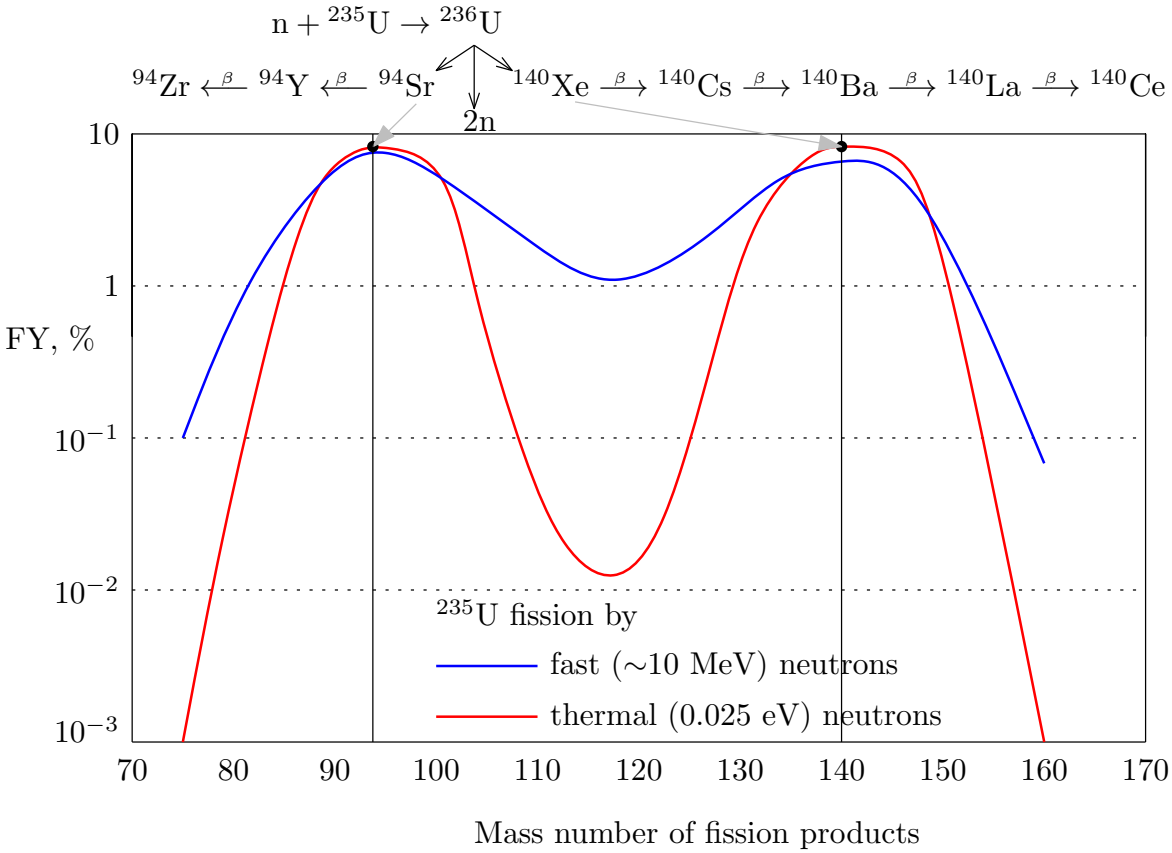

Figure 1.16: Fission yield of ^{235}U. Note that the curve is a result of a superposition of two curves. Schematic representation.

technique.

$$\bar{\nu}_e + p \to e^+ + n \tag{1.102}$$

Fig. 1.17c shows the cross section of the IBD reaction in Eq. 1.102, along with the antineutrino flux from four main isotopes present in the power reactor, and the measured spectrum, which is a product of the cross section and the total flux curves. The inverse β-decay reaction has a threshold $E_\nu \approx 1.8$ MeV. The positron travels a few mm on average before being annihilated with an electron inside the medium producing two 511-keV gammas going back-to-back.[3]

$$e^+ + e^- \to 2\gamma \tag{1.103}$$

The neutron keeps wandering around losing its energy while bouncing on hydrogen nuclei. When it becomes thermal (kinetic energy 0.025 eV) it is captured on the doping element with a high neutron-capture cross section. The duration between neutron emission and capture ranges between a few to a few hundred microseconds, depending on the dopant and densities.

For low momentum transfers, one can ignore the propagator of a massive W-boson, the matrix element has *leptonic current* $\times$ *hadronic current* structure:

$$\mathscr{M} = \bar{v}_{\nu_e}\gamma^\mu(1-\gamma_5)v_e \times \bar{u}_n\left(f_1\gamma_\mu + g_1\gamma_\mu\gamma_5 + if_2\sigma_{\mu\nu}\frac{q^\nu}{2M} + g_2 q_\mu\gamma_5\right)u_p \tag{1.104}$$

[3]In case of the mTC the two IBD-induced gammas escape the small detector volume.

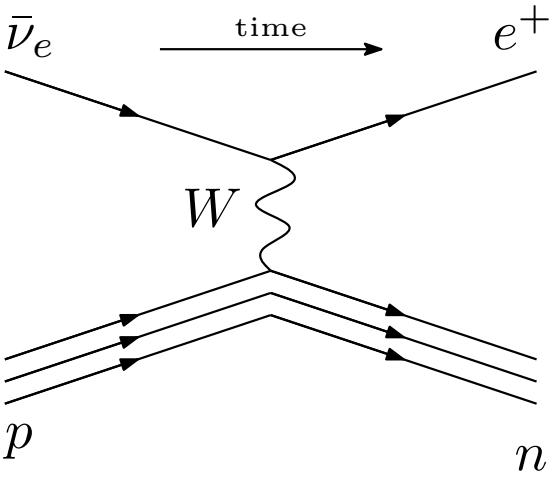

(a) Tree-level Feynman diagram.

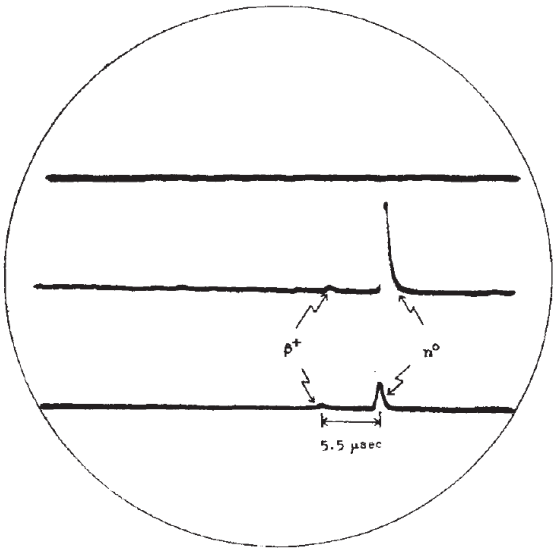

(b) One of the first recorded neutrino events by Reines & Cowan collaboration [65]. Three oscilloscope traces are shown.

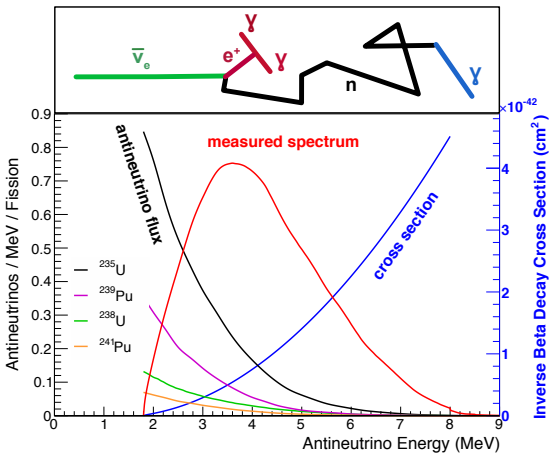

(c) Schematic representation of inverse β-decay reaction, along with the graphs of cross section of $\bar{\nu}_e p \to e^+ n$, antineutrino flux produced in fission of four main isotopes, and the rate, which is the product of cross section and total flux [66].

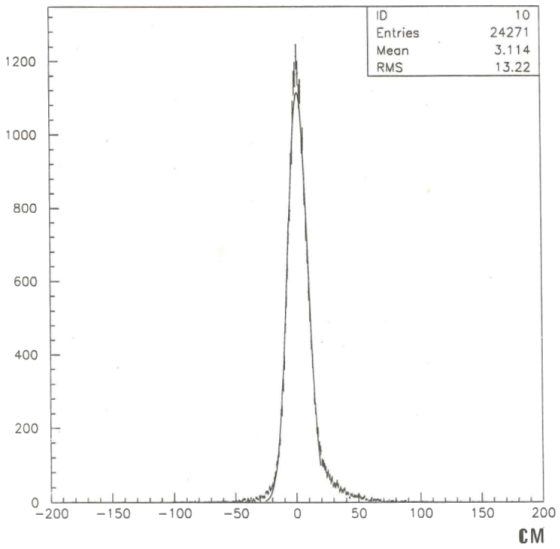

(d) One of the first Monte Carlo simulations indicating $\bar{\nu}_e$ directionality utilizing neutron capture average vertex displacement (of a few centimeters from zero) [67].

Figure 1.17: Inverse β-decay reaction.

where $M = (m_n + m_p)/2$.

Differential cross section, in terms of $t = q^2$, after averaging and sum of initial and final spins

$$\frac{d\sigma}{dt} = \frac{G_F^2 \cos^2\theta_C}{2\pi(s - m_p^2)^2} |\mathscr{M}|^2 \tag{1.105}$$

After doing some algebra that is similar to [68], one can find a naïve low-energy approximation for the total cross section

$$\sigma \approx 9.52 \times 10^{-44} \frac{p_e E_e}{\text{MeV}^2} \left[\text{cm}^2\right] \tag{1.106}$$

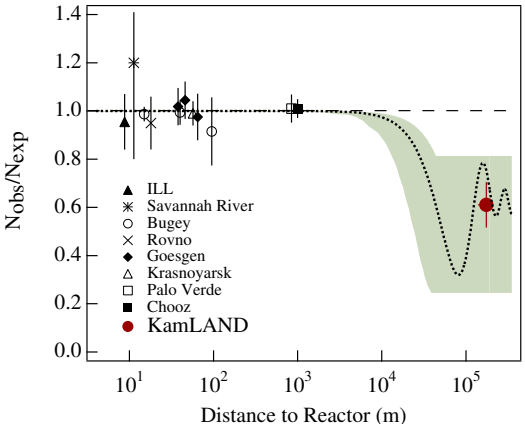

(a) Ratio of observed vs expected number of events in KamLAND and other reactor neutrino experiments as a function of distance. Figure is taken from [69].

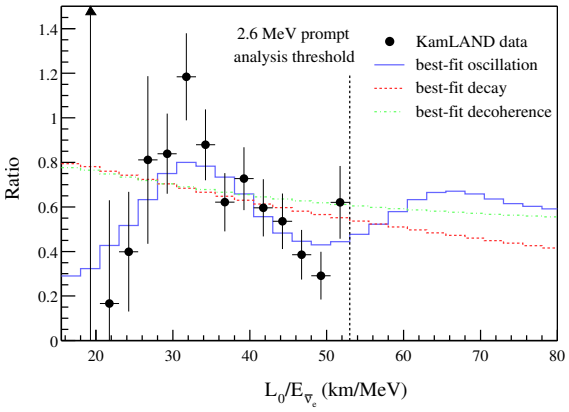

(b) Ratio of observed vs expected number of events as a function of baseline over neutrino energy, 515-day KamLAND data sample. Figure is taken from [70].

Figure 1.18: First evidence of reactor antineutrino oscillations.

where $E_e = E_\nu + (m_n - m_p)$ is a positron energy.

The first-ever detected neutrino was from a nuclear reactor by Reines and Cowan collaboration, Fig. 1.17b.

KamLAND was the first reactor experiment to confirm neutrino oscillations [69], which is not trivial taking into account different neutrino fluxes and baselines from more than fifty reactors. Fig. 1.18a shows the ratio of observed vs expected number of events in KamLAND and other reactor neutrino experiments as a function of distance. Fig. 1.18b shows a ratio of observed vs expected number of events as a function of baseline over neutrino energy, using KamLAND data with increased statistics shortly after the main discovery. In the Appendix, we discuss major reactor neutrino experiments. Besides answering fundamental physics questions such as the existence of sterile neutrinos and better understanding of the phenomenon of neutrino oscillations, reactor antineutrino experiments can contribute to the development of several important applications summarized in Table 1.3.

Independent on-line monitoring of the reactor power
The measurement is performed outside the core (safety issues) and does not affect the normal plant operations
Detector installation does not require any modification to the facility
Antineutrinos cannot be shielded and are only sensitive to fission material
Direct measurement of core nuclear activity and fuel burn-up
Early detection of unauthorized plutonium production and subtraction (sensitivity down to 10th kg)
Plant decommissioning after a nuclear disaster (eg Fukushima)

Table 1.3: Advantages of nuclear reactor monitoring via antineutrinos [71].

A systematic study of inverse β-decay, indicating the feasibility to extract neutrino directionality, was carried out by Vogel [72]. Essentially, Vogel's calculations posit that the positron carries the energy, and the neutron carries the momentum, the di-

rectional information of the original antineutrino. The CHOOZ experiment [73], and subsequently the DoubleCHOOZ, were pioneers experimentally proving that extracting antineutrino directionality is possible in the IBD reaction using a non-segmented detector. Palo Verde group, which uses a segmented detector, also published a paper around the same time, seeing similar effects but with lower statistics [74].

The neutron is not making a random walk in 3D until it becomes thermal. If it is coming from z-direction, it wanders around like a billiard having elastic scatters with protons, which makes its walk in xy-plane mostly random. An important part in identifying the neutron from IBD is choosing the right neutron capturer. The best candidate is ^{3}He, although nowadays it is not very practical. So, most detectors have boron, cadmium, gadolinium, or lithium, the elements with high neutron capture cross section. Many cross section measurements were made in the 1960-70s. Fig. 1.19 shows the cross section for three elements, and in Table 2.3, cross section values for neutron capture on ^{10}B are given. Effect of ^{10}B doping is shown in Fig. 1.20a. Fig. 1.20b illustrates that antineutrino directionality is better (i.e. narrower peak) for a small physical cross section of the detector, or a module in case of segmented detectors.

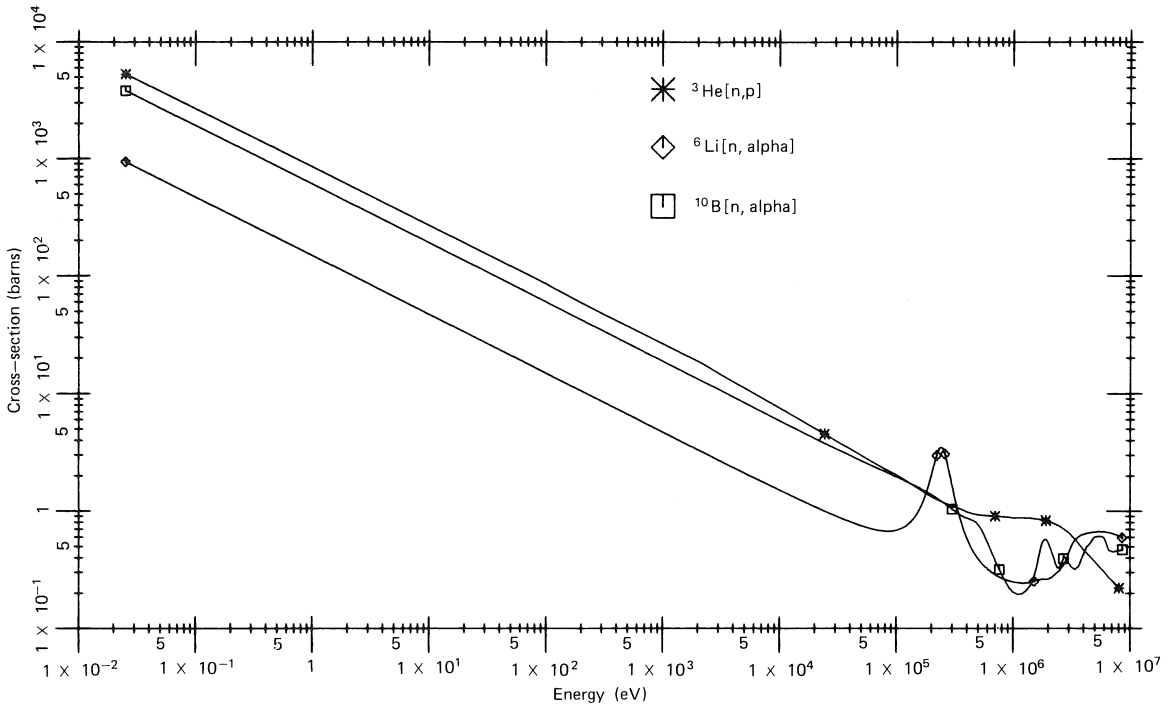

Figure 1.19: Neutron capture cross section for ^{3}He, ^{6}Li, and ^{10}B. Figure is taken from [75].

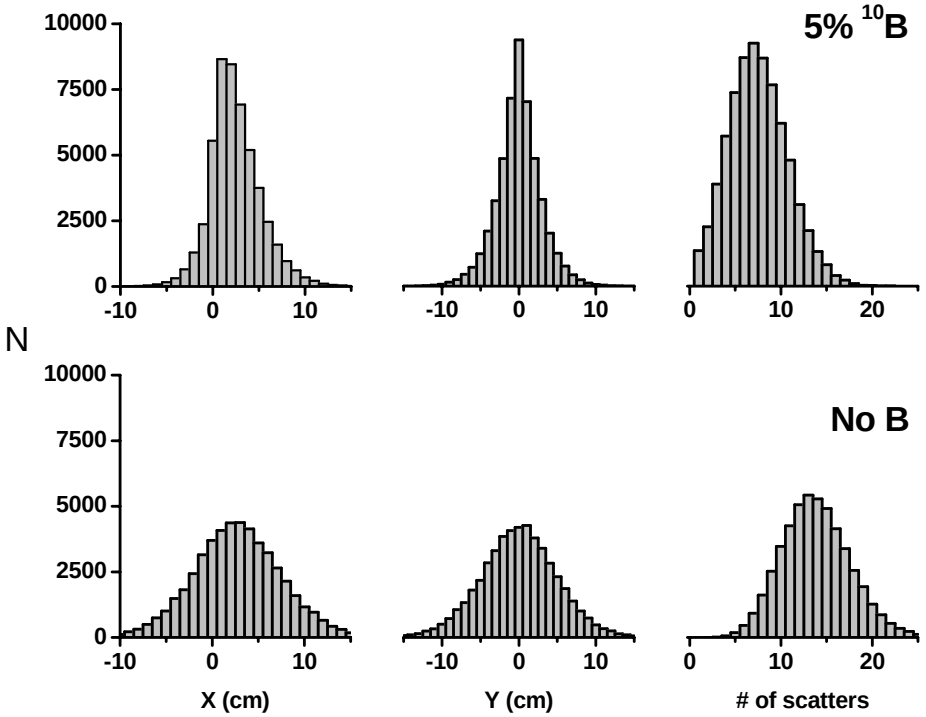

(a) The effect of ^{10}B loading on the neutron capture location. At the top a detector loaded with 5% ^{10}B; at the bottom a detector without B. The results represent 50k $\bar{\nu}_e$-capture simulations of reactor $\bar{\nu}_e$ coming in along the negative x-axis and interacting at $(x, y) = (0, 0)$ in a large volume detector.

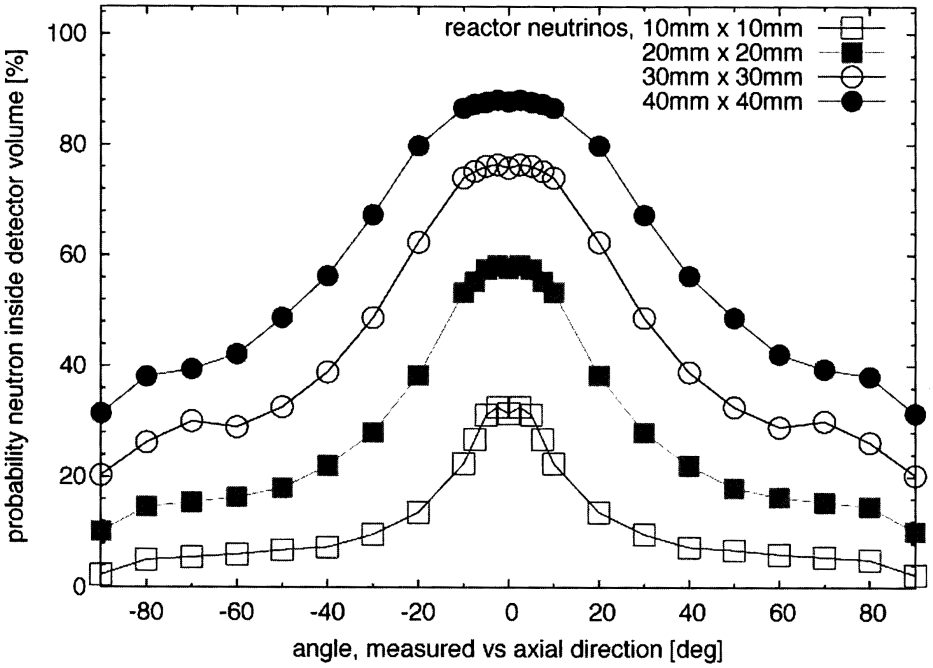

(b) Neutron-detection probability as a function of incident angle and detector cross section.

Figure 1.20: Simulation results and graph captions are taken from [76].

Chapter 2

miniTimeCube

> A human being in perfection ought always to preserve a calm and peaceful mind
>
> Frankenstein

Back in 2009, Hiroko Watanabe and John Learned explored the idea of getting antineutrino directionality in KamLAND, [77, 78], which subsequently led John to start the miniTimeCube project, or the mTC, as we usually call it. The novelty was in having fast-timing of electronics and photodetectors in a very confined space, making the mTC very small compared to all other neutrino detectors. The idea was to reconstruct the direction of particles propagating inside the scintillator using the timing information of the first arrival of Cherenkov and scintillation photons. A high spatial and temporal precision in capturing those photons is required to achieve this in a small volume. One of the primary goals was to reconstruct the direction of incoming antineutrinos from a nuclear reactor.

Starting in 2011 till the end of 2013, the main assembly was completed at UH. In 2014–2015, the mTC was at NIST undergoing multiple tests, including neutrons. At the beginning of 2016, a major electronics upgrade was performed. In the summer of that year, the mTC was deployed by the nuclear reactor, taking data July 13 – September 28. After that the mTC was shipped back to UH, where further tests were performed, studying detector neutron response and MCP-PMT cross-talk.

2.1 John's idea and early simulations

Watanabe studied neutrino directionality, doing simulations with different scintillators and investigating how different dopings affect the directionality in the inverse β-decay. So, John realized the possibility of directionality studies in a small-volume detector if one is able to detect the very first photons coming from the prompt and delayed signals — the positron annihilation and the neutron capture, as shown in Fig. 2.1. This is the inverse β-decay reaction, the key reaction in our experiment. Although gammas from both the prompt and delayed signals are likely to travel distances on the order of a meter and escape the small-volume detector, the Cherenkov and scintillation light yield from both should be sufficient to be detectable in a small volume. Therefore, one would be able to get all the information needed to get the directionality. A GEANT4 [79] simulation of such event is shown in Fig. 2.2.

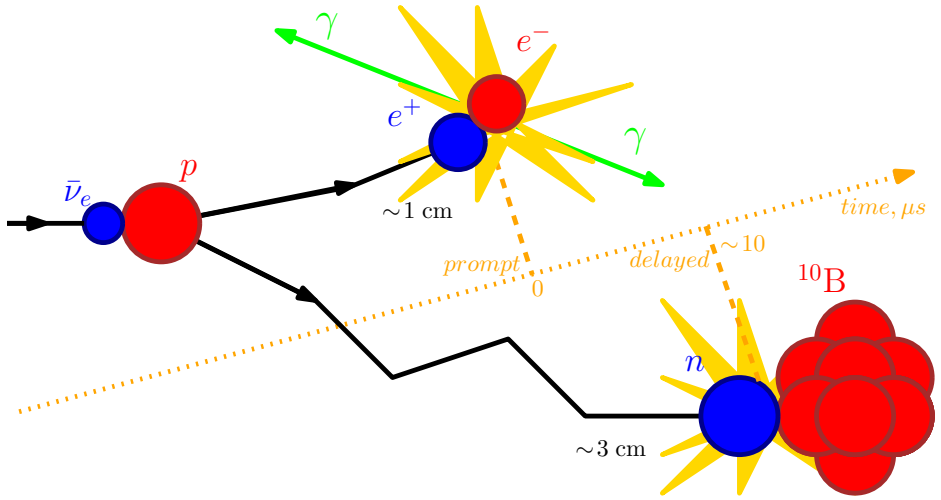

Figure 2.1: Main antineutrino signature in the mTC detector.

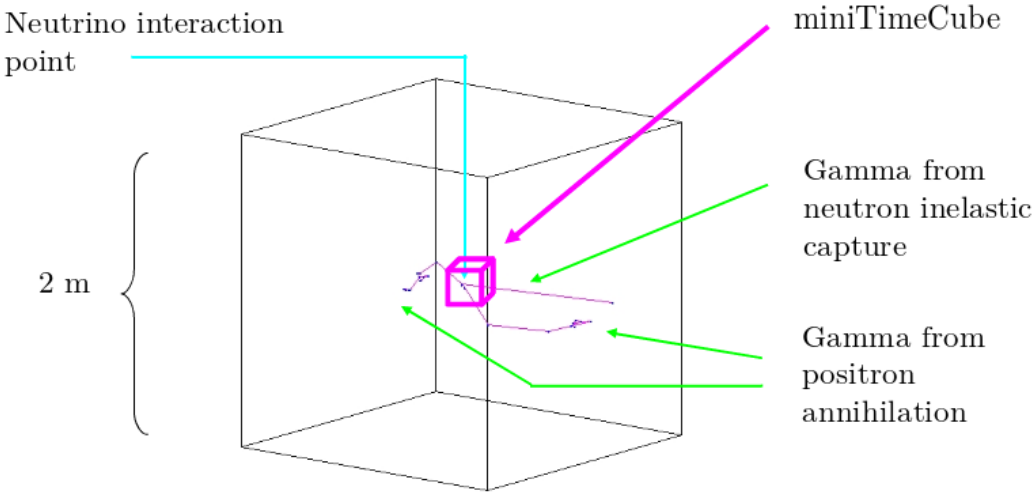

Figure 2.2: One of the first GEANT4 simulations for the mTC. Inverse β-decay reaction. 511-keV gammas from positron annihilation leave the detector, without affecting the vertex resolution [80].

As briefly discussed in the previous chapter, Vogel published a few papers indicating that it is experimentally feasible to get the antineutrino directionality from reconstructing IBD neutron momentum, as our early simulations also indicated, shown in Figs. 2.3–2.4. The neutron capture location is slightly shifted along the incoming antineutrino direction.

The photocoverage should be pretty high. Luckily, there are multi-anode MCP-PMTs produced by Photonis [81], previously known as Burle corporation. Another item needed is fast electronics. Luckily for us, there is a strong involvement in the Belle project at our department at UH, and specifically the iTOP subsystem of the Belle II detector, with Cherenkov ring imagers which operate very fast electronics with high channel density. Due to these resources, the experiment coalesced in a way that could not happen at any other institution.

We have a remarkable group working on the electronics led by Prof. Gary Varner, who developed the core of the readout system — the digitizer chip with high sampling

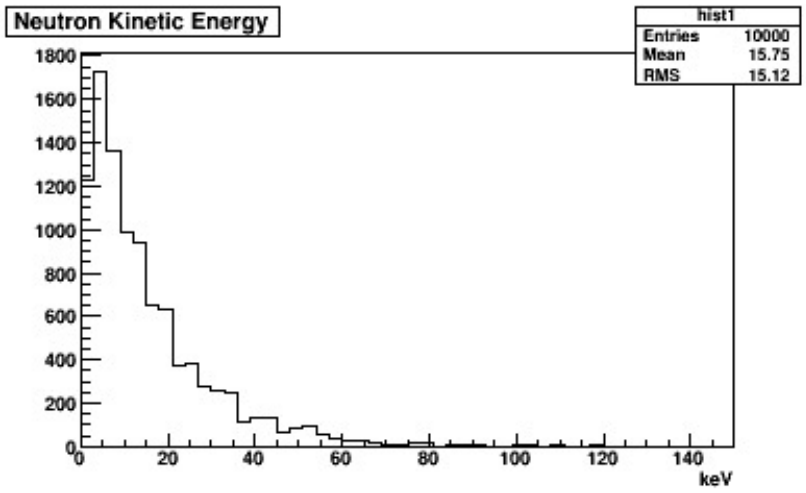

Figure 2.3: Neutron kinetic energy, mean is 15.75 keV, using reactor antineutrino spectrum [80].

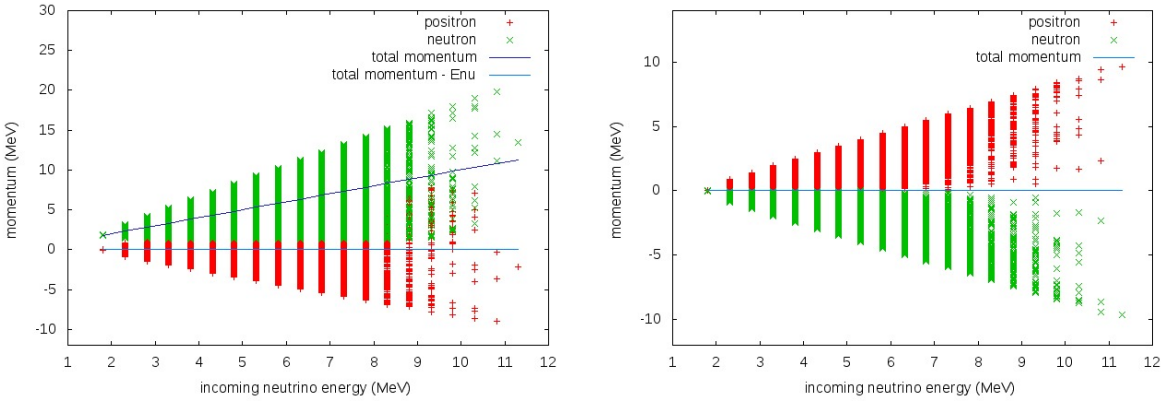

(a) Longitudinal. (b) Transverse.

Figure 2.4: Positron and neutron momenta — longitudinal (a) and transverse (b) components relative to the incoming antineutrino direction [80].

rates, or as he likes to call it, "an oscilloscope on a chip" system. We need to digitize with sub-100 picosecond timing in order to get the position inside the scintillator where the interaction takes place. We use electronics similar to what is used at the Belle project.

Although the scintillator decay time is on the order of a few nanoseconds, most of the light is emitted during the first instant. Knoll had a similar insight on using the first photoelectron timing and the feasibility of 100 ps timing resolution in scintillator detectors [75], promptly noting that the timing would worsen for smaller pulses. Pioneering work on first photoelectron timing was done by Lynch [82].

The concept is shown in Fig. 2.5. First photon arrival times, in principle, provide information on where positron annihilation and neutron capture happened. If we are able to temporally distinguish these photons, then we are able to reconstruct $\bar{\nu}_e$ direction. This is a pivotal point in the whole concept. It was also shown [83], that only in small modular detectors, reconstruction of IBD neutron directionality can be obtained in real time.

A combination of well-defined adjustable baselines, compact detectors, and well-

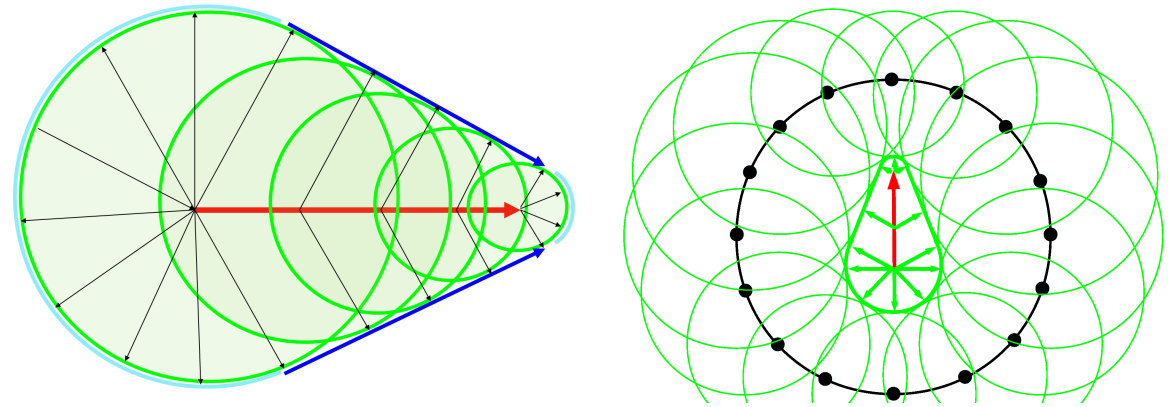

Figure 2.5: Left: Snapshot of a charged particle moving through a medium – Fermat surface. Green — Huygens' wavelets; blue — incoherent sum, coincident with the Cherenkov surface, not polarized; red — track (e.g. muon) [80]. Right: Fermat surface at an earlier time [80].

studied nuclear reactor cores is the next step in the development of very-short-baseline neutrino-oscillation experiments, and the mTC serves as a proof of concept for such detectors.

Imagine, if everything works, we could transform a piece of machinery that is the size of a building down to the size of a carton of milk. The mTC-display would look like KamLAND, shown in Fig. 2.6.

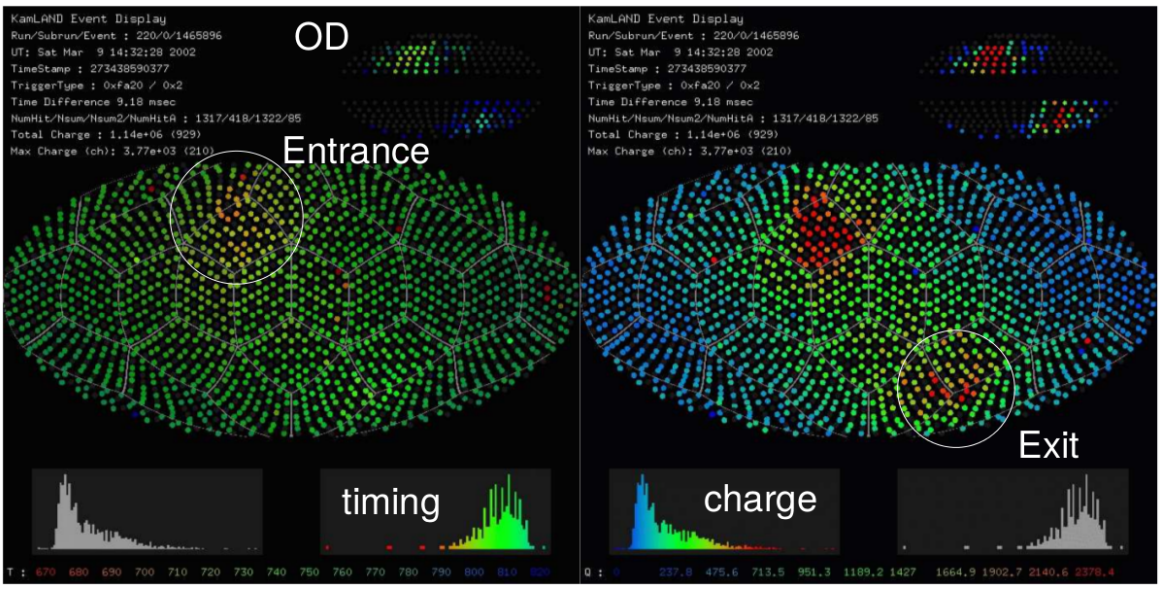

Figure 2.6: KamLAND event display. A muon event. Figure is taken from [84].

There were a few major simulations done before the design was finalized. The IBD vertex and track of the positron are reconstructed to mm precision. Figs. 2.8 show interactions of a simulated antineutrino and a cosmic muon within the mTC. One of the first CAD drawings is shown in Fig. 2.7a, and an early photograph to illustrate compactness is shown in Fig. 2.7b.

There are a lot of technical details that go into building this detector. Major

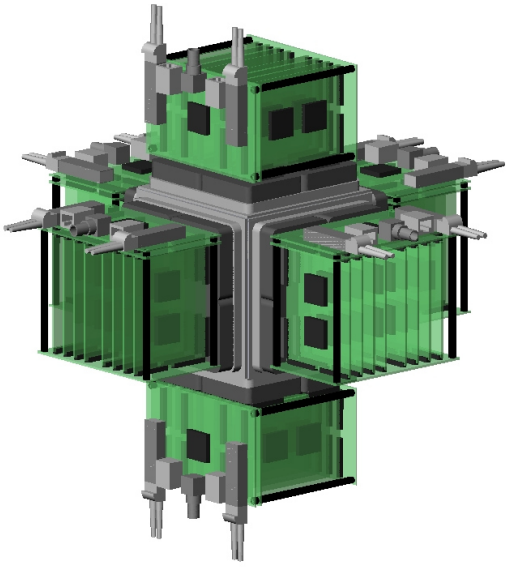

(a) An early CAD snapshot of the mTC — the scintillator surrounded by the MCP-PMT with mounted readout electronics. Figure is taken from [80].

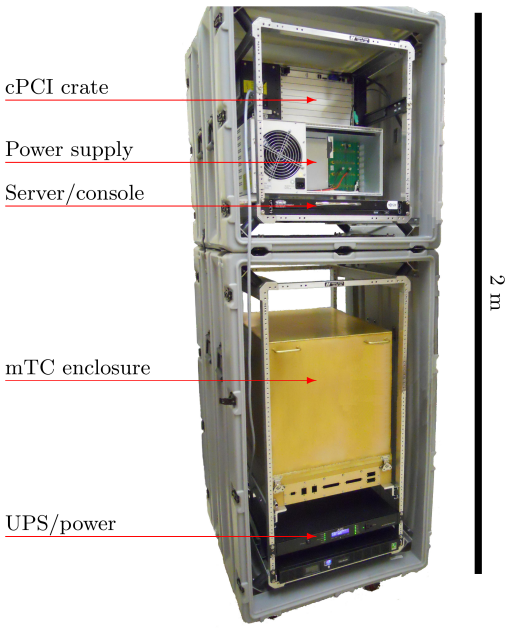

(b) An early photograph of the system. Two 19" racks. The mTC rack is 21 rack-units (U), the second (DAQ) rack is 11U. Figure is taken from [85].

Figure 2.7: mTC concept.

ones are discussed in this chapter. However, for clarity of the main text, some of them are moved to the Appendix. Main components of the mTC detector in its final configuration, and how they are mounted in two 11U and 21U 25″-deep racks, are shown in Fig. 2.9. The scintillator, photodetectors, and readout electronic modules with supplementary cooling and clock board are located in the $17.25'' \times 22.5'' \times 21.5''$ aluminum light-tight Faraday-cage enclosure (so called "yellow box"), which sits on a sliding shelf in the main rack. Table 2.1 shows the dimensions of the overall system (excluding cables and cooling pipes).

main crate	$27 \times 28 \times 49$
second crate	$27 \times 28 \times 28$
chiller	$19 \times 25 \times 32$

Table 2.1: Effective dimensions $w \times l \times h$ in inches of the mTC racks and chiller.

Due to the small volume and the emission of an alpha particle in neutron capture on boron, the light output is sufficient for the neutron capture event to be detectable. We did studies of different dopants at various concentrations. For the final configuration of the mTC, the decision was made to use a ^{10}B-doped plastic scintillator manufactured by the Eljen corporation.

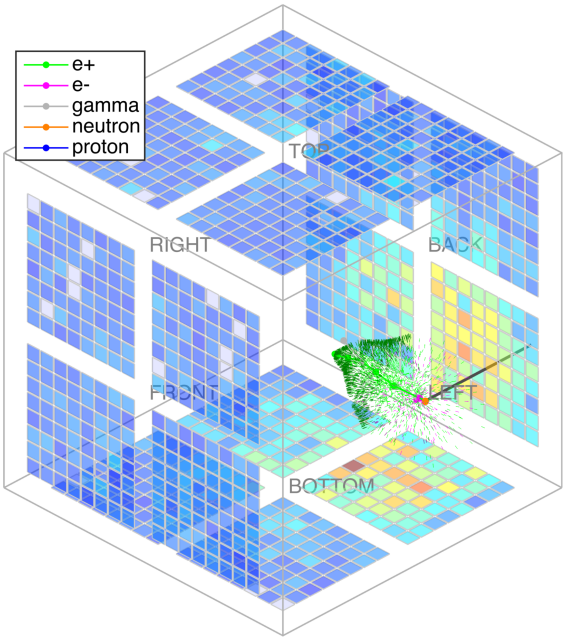

(a) A simulation of a 10 MeV $\bar{\nu}_e$ interacting in the 13 cm cubical mTC 100 ps after an inverse beta-decay (IBD) reaction. Cherenkov cone (dark green) is shown along with scintillation (light green) photons. Neutrino trajectory shown in black.

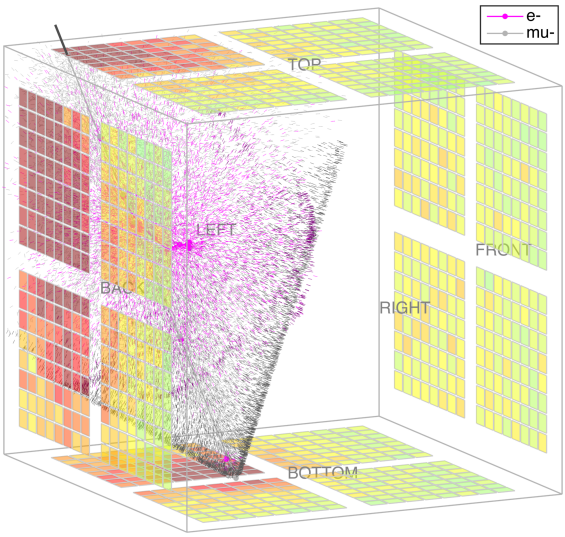

(b) Cherenkov (black) and scintillation (magenta) light for a cosmogenic muon going through the detector, with a clear indication of muon entry and exit points.

Figure 2.8: Monte Carlo simulations of the mTC. Front and rear faces are shown unpopulated for clarity of the figures. Figures are taken from [85].

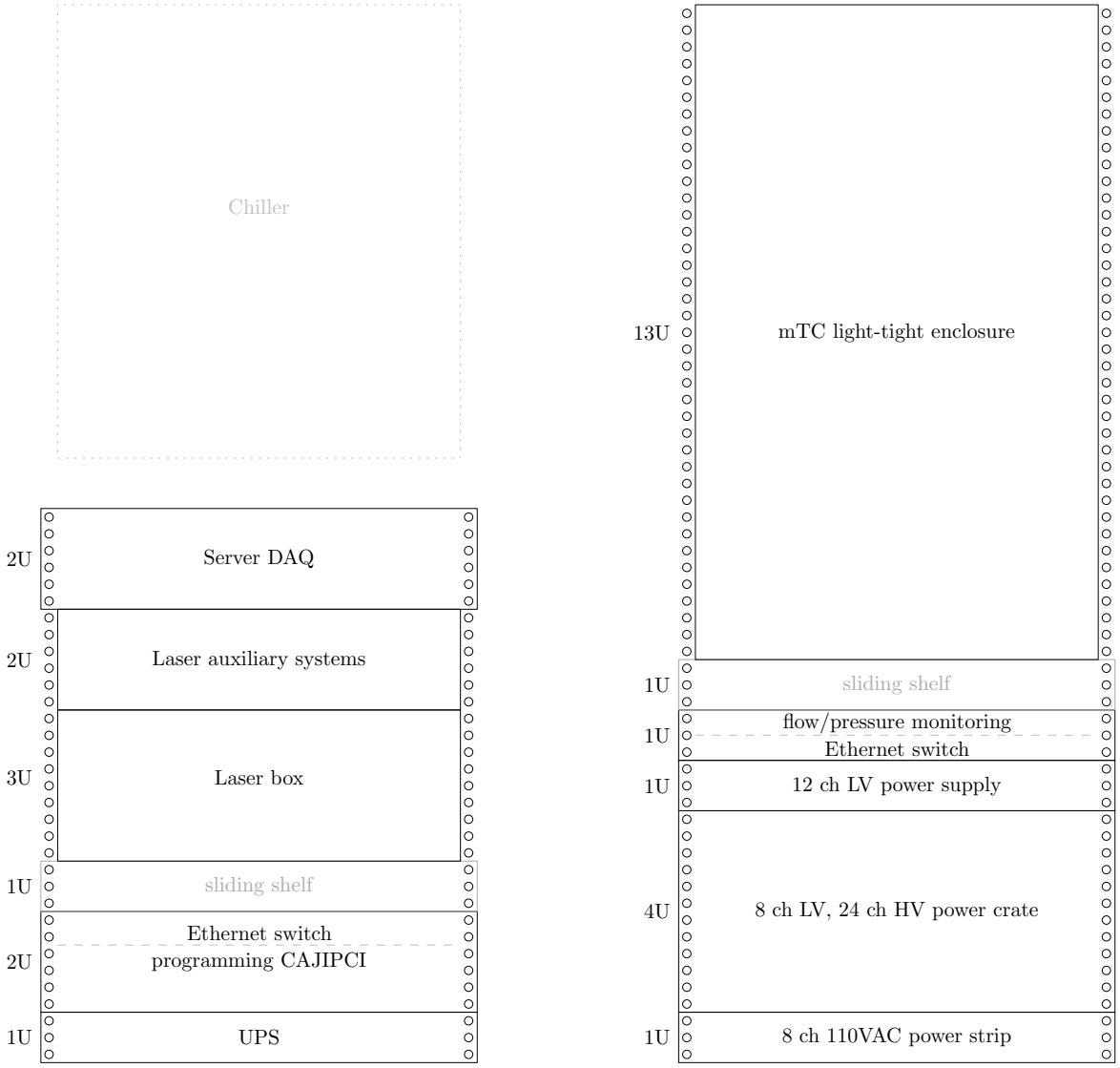

Figure 2.9: Main components of the mTC as mounted in two 11U and 21U racks. Chiller is not in the racks.

2.2 Scintillator

The core of the mTC where the interaction takes place is a plastic scintillator EJ-254 [86] with 1% natural boron doping. The natural boron has about 20% of ^{10}B, which corresponds to 0.2% ^{10}B overall doping of the scintillator by weight. ^{10}B is a neutron capturer. The scintillator is a proton-rich (atoms of hydrogen) target for the IBD reaction (Eq. 2.1).

$$\bar{\nu}_e + {}^1\mathrm{H} \rightarrow e^+ + n \tag{2.1}$$

For thermal neutrons, the capture cross section on ^{10}B is 3840 barns, which is quite large compared to most other elements. In most cases in Eq. 2.2, the energy of an alpha particle and lithium is equal to 2.3 MeV, which corresponds to a scintillation energy of a 76-keV electron (keVee), or up to about 500 detectable scintillation photons in the mTC (Fig. 2.13). For higher energy neutrons, the capture cross section grows rapidly as neutron energy goes down, as given in Table 2.3 and shown in Fig. 1.19. The neutron capture is most likely to produce 60 photoelectrons detectable in the mTC when everything is properly instrumented, as shown in Fig. 2.13.

$$\begin{array}{rlll} n + {}^{10}\mathrm{B} \longrightarrow \begin{cases} \rightarrow {}^7\mathrm{Li}(1015\text{ keV}) + {}^4\mathrm{He}(1775\text{ keV}) & \sim 6\% & Q = 2.8\text{ MeV} \\ \rightarrow {}^7\mathrm{Li}^* + {}^4\mathrm{He}(1471\text{ keV}) & \sim 94\% & Q = 2.3\text{ MeV} \end{cases} \\ \qquad\qquad \rightarrow {}^7\mathrm{Li}(839\text{ keV}) + \gamma(478\text{ keV}) \end{array} \tag{2.2}$$

Although less likely, a neutron can also be captured on hydrogen, with a mean time of ~ 180 μs, forming deuterium and emitting a 2.2-MeV gamma:

$$n + {}^1\mathrm{H} \rightarrow {}^2\mathrm{H} + \gamma \tag{2.3}$$

For thermal neutrons, the cross section of such reaction is 332 millibarns. Although it is more than a factor of 10^4 smaller than on ^{10}B, the number density of hydrogen atoms is much higher than ^{10}B. For our scintillator, per each capture of thermal neutron on hydrogen, there are about 25 captures on ^{10}B, quantity $\Sigma = \sigma n$ in Table 2.2.

The scintillator is a $13 \times 13 \times 13$ cm^3 cube, as shown in the Fig. 2.12a. The total volume is about 2.2 liters. The emission spectrum is in the visible light, and is peaking around 420 nm (violet), as shown in Fig. 2.12b. The scintillator properties are given in Table 2.2. As a dopant, ^{6}Li could have been better, since $^6\mathrm{Li}(n,\alpha)^3\mathrm{H}$ has a higher cross section and higher energy output than $^{10}\mathrm{B}(n,\alpha)^7\mathrm{Li}$.

$$n + {}^6\mathrm{Li} \rightarrow {}^3\mathrm{H}(2.73\mathrm{MeV}) + {}^4\mathrm{He}(2.05\mathrm{MeV}) \tag{2.4}$$

Unfortunately, the plastic ^{6}Li-doped scintillators were not available on the market until a couple of years ago, unlike ^{10}B which were available for a couple of decades [87] and are well-studied. We were considering using a liquid scintillator with ^{6}Li. A special acrylic "fish tank" was made and tested. However, for the final deployment, we abandoned this path because nuclear facility safety constraints at NIST precluded the use of flammable liquids.

For fast neutrons, the delay between the first recoil-proton pulse and the capture is about 13.5 μs [86, 87], which is approximately equivalent to the average time interval between prompt and delayed signals for an IBD event. The full timing distribution

for IBD neutron capture on ^{10}B is shown in Fig. 2.10, with an average time of about 10 μs and the most probable time of being captured around the first microsecond. Fig. 2.11 shows the position displacement for an IBD neutron capture relative to the IBD interaction vertex. To better navigate through the text, different nomenclature names for neutrons of different energies are given in Table 2.4.

511-keV gammas produced from e^+e^- annihilation (Eq. 2.5) deposit about 1/3 of their energy in the scintillator [85].

$$e^+ + e^- \rightarrow \gamma(511 \text{ keV}) + \gamma(511 \text{ keV}) \tag{2.5}$$

Properties	EJ-254-5%	EJ-254-2.5%	**EJ-254-1%**
Light Output (% Anthracene)	48	56	60
Scintillation Efficiency (photons/1 MeV e$^-$)	7,500	8,600	9,200
No. of H Atoms per cm^3 ($\times 10^{22}$)	5.18	5.17	5.16
No. of C Atoms per cm^3 ($\times 10^{22}$)	4.44	4.55	4.62
No. of ^{10}B Atoms per cm^3 ($\times 10^{20}$)	5.68	2.83	1.14
Ratio $\Sigma(^{10}\text{B})/\Sigma(^{1}\text{H})$	127.6	62.4	25.6
Density (g/cc)	1.026	1.023	1.021
No. of Electrons per cm^3 ($\times 10^{23}$)	3.33		
Wavelength of Maximum Emission (nm)	425		
Rise Time (ns)	0.85		
Decay Time (ns)	1.51		
Pulse Width, FWHM (ns)	2.24		
Polymer Base	Polyvinyltoluene		
Refractive Index	1.58		
Softening Point	75°C		
Vapor Pressure	Vacuum-compatible		
Coefficient of Linear Expansion	7.8 x 10^{-5} below 67°C		
Light Output vs. Temperature	At 60°C, L.O. = 95% of that at 20°C No change from 20°C to -60°C		
Temperature Range	-20°C to 60°C		

Table 2.2: mTC scintillator properties [86].

A special Monte Carlo model has been constructed [85, 88]. Figs. 2.13 show the number of photoelectrons as a function of both neutrino energy and position in the scintillator cube for an IBD event (all prompt and all delayed events plotted).

It should also be noted, that the scintillator does not have pulse-shape discrimination (PSD) capabilities. In other words, neutron and gamma interactions don't have well-defined distinct signatures as they do in PSD scintillators. PSD affects the rise and fall waveform shapes (different light outputs, microsecond long waveforms). PSD would have been a double-edged sword for the mTC: the ability to distinguish between gammas and neutrons by analyzing rise/fall light outputs at the expense of losing fast timing capabilities, its key feature.

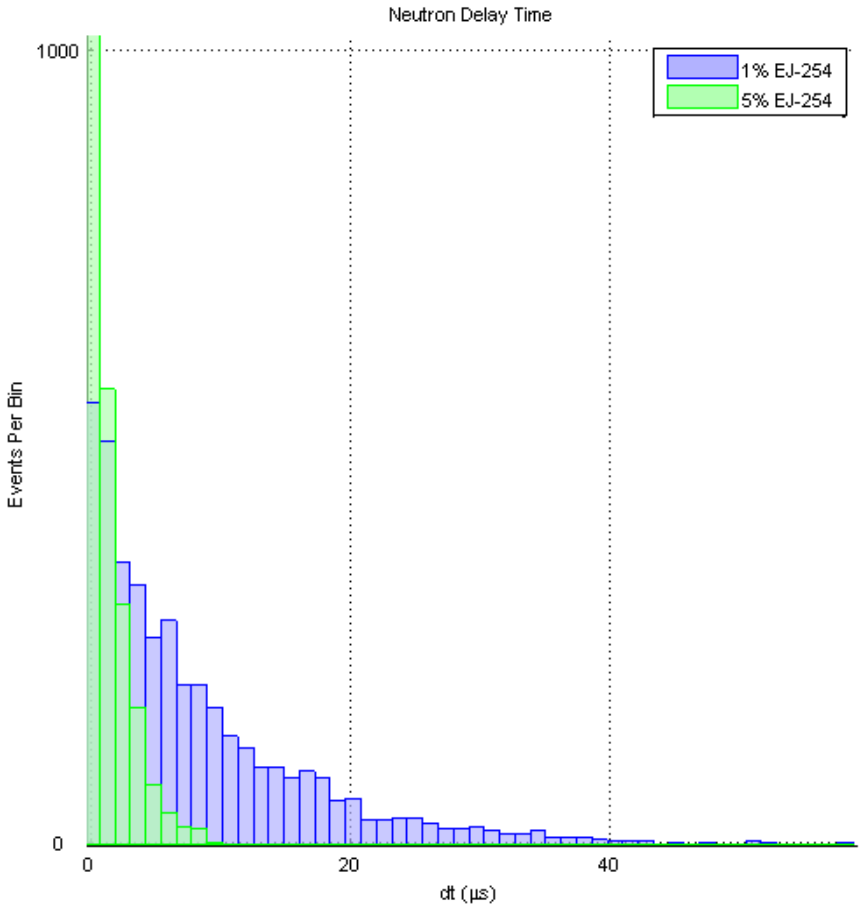

(a) 1% and 5% nat. boron EJ-254, [88].

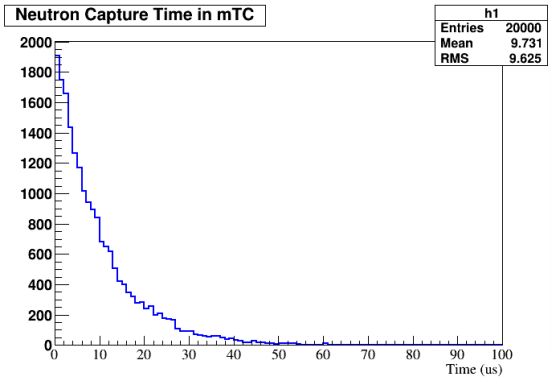

(b) Linear scale, 1% nat. boron EJ-254, [89].

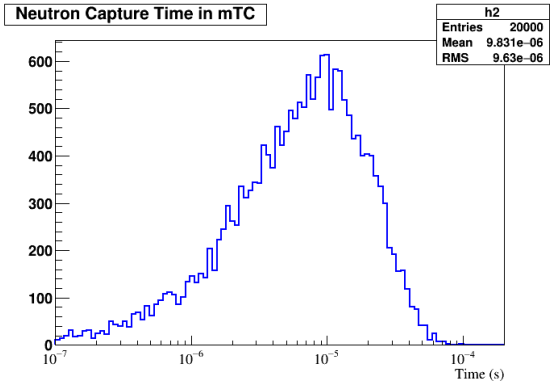

(c) Log scale, 1% nat. boron EJ-254, [89].

Figure 2.10: Timing of IBD neutron capture after the emission. Different simulations.

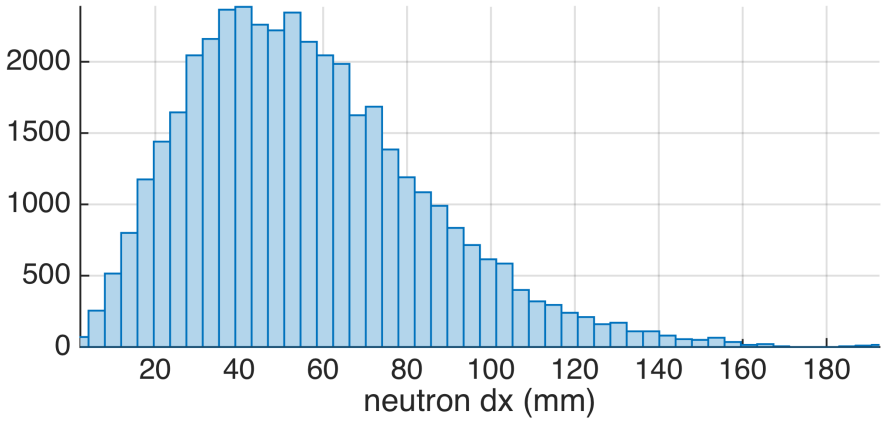

Figure 2.11: Position for an IBD neutron capture on ^{10}B in the mTC Monte Carlo simulation. Figures are taken from [85].

Energy		Barns
0.025	eV	3836
0.1	eV	1929
1	eV	610
10	eV	193
100	eV	60.6
1	keV	19
10	keV	5.89
20	keV	4.17
30	keV	3.41
40	keV	2.98
50	keV	2.68
100	keV	1.96
120	keV	1.8
150	keV	1.61
200	keV	1.36
225	keV	1.28
250	keV	1.19

Table 2.3: Neutron capture cross section on ^{10}B [86, 90].

Name	Kinetic energy, in eV
Ultracold	$<\sim 10^{-7}$
Cold	$\sim 10^{-7}$ .. 10^{-3}
Thermal	0.025, or $\sim 10^{-3}$ .. 10^{-1}
Epithermal	$\sim 10^{-1}$ .. 1
Slow	~ 1 .. 10
Resonance	~ 10 .. 10^{4}
Intermediate	$\sim 10^{4}$ .. 10^{5}
Fast	$\sim 10^{6}$ .. 10^{7}
Ultrafast	$>\sim 10^{7}$

Table 2.4: Names for neutrons of different energies.

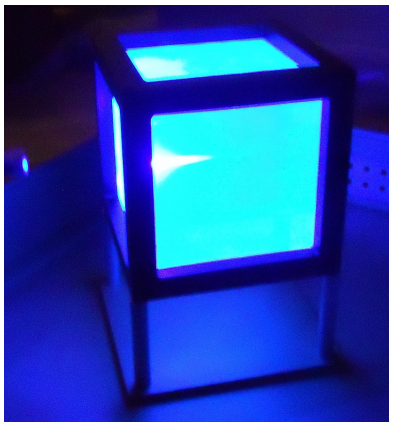

(a) mTC scintillator illuminated by a blue laser.

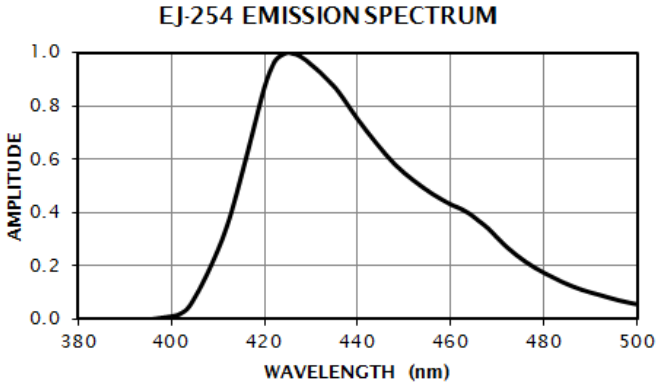

(b) Scintillator EJ-254 emission spectrum [86].

Figure 2.12: mTC scintillator EJ-254 doped with 0.2% ^{10}B (1% natural boron).

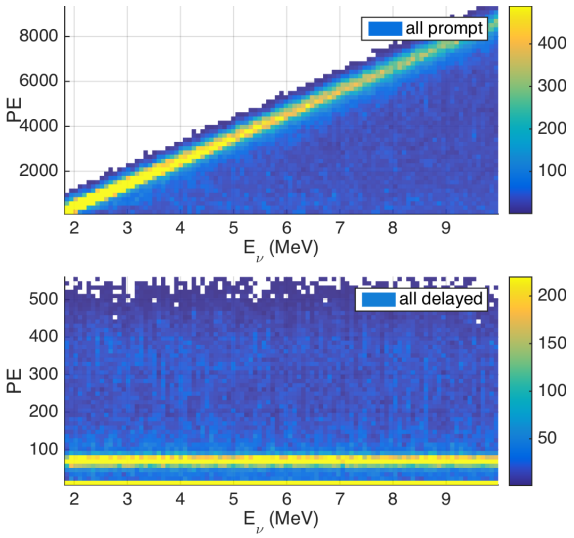

(a) As a function of neutrino energy.

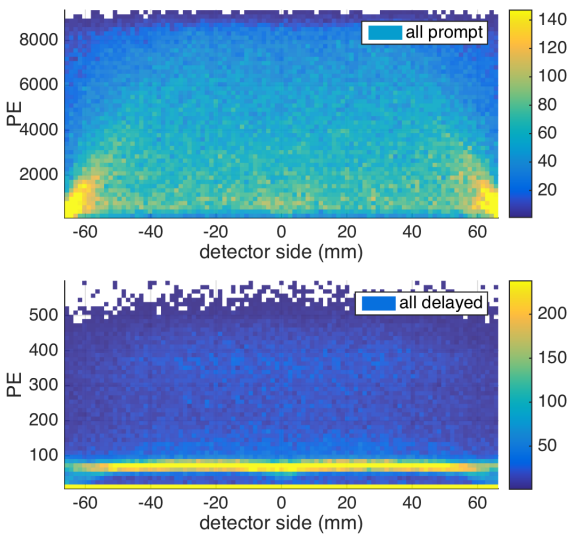

(b) As a function of detector x-coordinate.

Figure 2.13: Number of photoelectrons produced in a simulated IBD event in the mTC, for both prompt (top) and delayed (bottom) events. Figures are taken from [85].

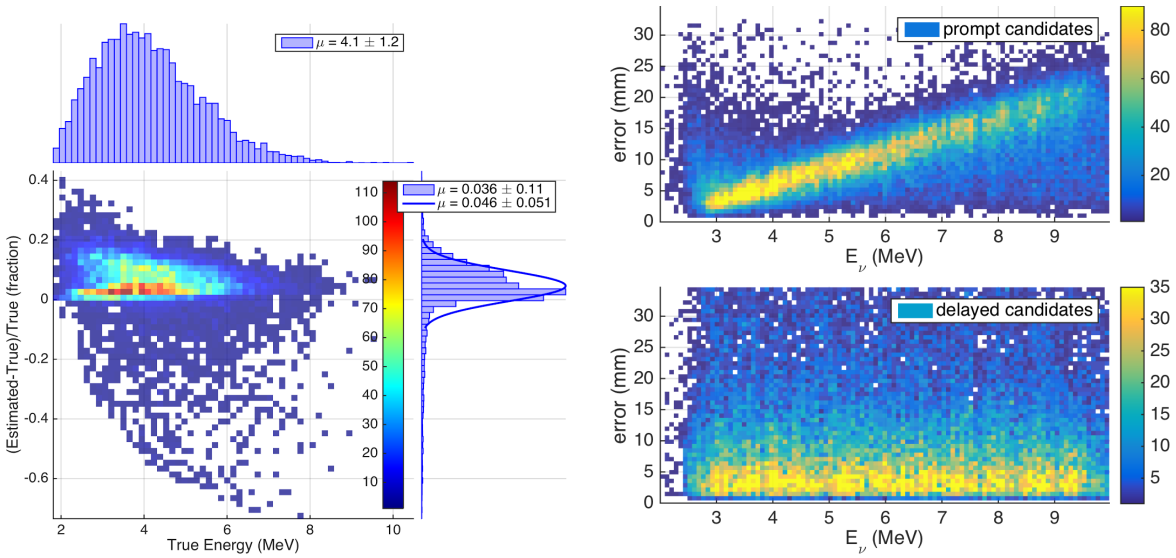

(a) Neutrino energy resolution, for a realistic reactor antineutrino spectrum.

(b) Position resolution for prompt and delayed signals.

Figure 2.14: Monte Carlo simulations of IBD events in the mTC. Energy and position resolution as a functions of neutrino energy. Figures are taken from [85].

2.3 MCP-PMT

The photocoverage along with the spatial resolution should be rather high for the whole concept to work, i.e. the first PE timing and interaction vertex reconstruction. The micro-channel plate PMTs, which have recently become available, would suffice for our needs. It is currently the fastest photodetector technology available [91]. The development of MCPs made it possible to make a PMT with a multi-anode structure in a very compact package. We chose Photonis MCP-PMT XP85012 for our detector [81]. Another choice would have been Hamamatsu MCP-PMT, like the ones that are used in the Belle II iTOP project [92–94]. Although doable, there would be a technical problem getting everything in a very small volume with a proper grounding as they need a positive high voltage unlike Photonis MCP-PMTs, which require negative HV.

A Bialkali photocathode is deposited on a 3 mm-thick Schott 8337B glass [95]. When a violet photon hits the photocathode there is a 20% chance that it will produce a photoelectron which then subsequently is multiplied in the MCP, Fig. 2.15a.

There are 24 of the MCP-PMTs in total — four per mTC face. Each MCP-PMT has 64 square anodes, which can be individually read out. Taking into account geometric dimensions of the MCP-PMT active area, as illustrated in Fig. 2.16b, the photocoverage is

$$\frac{24(.053)^2}{6(.13)^2} \approx 66.5\% \tag{2.6}$$

However, the quantum efficiency on the edges of the active area is rather low. If we include only individual pixel dimensions 5.9×5.9 mm^2 then the more realistic photocoverage is about 53%

$$\frac{24 \times 64(.0059)^2}{6(.13)^2} \approx 52.7\% \tag{2.7}$$

The PMTs are mechanically clamped to the scintillator, and an optical grease EJ-550 [96] is applied between the PMT glass and the scintillator surface for index matching (Table 2.5). Small mechanical pressure is uniformly applied to mount a PMT to the scintillator without air bubbles forming in the optical grease. However, it is hard to avoid air pockets completely, and when all PMTs are mounted it is a non-trivial operation to check for air pockets building up. There were a few concerns, later in operation, that a few air pockets might have been developed at the corners on several PMTs.

The first tests to check gain were performed with a pair of MCP-PMTs coupled to a smaller piece of the scintillator to which a laser fiber was optically coupled, as shown in Fig. 2.21a. More details on initial gain calibration can be found in the Appendix (Section A.5). The gain mostly follows the gain power law as expected, Fig. 2.21b.

Figs. 2.17a show both scintillation and Cherenkov light probability density functions based on our GEANT and MATLAB simulations. Taking into account the MCP-PMT quantum efficiency, shown in Fig. 2.18, it is clear that mostly the scintillation light is detectable by the MCP-PMTs above $\sim$ 400 nm; the Cherenkov light is dominant below $\sim$ 400 nm.

First tests with all 24 MCP-PMTs mounted on the mTC scintillator were performed with each MCP-PMT acting as a conventional PMT, i.e. single-anode. The backs of the MCP-PMTs were covered with a conductive foam to short out the pins to ground. A special interconnect board was made that connects MCP-PMT common-dynode

coax outputs to pin connectors on the readout board stacks. We used ^{60}Co as a γ-emitter, and were able to clearly distinguish between muon and gamma events.

During the course of running the experiment, we had a couple of MCP-PMTs replaced, Fig. 2.15b. To replace a dead tube is a challenge: all the electronics need to be unmounted, the suction between the tube and the scintillator is enormous, and the frame doesn't allow the tubes to be easily removed. There was an overheating accident that resulted in loss of more than half of the MCP-PMTs; it will be discussed in Section 2.10.1.

Scintillator	1.58
Optical grease	1.46
MCP-PMT glass window	1.478

Table 2.5: Refractive index.

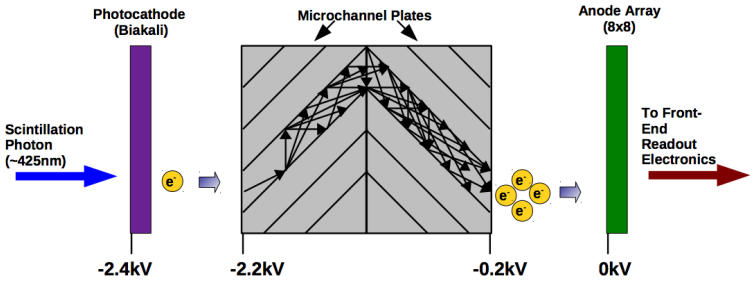

(a) Concept of electron multiplication [80].

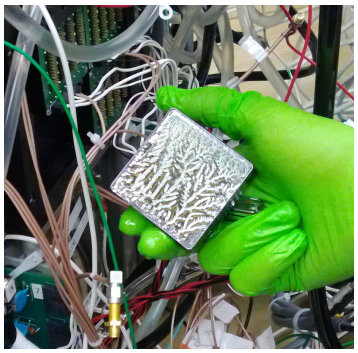

(b) Dead tube removed from the cube, covered in optical grease [97].

Figure 2.15: MCP-PMT.

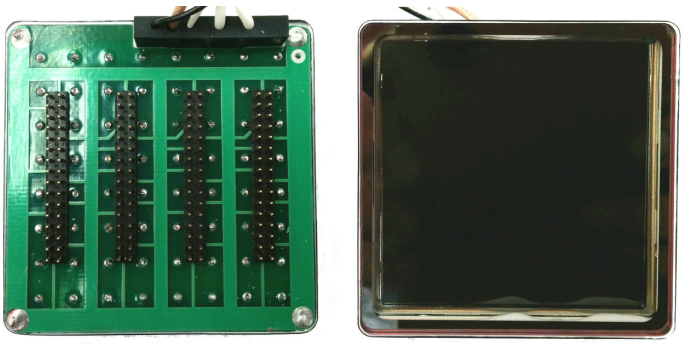

(a) Photograph of front and back, one of the 24 used in the mTC.

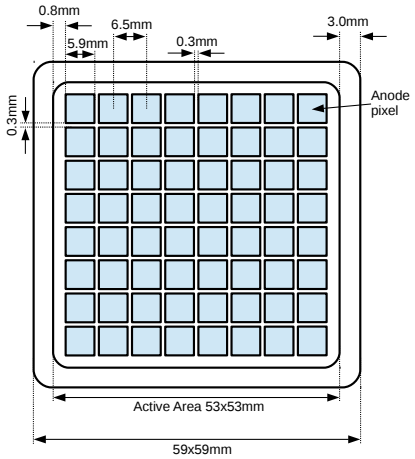

(b) Dimensions.

Figure 2.16: Photonis MCP-PMT XP 85012. Figures are taken from [85, 98].

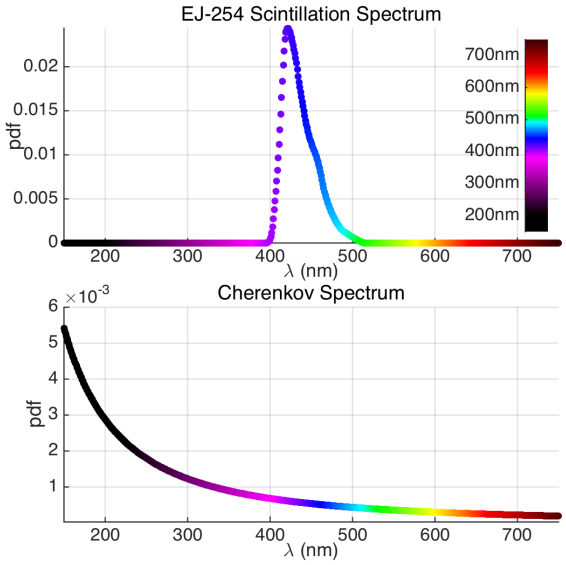

(a) Scintillation and Cherenkov spectrum probability distribution functions [85].

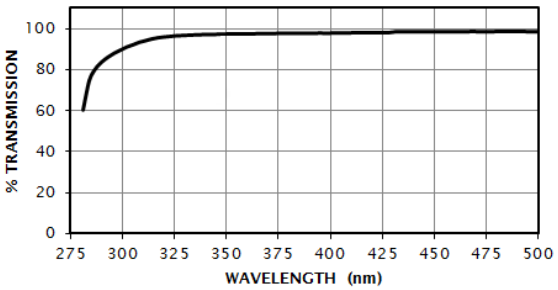

(b) Transmission for 0.1 mm thick silicon grease EJ-550 [86].

Figure 2.17: Spectra.

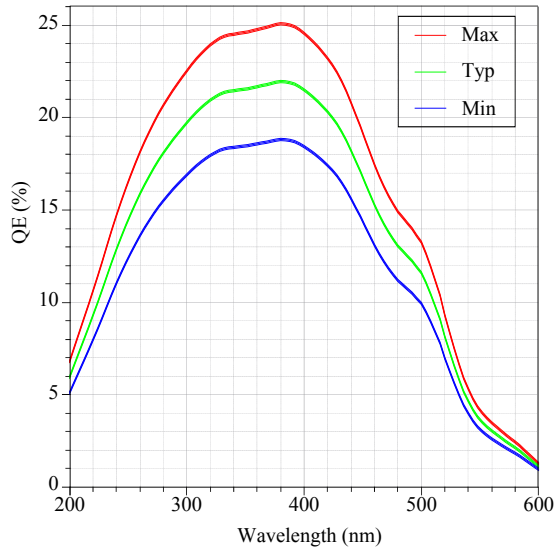

(a) Absolute quantum efficiency of the MCP-PMTs installed in the mTC. Figure is adapted from [99].

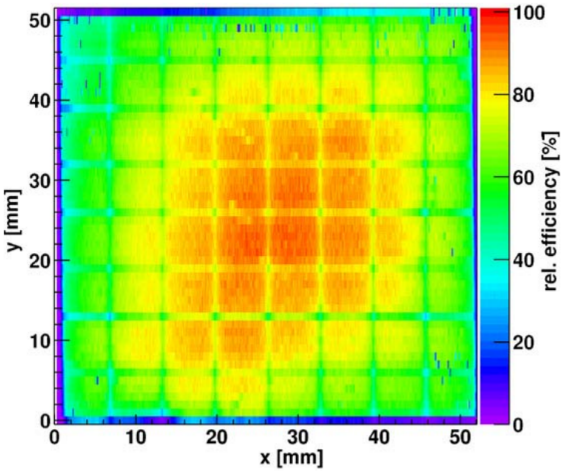

(b) A relative quantum efficiency map of an early version of MCP-PMT Photonis. Figure is taken from [100].

Figure 2.18: MCP-PMT efficiency.

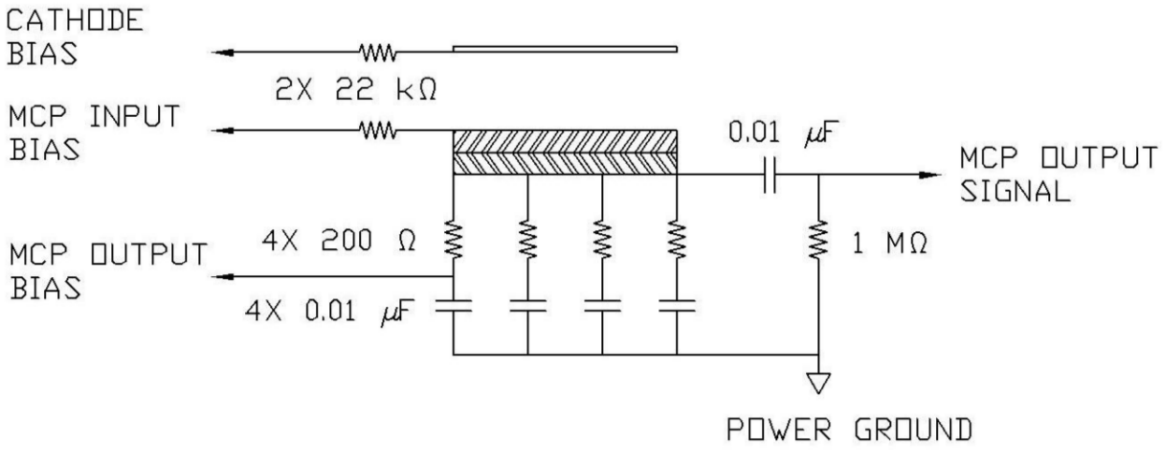

Figure 2.19: Internal and external connections of the MCP-PMT, [81].

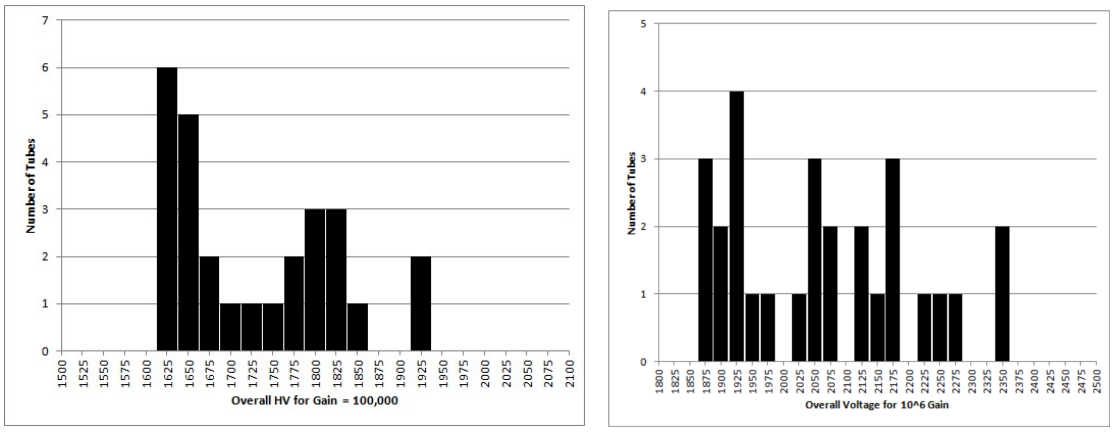

Figure 2.20: High voltage values for 10^5 (left) and 10^6 (right) gain of the MCP-PMTs used in the mTC, manufacturer's data.

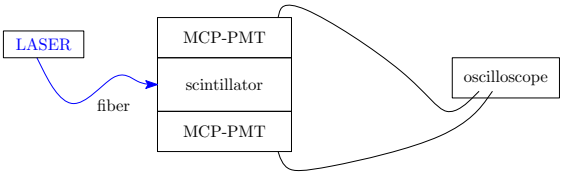

(a) The setup for the initial test of MCP-PMT gain linearity. A piece of plastic scintillator is sandwiched in between two MCP-PMTs.

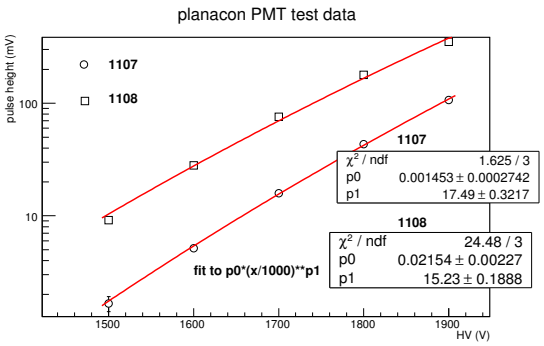

(b) Average pulse height on MCP-PMTs 1107 and 1108 [101].

Figure 2.21: Initial MCP-PMT gain linearity test.

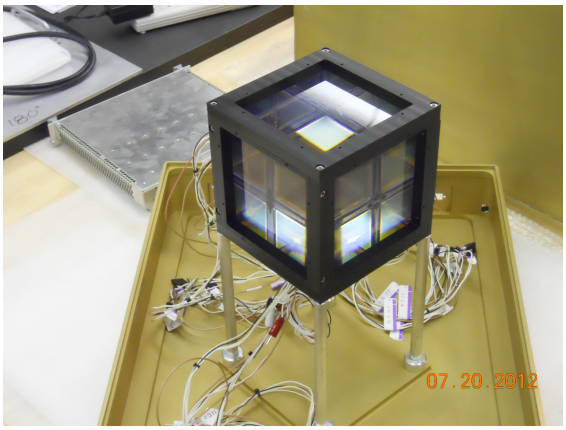

(a) mTC scintillator cube with three faces populated with 12 MCP-PMTs.

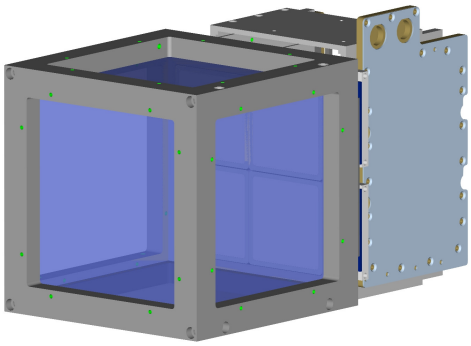

(b) CAD of the mTC scintillator cube with one face populated with four MCP-PMTs and two electronics board stacks connected. The green dots indicate the holes for the MCP-PMT clamps.

Figure 2.22: Scintillator cube partially populated. Figures are taken from [102].

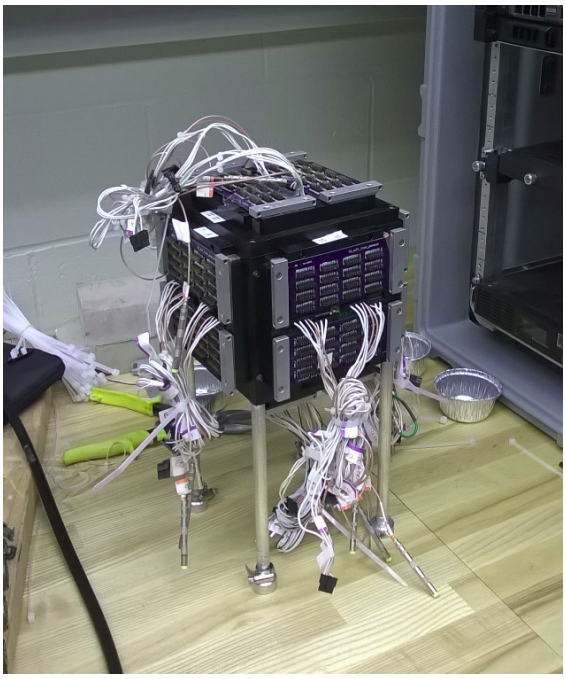

(a) MCP-PMT with front boards attached on each face of the mTC.

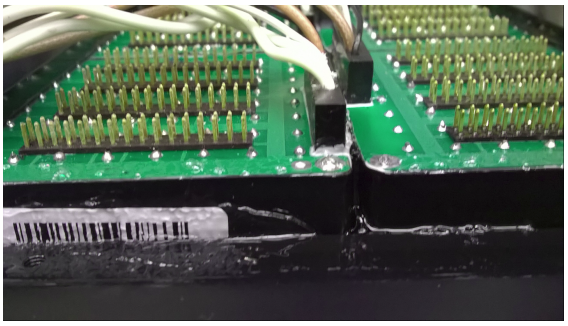

(b) After a few years some optical grease leaked on the bottom face under gravity.

Figure 2.23: mTC without electronics.

2.4 Electronics, trigger, and data

To read out data from the MCP-PMTs, special readout modules are each mounted on the back of two MCP-PMTs. These are unique since most digitizers are rack-mounted and require much more space, power, and cabling. The first version of the readout electronics used the IRS 3B ASIC, digital signal processing compact-PCI (DSP cPCI) boards, and a clock board that was later replaced. Everything was designed at the University of Hawai'i. Each readout module has a Standard Control and Read-Out of Data (SCROD) board with an FPGA made by the Xilinx corporation, four carrier boards, and an interconnect board. A carrier board has four application-specific integrated circuits (ASICs). For the sake of simplicity, a readout module is also known as a board stack or SCROD. There are about 645 registers for setting SCROD/ASIC parameters. The SCROD local clock runs at 250 MHz. Historically, IRS stands for Ice Radio Sampler. IRS ASICs have been in use in a variety of projects where fast digitization and primary *in situ* analysis are key. Other similar ASICs based on switched capacitor arrays include LABRADOR [103] and PSEC4 [104], which were also primarily developed at our Instrumentation Development Laboratory, and DRS4 [105, 106].

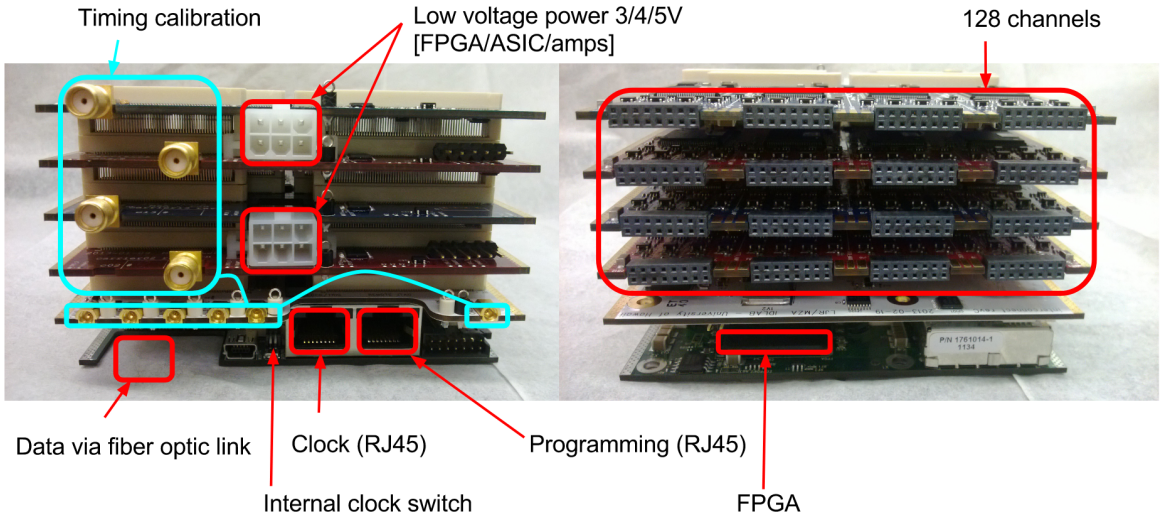

Figure 2.24: Front and back of one of the twelve mTC readout modules; each covers 2 MCP-PMTs, 128 individual channels in total.

The ASIC IRS3 B/D parameters are summarized in Table 2.6. Each chip has eight channels. Each channel can store 128 samples × 256 windows = 32,768 samples, which is ∼ 12 μs at the clock setting we use. During each cycle of the master clock, each IRS3B acquires 128 samples, giving the detector a sampling rate of 2.73 GSa/s, the inverse of which corresponds to a ∼ 366 ps sample time. The board-stack FPGA controls both sampling and digitization of the analog signals. There is a limit on the total amount of data we can digitize/store. Consequently, only the region of interest gets stored — window(s) with pulses and neighbors. The internal storage is analog. The SCROD digitizes it, and it gets recorded.

There is always some voltage at the capacitor cell. That voltage, although slightly fluctuating, is unique for each individual cell. It is called a pedestal, and there are 32,768 unique offsets (pedestals) for each channel, shown in Fig. 2.27. In total, over 50 million individual pedestal values $(1,536 \times 32,768)$ are required to run all the channels

of the detector. Fig. 2.28 represents an example of a pedestal for one channel. To work with waveforms without worrying about those voltage offsets for each set, it is important to subtract them. There are 3 arrays: sampling, intermediate, and storage. The structure is:

$$\underset{\text{(128 cells)}}{\text{Sampling}} \rightarrow \underset{\text{(128 cells A, 128 cells B)}}{\text{Intermediate}} \rightarrow \underset{\text{(16,384 cells A, 16,384 cells B)}}{\text{Storage}} \tag{2.8}$$

The full block-diagram of the ASIC is shown in Fig. 2.26, and a photograph of the die is shown in Fig. 2.29a. The reason for the A/B intermediate array alternating is due to what are effectively timing constraints inside the ASIC. Writing directly from sampling into storage in previous revisions ended up causing some issues where addresses couldn't settle fast enough and data was corrupted [107].

Imagine, a 1536-channel oscilloscope with the coincidence set to the number of channels to trigger. Once the trigger threshold is set on a channel-by-channel basis, the data will be digitized and read out, matching the trigger look-back window which is approximately 64 windows for each pixel. Fig. 2.31 illustrates the concept. The first version of the trigger, Fig. 2.31a, was limited by firmware and later replaced by a two-level triggering scheme. Tables 2.7, 2.8, and 2.9 describe the terminology of different trigger levels.

Table 2.10 is an example of the readout interface that an operator sees in the terminal.

One of the problems with the first version of the electronics was that the clock board had not one, but a group of four jitter cleaners. As a consequence, the timing on 12 readout modules was grouped in four, as shown in Fig. 2.32.

An earlier version of the electronics also had a minor problem with different SCRODs having different reference windows. Fig 2.33 is a set of histograms representing the difference between the reference window on a selected SCROD and on SCROD 0 within the same event. All events are for row 0 col 0 ch 0. The reference window differences between SCRODs are more or less fixed for the entire run, so we could have potentially accounted for that in software if we had kept the original version of the electronics.

Below is the summary of issues with the first version of the electronics:

- Single-PE level was not feasible to reach due to low amplifier gain.
- The ASIC IRS3B had a stronger timing dependence on temperature than the newer IRS3D version, making it hard to calibrate.
- The clock board had not just one but several jitter cleaners affecting the timing among different SCRODs.
- DSP-cPCI DAQ had a much slower performance, so the data would pile up at high rates without being stored.

All of these were resolved before installation by the guide hall at NIST: higher-gain amplifiers were installed on new carrier boards along with IRS 3D ASICs, the new clock board was made, and the DAQ system was completely replaced by off-the-shelf Intel 1Gb Ethernet cards installed in a newly-acquired server. Although the trigger efficiency improved, increasing from $\sim 50\%$ to $\gtrsim 90\%$, the trade-off for installing a higher gain amplifier was that the dynamic range suffered, i.e. more saturated pulses in the data.

(a) Original electronics scheme.

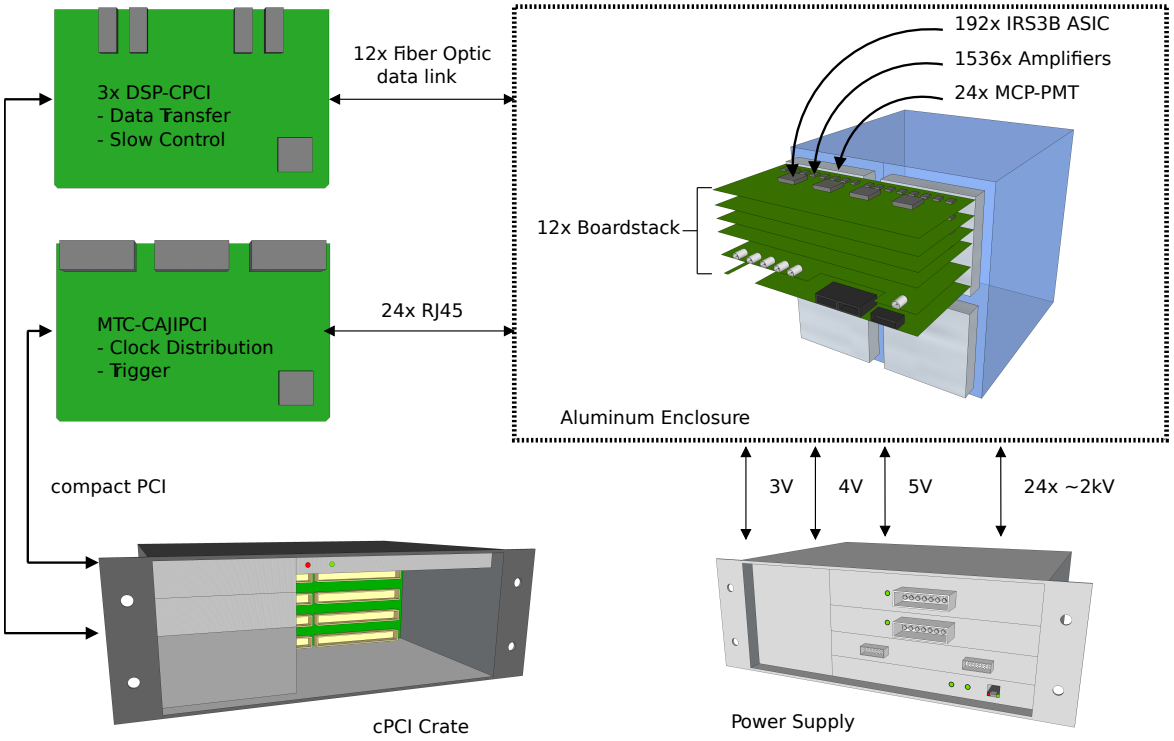

(b) Electronics after the upgrade.

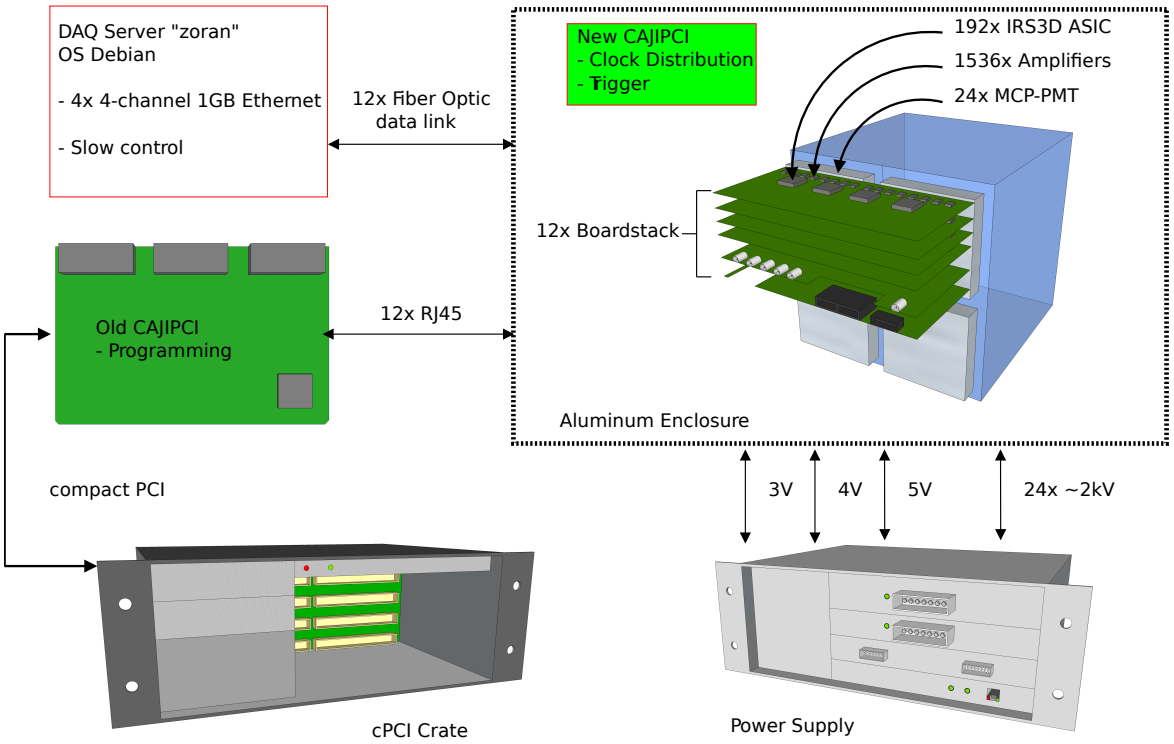

Figure 2.25: Electronics concept of the mTC. Figures are adapted from [108].

Despite resolving these multiple issues, new problems were discovered. There were a few hiccups in the system, one being a corrupted data on a specific ASIC in row 1 column 3 within each board stack — 8 of 128 channels would always have flawed data.

The instrument also had pathologies:

(a) Gap between windows caused a scramble at the window boundaries (stitching effect).

(b) Leading edge timing was affected by the noise (especially crucial for dim signals) for dim pulses.

(c) For bright saturated signals the timing suffered due to the pulse-reconstruction techniques (Fig. 2.36).

These unresolved pathologies resulted in the timing resolution above the desired few 100-ps level.

In addition to those pathologies, one of the major challenges was dealing with faulty electronics channels, which can be due to a malfunctioning amplifier or ASIC. A special pruning list was created to mask out those bad channels in the data. After upgrading the firmware, the faulty channels were no longer triggered.

Another procedure besides taking pedestals data, associated with the unique voltage baseline for any given channel, is the procedure of setting threshold values. To set a threshold (L0 trigger) properly on any given channel, a threshold scan is taken beforehand, due to the unique voltage values on every sample within that particular channel. The procedure counts the number of triggers per a preset level in ADC counts. One should also note that the L0-trigger setting does not exactly correspond to the threshold values.

To properly set the L1 trigger for the detector, a trigger scan is performed, which gives trigger rate per any present L1. Fig. 2.37 shows the concept.

Raw data that is getting stored in *dat* files is binary. Then, it can be converted into several different formats depending on the purpose. The most commonly used format for the data has the structure presented in the Table 2.12, which among our collaboration is called *glenn* format.

To better understand the reference window concept, it is important to remember that there are 512 windows (each having 64 samples) inside the IRS ASIC storage array. Let's say we have a reference window w_{ref} equal to 75, and we recorded the waveform, as shown in Fig. 2.41, in windows $[37, 40]$, inside the storage array it is located at the following windows $[475, 478]$ (adjusted windows, as we call them). To get adjusted windows, one needs to use the following equation:

$$w_{adj} = \begin{cases} w - w_{ref} + 1, & w \geq w_{ref} \\ w - w_{ref} + 1 + 512, & w < w_{ref} \end{cases} \tag{2.9}$$

After subtracting the pedestals, if we read out all the channels on all the ASICs, we would have a picture similar to the one shown in Figs. 2.44.

Each chip IRS3D was calibrated during the production using the fast pulser and two delayed pulses, Fig. 2.55. The time resolution essentially goes from $\sim$500 ps to $\lesssim$ 50 ps.

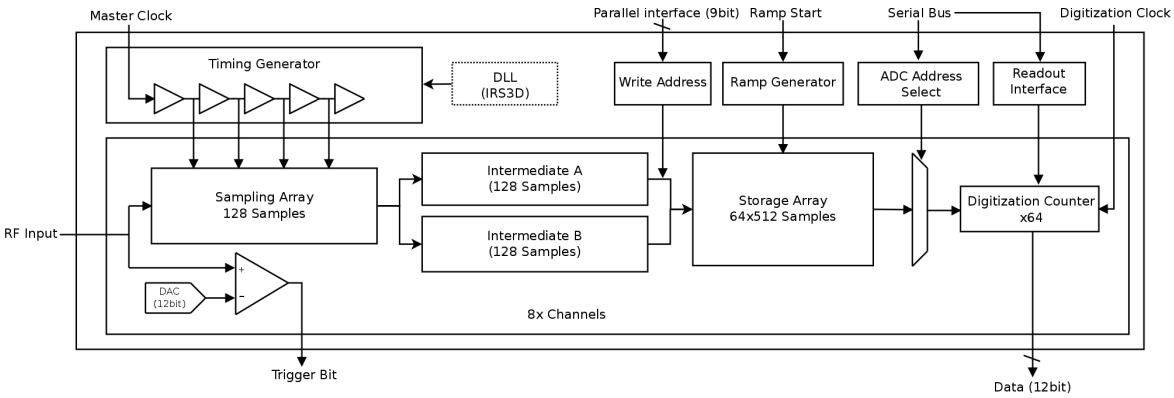

Figure 2.26: IRS3-family ASIC chart. Figure is taken from [85].

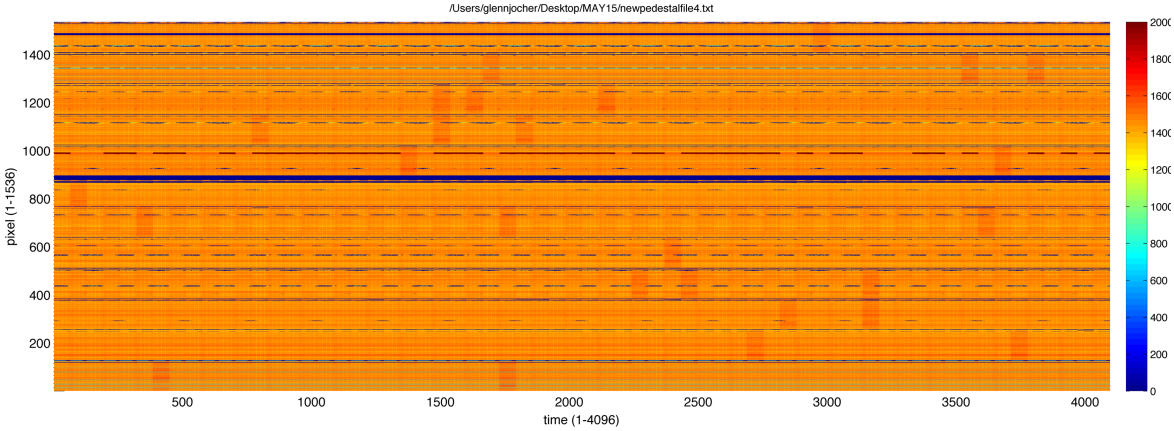

Figure 2.27: Pedestals for all 1536 channels. IRS3B, [88].

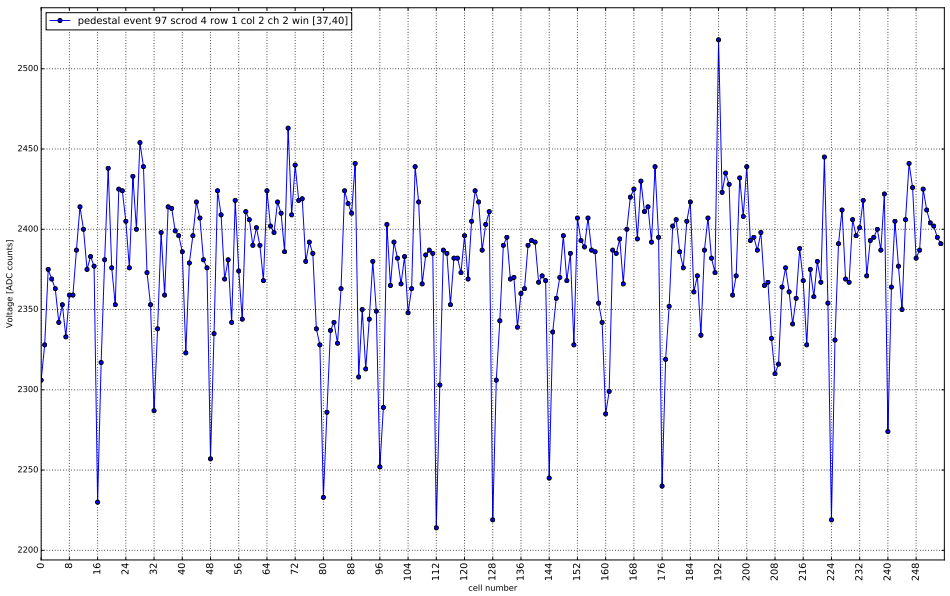

Figure 2.28: Pedestals for one channel's 256 samples, IRS3D version of the ASIC.

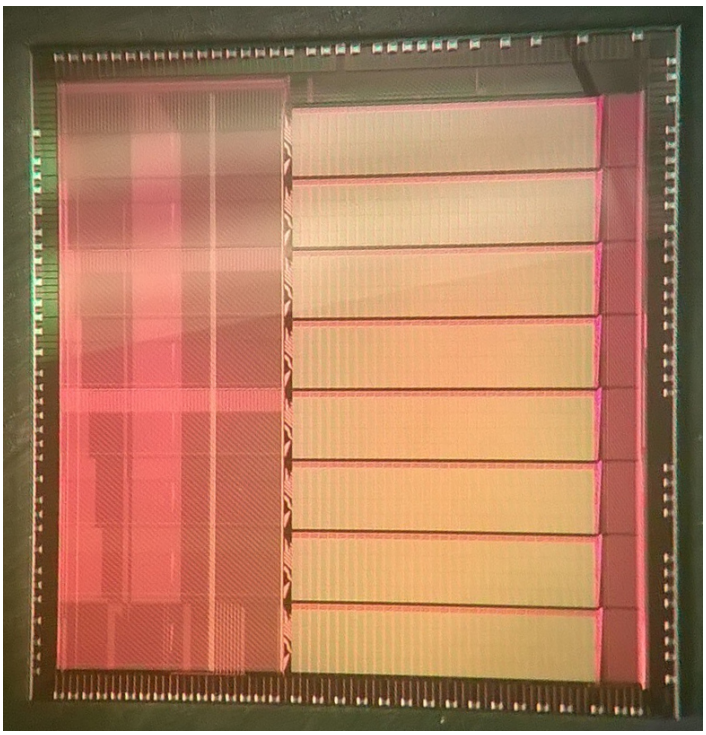

(a) Microscope image of IRS ASIC die. ∼2.6M transistors, 7.7k resistors on 8×8 mm^2 die. Each has 8 individual channels — 8 storage arrays are visible.

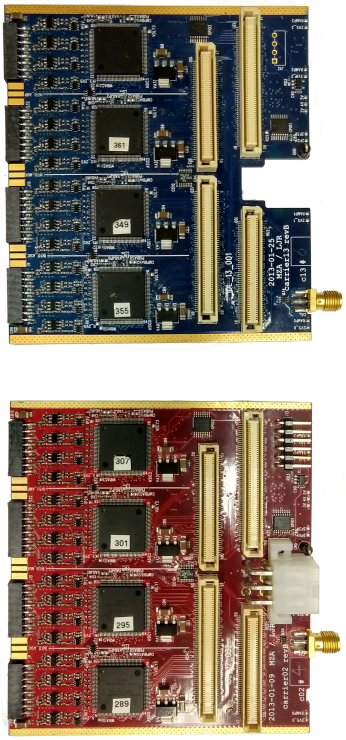

(b) Carrier boards, each has 4 ASICs.

Figure 2.29: IRS3B ASIC.

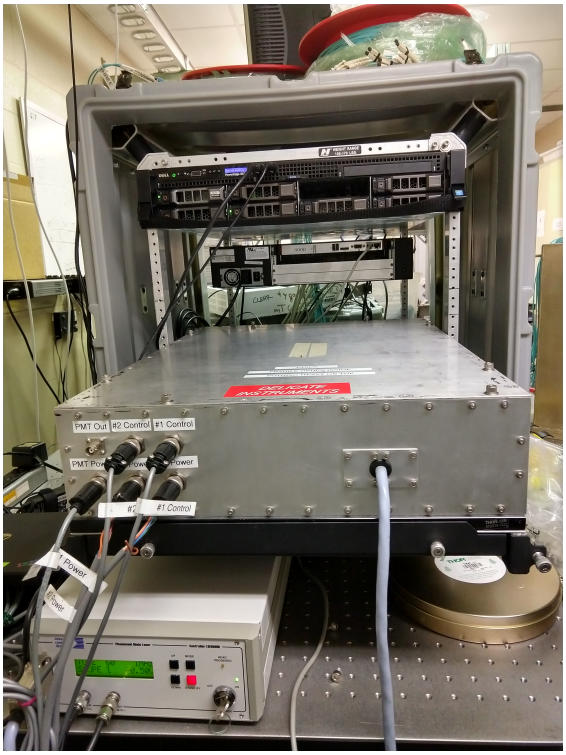

(a) DAQ crate with the laser box on the sliding shelf.

(b) Wooden model of the cube indicating the locations of the PMTs and readout modules.

Figure 2.30: mTC 2nd crate and the mapping tool.

Parameter	IRS Range	mTC Setting
Channels	8	
Sampling cells	128	
Storage depth	32,768	
Analog bandwidth	> 300 MHz	
Digitization	on-chip Wilkinson	
Quantization	12(9)-bits logged(effective)	
Dynamic range	~ 2 V	
Typical noise	~ 1 mV_{RMS}	
Sampling rate	1–4 GSa/s	2.73 GSa/s
Sample time	.25–1 ns	366 ps
Master clock	8–31 MHz	21.3 MHz
Buffer time	8–32 μs	12.0 μs
Conversion time	> 2 μs	6.2 μs

Table 2.6: Operating parameters for the IRS family of ASICs, and nominal ASIC operating conditions for the mTC. Table is adapted from [85].

L0	threshold for each of 1536 channels
L1	number of triggered channels for one SCROD (out of 128 channels)
L2	number of triggered SCRODs, out of 12

Table 2.7: First implemented trigger terminology.

L0	threshold for each of 1536 channels
L1	number of triggered channels for the entire mTC (out of 1536 channels)

Table 2.8: Second implemented trigger terminology.

L0	threshold per each of 1536 channels
$L1_{min/max}$	minimum/maximum number of triggered channels for the entire mTC

Table 2.9: Second (and final) implemented trigger terminology.

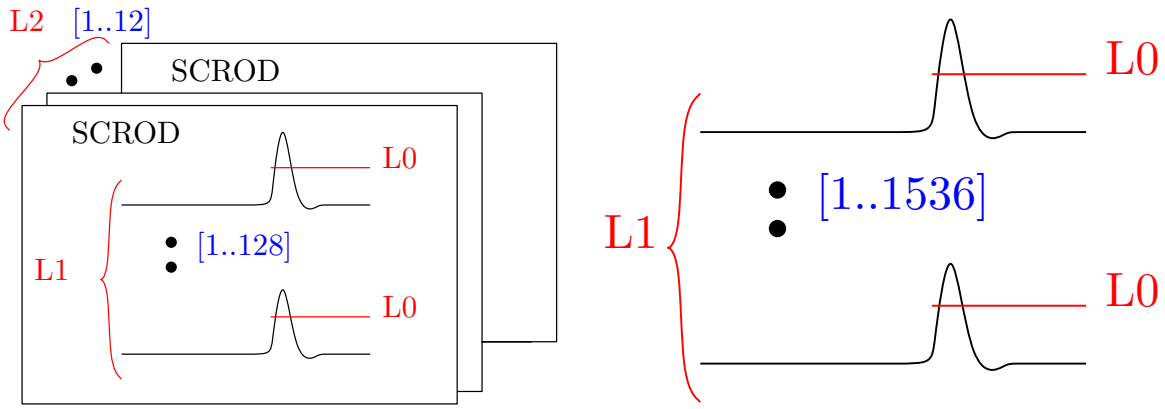

(a) Old 3-level triggering scheme.

(b) New 2-level triggering scheme.

Figure 2.31: Trigger scheme with old and new electronics firmware.

Interfaces

If	Name	P/s	MB/s	MB	Packets	Errors
0	scrod1	1000	0	113.3545	708001	0
1	scrod2	0	0	0.0312	692	0
2	scrod3	0	0	42.5381	266001	2
3	scrod4	774	0	55.8359	349001	2
4	scrod5	1000	0	112.7129	704001	0
5	scrod6	0	0	0.0312	692	0
6	scrod7	0	0	0.0000	0	0
7	scrod8	1000	0	113.5146	709001	0
8	scrod9	0	0	0.0312	692	0
9	scrod10	1000	0	113.5146	709001	0
10	scrod11	1000	1	112.0723	700001	0
11	scrod12	0	0	0.0312	692	0

Triggering

L2:	0	F Delay:	0
Mask:	111111111111	C Delay	0
Trg #:	42	Cal Mode:	NO
Veto On:	ON	Veto Needed:	NO

Network

Storage:	0	Queue depth:	0

Storage

Storage Path: /data/2016_07_26/exp_0001_run_0837.dat

Table 2.10: Readout interface, during a run by the nuclear reactor, July 26th, 2016. If looking at the amount of collected data, the SCRODs with both dead tubes (1, 5, 6, 8, 11), just one tube (2 and 3), and with both tubes alive (0, 4, 7, 9, 10), are clearly visible.

Figure 2.32: Timing offsets. Four timing-groups among 12 board stacks for different function generator calibration runs. The data were taken using a pulser with the following parameters: 2.6Vpp, 1.5kHz, 8ns width, 5ns rise/fall, no offset; the pulser signal was fed through a 12-way power splitter to each SCROD calibration input. In reality, one bin corresponds to $\sim$ .3–.4 ns. Figure is taken from [88].

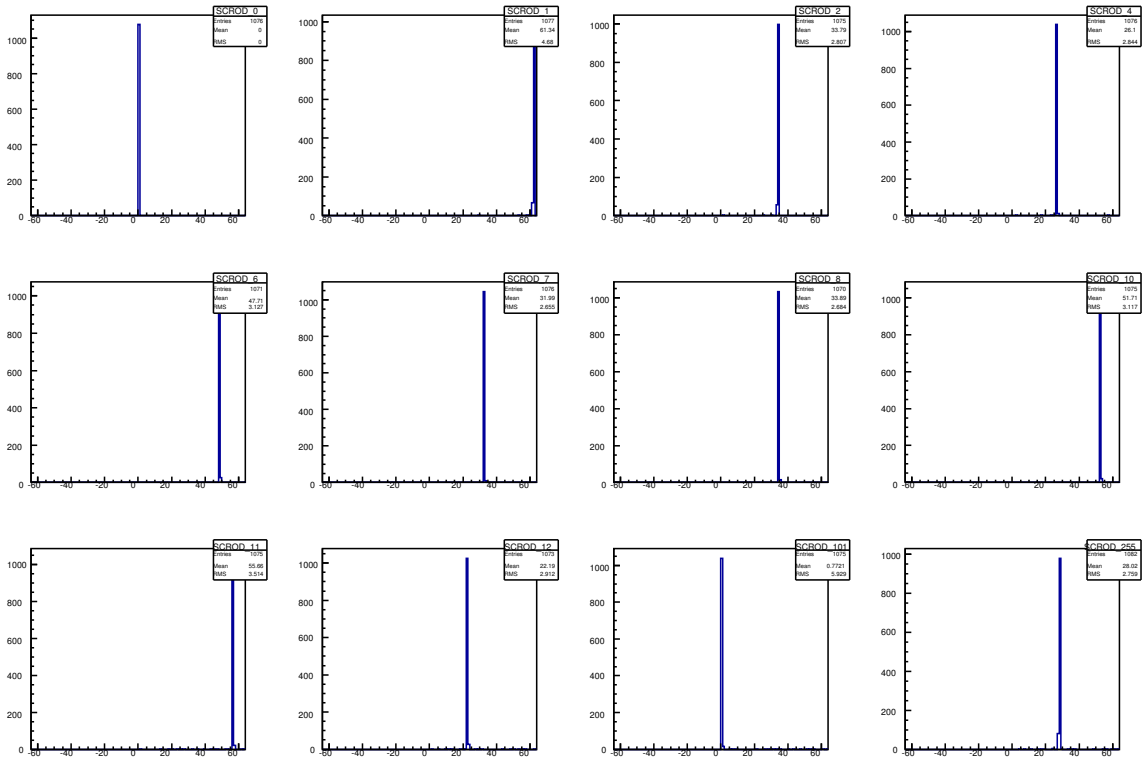

Figure 2.33: Reference window differences on a selected SCROD with respect to the SCROD 0 within the same event. IRS3B version of ASIC.

Figure 2.34: mTC unplugged situated on the lab bench. Two crates are nearby.

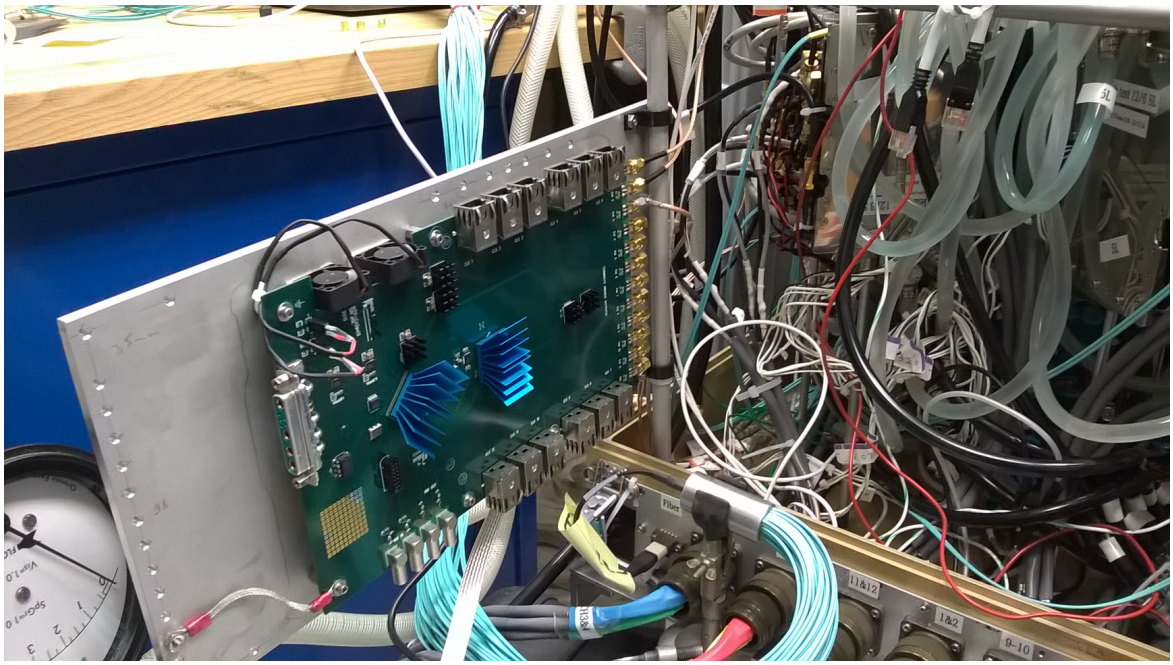

Figure 2.35: New clock and calibration board (CAJIPCI) mounts inside the main mTC enclosure.

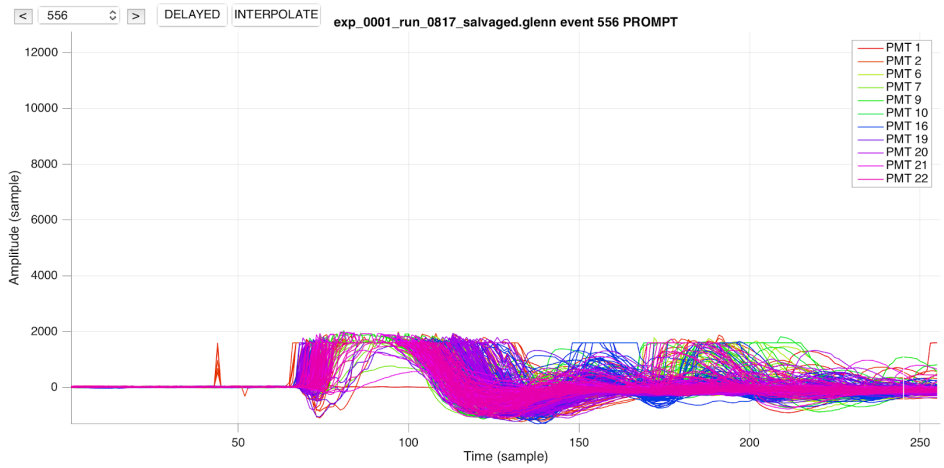

(a) Original.

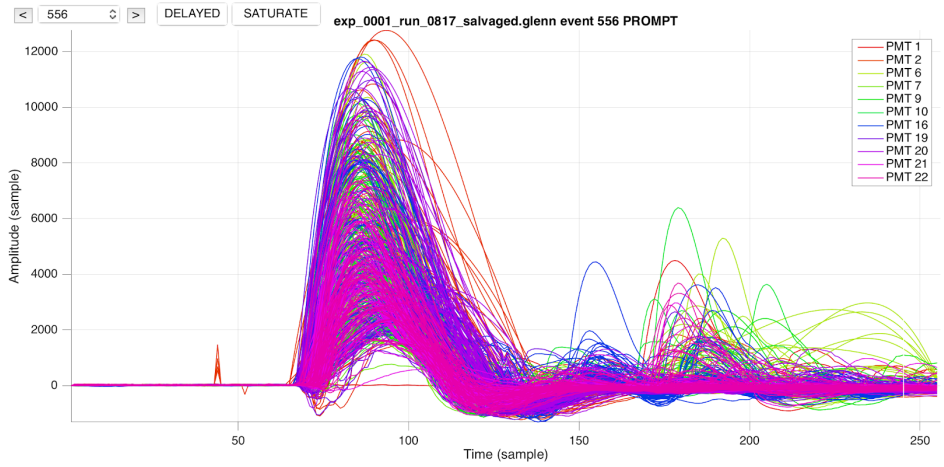

(b) Splined.

Figure 2.36: Saturated pulses. Figures are taken from [88].

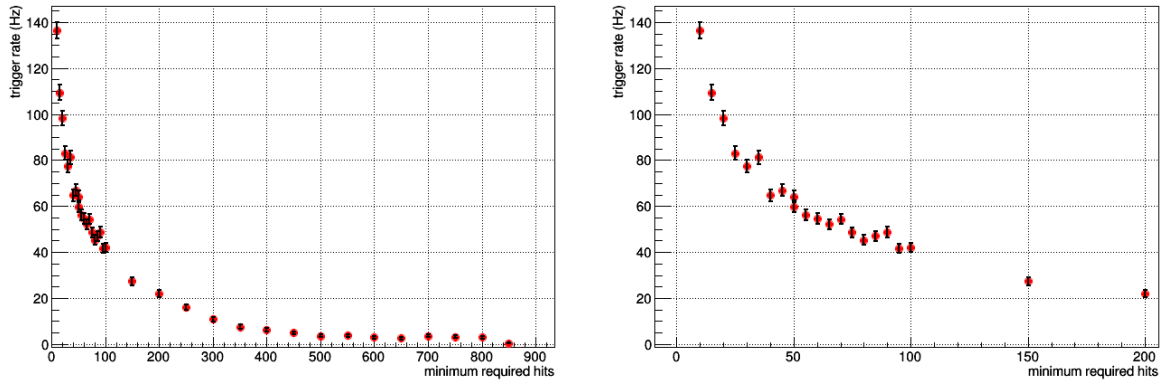

(a) Full scan. (b) Zoomed portion of the plot on the left.

Figure 2.37: C-trigger scan — trigger rate vs minimum number of hits required. mTC with half working tubes. Figures are taken from [107].

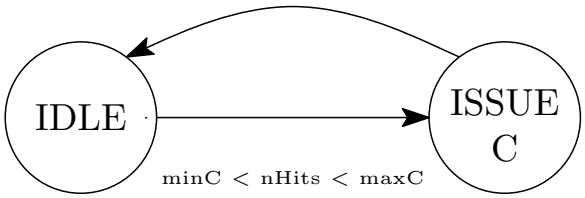

Figure 2.38: Simple (C) trigger after the electronics upgrade.

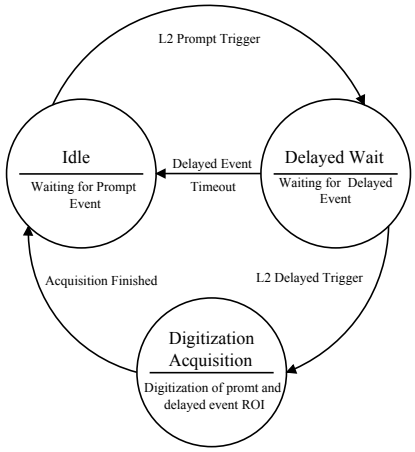

(a) Trigger scheme before the firmware upgrade. Figure is adapted from [108].

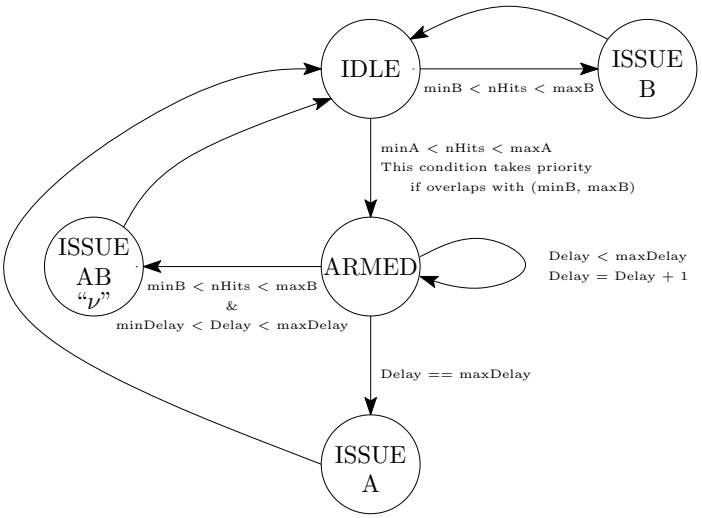

(b) New AB trigger. Figure is adapted from [107].

Figure 2.39: State machine diagram of the neutrino trigger.

```
1850 36
1851 4509
1852 65535
1853 65535
1854 65535
1855 65535
1856 65535
1857 65535
1858 65535
1859 3361
1860 17
1861 1
1862 4
1863 3
1864 1
1865 0
1866 3
1867 2
1868 0
1869 3
1870 3
1871 1
1872 1
1873 0
1874 0
1875 0
1876 1
1877 1
1878 0
1879 0
1880 0
1881 0
1882 0
1883 1
1884 0
1885 0
1886 0
1887 0
1888 0
```

Table 2.11: Scaler scan output. For this particular channel, value 1861 would be a good value to set zero.

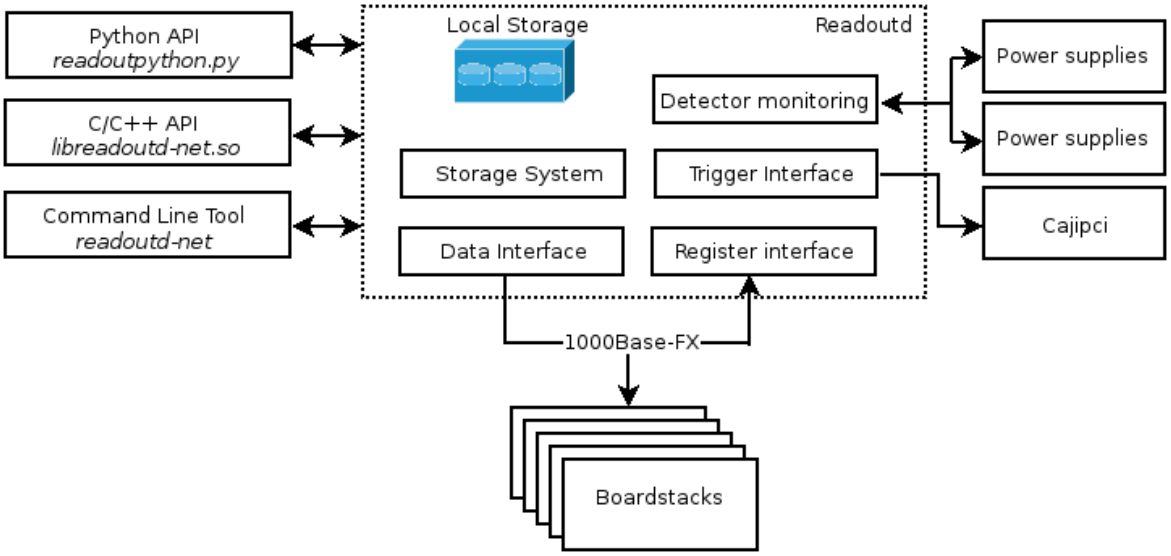

Figure 2.40: mTC readout diagram [108].

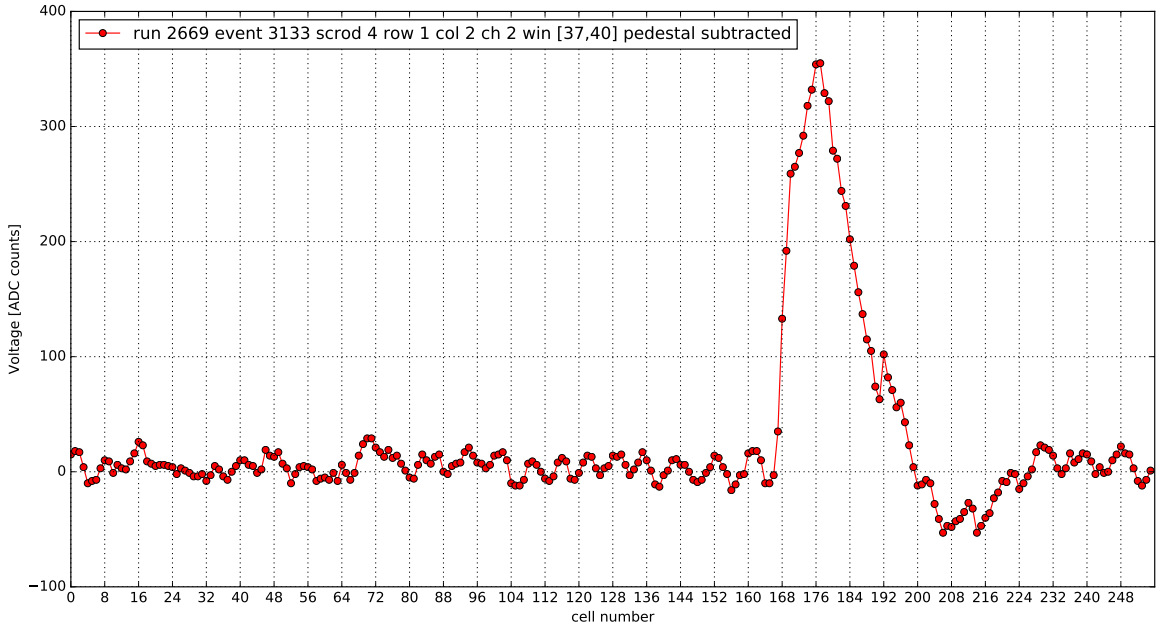

Figure 2.41: Raw data after pedestal subtraction within single channel.

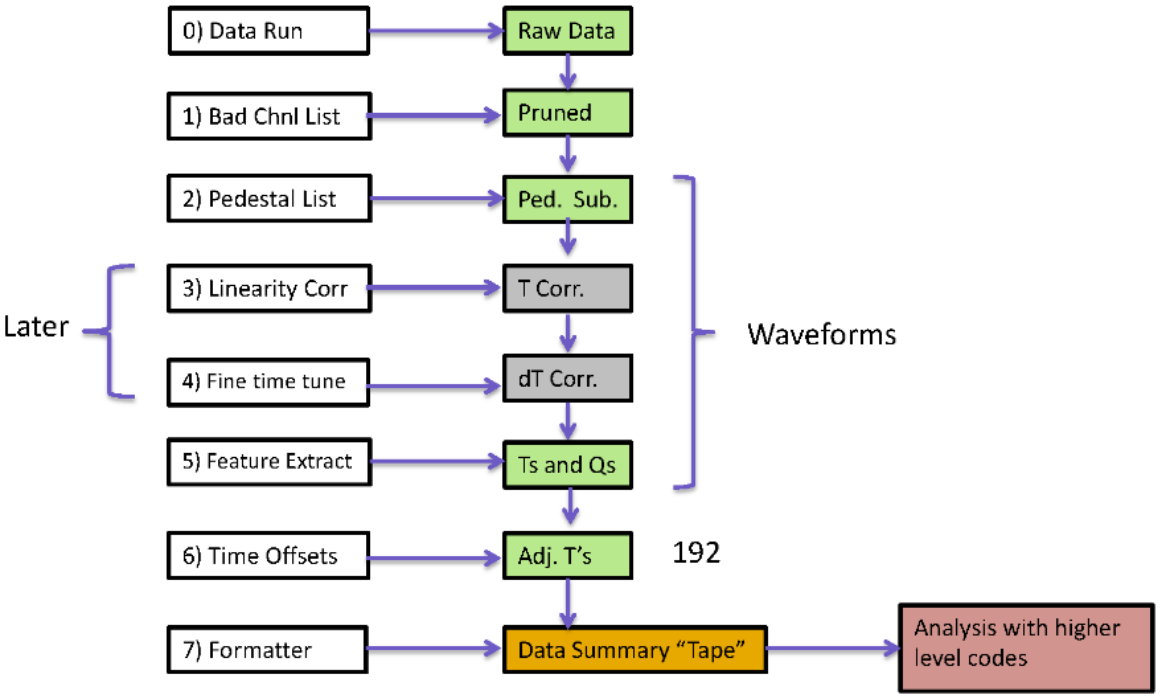

Figure 2.42: mTC data flow diagram, [109].

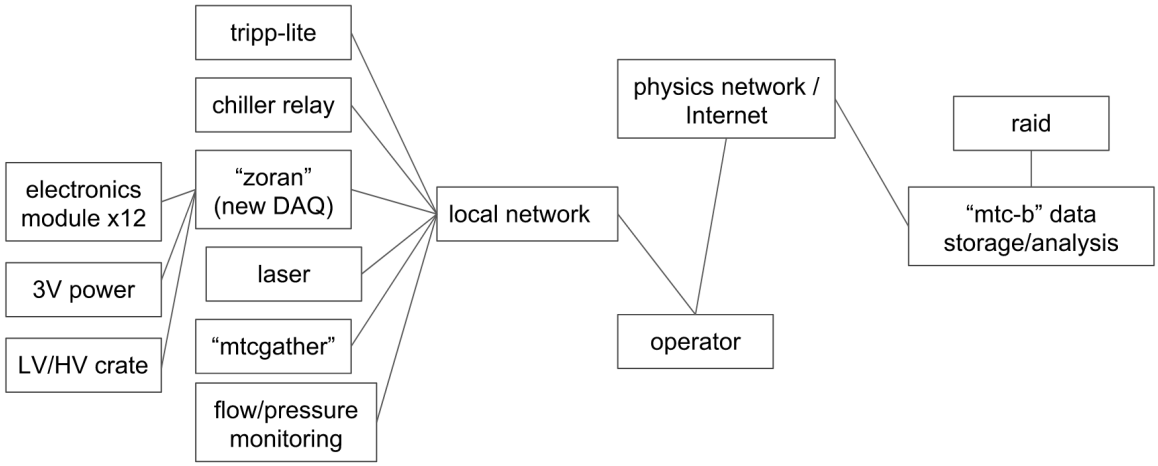

Figure 2.43: mTC network diagram.

Unix Time	Event	S	R	C	CH	ref	win	trgbit	64 voltage values
1467893327085081	2723	1	0	0	0	383	42	0	2329 2342 2400 ...
1467893327085081	2723	1	0	0	0	383	43	1	2264 2309 2335 ...
1467893327085081	2723	1	0	0	0	383	44	1	2182 2183 2186 ...
.	.	.	.	.	.	.	.	.	.....

Table 2.12: Data format structure. S — SCROD ID, R — row, C — column, CH — channel, ref — reference window, win — window, trgbit — trigger bit. Voltages are in ADC counts (before pedestal subtraction in this example).

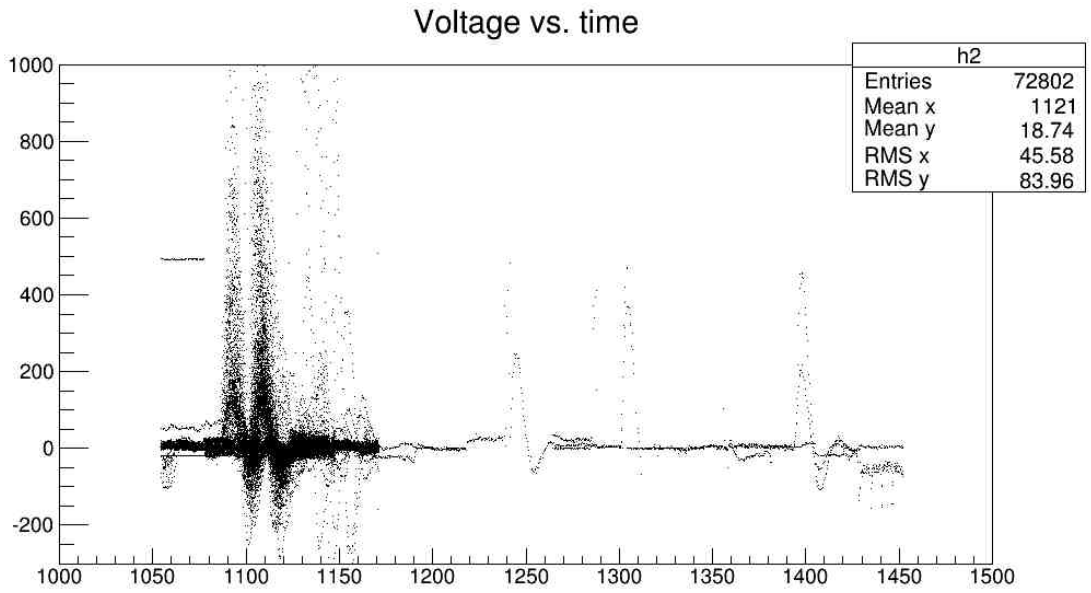

Figure 2.44: All the waveforms plotted on single plot after pedestal subtraction, with an early version of electronics, without time correction.

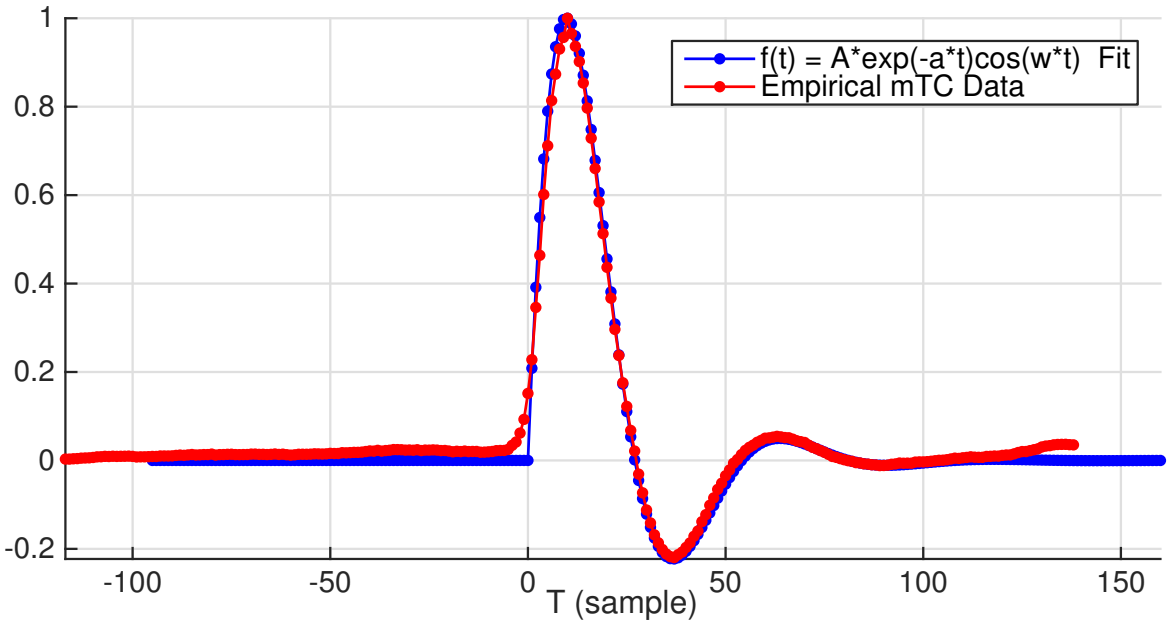

Figure 2.45: Spline of the waveform, [88].

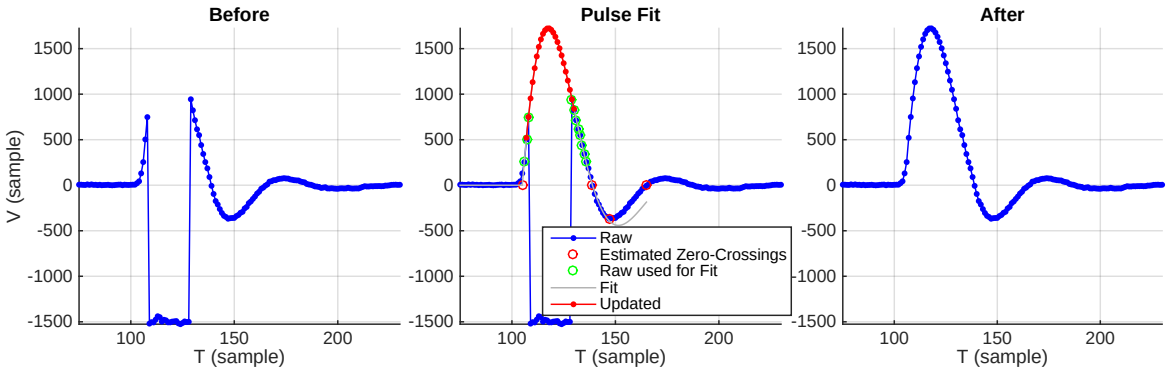

Figure 2.46: Saturated pulse reconstructed, [88].

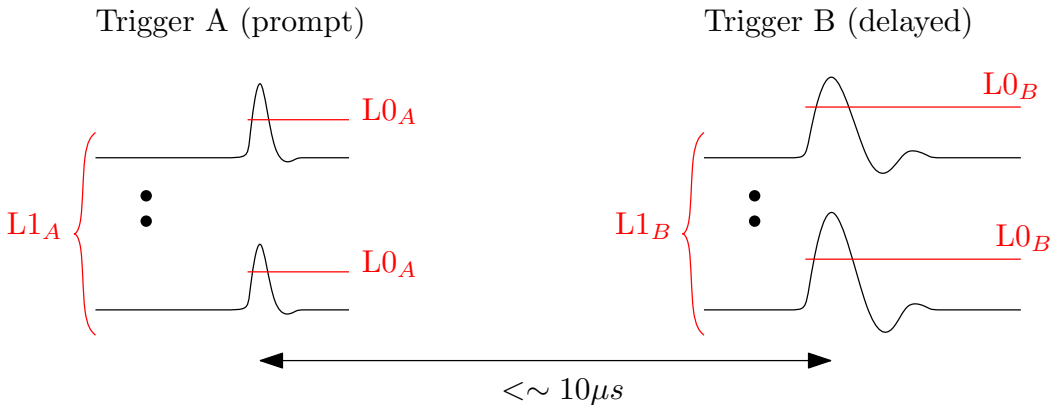

Figure 2.47: Neutrino trigger (AB) illustration.

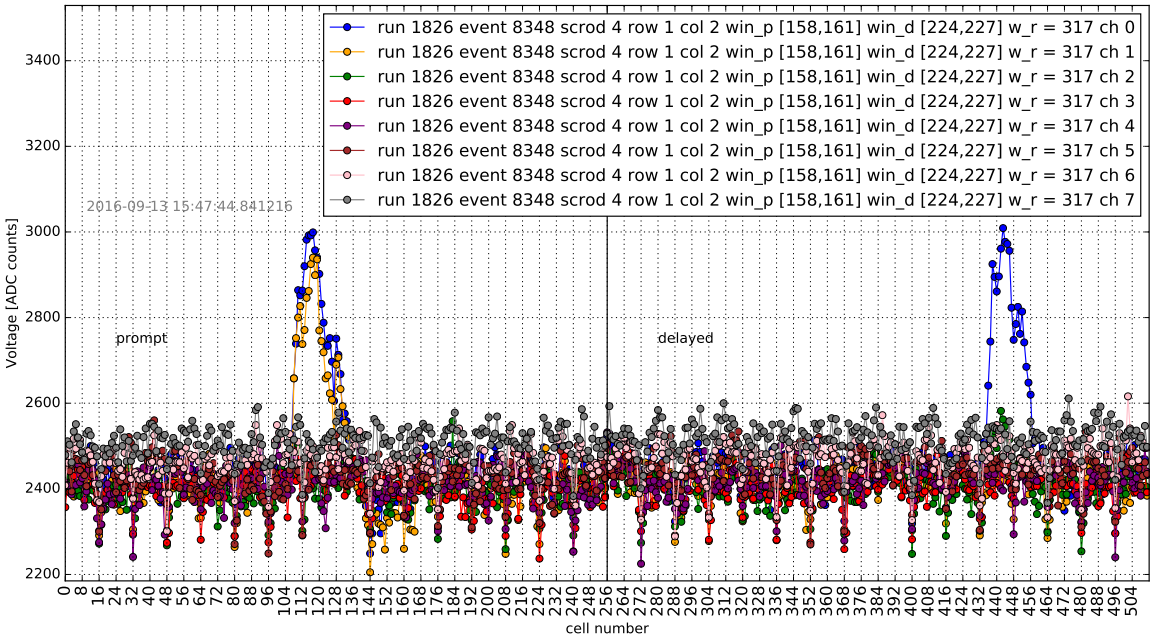

Figure 2.48: A neutrino-type event, with the delayed and the prompt event waveforms on one of the ASICs.

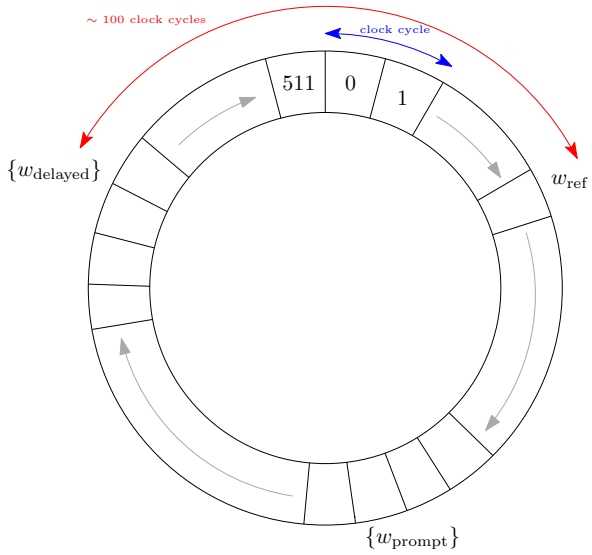

Figure 2.49: Neutrino trigger (AB) illustration of how the data is written in the storage array (ring buffer) of 512 windows, each 2^{15} samples long, or approximately 10 μs (if one clock cycle is 1/21.33 MHz).

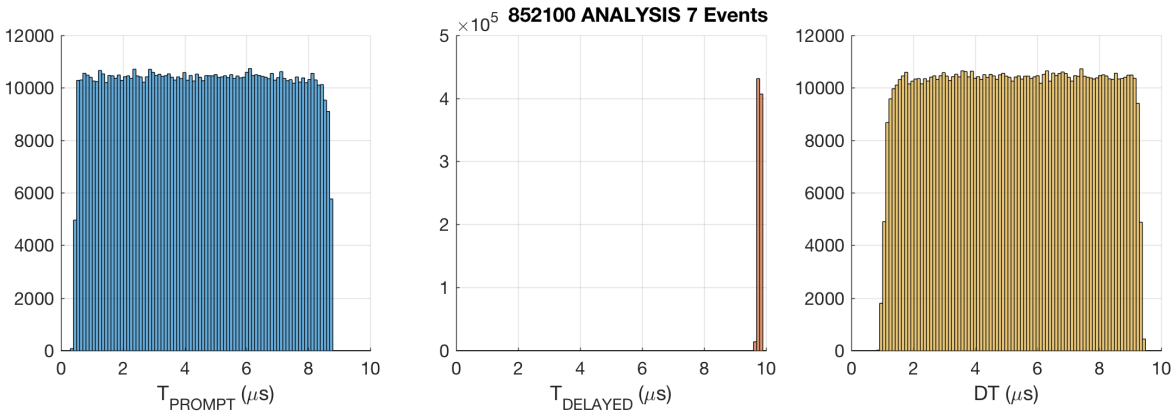

Figure 2.50: AB distribution times, [88].

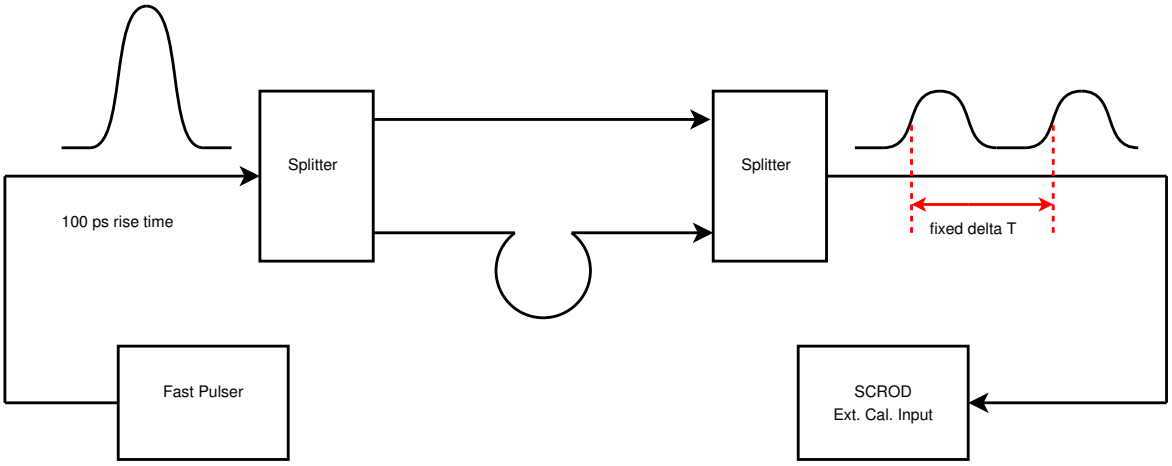

Figure 2.51: Setup for production fast-timing calibration.

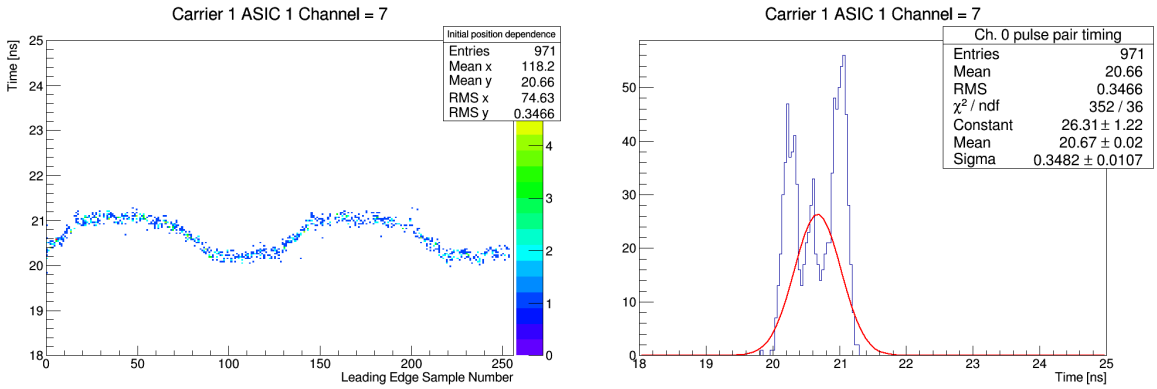

Figure 2.52: Timing sample dependence (left) and time difference Δt between two pulses (right) before the calibration. RMS = 347 ps.

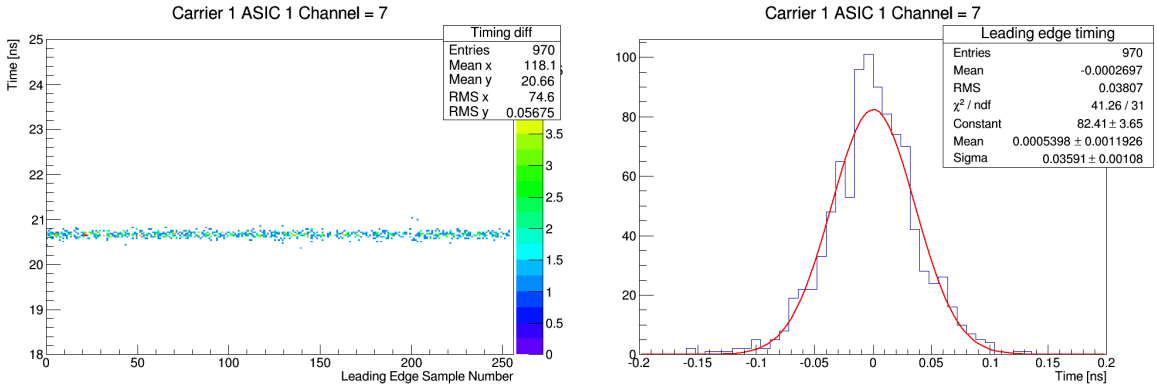

Figure 2.53: Timing sample dependence (left) and time difference Δt between two pulses (right) after the calibration. RMS = 38 ps.

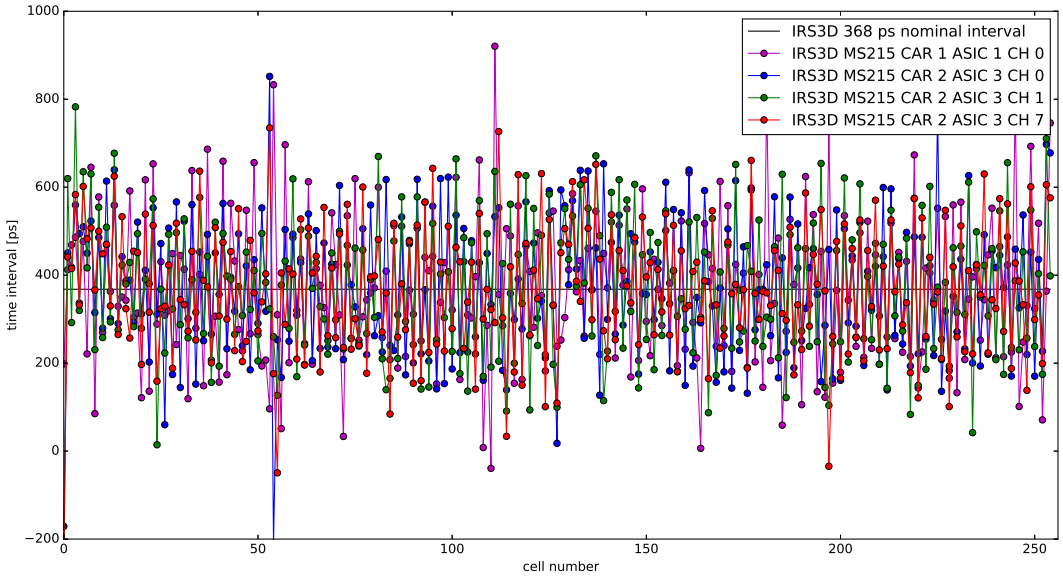

Figure 2.54: Time intervals for IRS3D, after performing production test.

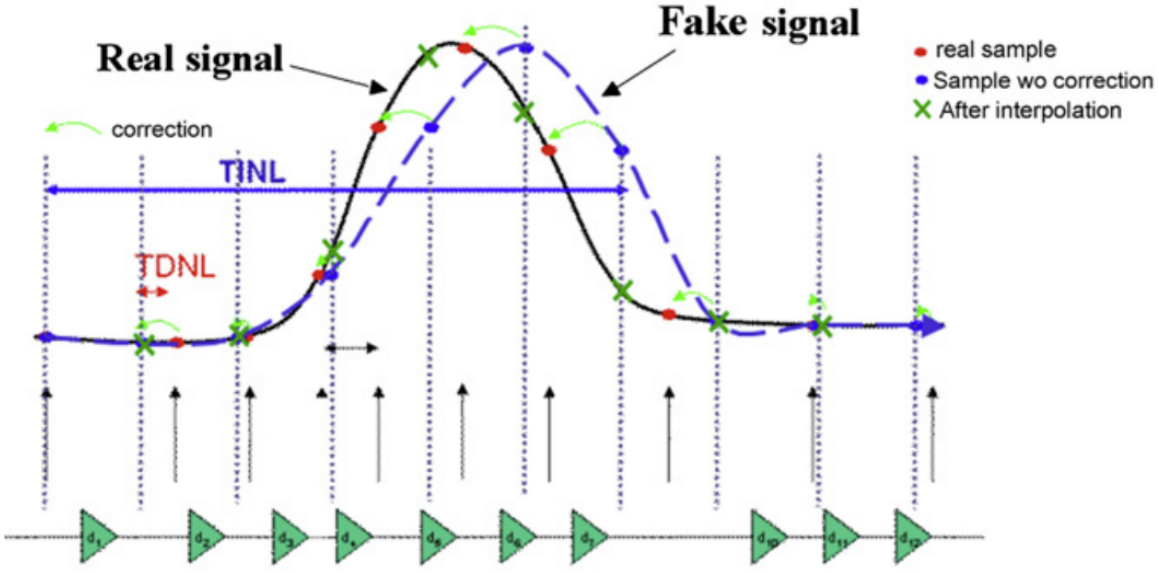

Figure 2.55: The concept behind timing calibrations, [110]. TDNL and TINL — differential and integral non-linearities in time.

2.4.1 Power supply

To power the readout electronics and the MCP-PMT, we used a commercially available power supply made by Exelsys and Wiener. The former provides 3V in 12 individual channels to power the 12 board stacks, and to operate remotely, it is connected to a specially designed controller board, which is connected to the main server. 3V power supply is shown in Fig. 2.56a. The Wiener crate, shown of Fig. 2.56b, houses 3 modules:

1. 8-channel low voltage module — 3 channels of 4V, 4 channels of 5V, and 1 spare
2. 8-channel high voltage module
3. 16-channel high voltage module

Wiener crate can be completely remotely controlled, including adjusting voltages and setting current limits. Table 2.13 shows the power monitor for the crate. Exelsys power supplies can be only turned on/off remotely, adjusting voltages requires the main enclosure box to be opened.

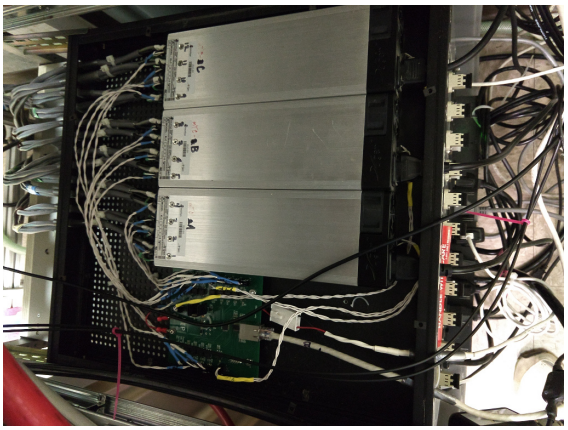

(a) Three 4-channel modules to provide 3V, next to the controller board.

(b) Wiener crate with a low-voltage and two high-voltage modules.

Figure 2.56: Main power supplies.

To provide high voltage for the MCP-PMTs, two 12-channel voltage divider boards were made, following recommendations from the Photonis data sheet. Each channel powers one MCP-PMT, and has three resistors and three capacitors, as shown in Fig 2.118a.

Our experience taught us that crimped connectors, although easy to make, are not very reliable; the lower gauge wires should have been used for high-current 4V and 5V; there should have been 12 individual channels for 4V and 5V; and there should have been a more reliable power supply chosen instead of Wiener. The total power consumption of the electronics is a couple of hundred watts.

CH	V_{set}	I_{limit}	I_{msr}	V_{term}	ON
U 0	2063.0 V	2.0 mA	372.9 μA	2063.0 V	ON
U 1	2016.0 V	2.0 mA	369.0 μA	2016.0 V	ON
U 2	2196.0 V	2.0 mA	384.1 μA	2196.0 V	ON
U 3	2436.0 V	2.0 mA	430.7 μA	2436.0 V	ON
U 4	2041.0 V	2.0 mA	361.3 μA	2041.0 V	ON
U 5	2037.0 V	2.0 mA	358.5 μA	2037.0 V	ON
U 6	2372.0 V	2.0 mA	444.4 μA	2372.0 V	ON
U 7	2203.0 V	2.0 mA	398.5 μA	2203.0 V	ON
U 8	2052.0 V	2.0 mA	362.8 μA	2052.1 V	ON
U 9	2204.0 V	2.0 mA	388.8 μA	2204.1 V	ON
U 10	2233.0 V	2.0 mA	403.7 μA	2233.1 V	ON
U 11	2256.0 V	2.0 mA	390.3 μA	2256.1 V	ON
U 12	2208.0 V	2.0 mA	404.0 μA	2208.1 V	ON
U 13	2259.0 V	2.0 mA	437.1 μA	2259.0 V	ON
U 14	2028.0 V	2.0 mA	360.9 μA	2028.1 V	ON
U 15	2135.0 V	2.0 mA	378.1 μA	2135.1 V	ON
U100	2322.0 V	2.0 mA	416.2 μA	2322.0 V	ON
U101	2267.0 V	2.0 mA	397.9 μA	2267.0 V	ON
U102	2061.0 V	2.0 mA	372.6 μA	2061.0 V	ON
U103	1987.0 V	2.0 mA	353.2 μA	1987.0 V	ON
U104	2216.0 V	2.0 mA	377.7 μA	2216.0 V	ON
U105	2161.0 V	2.0 mA	379.3 μA	2161.0 V	ON
U106	2034.0 V	2.0 mA	359.6 μA	2034.0 V	ON
U107	2025.0 V	2.0 mA	373.2 μA	2025.0 V	ON
U200	5.0 V	6.0 A	1738.3 mA	4998.5 mV	ON
U201	5.0 V	6.0 A	5213.4 mA	5001.0 mV	ON
U202	5.0 V	6.0 A	5147.0 mA	5003.4 mV	ON
U203	5.0 V	6.0 A	5176.3 mA	5001.0 mV	ON
U204	4.4 V	6.0 A	3736.8 mA	4399.4 mV	ON
U205	4.4 V	6.0 A	3827.1 mA	4399.4 mV	ON
U206	4.4 V	6.0 A	3832.0 mA	4400.4 mV	ON
U207	6.0 V	6.0 A	0 A	0 V	OFF

Table 2.13: Wiener crate power monitor (5/7/14, ^{240}Pu runs).

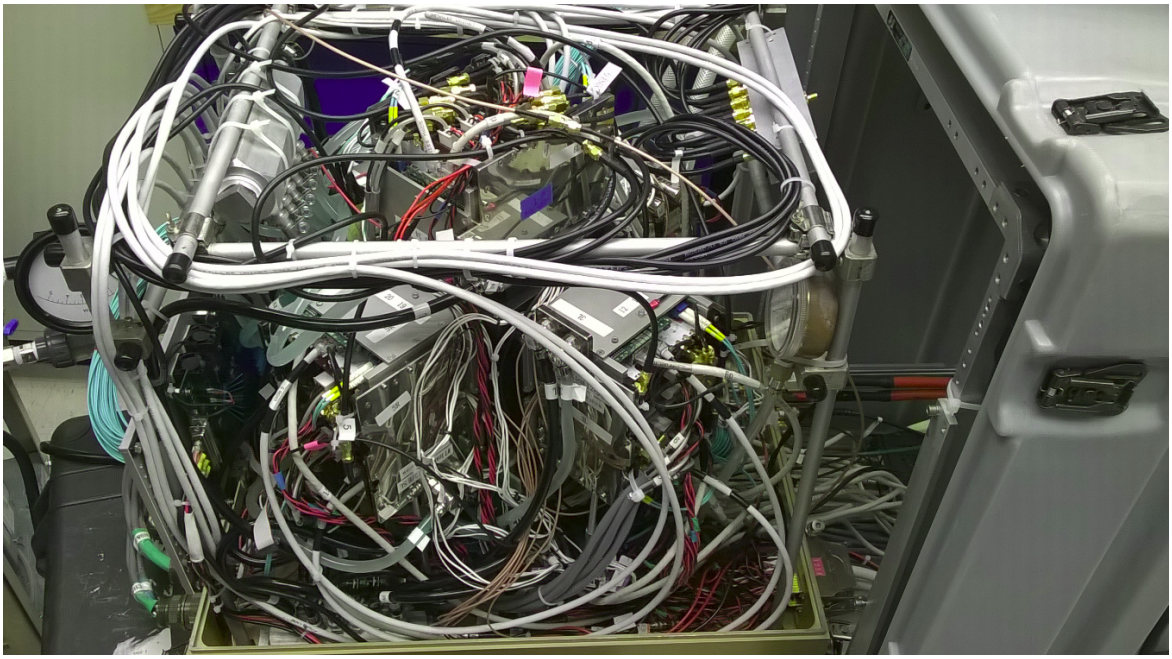

Figure 2.57: mTC fully assembled nested inside the aluminum enclosure (lid open).

2.4.2 Cooling system

In order to cool down the electronics, special board-stack card cages were made, shown in Fig. 2.61, and hard drive chiller plates were mounted on the board stack cages. Two identical manifolds were machined for in- and out-flow coolant to distribute among the twelve chiller plates, shown in Fig. 2.63. There is a humidity monitor inside the mTC and inside the shielding cave. One of the earlier coolants was de-ionized water, which was a poor choice as we later found out. It caused corrosion and biological growth in the cooling system, as shown in Fig. 2.65. When the cover was opened, moisture was visible on the chiller plates, manifolds and tubing.

Later, we switched to an industrial graded coolant: ProTek-100, propylene glycol. It has a certain disadvantage — lower heat capacity compared to water, which led to higher ASIC temperatures. All tygon tubing was replaced inside the mTC enclosure and chiller plates were opened and cleaned.

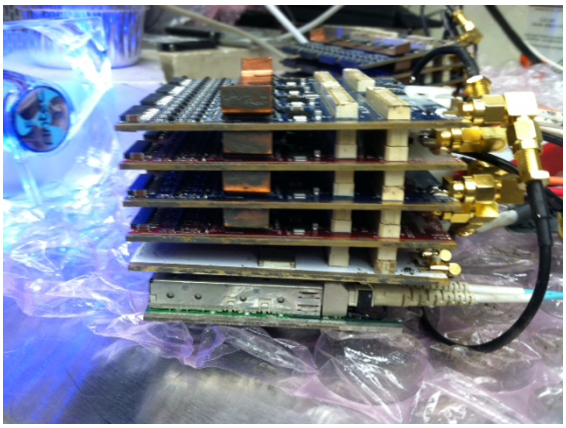

(a) 4 copper heat sinks each covering 4 chips installed in a readout module.

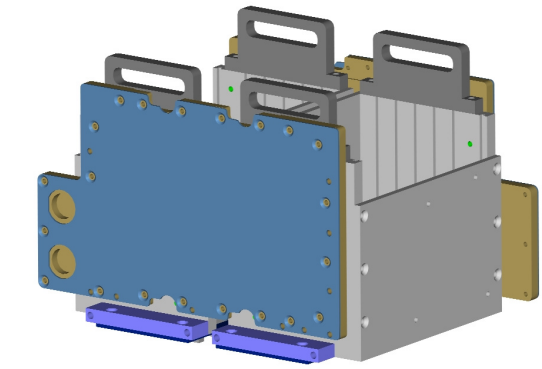

(b) Chiller plates attached to the electronics readout card cages.

Figure 2.58: Cooling the readout modules.

	SCROD 11						SCROD 12					
	S	T	0	1	2	3	S	T	0	1	2	3
before	31.0	30.1	51.0	53.5	53.5	50.0	32.8	30.1	50.8	55.0	56.5	54.5
after	31.3	23.1	40.8	39.8	41.5	43.5	29.8	22.8	35.5	37.0	37.0	35.8

Table 2.14: Top face electronics temperatures in °C before and after installing heat sinks. S — SCROD temperature; T — transceiver; 0, 1, 2, 3 — temperatures on corresponding carrier boards.

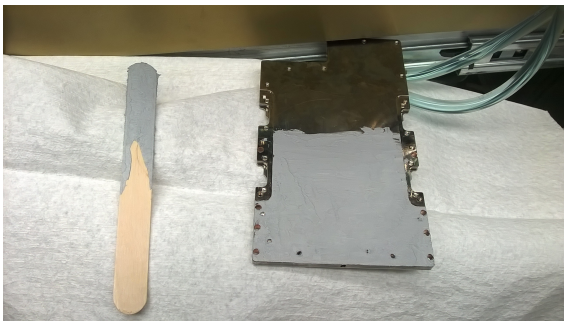

(a) Arctic silver thermal paste on one of the bottom-face chiller plates.

(b) Chiller front panel. Nominal pressure to process is ~ 20 psi.

Figure 2.59: Cooling system.

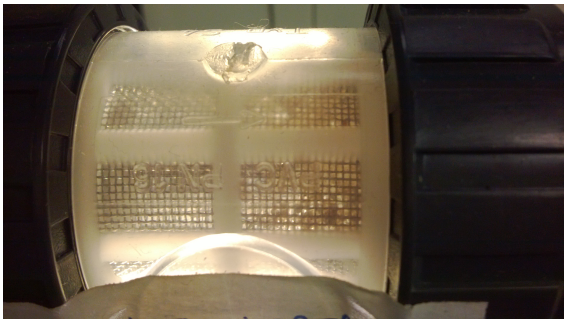

(a) Coarse filter. The net is changed monthly.

(b) Dusty substance started growing on cooling lines while in the cave.

Figure 2.60: Different parts of cooling system.

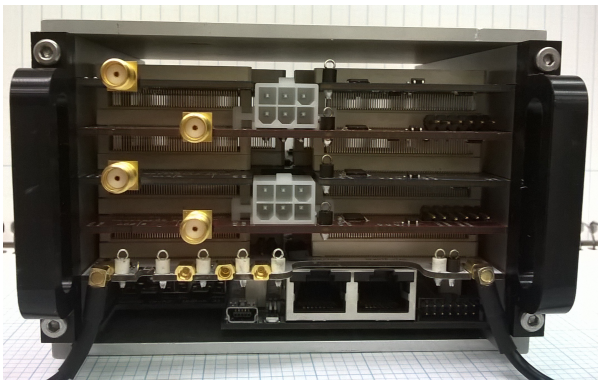

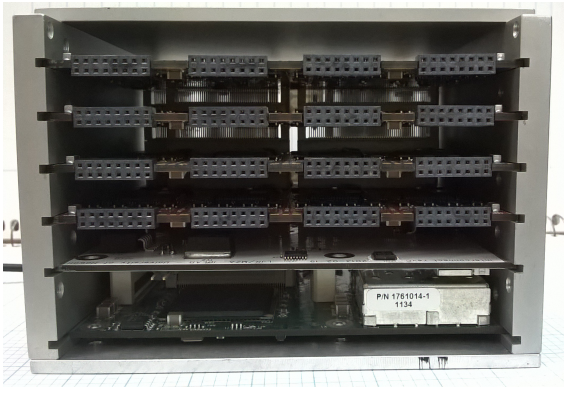

Figure 2.61: Left: Back of one of the twelve board stacks. LV (2 molex connectors), JTAG and clock (2 RJ-45 connectors), fiber optic interface.
Right: Front of the board stack that connects to 2 MCP-PMTs, covering 128 channels.

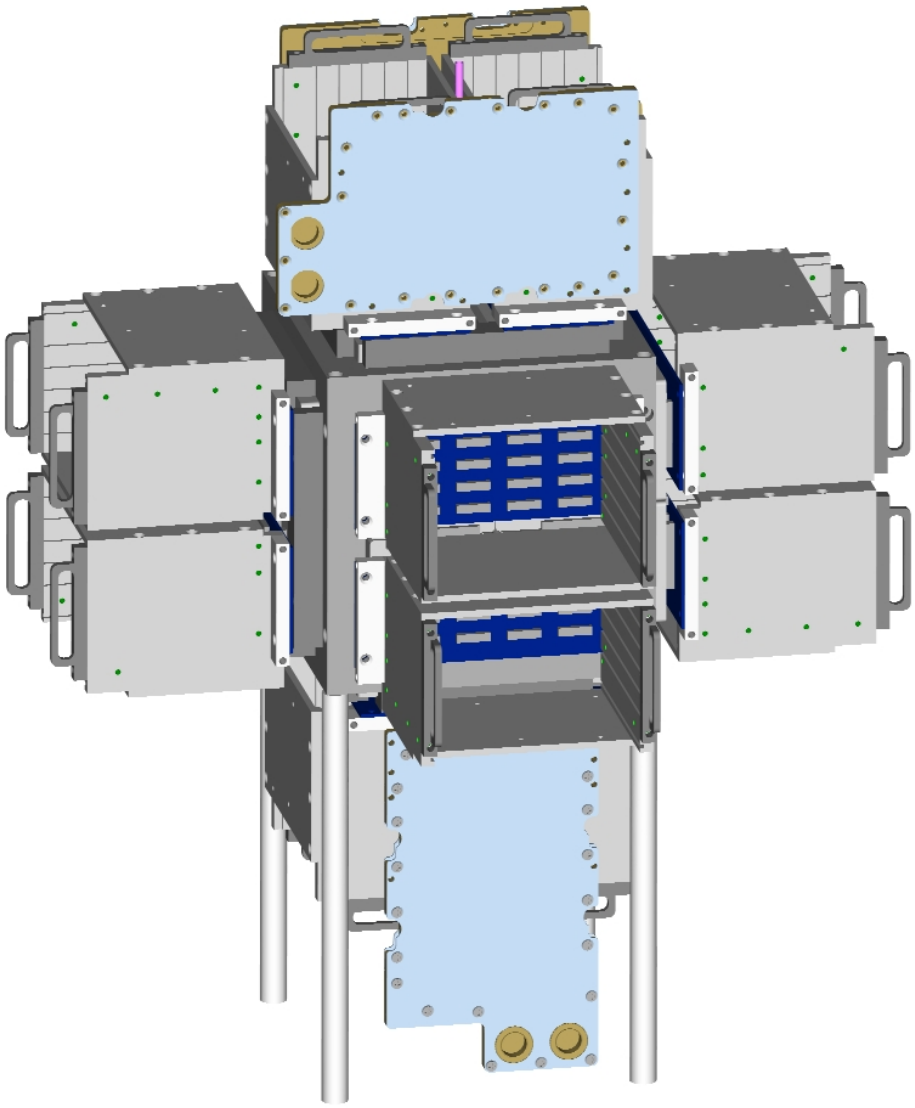

Figure 2.62: CAD snapshot showing mTC without electronics. All 12 card cages, chiller plates attached to top and bottom faces. Green dots indicate mounting point for chiller plates on the side-face card cages. Grooves in the side cheeks are visible, allow for mechanical support and better heat exchange.

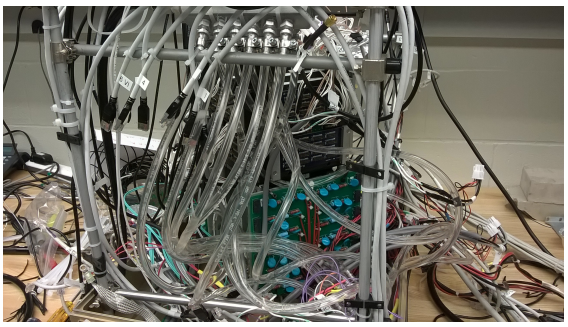

(a) Out-flow manifold with newly-installed tygon tubes, during the electronics upgrade.

(b) In-flow manifold, made of a solid piece of aluminum. 12 tubes go into chiller plates.

Figure 2.63: In- and out-flow manifolds.

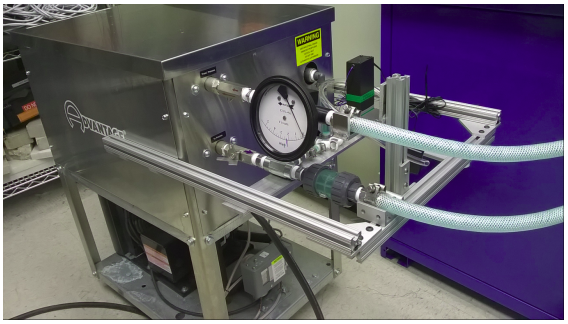

(a) Chiller with analog flowmeter, pressure release valve, and coarse filter.

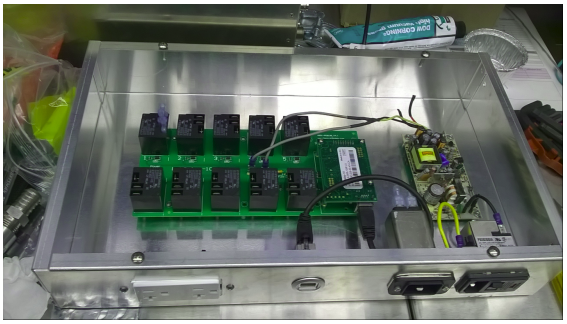

(b) Chiller relay for remote operations. Only one relay out of 10 is used in our setup.

Figure 2.64: Chiller.

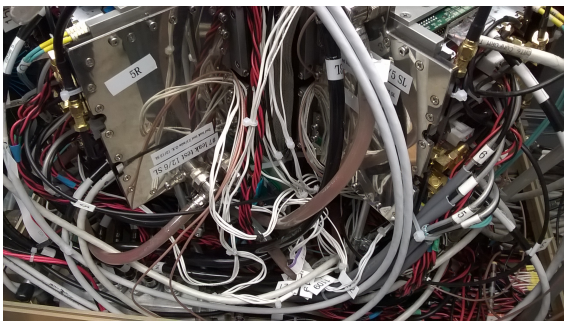

(a) Bio-stuff growing in the cooling system.

(b) Chiller plate opened after the corrosion.

Figure 2.65: Cooling system after a few months of no operation.

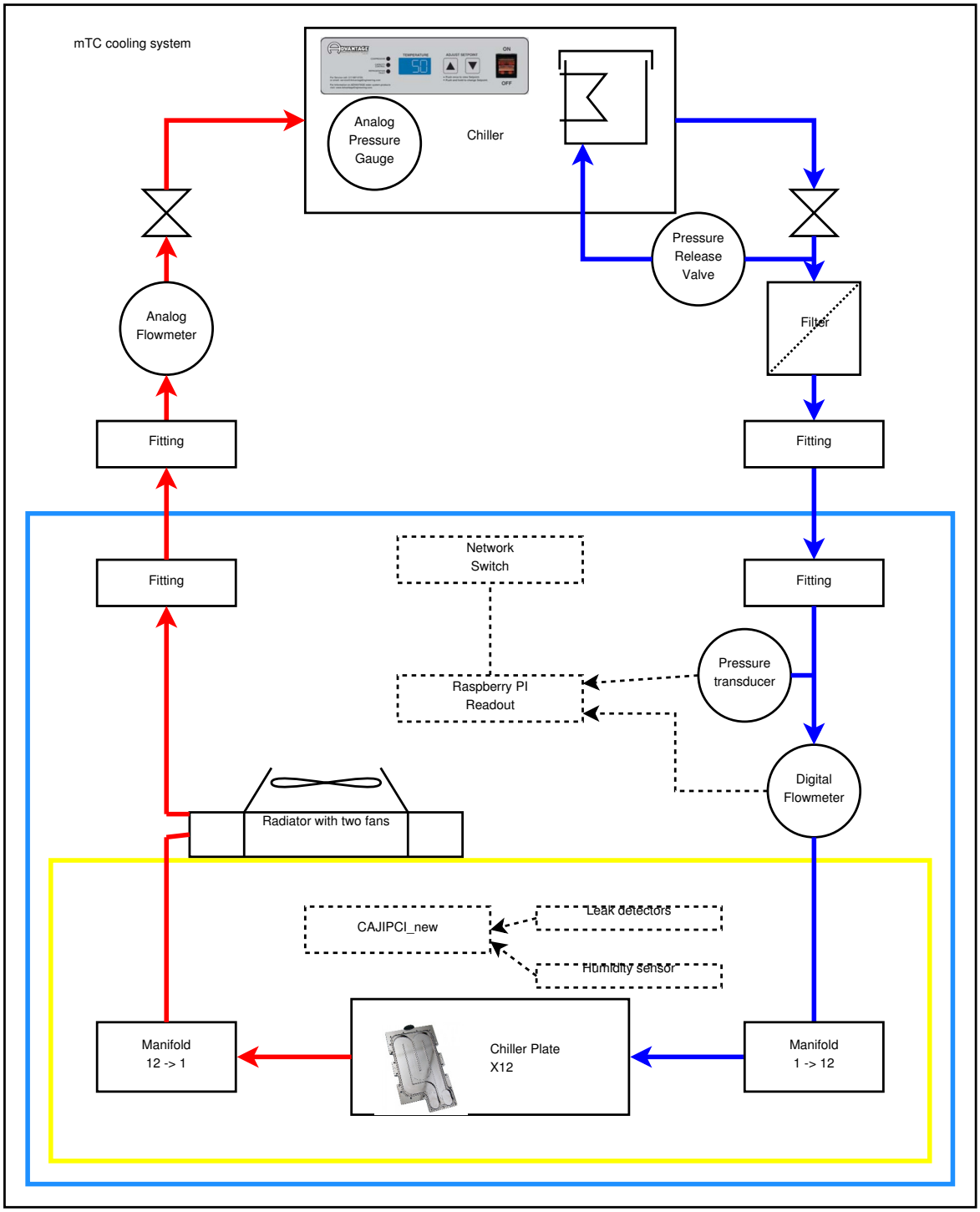

Figure 2.66: mTC cooling system.

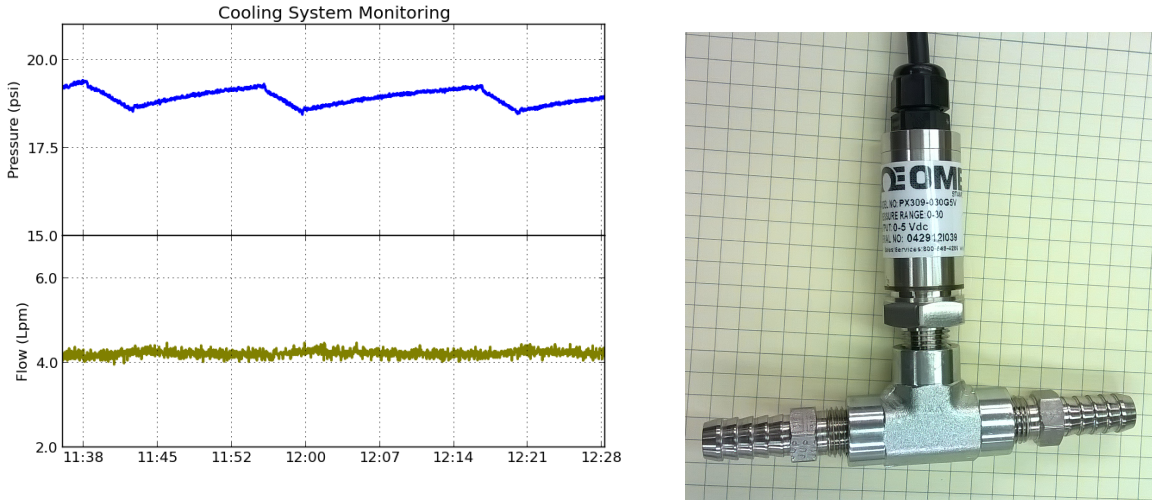

Figure 2.67: Left: Pressure and temperature readings from online cooling system monitoring. Longer periods are with chiller refrigeration off followed by short on periods [107]. Right: One of many elements of cooling system, pressure transducer that connects to a RaspberryPi computer for online monitoring.

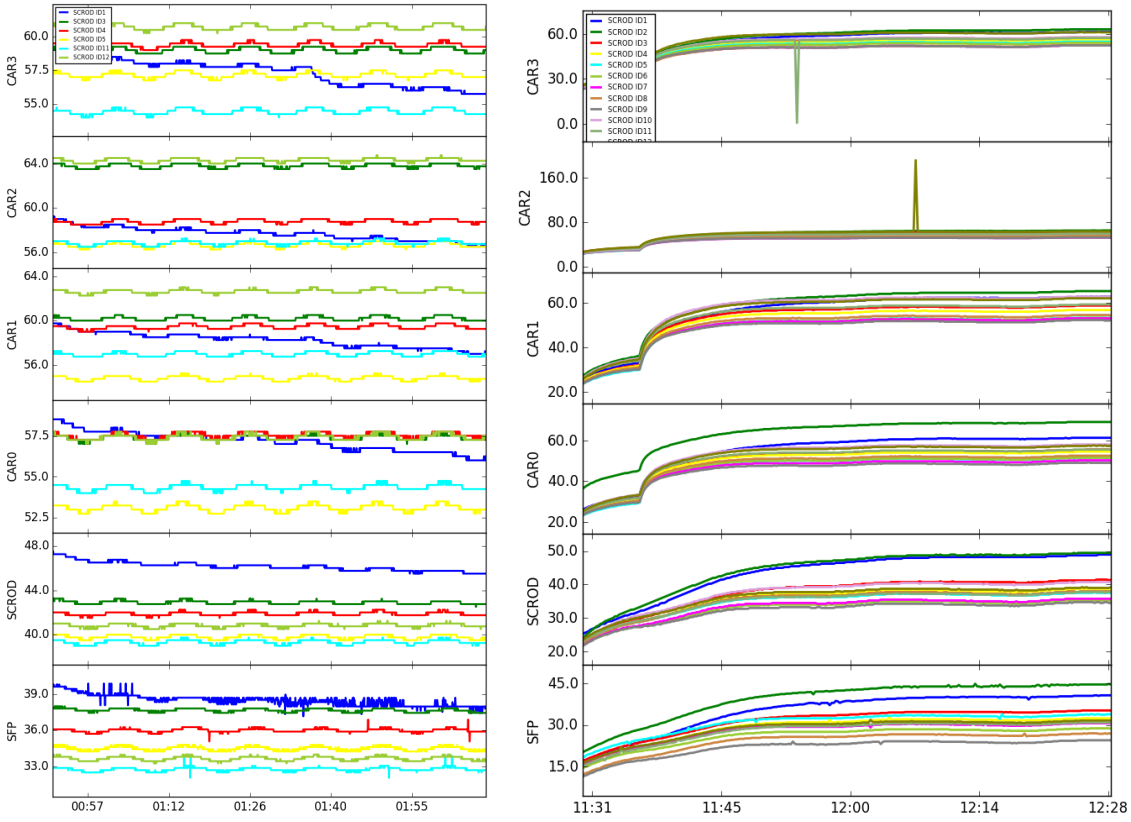

Figure 2.68: Left: fine front-end temperature fluctuation due to the chiller cycle; Right: front-end temperature rising on start-up, and becoming stable [107]. The spikes are non-physical due to the ADC board glitch.

2.5 Neutron, gamma, and muon detection

In this section, I will be examining mTC neutron capabilities, distinguishing neutrons from gammas, and finally demonstrating the detector response to muons.

Neutrons are essential to our project, given that they have largely influenced our funding through special nuclear material detection. Expanding upon this, in principle, when a fast neutron interacts with the scintillator, making multiple scatters, we can reconstruct the incoming neutron direction, which is done through fast timing.

In addition to its neutrino detection capabilities, the mTC is also a useful neutron detector with a nearly isotropic response. Fast neutrons leave enough light when they bounce off hydrogen (60% of the time) and ^{12}C ($\sim$ 40%) in the plastic scintillator, shown in Fig. 2.69b. When two neutron scatters are detected, one can calculate an angular cone, Eq. 2.10, representing the locus of directions pointing backwards to the neutron source.

$$\sin\Theta = \sqrt{\frac{\Delta E_{10}}{\Delta E_{10} + \frac{1}{2}m\left(\frac{\mathbf{r}_2-\mathbf{r}_1}{t_2-t_1}\right)^2}} \tag{2.10}$$

where $\mathbf{r}_1$ and $\mathbf{r}_2$ are the positions of the first and second scatters, and t_1 and t_2 — the associated deflection times; ΔE_{10} is the neutron energy difference (energy of the first recoil proton) which is directly observable [111]. The concept is illustrated in Figs. 2.69.

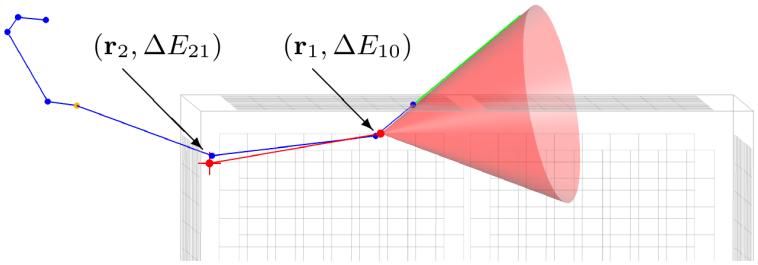

(a) A diagram of neutron direction estimation. The incoming neutron is in green, the true travel path in blue, and the estimated travel path in red. The angle cone Θ about the $\mathbf{r}_2 - \mathbf{r}_1$ vector is shown in red. Figure is adapted from [111].

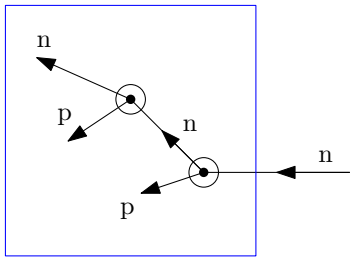

(b) Conceptual diagram behind fast neutron detection with multiple proton recoils.

Figure 2.69: Neutron detection mechanism using multiple scatters.

Vertex and energy reconstruction is similar to the one in the Double CHOOZ experiment [112]. To determine event geometry — four-vertex (x, y, z, t) in case of a point source, directional in formation (ϕ, Θ), and energy E; an event likelihood function is constructed as a product of charge Q and time t likelihood functions

$$p(\theta|z) = p_Q p_t \tag{2.11}$$

where $\theta = (x, y, z, t, \phi, \Theta, E)$ is a set of event parameters.

We used deuterium-deuterium (DD) and deuterium-tritium (DT, shown on Fig. 2.70a) neutron generators, where the neutrons are produced in the following reactions:

$$\begin{aligned} D + D &\rightarrow n + {}^3\text{He}, \qquad E_n = 2.5 \text{ MeV} \\ D + T &\rightarrow n + {}^4\text{He}, \qquad E_n = 14.1 \text{ MeV} \end{aligned} \tag{2.12}$$

However, that was done with the early version of the electronics, and no significant reconstructions were made. ^{252}Cf sources were used both at UH and NIST CNIF. Fig. 2.71 shows the mTC next to the ^{252}Cf neutron source at UH. We performed multiple tests at different distances and angles. Figs. 2.72–2.74 show reconstruction modeling in the mTC using two-bounce neutron events.

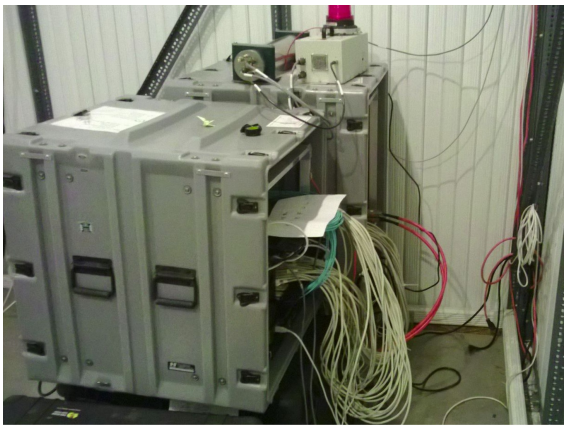

(a) Deuterium-tritium 14-MeV neutron generator (Thermo Scientific P 385) on top of mTC main crate. Spring 2014.

(b) ^{252}Cf in the white poly shield is located on an adjustable platform, next to the mTC. Spring 2017.

Figure 2.70: mTC neutron tests.

Multiple-scattered neutrons are likely to have a first bounce closer to the mTC face where the neutrons come from. In contrast to neutrons, *gammas* interact with the scintillator uniformly in space, manifesting on any side of the cube.

At the early stages of the mTC project, we had an idea to install a gamma-radioactive source inside a lead collimator on one side of the mTC and the gamma-telescope 90° on the other side. That way, we would tag the gammas that rescattered at 90° using a coincidence module. It would have allowed us to better understand the detector directional capabilities and how it responds to gammas. The setup is shown in Fig. 2.80a. We didn't perform these studies because the electronics were not ready at that time. Later, by the end of the project, the other priorities took precedence over completing these tests.

However, despite the lack of electronics mounted on the backs of the MCP-PMTs, we did the following test, as mentioned in the earlier section 2.3, and shown in Fig. 2.80b. The backs of the MCP-PMTs were covered with a conductive foam to short out the pins to ground. A special interconnect board was made that connects MCP-PMT common-dynode coax outputs to pin connectors on one of the readout board stacks, which was placed outside of the main mTC enclosure during these tests. We used ^{60}Co as a γ-emitter, and were able to clearly distinguish between muons and gamma events, as illustrated in Fig. 2.79.

Another unimplemented idea, along with the Compton scattering tests, was to place a radioactive source (gamma or neutron) at the center of the mTC. It would have been advantageous for both timing and energy calibrations. It would require drilling a tiny hole in the mTC scintillator; that was the main reason behind the abandonment of the plan.

Fig. 2.81 shows a typical gamma event in the mTC. There are a few clusters, which are likely due to the cross-talk 2.0 in the MCP-PMT.

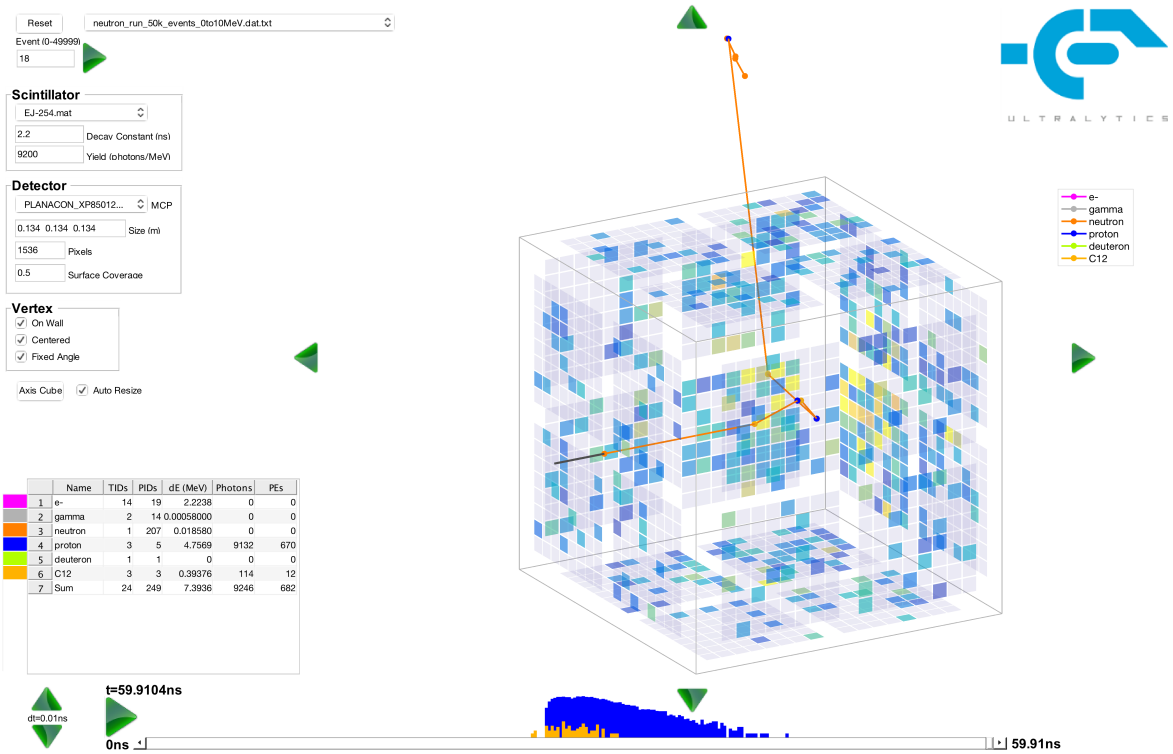

Figure 2.71: A simulation of 2.6-MeV neutron interacting within the mTC. 670 PEs and 12 PEs, for 3 proton and 1 ^{12}C re-scattering respectively. Glenn's simulation interface for the mTC written in MATLAB. Figure is taken from [88].

In the later calibration with ^{60}Co, a month prior to the installation by the reactor, we were able to reconstruct one of ^{60}Co gamma peaks correctly. To be thorough, analysis was redone with the 5th order polynomial energy calibration instead of the neutral network, producing similar distributions [88]. We are definitely seeing the ^{60}Co 1173-keV and 1332-keV peaks at 1.2–1.3 MeV, although the energy resolution is relatively low, so two peaks appear as one. Based on this result, we made a conclusion that the mTC is capable of distinguishing the real world point sources $\leq$ 1.2 MeV with 10 mm position and 12% energy resolution. Figs. 2.82–2.87 show real data and MC simulations.

In muons, we are quite confident. Cosmogenic muons are abundant and come from the atmosphere. Their flux at sea level is well understood, which is advantageous for any particle detector. They are high energy and they zip through our detector from top to bottom. Compared to neutrons and gammas, muons deposit a lot of their energy in the mTC, causing the whole detector to light up, excluding occasions where the muons are corner clippers. For muons, it is possible to reconstruct direction without using timing and instead only using charge.

A muon enters our detector through one of the five faces, and exits through the other five, excluding the top. The rate is approximately 1 Hz with the muon mean energy around 2 GeV at sea level. It falls off as cos^2 of the zenith angle. The time it takes for a vertically-going muon to transverse the detector if entered from the top face and exiting at the bottom is about 400 ps ($\sim$ .13 m / 3×10^8 m/s). We never employed timing to reconstruct muons, only the energy, i.e. the brightness of the pixels. The mean energy loss dE/dx for a muon is about 2.3 MeV/cm. Fig. 2.89 shows key parameters extracted in cosmic-ray muon reconstruction in the real mTC

data [88]. About 10% of the muons passing through the mTC have knock-on electrons, as shown in Fig. 2.88. Muons can also produce long-lived isotopes, along with gammas and neutrons. ^{8}He and ^{9}Li have lifetimes on the order of a second, and beta decay into unstable daughter nuclei, which can mimic IBD. Our simulations showed that this happening is rather rare, shown in Figs. 2.152.

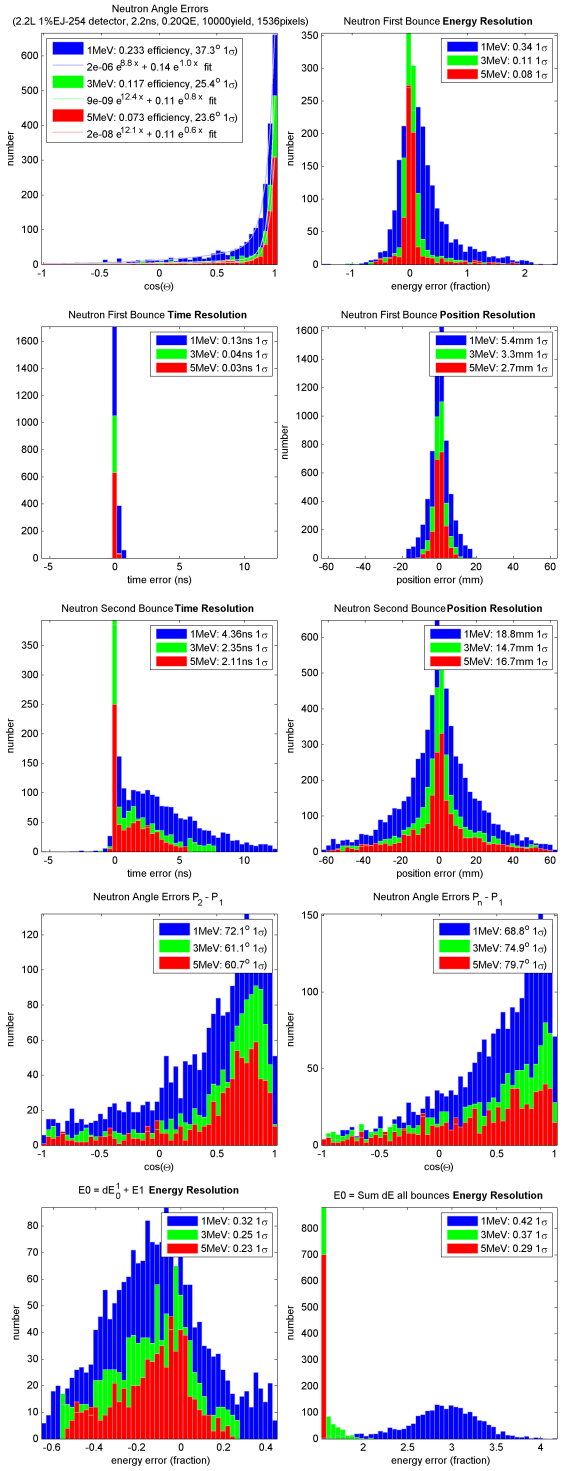

(a) Key output metrics.

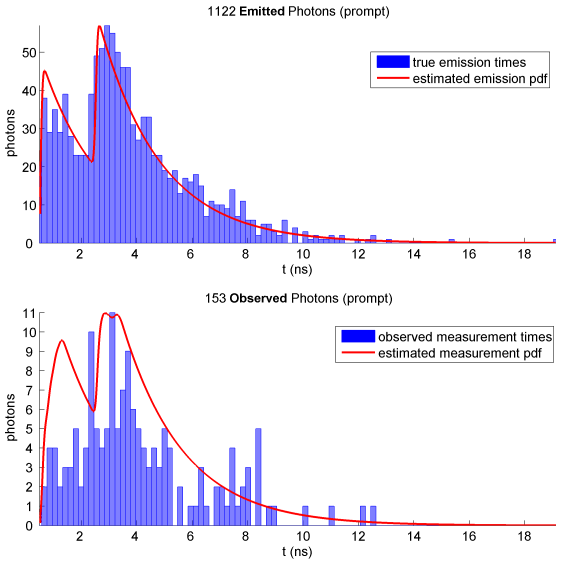

(b) Estimated photon emission and observation.

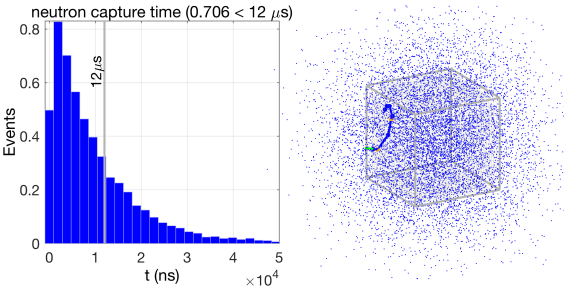

(c) 1-MeV neuron capture times (left) and locations (right). Note many neutrons escape the small-volume mTC.

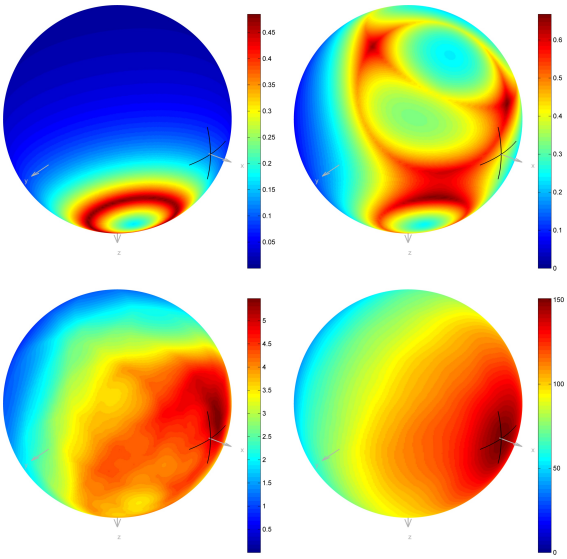

(d) Neutron angular probability density functions for 1, 3, 30 and 1000 neutrons displayed on unit spheres.

Figure 2.72: Neutrons in the mTC. Glenn's Monte Carlo simulations. Figures are taken from [111].

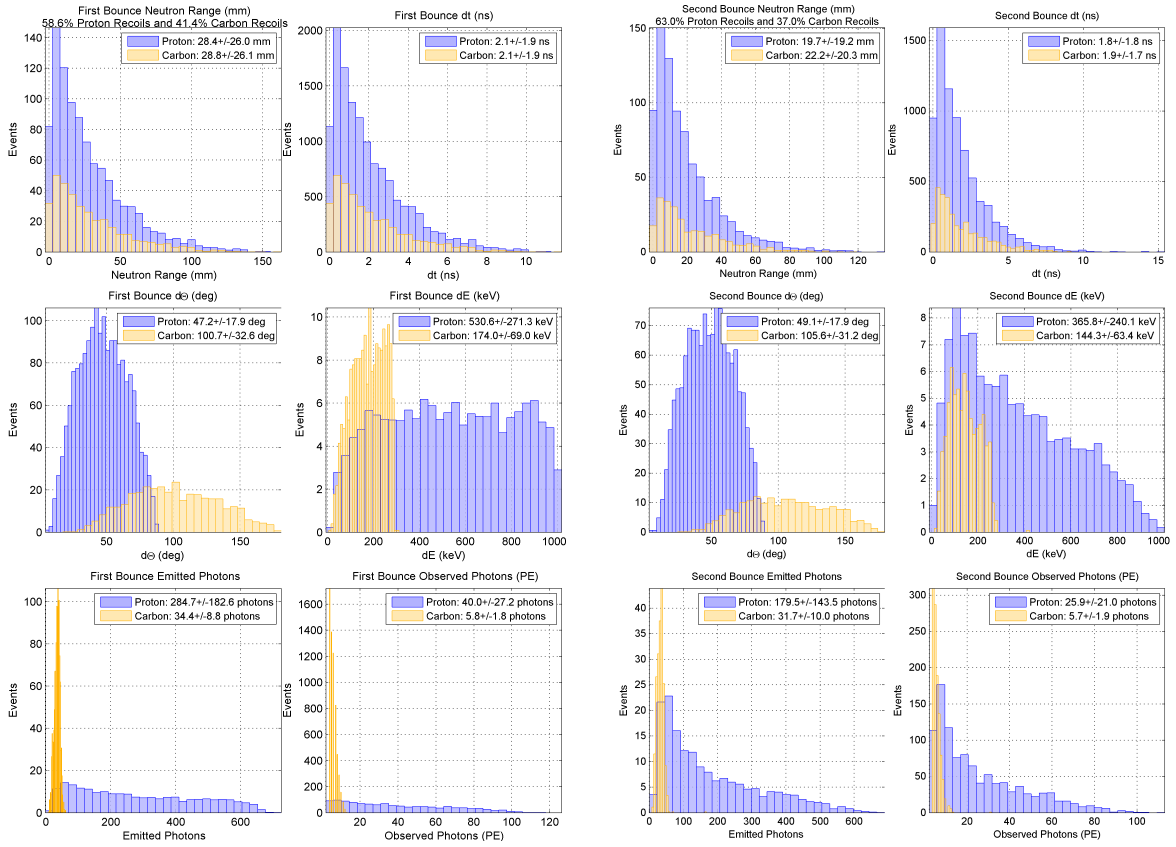

(a) 1st bounce. (b) 2nd bounce.

Figure 2.73: Neutrons in the mTC. Glenn's Monte Carlo simulations. Figures are taken from [111].

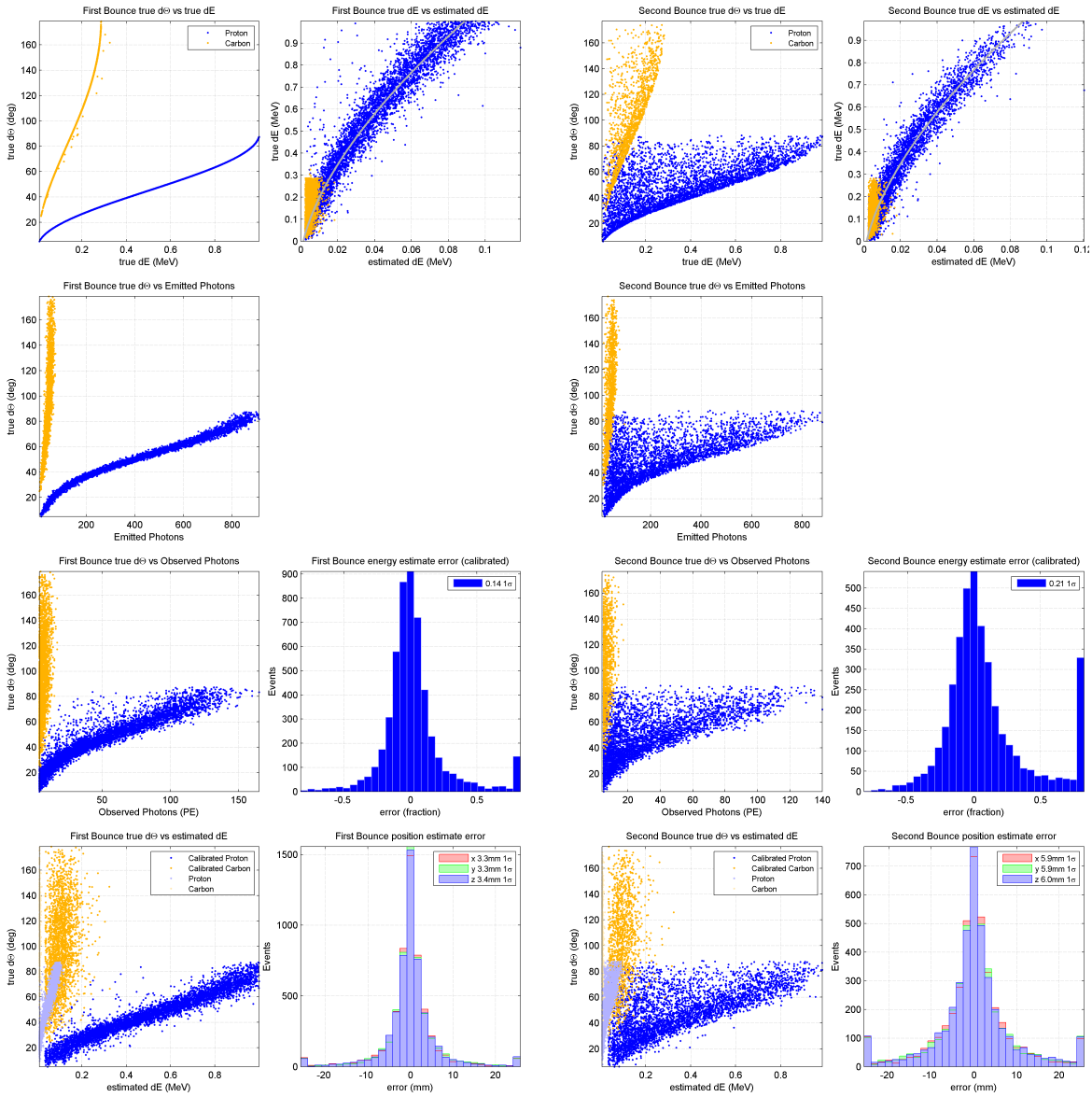

(a) 1st bounce. (b) 2nd bounce.

Figure 2.74: Neutron statistics in the mTC. Glenn's Monte Carlo simulations. Figures are taken from [111].

Trigger Configuration:

Trigger	Status	Min Reqd. Hits	Max Reqd. Hits	Prescale	Min Delay	Max Delay
Type A	Disabled	200	768	0	---	---
Type B	Disabled	15	60	0	---	---
Type C	Enabled	40	150	10	---	---
Type AB	Disabled	---	---	0	20	200

Trigger Status:

	Type A	Type B	Type C	Type AB
Rates (Hz)	0.0	0.0	86.8	0.0
	Link Status		Live Time(%)	
	ALL UP		99.2	

Figure 2.75: Live monitor of trigger settings and rates (5/2/17 neutron source run shown as an example).

Run	Operator	Date (HT)	Trigger	L0	$C_{\min}$	$C_{\max}$	PS	Comments
2737	Ryan, Slava	5/18/2017	C. Co-60	350	70	150	10	Co-60 source taped on the outer side of the mTC golden box. Directed at face 5. PMT 6 ON. rate 100 Hz
2738	Slava	5/18/2017	C. Co-60	350	70	150	10	Co-60 source taped on the outer side of the mTC golden box. Directed at face 4. PMT 6 ON. rate 135 Hz
2740	JohnK, Slava	5/19/2017	C. Cf-252	150	40	150	20	Cf-252 neutron source, 4 x 1/8" layers of lead, located on the concrete optical bench. Directed at face 4, slightly from the top. plug open. rate 190 Hz
2741	JohnK, Slava	5/19/2017	C. Cf-252	150	40	150	20	Cf-252 neutron source, 4 x 1/8" layers of lead, located on the concrete optical bench. Directed at face 4, slightly from the top. plug closed. rate 160 Hz.
2742	JohnK, Slava	5/19/2017	C. no source	150	40	150	20	No source. Rate 105 Hz.
2745	JohnK, Slava	5/25/2017	C. no source	100	40	150	20	No source. Rate 115 Hz.
2746	JohnK, Slava	5/25/2017	C. Cf-252	100	40	150	20	Neutron source positioned on the cart, directed at face 5, plug opened, 4* 1/8" lead. 410 Hz.
2747	JohnK, Slava	5/25/2017	C. Cf-252	100	40	150	20	Neutron source positioned on the large optical bench, directed at face 3, plug opened, 4* 1/8" lead. rate 250 Hz.
2748	JohnK, Slava	5/25/2017	C. Cf-252	100	40	150	20	Neutron source positioned on the concrete optical bench, directed at face 4, plug opened, 4* 1/8" lead. rate 330 Hz.

Table 2.15: Excerpt from run description log. Last sets of neutron and gamma runs with ~ 400 active channels. PS indicates the prescaler value.

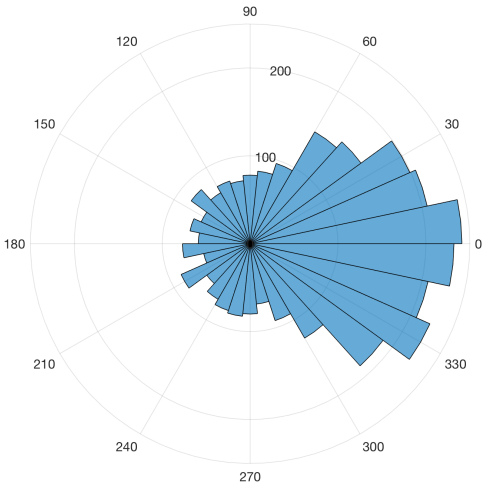

(a) GEANT4 simulated data with ^{252}Cf-source.

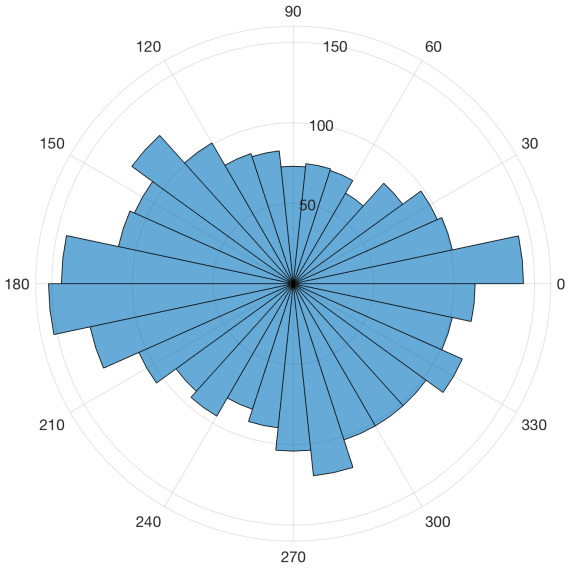

(b) Run 2745 with no source.

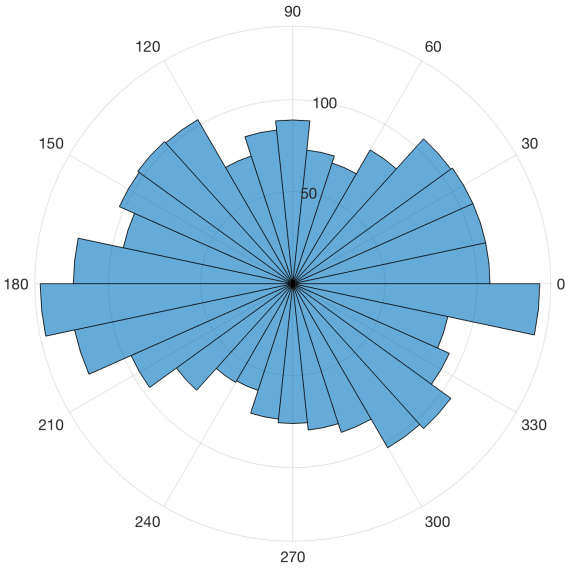

(c) Run 2746 with ^{252}Cf-source.

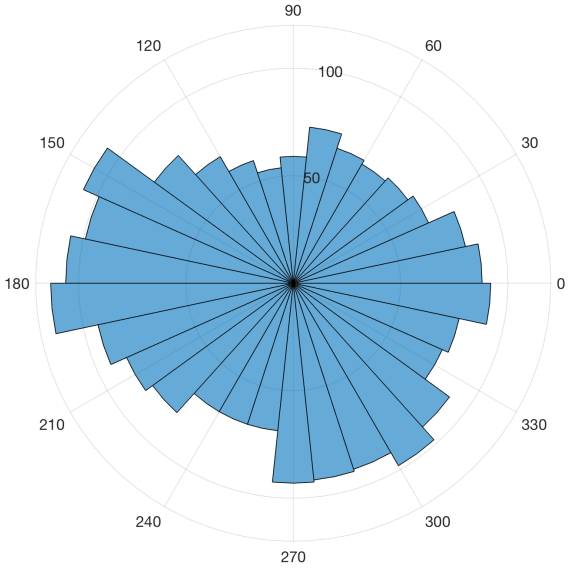

(d) Run 2747 with ^{252}Cf-source.

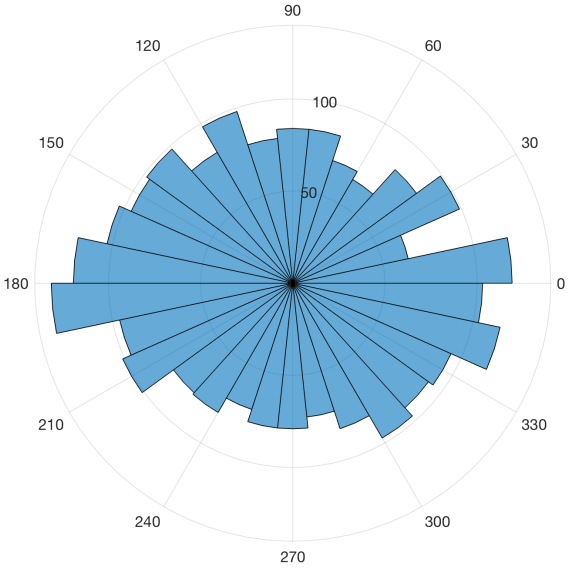

(e) Run 2748 with ^{252}Cf-source.

Figure 2.76: Azimuth angle. Last neutron directionality tests, with $\sim$ 400 active channels. Angle 0 is the front face of the detector. Figures are taken from [88].

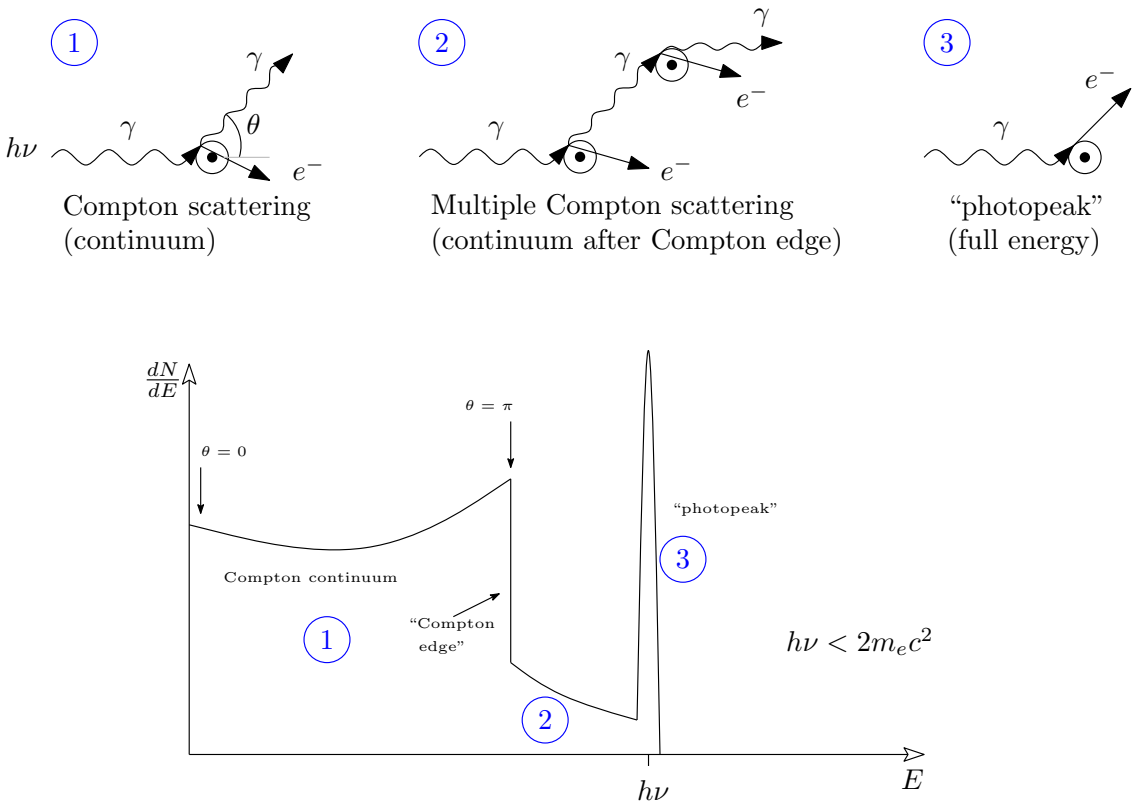

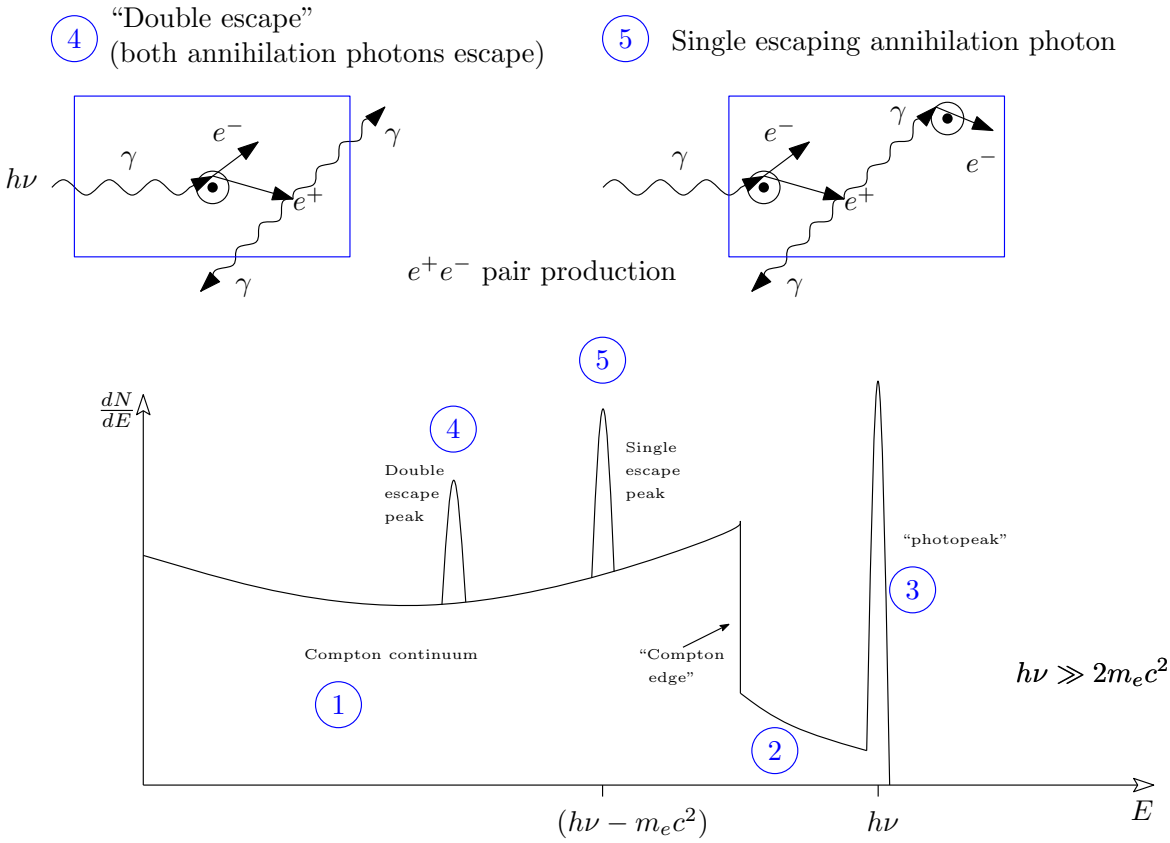

Figure 2.77: Conceptual diagrams behind different types of gamma interactions in the mTC-size detector, for low ($E_\gamma < 2m_e c^2$) and high ($E_\gamma \gg 2m_e c^2$) gamma energies.

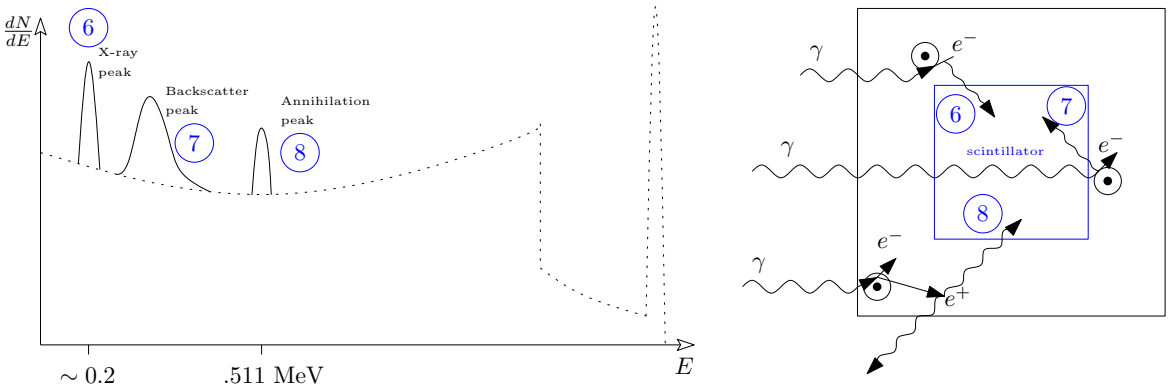

Figure 2.78: Conceptual diagrams behind different types of gamma interactions in material surrounding the scintillator. Figure is adapted from [75].

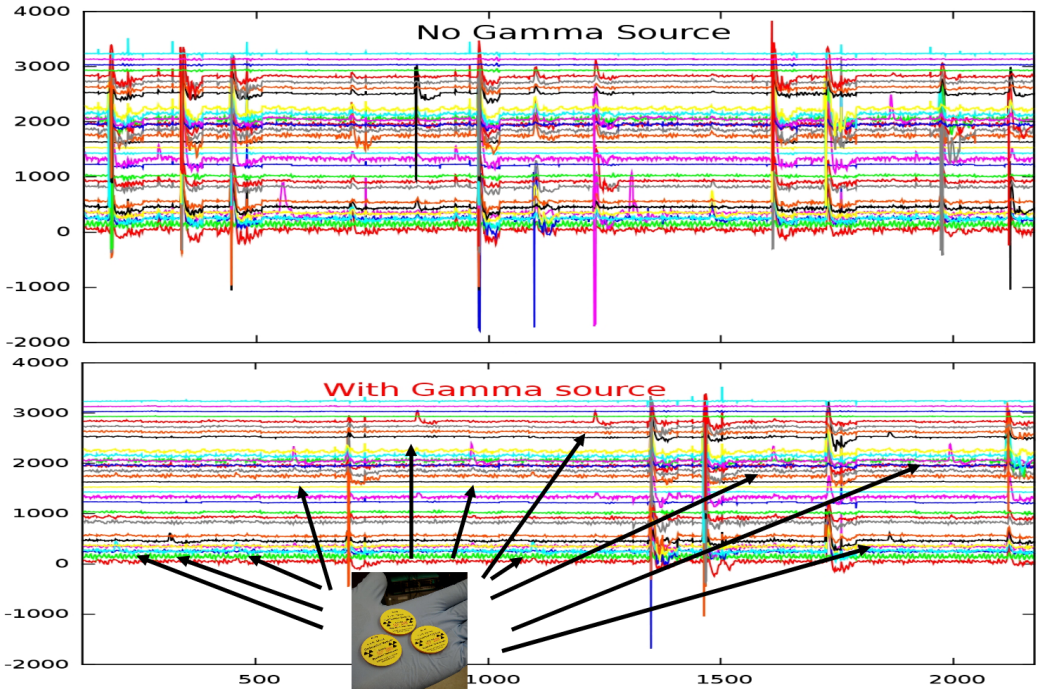

Figure 2.79: Gamma source tests, with (bottom) and without (top) the source. 16 event sample, events are plotted back to back. 24 MCP-PMTs common-dynode outputs are connected to the readout SCROD. 32 waveforms in total (ignore the eight empty waveforms). ^{60}Co (1.7 μCi) placed in a lead collimator, directed at the center of one of the mTC faces.

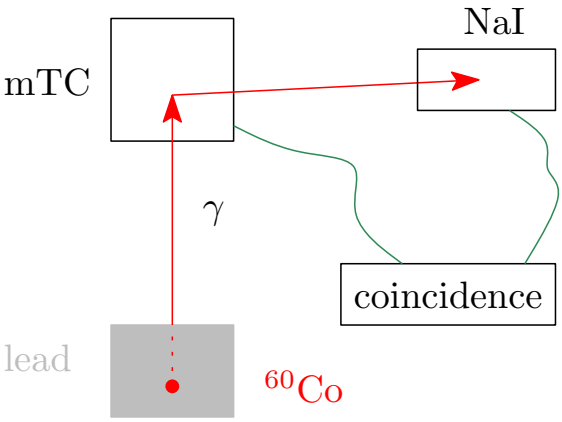

(a) Compton scattering with NaI crystal.

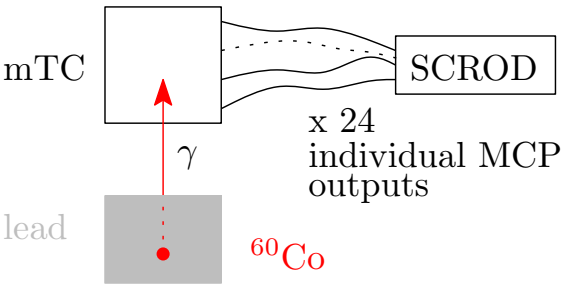

(b) 24 MCP-PMTs acting as conventional PMTs connected to a SCROD.

Figure 2.80: Gamma source tests.

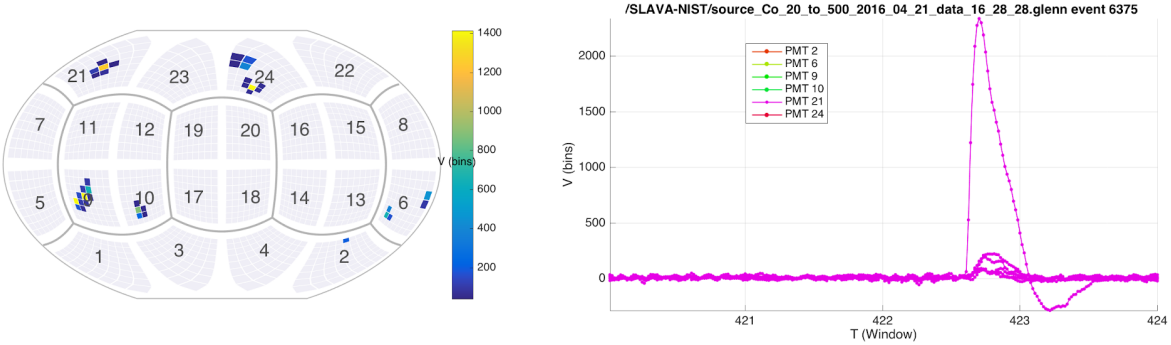

Figure 2.81: ^{60}Co is located on top of the aluminum mTC enclosure. April 21, 2016, half of the tubes are dead (after the accident). Figure is taken from [88].

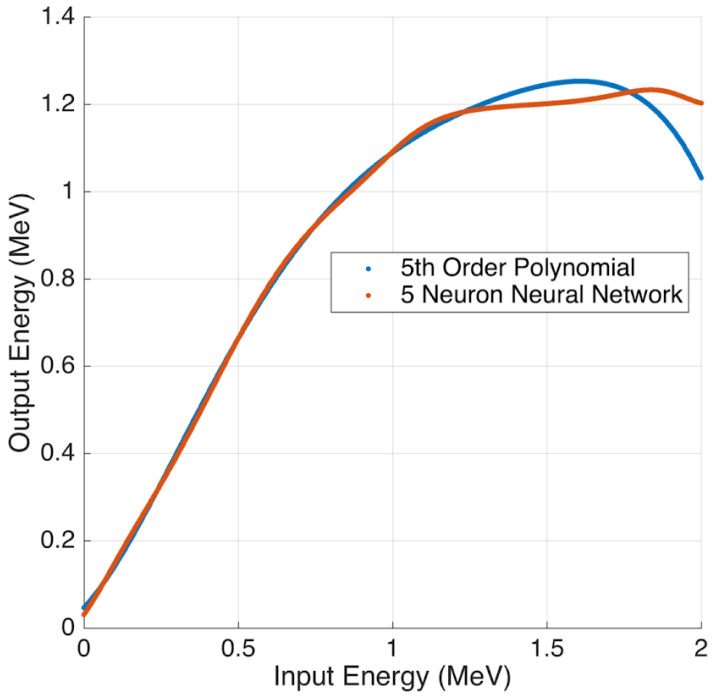

Figure 2.82: Energy calibration, two models — neural network and 5th-order polynomial. Figures are taken from [88].

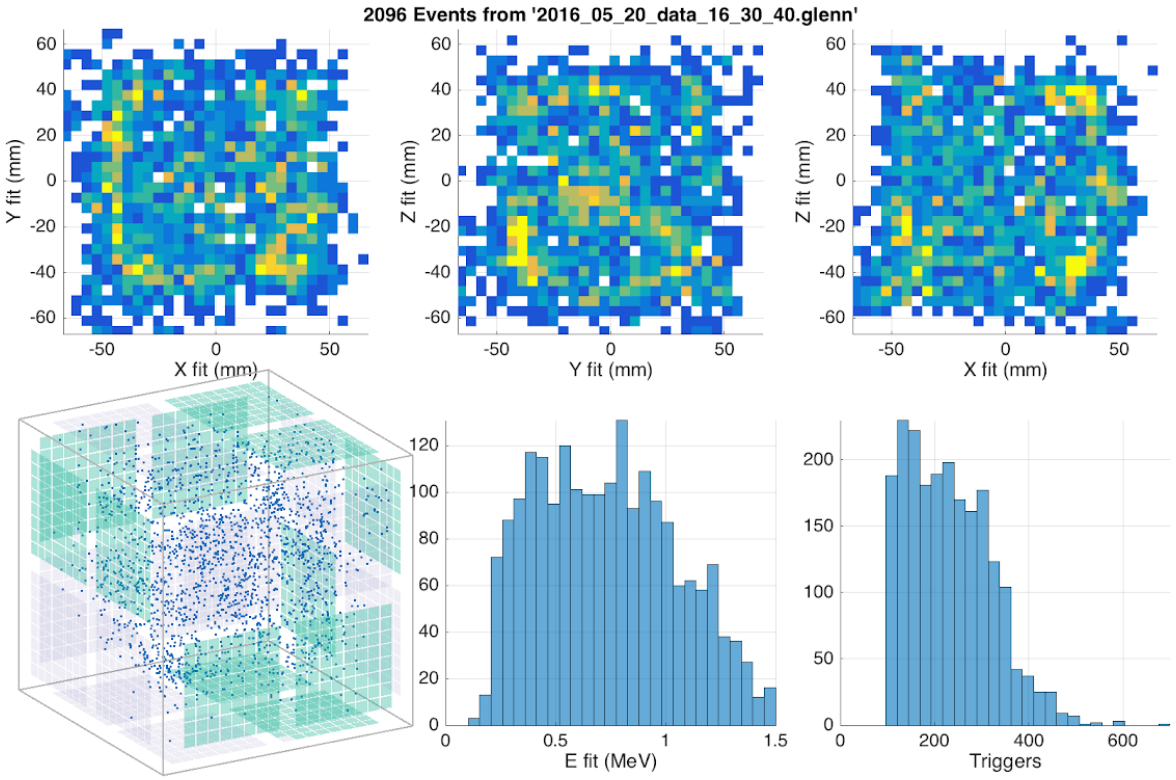

(a) No energy calibration.

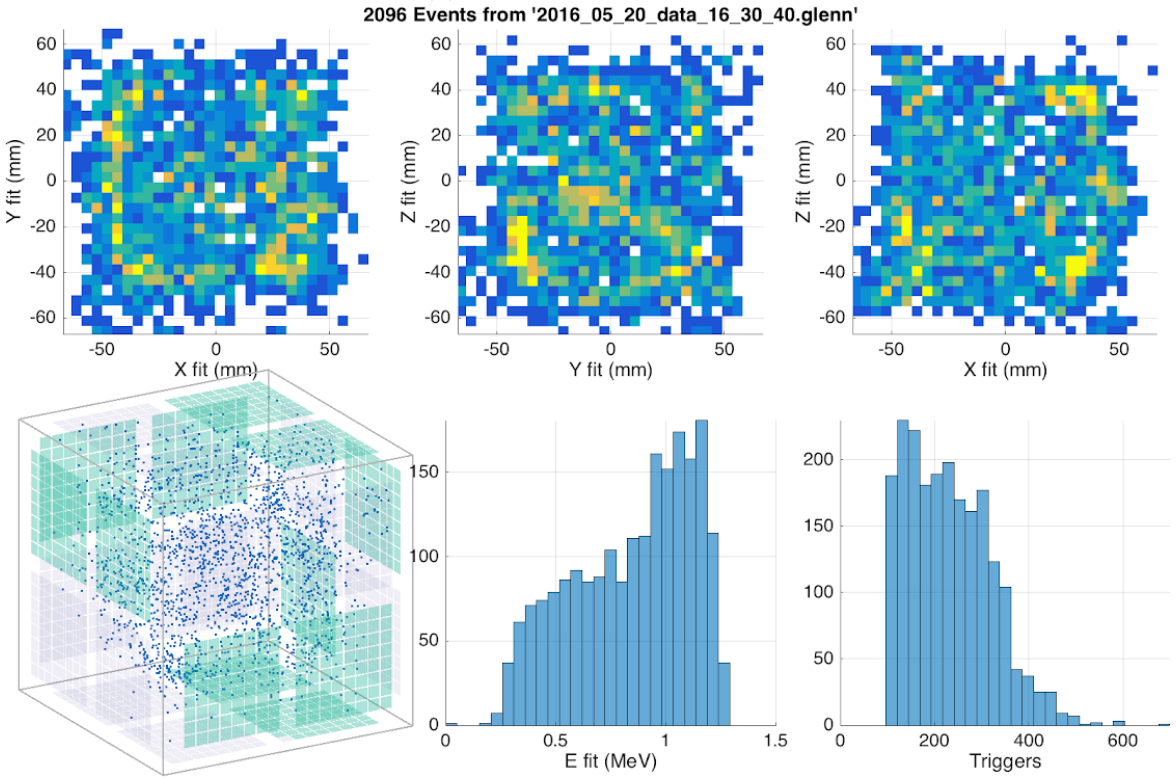

(b) Adjusted after energy calibration based on 5th-order polynomial.

Figure 2.83: Real data with ^{60}Co. Figures are taken from [88].

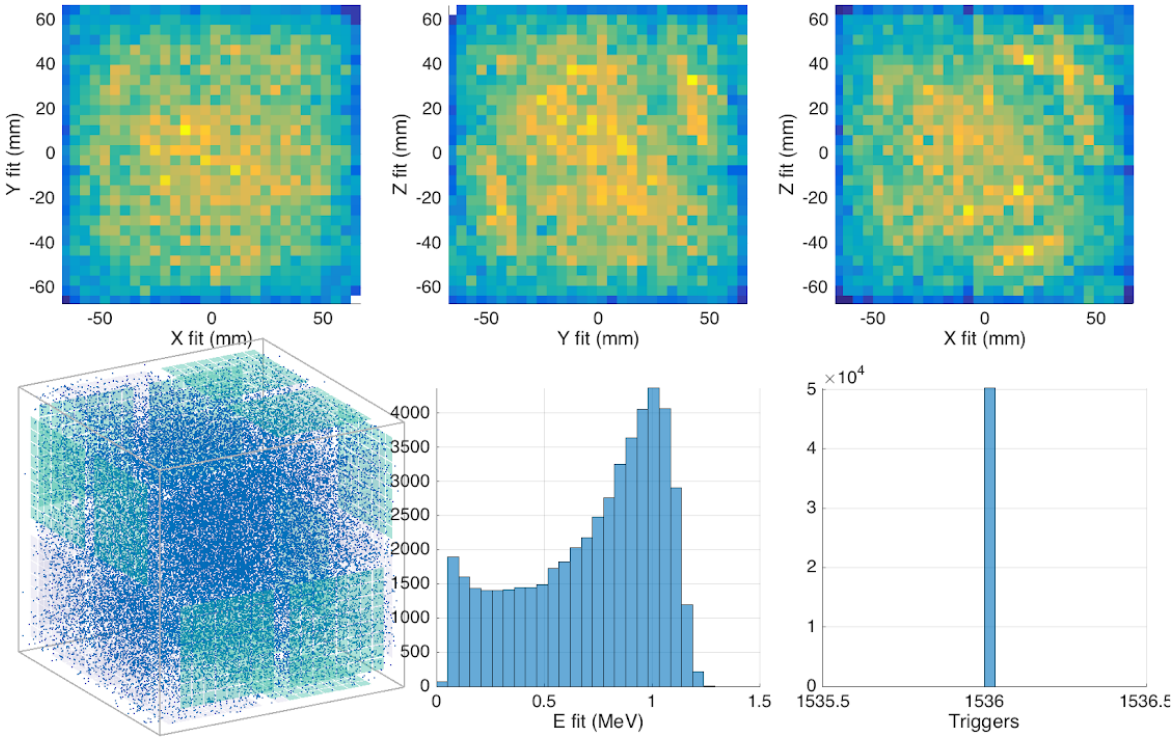

Figure 2.84: Simulated ^{60}Co data with half working tubes, 766-channel mTC. Figures are taken from [88].

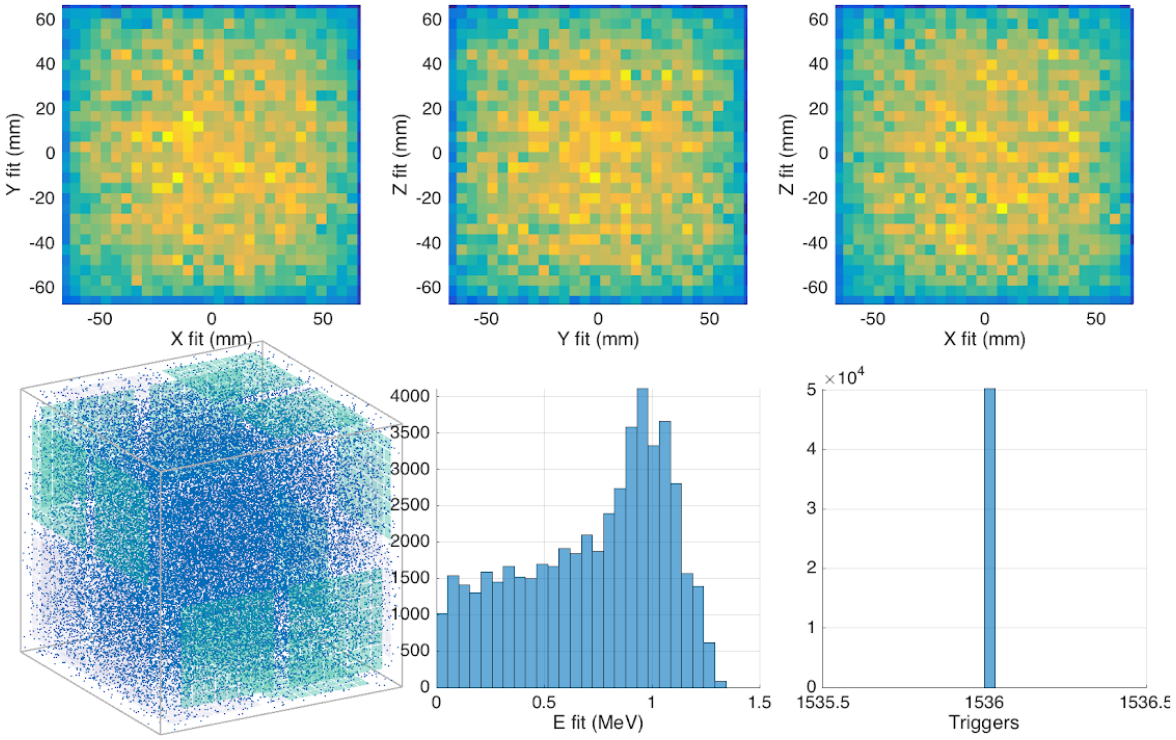

Figure 2.85: GEANT4 simulation of ^{60}Co events. Full 1536-channel mTC. Figures are taken from [88].

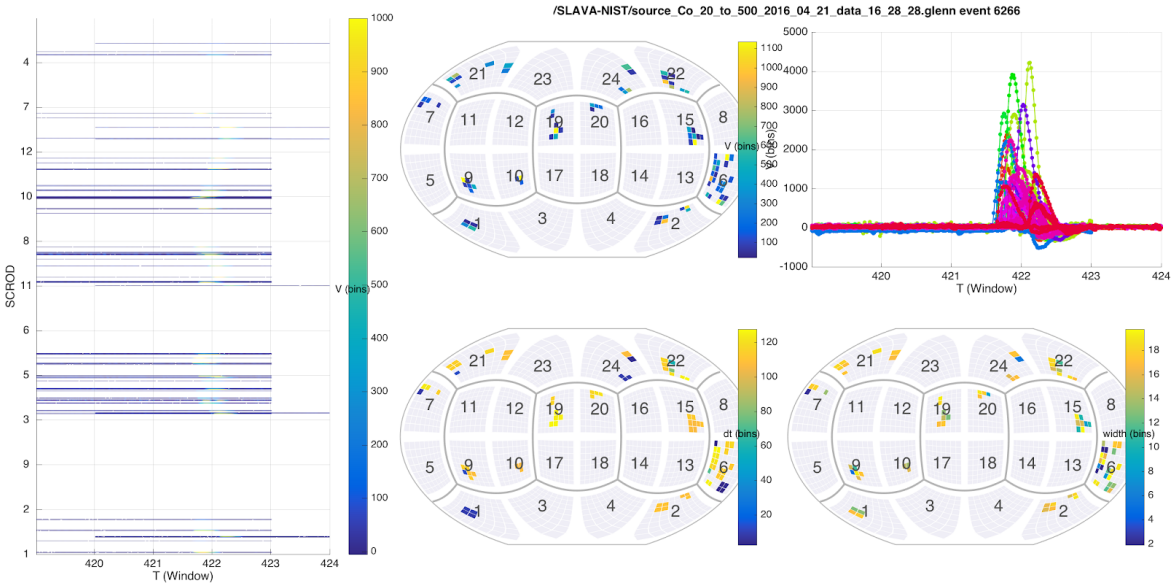

(a) Data (after the PMT meltdown).

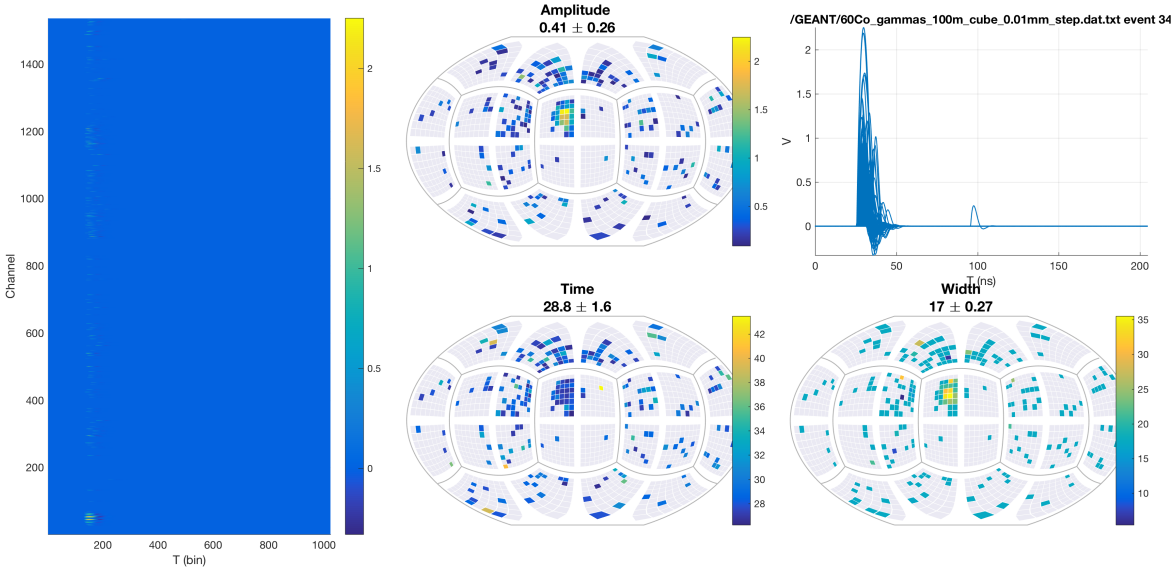

(b) Simulations.

Figure 2.86: ^{60}Co single event photon distribution. Figures are taken from [88].

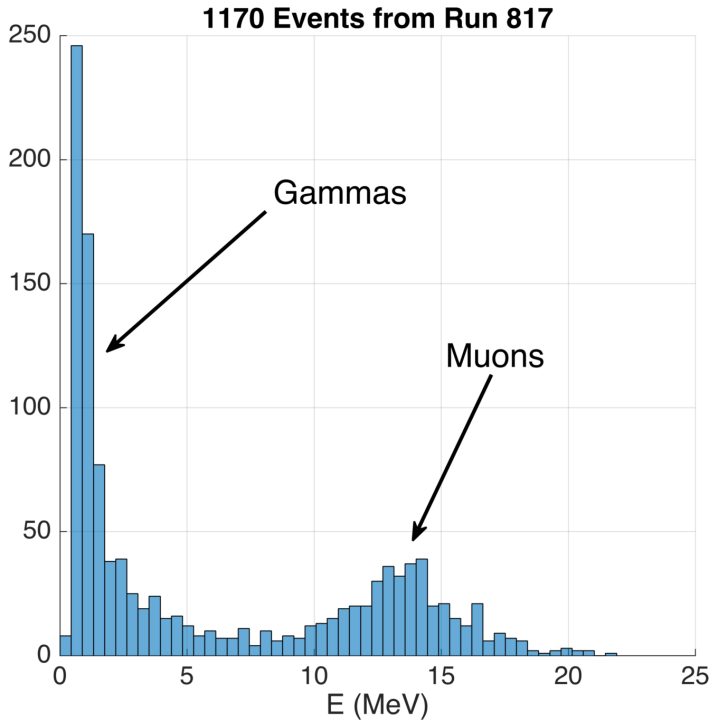

Figure 2.87: Muons vs gammas. Figure is taken from [88].

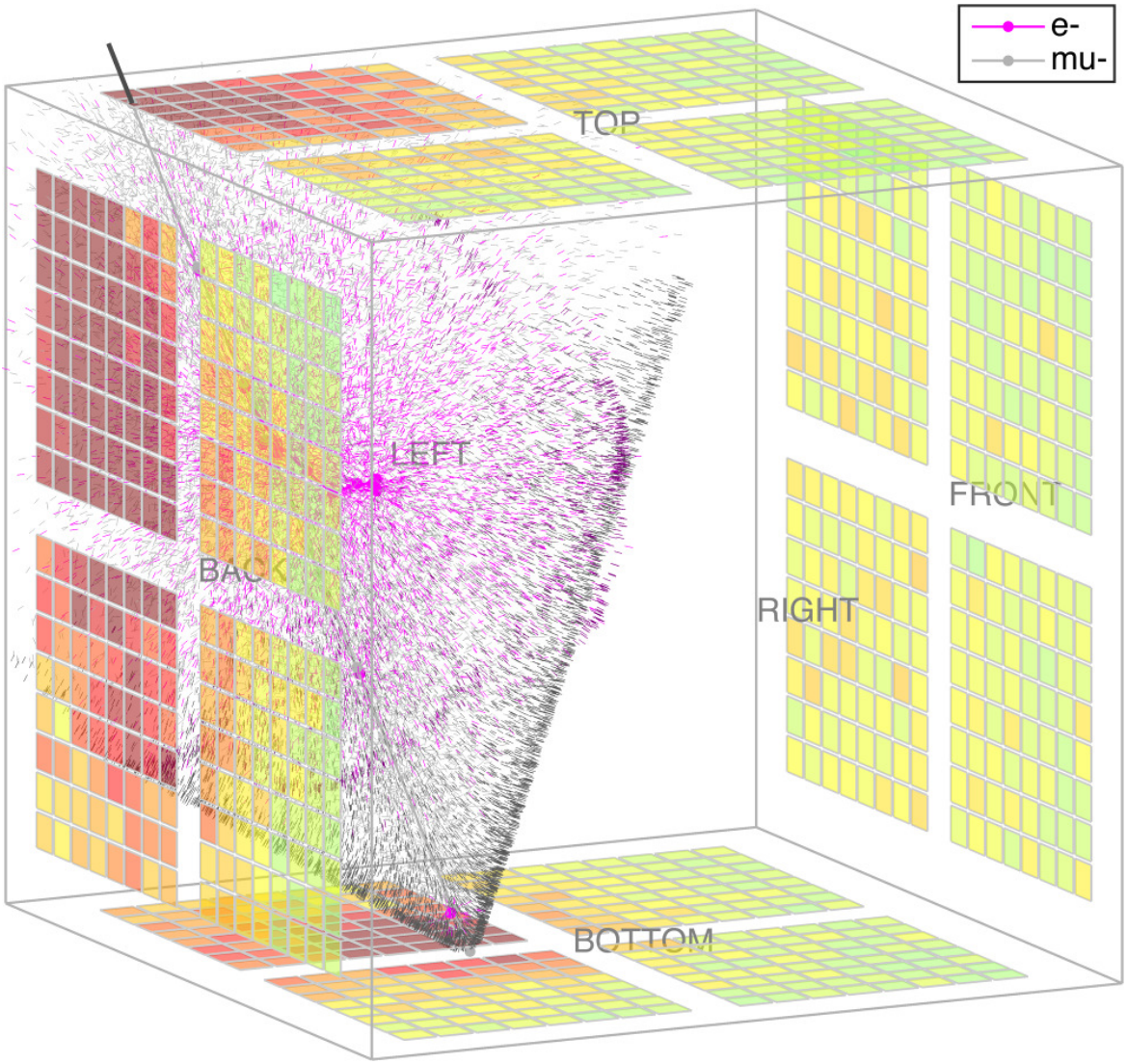

Figure 2.88: A simulated muon traversing the mTC, with scintillation photons and Cherenkov cone visible. A couple of knock-on electrons are also visible along the muon track. Figure is taken from [85].

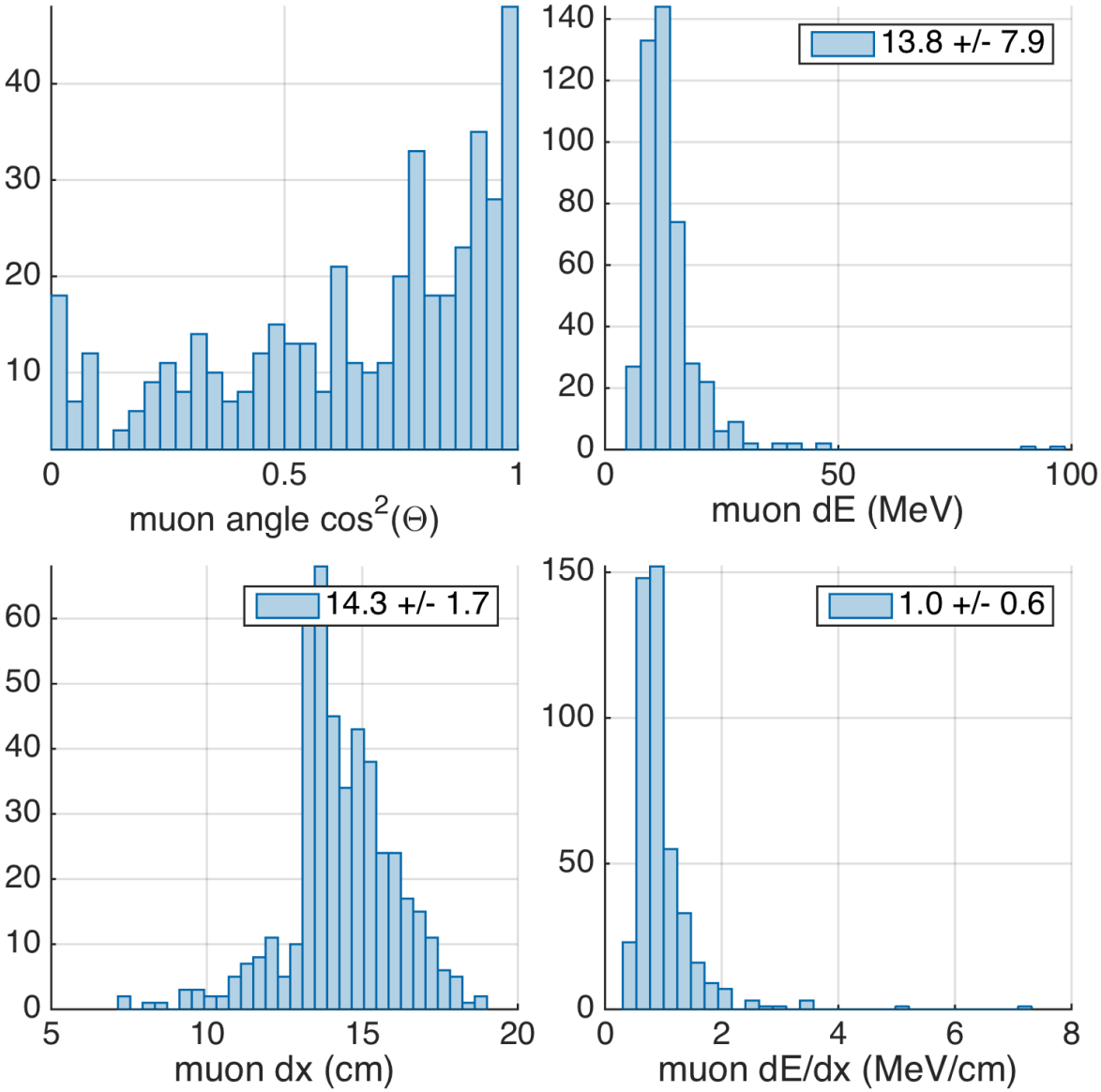

Figure 2.89: Distributions of reconstructed cosmic ray muon parameters using data collected with the mTC, showing reconstructed incident angle (top left), energy deposition (top right), muon track length within the mTC (bottom left), and muon energy deposition per unit track length (bottom right). These distributions reflect a 500 event data sample. Figures are taken from [85].

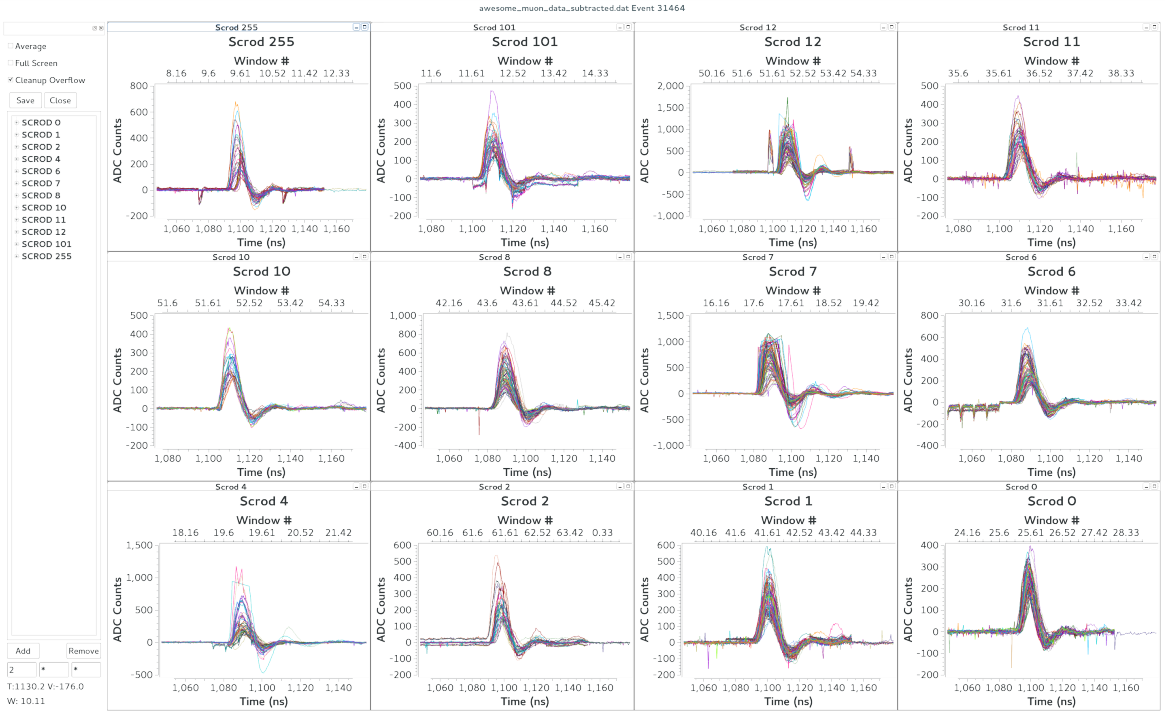

Figure 2.90: One of the first muon events visible across most channels of the detector, after improvements of the clock board were made in August 2015 [108]. These are IRS3B digitizers.

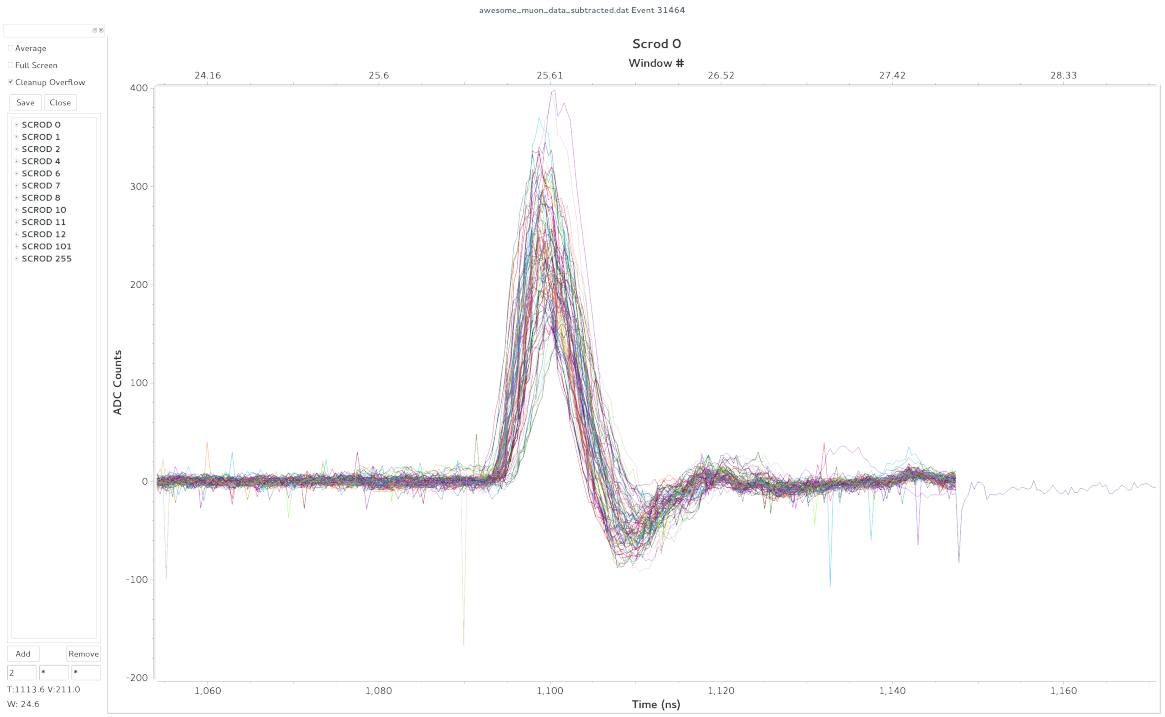

Figure 2.91: One of the first muon events visible across one of the SCRODs, triggered channels out of 128 total [108].

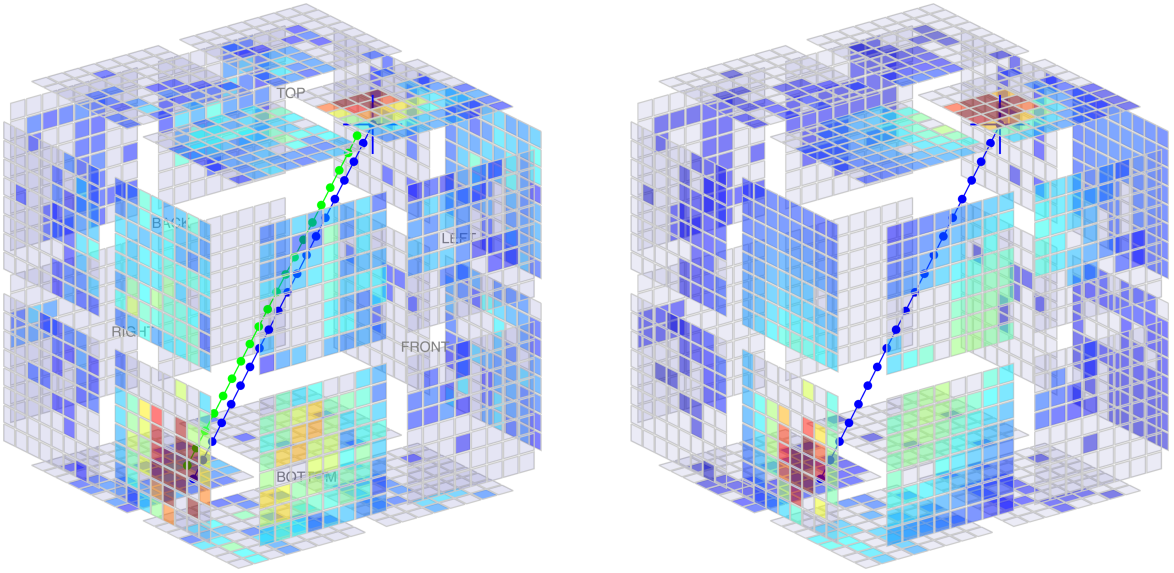

Figure 2.92: Simulated muon event on the left — real (green) vs reconstructed (blue) track. Right panel is data [85].

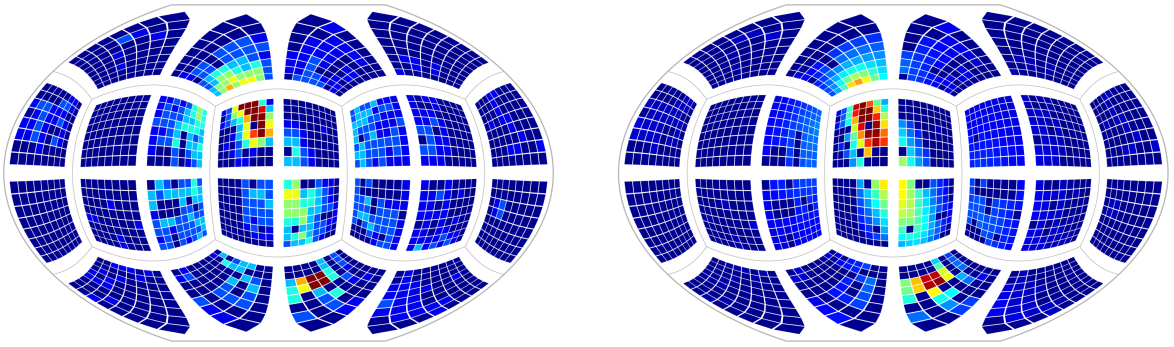

Figure 2.93: Entry and exit point of a through-going muon. Real data is shown on the left, and simulated is on the right [85].

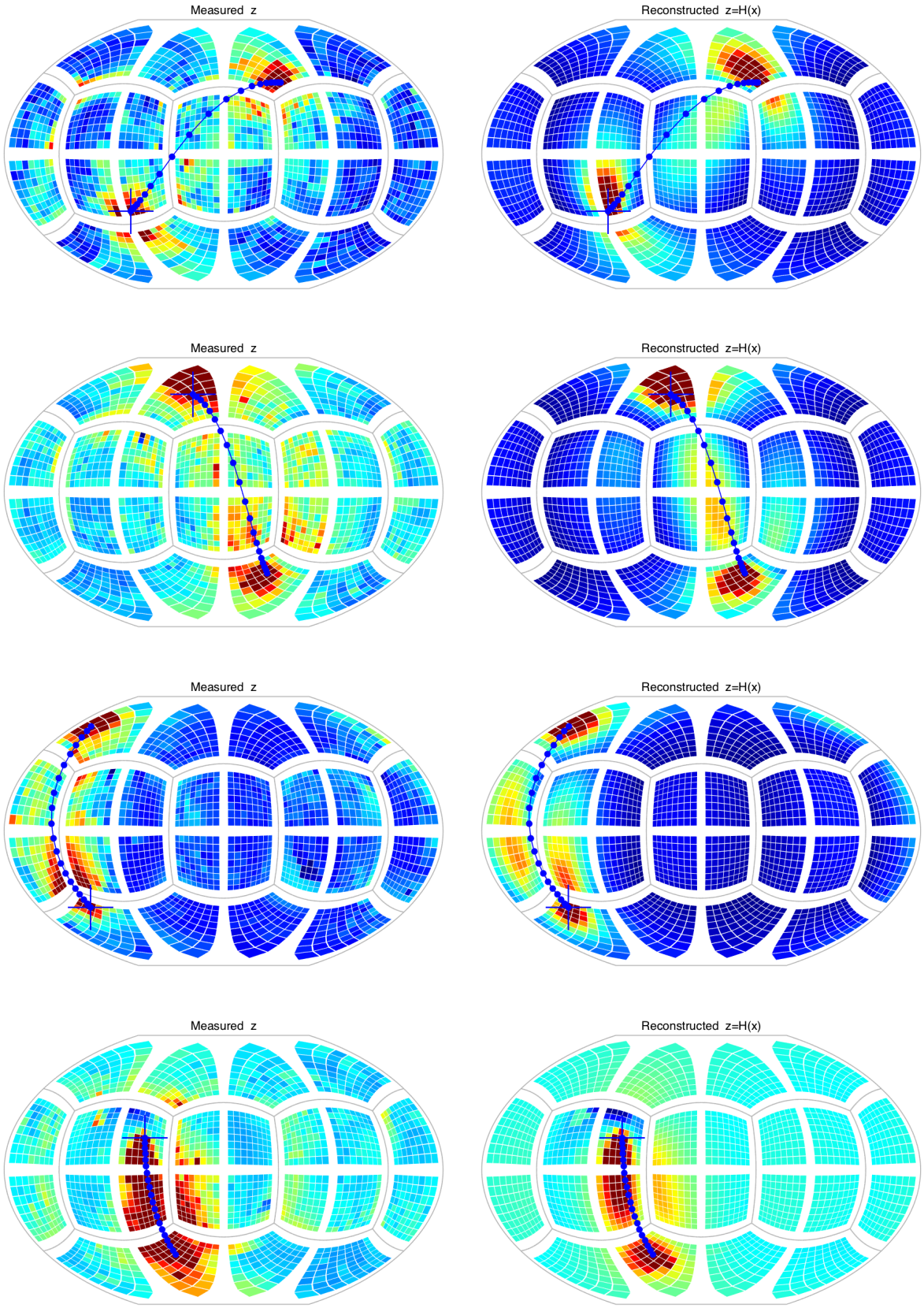

Figure 2.94: Charge distributions in mTC muon data. Real data is shown on the left, and simulated is on the right, with the muon reconstructed track. Figures are taken from [88].

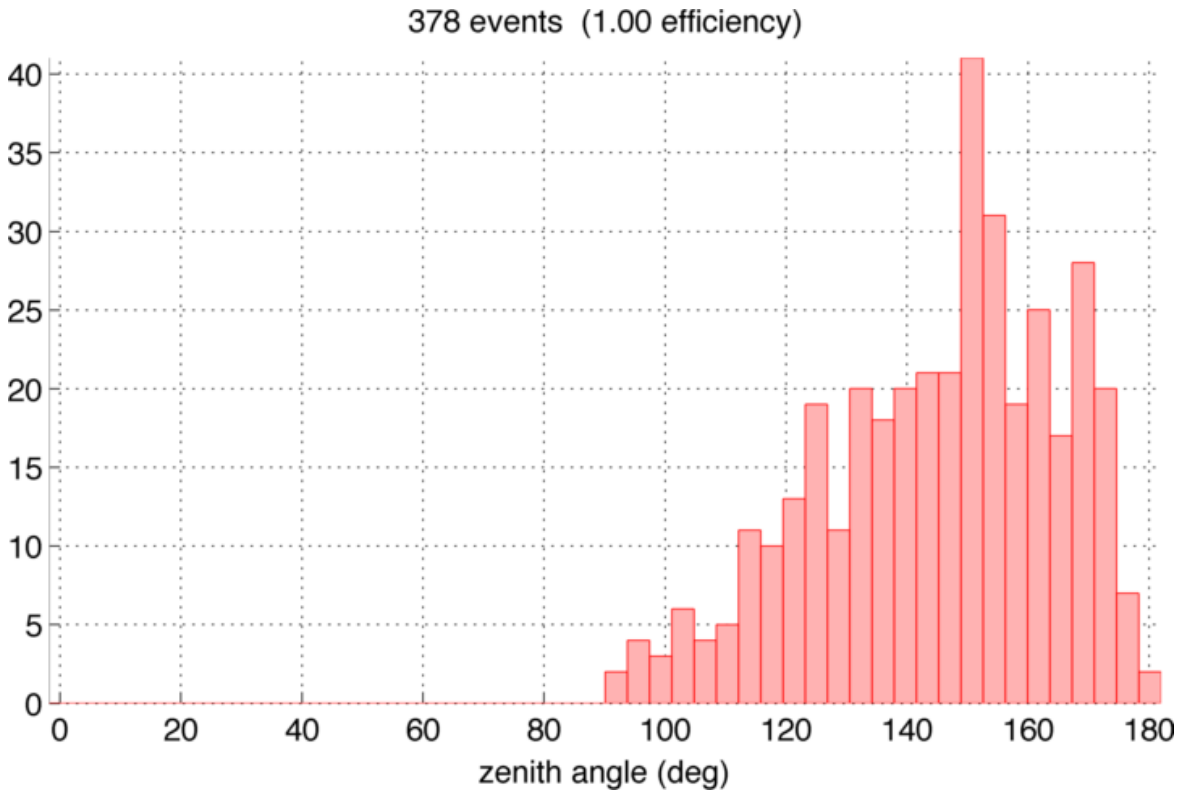

Figure 2.95: Angular distribution for muons [88].

2.6 Neutrino detection capabilities

This section highlights the feasibility studies of mTC directional detection capabilities for neutrinos, as discussed in [85] and based on Glenn's algorithms [88], similar to the one used in the Double CHOOZ experiment [112]. The simplest test is a single point-source fit — allowing for the exploitation of *a priori* knowledge about the event, and providing more accurate reconstructions as long as correct assumptions are applied [111].

In general, the likelihood of observing a single photo-electron (PE) z from a single point-source θ is

$$p\left(z|\theta\right) = \Lambda_t P_\Omega P_\gamma P_T Q \tag{2.13}$$

where Λ_t is the temporal likelihood, P_Ω is the solid angle probability, P_γ is the unattenuated energy probability, P_T is the transmission (or non-reflecting) probability, and Q is the PMT quantum efficiency. Equation 2.13 then forms the basis of our likelihood function, defining the likelihood of point-source θ given measurements z:

$$p(\theta|z) = \prod_j p\left(z_j|\theta\right) p\left(\theta\right) \tag{2.14}$$

where the likelihood $p(z_j|\theta)$ of measurement j with prior $p\left(\theta\right)$ is simply an evaluation of the measurement space created by θ at z_j. Eq. 2.14 extends to multiple point sources as well:

$$p(\theta|z) = \prod_j \sum_i w_i p\left(z_j|\theta_i\right) p\left(\theta_i\right) \tag{2.15}$$

For point source i, the likelihood $p(z_j|\theta_i)$ of measurement j given source i with weight w_i and prior $p\left(\theta_i\right)$ is simply an evaluation of the measurement space created by θ_i at z_j. Several detector and scintillator characteristics, including but not limited to the list below, affect the measurement space θ of a point source (x, y, z, t).

- Scintillator — spectrum, yield, decay constant(s), quenching factors for heavy particles, attenuation length, refractive index, re-emission efficiency of attenuated photons
- PMT — quantum efficiency, gain, transit-time spread, glass refractive index
- Cherenkov spectrum
- Time and energy calibrations

From the point sources of Eq. 2.15, which is the basis for parameter estimators in the mTC, many complex shapes can be built. These shapes can range from muon tracks to neutron scatters, and can include many more shapes.

Before they are considered as possible $\bar{\nu}_e$ candidates, measured events in the mTC pass through several candidate cuts, which are shown along with their related candidate candidate efficiencies in Fig. 2.97a. To improve the quality of $\bar{\nu}_e$ events and to reduce the likelihood of backgrounds entering into the $\bar{\nu}_e$ candidate dataset, these cuts are implemented.

Events with prompt or delayed vertices < 5 mm from the wall are rejected by the 5 mm edge cuts. Furthermore, this cut rejects potentially unreliable fits, as points that

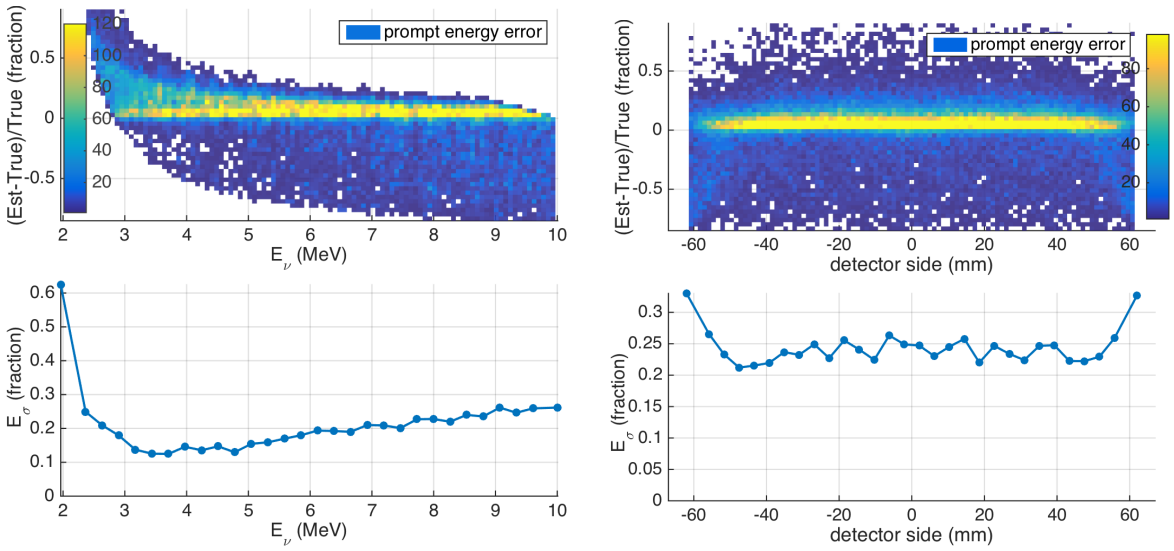

(a) $\bar{\nu}_e$ energy resolution vs $\bar{\nu}_e$ energy.

(b) $\bar{\nu}_e$ energy resolution vs vertex location.

Figure 2.96: Simulated mTC $\bar{\nu}_e$ energy resolution. Figures are taken from [85].

are too close to the wall tend to suffer from low reconstruction quality. Additionally, the edge cut reduces the likelihood of a position from leaving the detector volume, potentially resulting in severe underestimation of the $\bar{\nu}_e$ energy. The edge cut also reduces the detector fiducial volume by 20%, from 2.2 to 1.7 liters.

There are timing restrictions imposed by hardware on the prompt-delayed $dt \in \sim [1, 9.5]$ μs, as shown in Fig. 2.50. The lowest boundary also prevents any late prompt PEs from entering the delayed signal dataset. Figs. 2.47, 2.48, and 2.49 illustrate neutrino trigger.

In addition, energy and number of PEs cuts are imposed. For the prompt signal, energies of 1–8 MeV and PE counts 20–10,000 are accepted. The delayed signal has much stricter energy cuts, as it has a more consistent energy output; delayed candidates with 40–400 keV and 20-400 PEs are accepted.

To be accepted in to the candidate pool, $\bar{\nu}_e$ candidates must meet all these requirements. In the mTC simulations, we find about 30% $\bar{\nu}_e$ candidate efficiency at 3–4 MeV. The dominant source of efficiency loss is neutrons leaving the detector volume, which happens 45% of the time, and from neutrons leaving the 12 μs time window, which happens 30% of the time. These two causes alone reduce the mTC $\bar{\nu}_e$ candidate efficiency to <40%, while the other cuts only have minor effects.

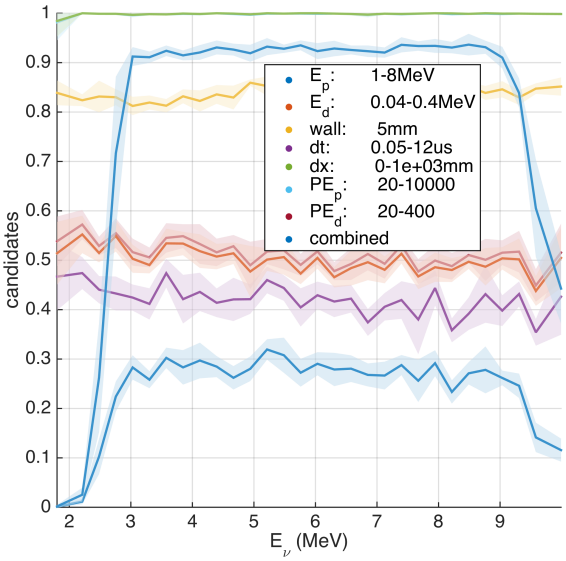

(a) Simulated mTC $\bar{\nu}_e$ candidate efficiency.

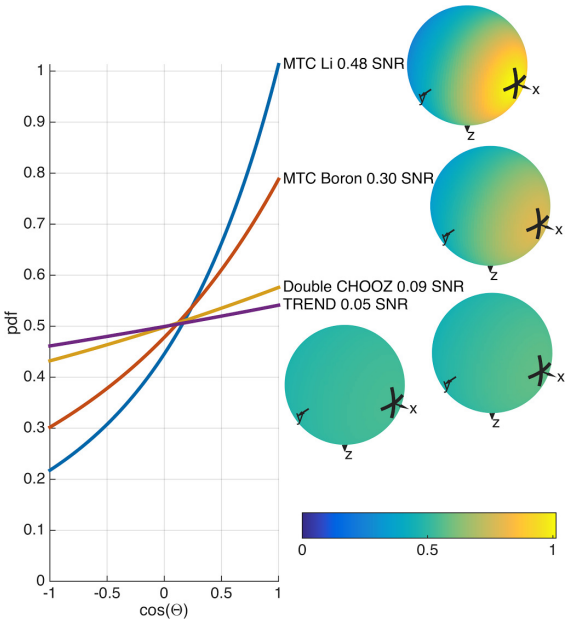

(b) Angular resolution for the mTC and mTC Li-doped, along with the CHOOZ experiment and TREND model.

Figure 2.97: Neutrino detection in the mTC. Figures are taken from [85].

2.7 Laser calibration system

In order to further verify timing and make MCP-PMT gain maps, a laser calibration system was designed. Most of the components of the laser calibration system are situated in a light-tight 3-rack-unit-high aluminum box ($17.5'' \times 23.5'' \times 5''$) that is mounted in the second mTC crate where the DAQ system is located. There are six fibers coming out of the laser box. The fibers go into the main mTC enclosure. The tip of each fiber is enclosed in a special custom-made connector, which is called needle connector. Each needle connector is optically coupled in the middle of each mTC face. The laser calibration system diagram is shown in Fig. 2.98.

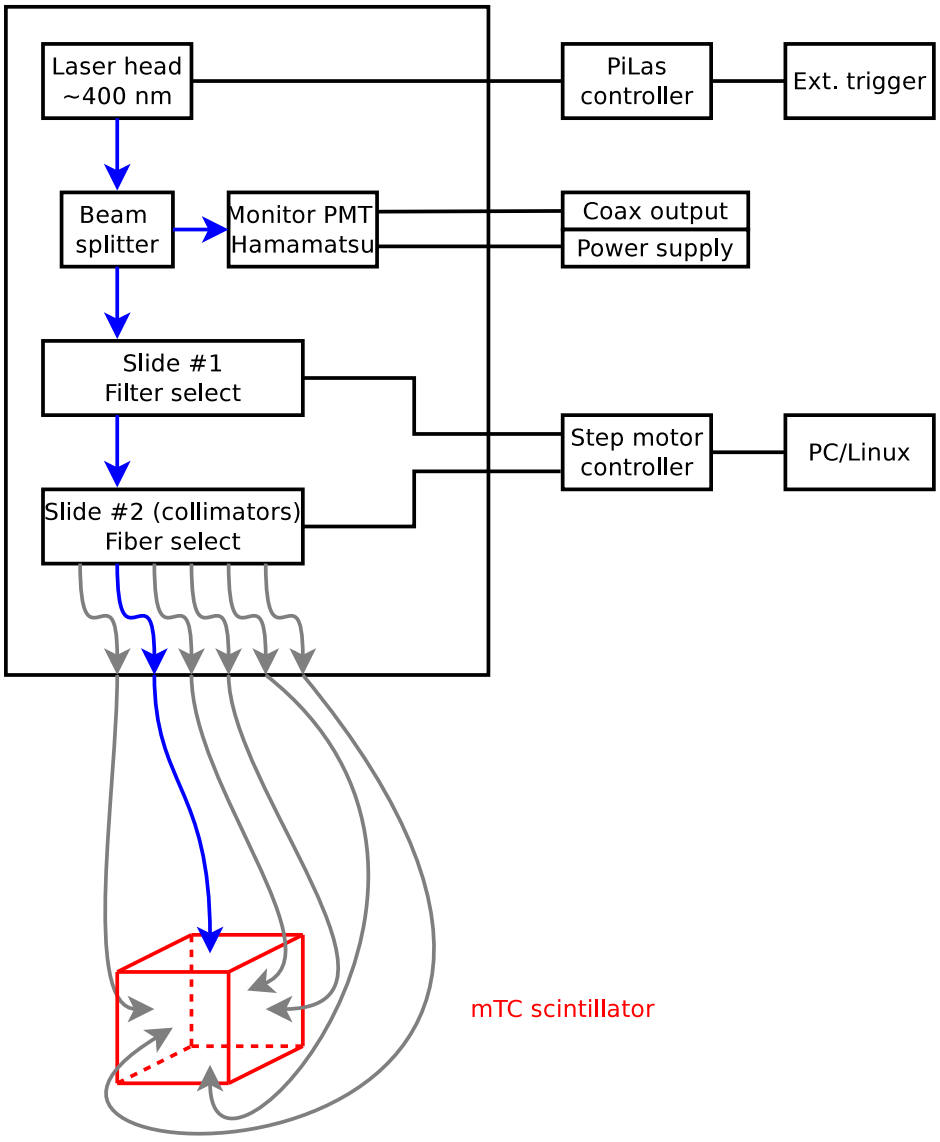

Figure 2.98: Diagram of the laser calibration system.

The laser head is controlled by the pico-second laser controller (PiLas). The 404-nm laser is directed at a beam splitter. A few percent, passed through a filter and diffuser, enter the monitor PMT. The rest of the laser beam is sent to the mTC through a pre-select neutral-density filter and a pre-select collimator lens with a fiber attached to it. The laser system is designed to only fire at one mTC face at a time.

#	Peak voltage output, mV	Length, cm
1	81.7	404.7
2	65.6	404.5
3	30.2	403.7
4	70.0	404.5
5	50.8	404.4
6	130.2	404.0
7	67.0	404.3
8	46.2	405.0

Table 2.16: Needle connector fiber properties, only six were used, two were made as spares.

Although each fiber has its own light yield as a result of polishing, orientation (tilt), rotation, and optical coupling to the scintillator, it doesn't affect *relative* time and gain calibrations, especially at a single photoelectron level. All the fibers inside and outside the laser box have numerical aperture value of .22 and core diameter 105 μm.

A total of eight fibers with needle connectors were produced, with six installed and two spares. Table 2.16 shows lengths of the fibers and production test light output. The voltage was measured using a 1-cm Hamamatsu PMT with an optical diffuser and neutral density filter installed on it.

CAJIPCI, the clock board, is also capable to issue a pulse, well-defined in the time domain. We use it to trigger the PiLas controller. Below are the figures showing the measured jitter between the signal issuing the laser trigger and MCP-PMT SCROD readout using nominal dT values (Fig. 2.102), MCP-PMT common dynode (Fig. 2.103), and the reference Hamamatsu PMT inside the laser box (Fig. 2.104). $\sigma \sim 290$ ps measured with the mTC digitizers is consistent with $\sigma \sim 279$ ps using the direct scope measurements. The $\sigma \sim 12$ ps using the reference PMT is much lower. Thus, the main jitter contributor is the MCP-PMT. The setup and the scope readout are shown in Figs. 2.99–2.100.

Later, we also established that four PMTs on the face where the laser is entering the cube could be left on without damaging them; that also helps with the timing, as there is a delay between photon arrival times for two opposite faces (one face with the fiber). We also found that the wavelength might be inadequate. We noticed that the brighter illumination appears on the side faces of the cube, not the front face, relative to the laser. That might indicate that there is a reemission causing this behavior.

Figs. 2.106 show the needle connector sandwiched between the two electronics card cages, centered between the four inner corners of the MCP-PMTs. It fits there nicely, with an optical grease at the end to improve the coupling with the scintillator surface. After laser calibrations are performed, a gain map is made, that can then be applied to real data [88]. The laser entry point can also be reconstructed by using charge (amplitude) only, without using any timing, as shown in Figs. 2.108.

Figure 2.99: Channel 1 — MCP-PMT common-dynode output. Channel 2 (trg 2 V) — PiLas TRG OUT. Channel 3 — PiLas TRG IN (after the splitter, +8 ns delay). Channel 4 — CAJIPCI clock.

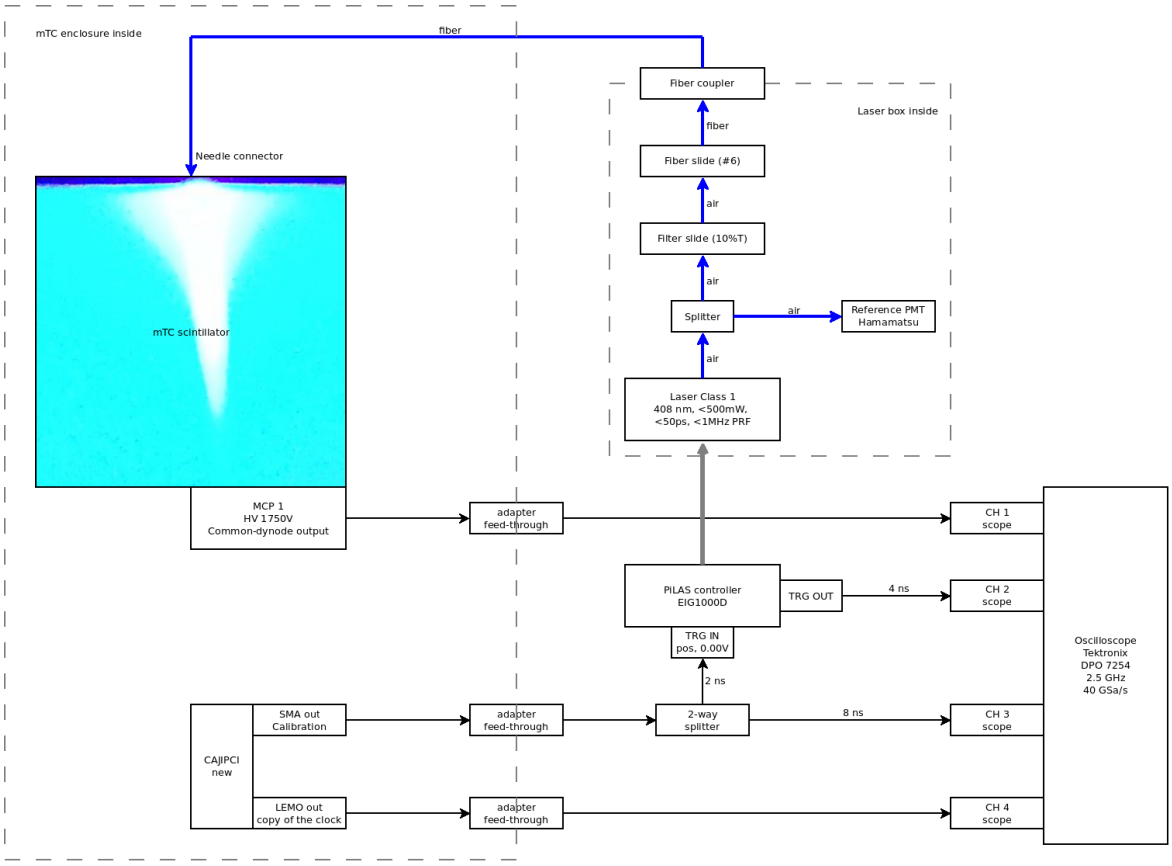

Figure 2.100: One of the setups to verify timing using the scope.

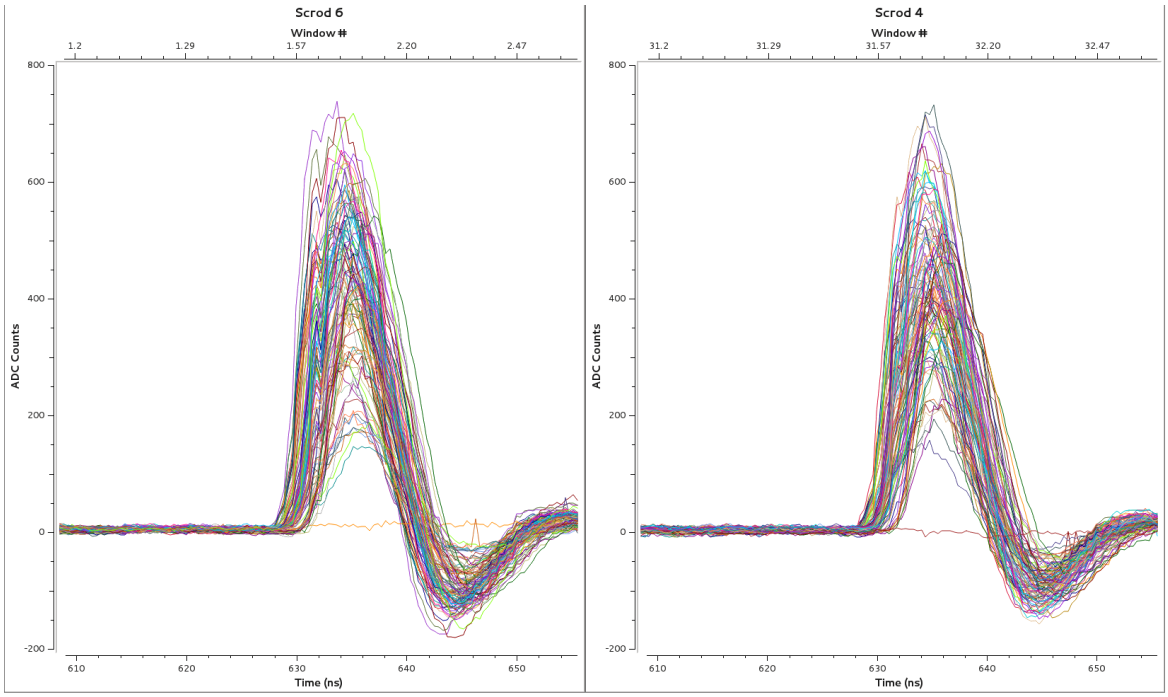

Figure 2.101: Laser pulse visible across two SCRODs (four MCP-PMTs).

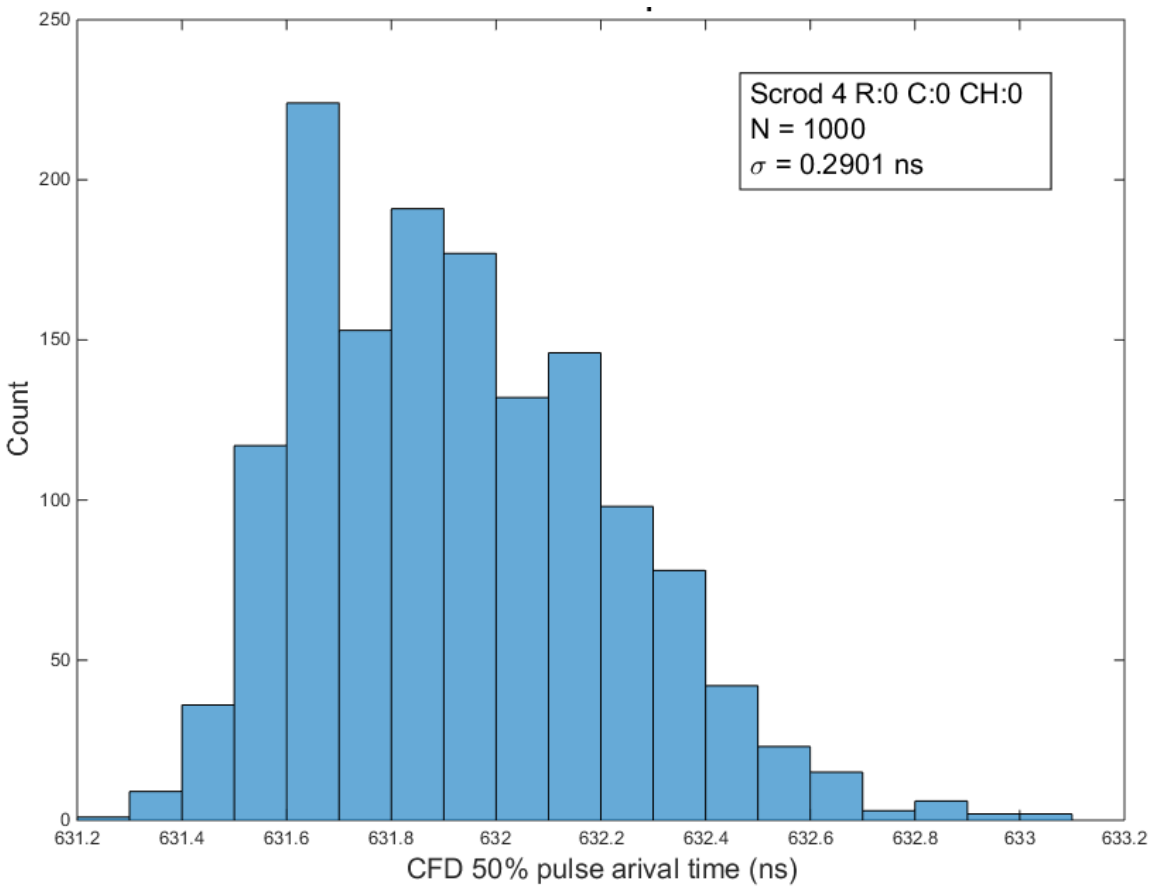

Figure 2.102: Distribution of the laser pulse arrival time. $\sigma \sim 290$ ps is consistent with the direct scope measurements [108].

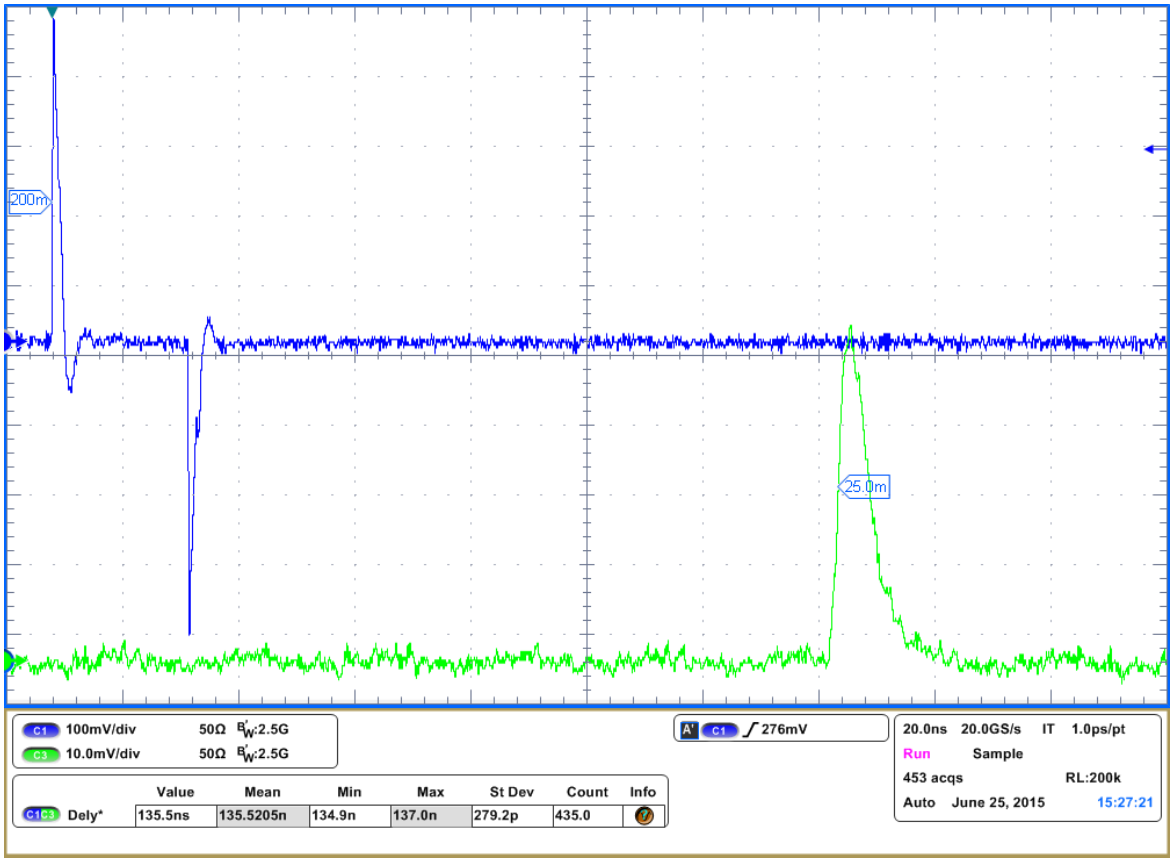

Figure 2.103: Cajipci calibration pulse vs. common dynode output on one of the MCP-PMTs, $\sigma \sim 279$ ps.

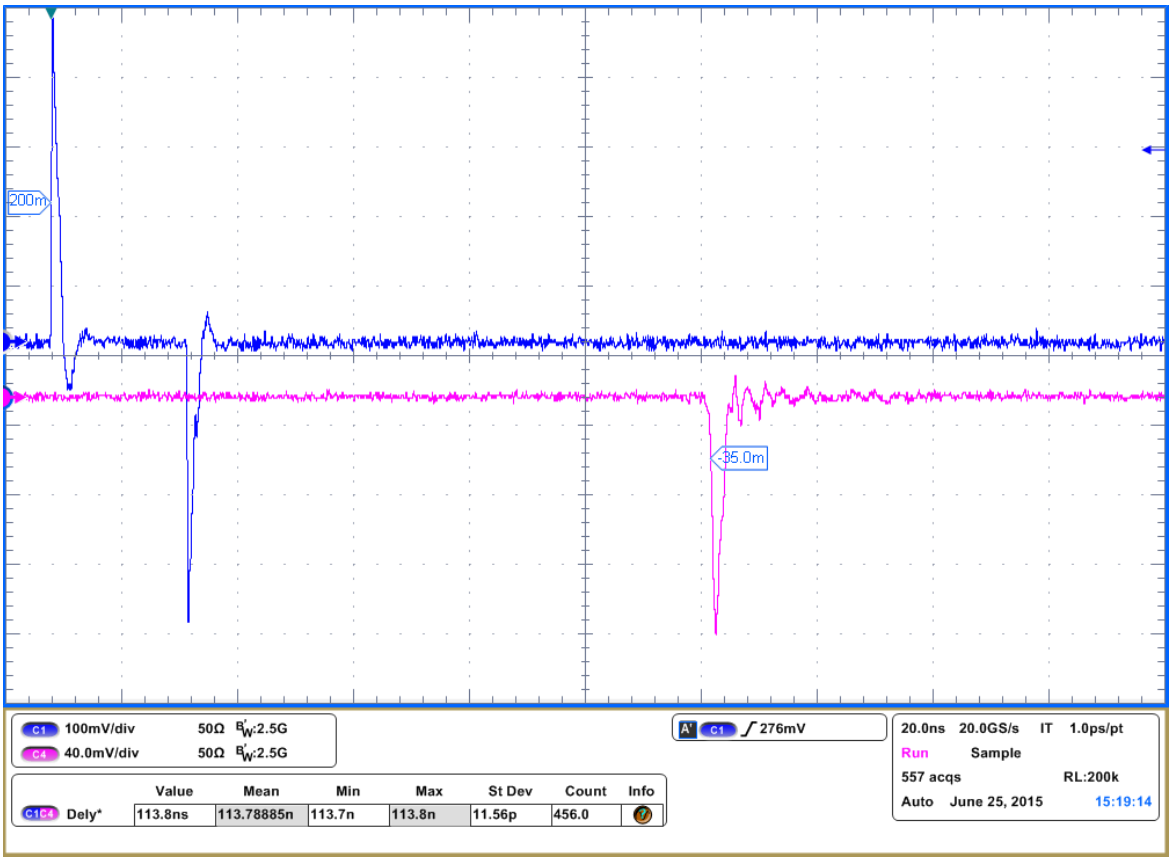

Figure 2.104: Cajipci calibration pulse vs. the reference Hamamatsu PMT, $\sigma \sim 12$ ps.

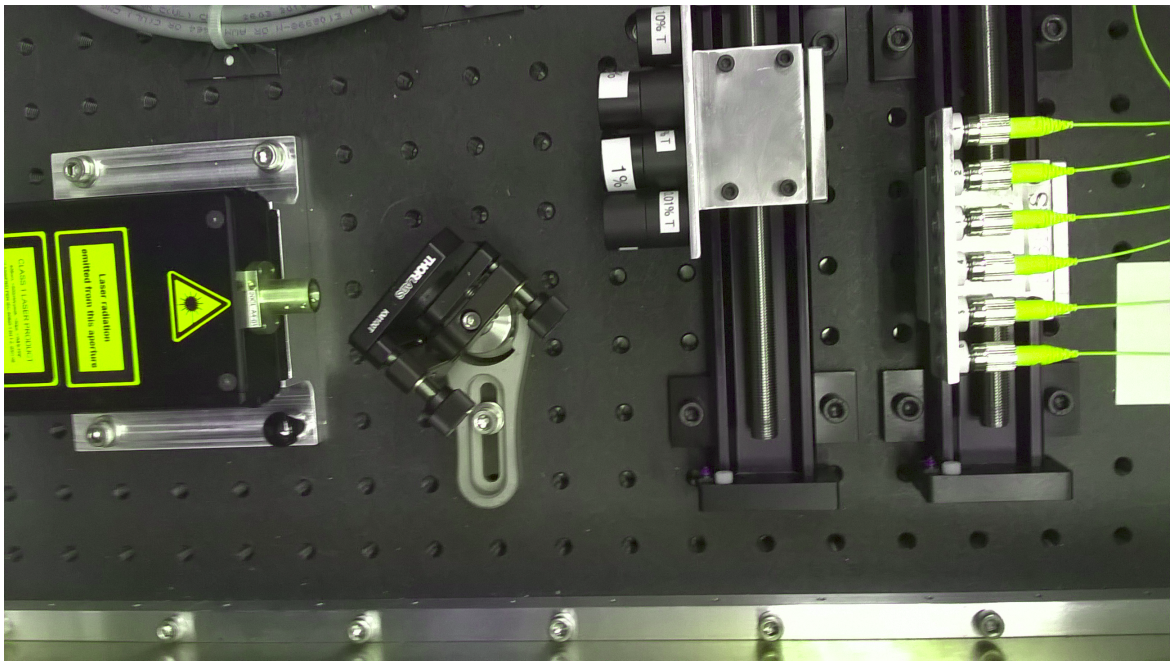

(a) Inside the laser box: laser head, and two slides — filters and collimator lenses with six fibers connected.

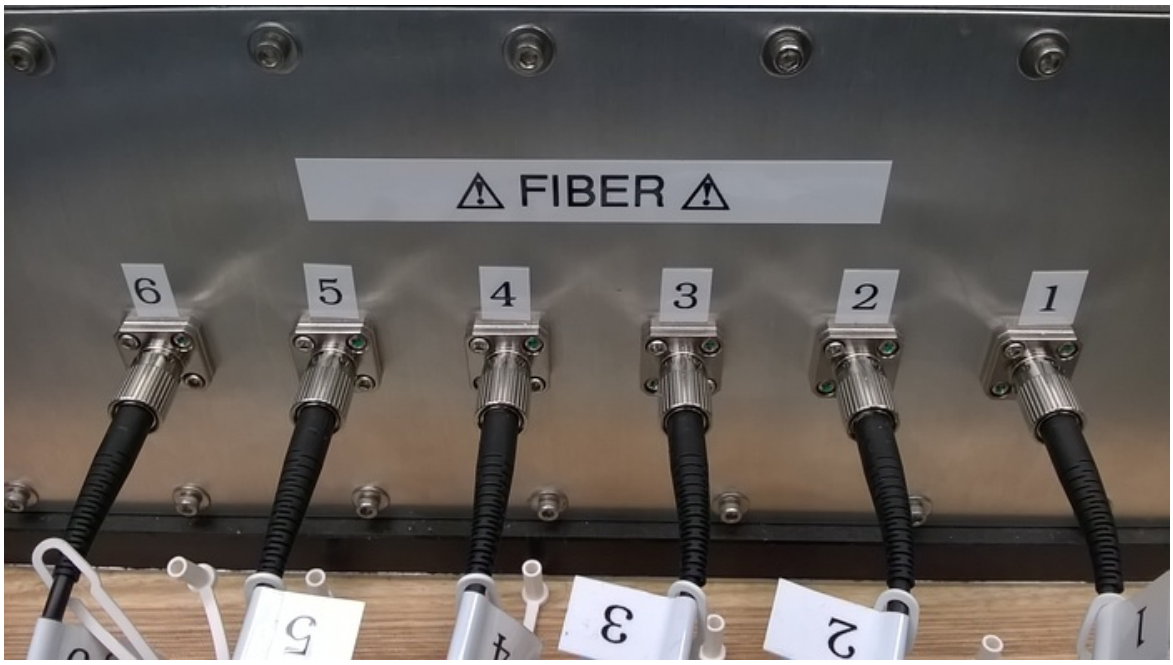

(b) Six laser calibration fibers connectors outside the laser box.

Figure 2.105: The laser box.

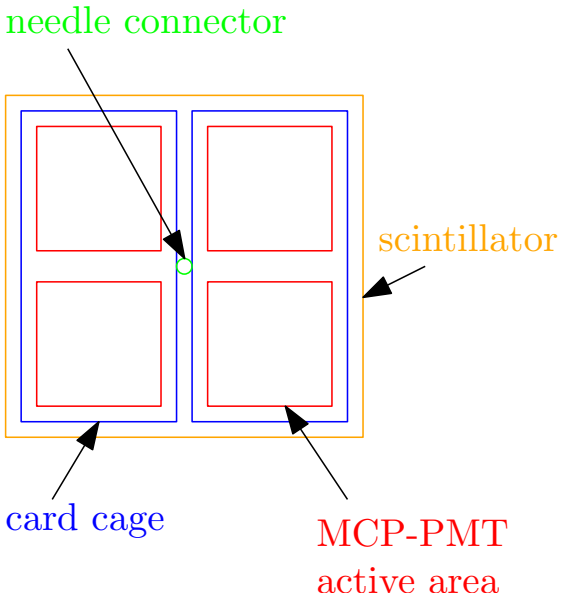

(a) Diagram showing needle connector fit on one face.

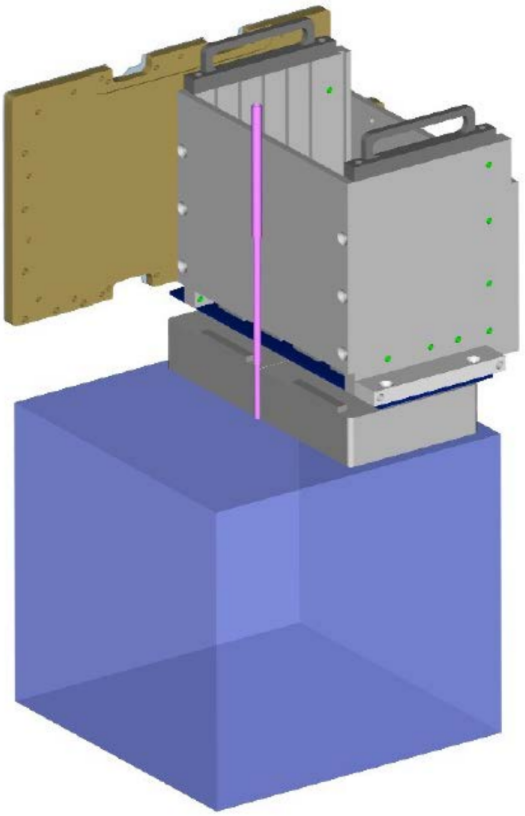

(b) CAD drawing.

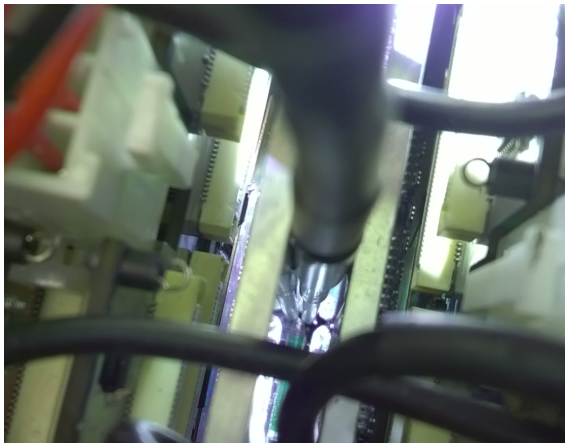

(c) Needle connector sandwiched between two card cages and four inner corners of the MCP-PMTs.

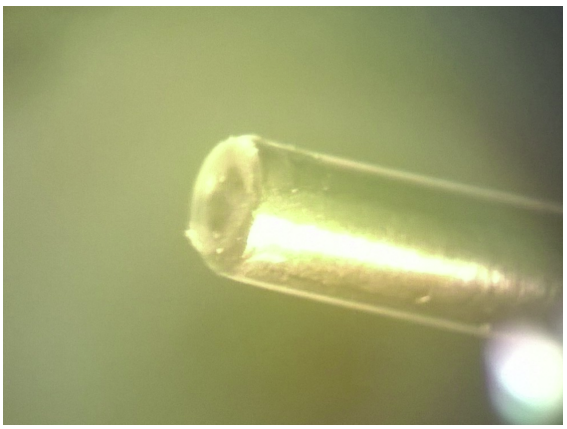

(d) Microscope photograph of the tip of the needle connector, the polished fiber is inside the epoxy.

Figure 2.106: Needle connector.

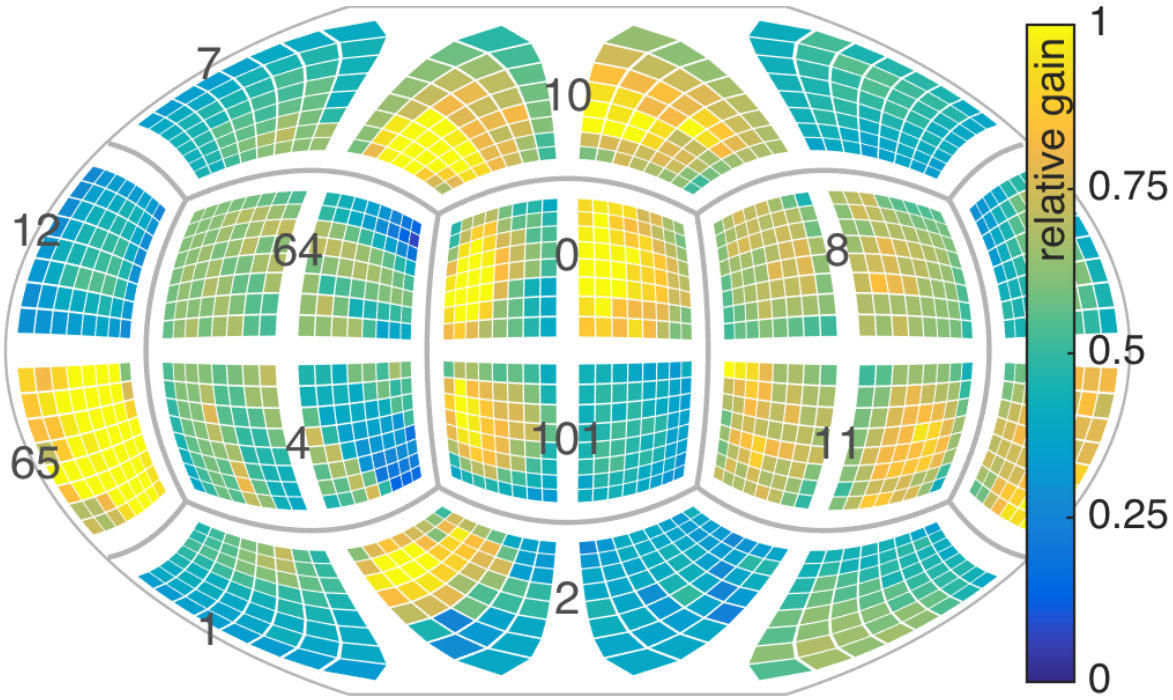

Figure 2.107: Gain map obtained after laser calibration is performed. Figure is taken from [85].

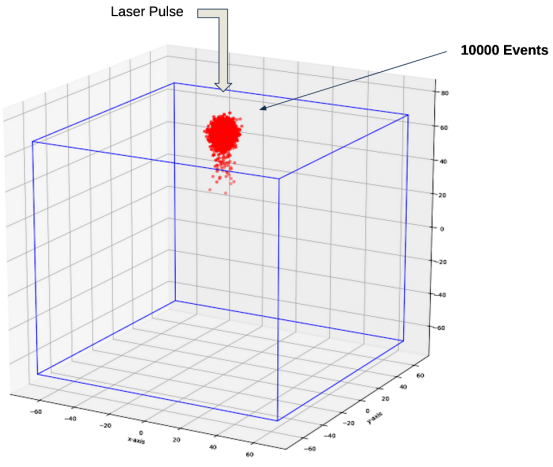

(a) Figure is taken from [113].

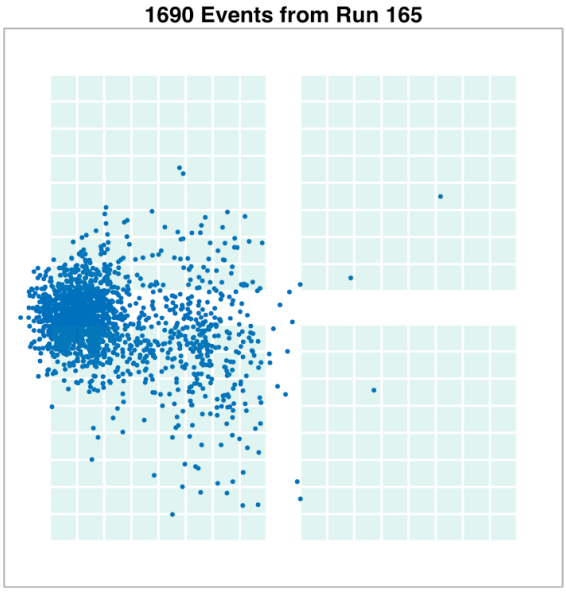

(b) Figure is taken from [88].

Figure 2.108: Two independent analyses of the laser entry point. Different data samples.

2.8 Cross-talk 1.0

This section recounts an accidental discovery of a previously-unknown phenomenon in an array of MCP-PMTs.

On a dark and stormy night, I was performing calibration tests. Only one tube was powered. On the event viewer, I observed waveforms on the powered tube. At that point I also noticed waveforms I could not explain. They were mostly on the edges of the MCP-PMTs neighboring the powered tube on the same face. The artificial/*phantom* waveforms were less prominent on the unpowered tube kitty corner from the powered tube, compared to the two adjacent tubes. Fig. 2.109 is the very first screenshot made on that stormy night, showing the event viewer with phantom waveforms on the edges of the three unpowered PMTs. The phantom pulses were a few hundred counts high, shown in Fig. 2.110, and had a distinct negative-going pulse preceding a positive-going peak, which made us think of a capacitive coupling between the tubes. High pulses caused by muons don't have such pre-pulsing features. This effect is new and hasn't been discussed in the literature. Moreover, as it turned out, we are the only customer of Photonis who uses their MCP-PMT in such a densely-packed configuration with four tubes next to each other. Most of their customers use them for medical PET application.

The following series of tests confirmed that the effect is not due to the electronics. We removed the two readout modules and injected different RF pulses into individual pins as well as into an MCP output. Figs. 2.115 and 2.116 best illustrate the tests.

It also became apparent that this effect affects timing performance of the detector, since in reality, when everything is powered up, the waveforms on the edge pixels are superpositions of the phantom and real pulses. The leading edge becomes quite distorted, especially for dim signals. The detector would also be triggered on those pulses as they were quite large. Figs. 2.111 show the phantom waveforms on SCRODs 1 and 2 (different events), which both are located at the bottom face.

Many ideas and solutions were explored. The following completely solved the problem. A special frame made of .004″-thick 99.97%-pure copper was designed and manufactured, shown in Figs. 2.112. The frame goes all the way around the perimeters of all four MCP-PMTs sharing one face. Another key feature is that it touches four grounding pins at the four corners of each PMT and grounds to the electronics card cages. The grounding cables of the MCP-PMTs were also removed, as they also contributed to the cross-talk.

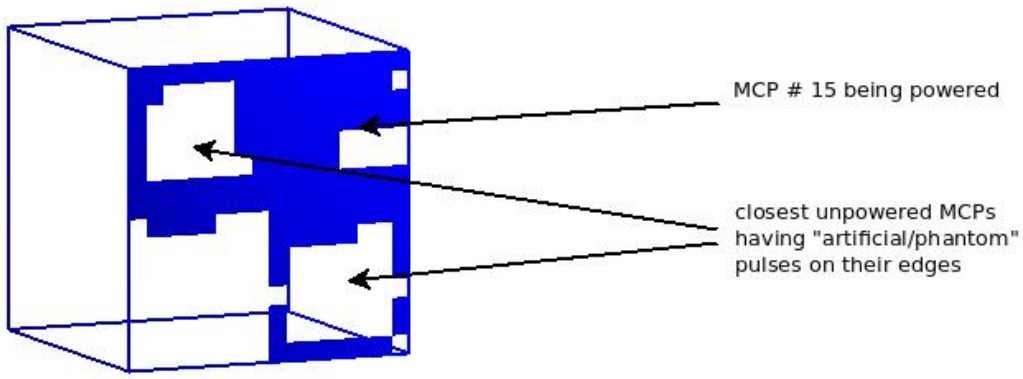

Figure 2.109: The very first screenshot of the event viewer showing cross-talk within four MCP-PMTs mounted on one face of the mTC. Each blue square indicates a pixel with a pulse recorded.

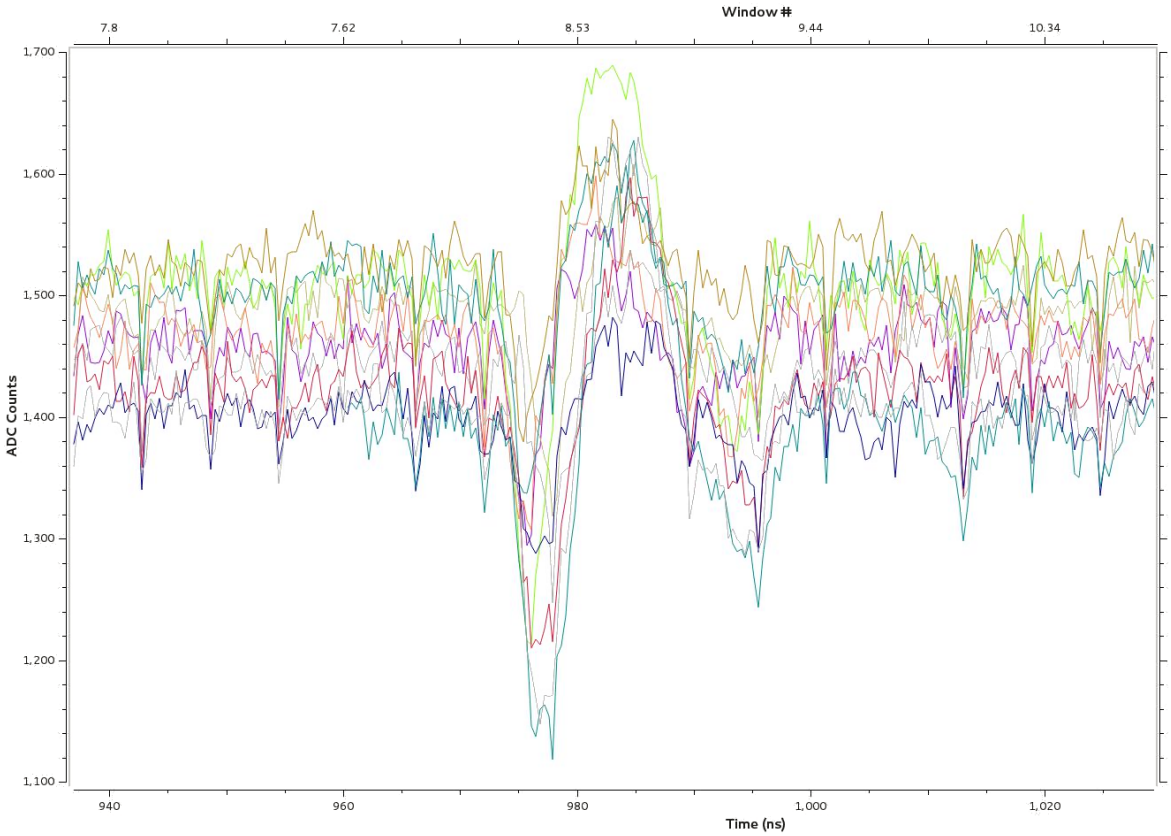

Figure 2.110: One of the very first observations of phantom pulses.

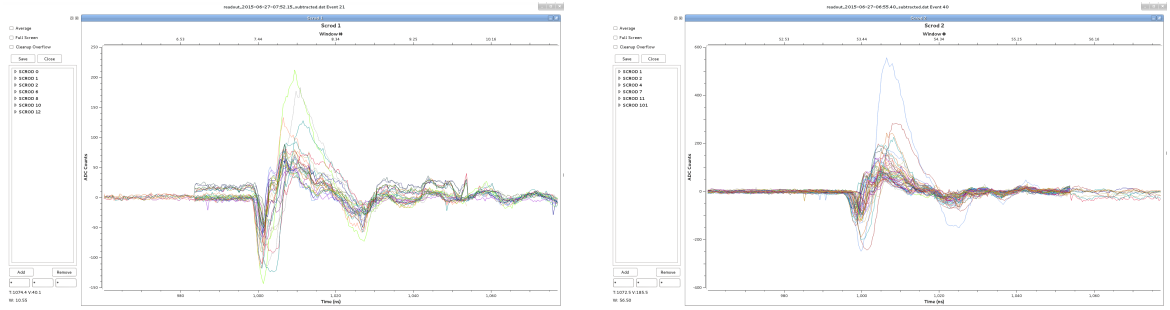

(a) SCROD 1. (b) SCROD 2, different event.

Figure 2.111: Triggering on phantom pulses.

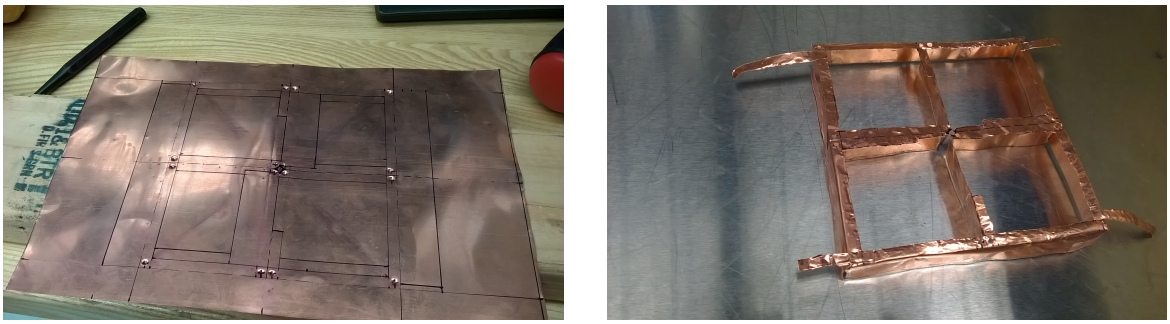

(a) Copper sheet with markings. (b) Frame ready to be installed.

Figure 2.112: Copper frame in the making.

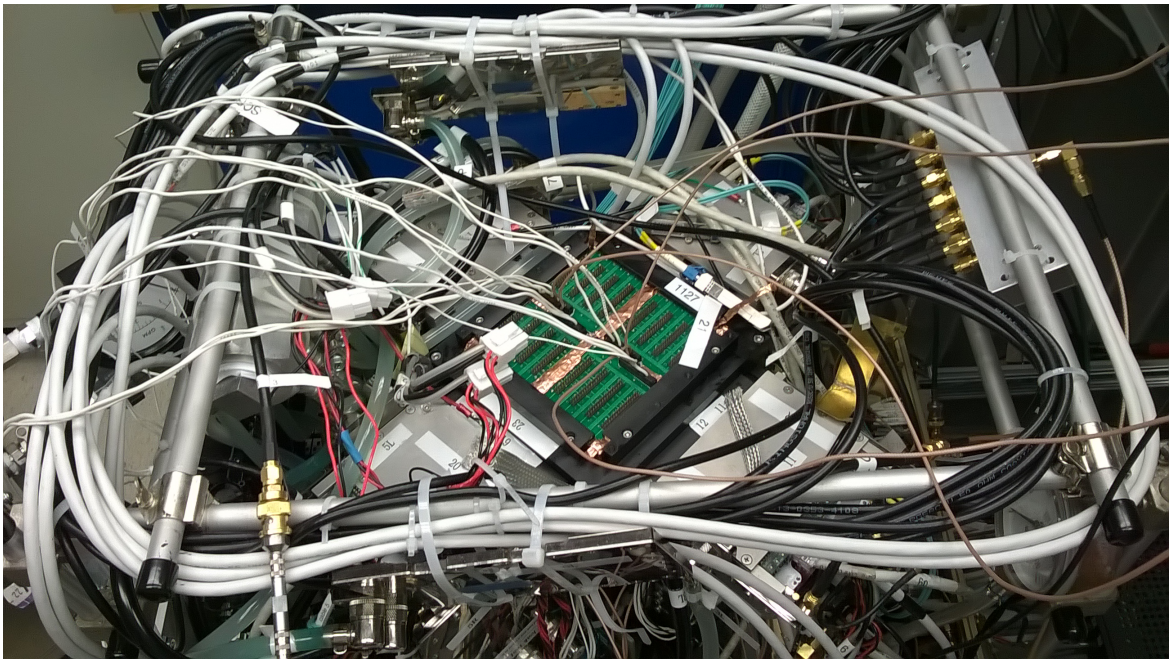

Figure 2.113: There were many cross-talk studies before finding the proper solution.

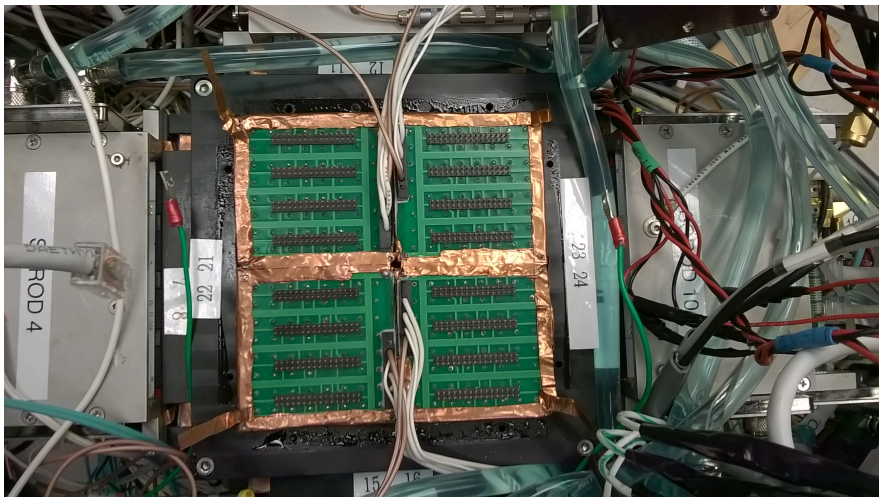

(a) First-made copper frame mounted on the top face. Copper strips at the corners will be bent and grounded to the card cages.

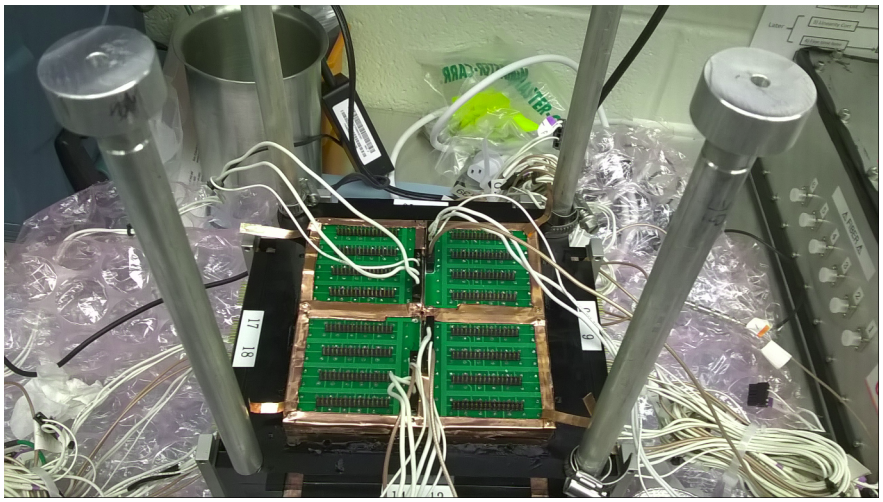

(b) Copper frame mounted on the bottom face (during the electronics swap).

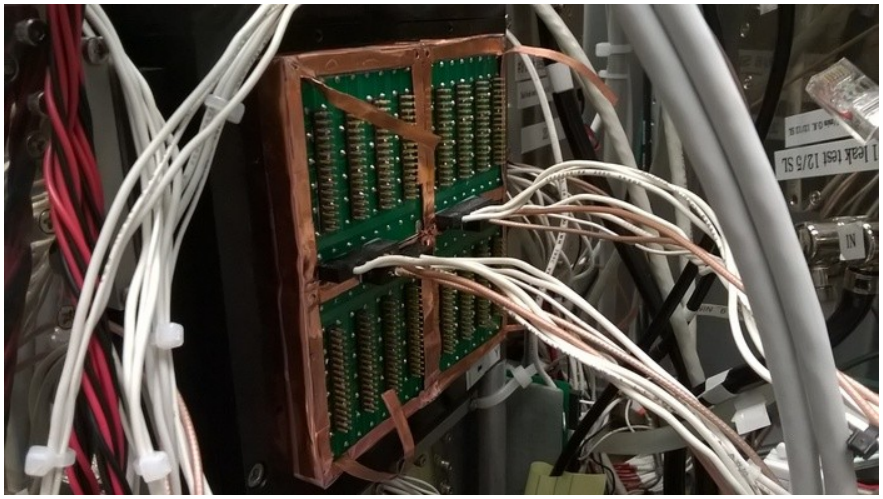

(c) Copper frame on one of side faces.

Figure 2.114: Copper frames.

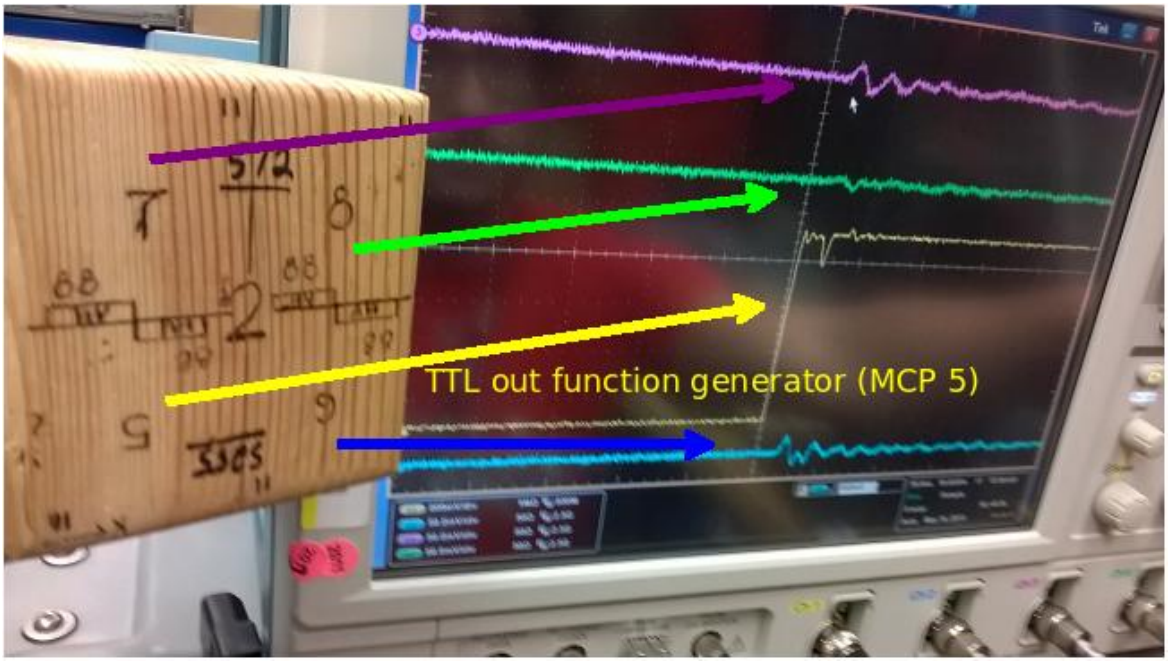

Figure 2.115: Oscilloscope screen capture. Test of the cross-talk 1.0 without electronics modules and front boards attached to the PMTs. Function generator pulse was fed to common-last-dynode output on MCP-PMT 5. Scope channel 1 (yellow) is TTL out on the function generator, channels 2 3 4 (cyan, magenta, green) are PMTs 6 7 8 respectively. The remaining three signals are pick-up observed on common-dynode of the other three MCP-PMTs. The kitty-corner PMT has the weakest signal. Pulse parameters: 600 mV, 100 kHz, 8 ns width, 5 ns rise/fall time.

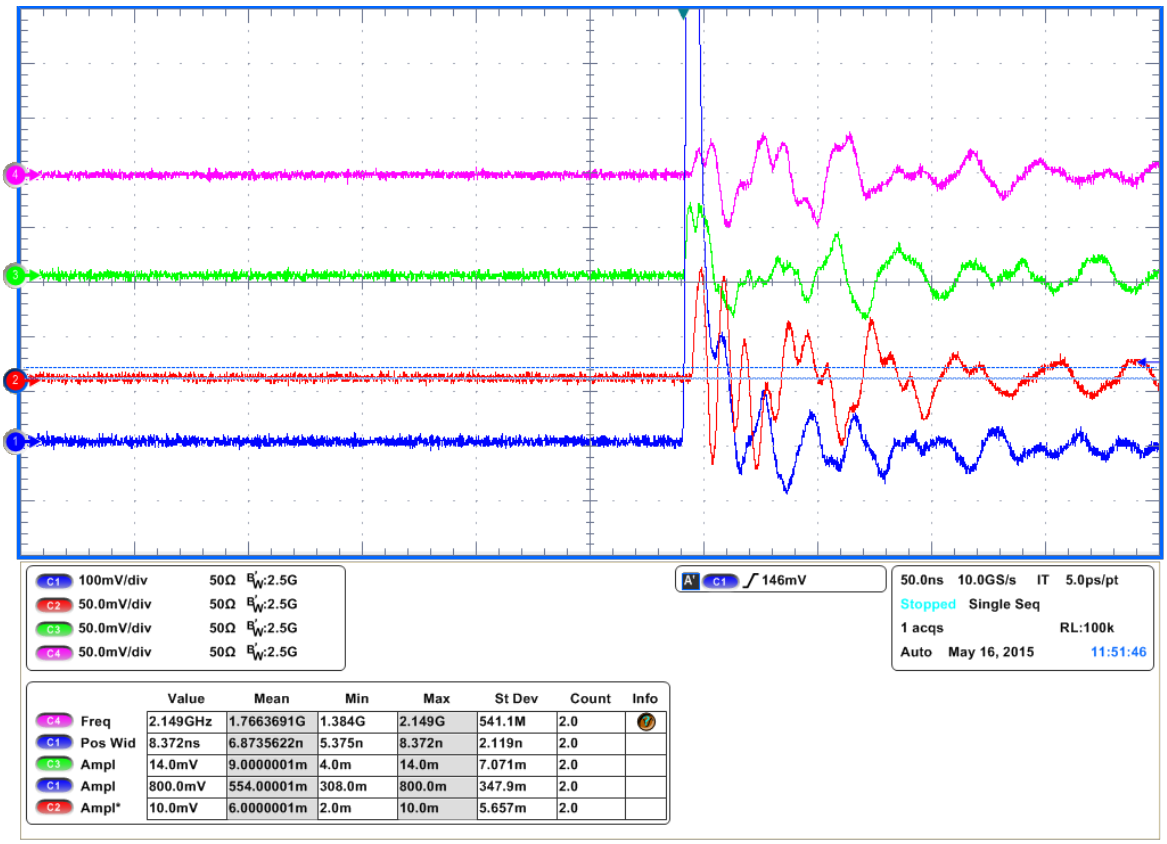

Figure 2.116: Muon, no electronics. Oscilloscope screen captures. Test of the cross-talk 1.0 without electronics modules attached. Front boards were also removed from the MCPs 5 6 7 8 (scope channels 1 2 3 4). Only PMT 5 is ON (HV 2041 V), observing muons.

2.9 Cross-talk 2.0

A completely different phenomenon was discovered while performing single-PE tests. Although at first it resembles a cross-talk between neighboring pixels within a single MCP-PMT, the nature of this phenomenon is not a cross-talk; however, we refer to it as cross-talk 2.0, for the sake of brevity.

At low light output in the laser data, we would often see a single pixel light up accompanied by its neighbors rather than by itself. After performing more tests and researching the literature [91, 114], we realized that it is a charge-sharing effect on the multi-anode structure of MCP-PMTs. Fig. 2.117 provides an illustration of the charge-sharing effect caused by the spread of the electron shower after the MCP and elastic (or inelastic) photo-electron back-scattering. It is worth noting here that a similar problem was solved by Hamamatsu [114] by segmenting MCP electrode.

The charge sharing can also introduce a delay in the waveform. The maximum delay and distance can be estimated to be [115]

$$t_{max} \approx 2t_0, \qquad d \approx 2l \tag{2.16}$$

where $t_0 = l\sqrt{2m_e/(eV)}$ is the approximate time of flight for a photoelectron from the photocathode to the MCP. Both elastic (longer delay) and inelastic (shorter delay) scattering off the MCP are possible. If the distance between photocathode and MCP is on the order of a few mm then we get the next pixel within the range for backscattered photoelectron to reach a neighboring pixel, thus, creating cross-talk that we see.

Unlike cross-talk 1.0, which we could solve on a hardware level, in order to cure this problem we thought of a variety of software algorithms. To make a detailed characterization of the charge-sharing effect, a special 64-hole aperture was made that covers the glass of the MCP-PMT with holes centered at the centers of the pixels. A laser fiber can be inserted on the other side of the hole, as shown in Fig. 2.118a.

The goal was to make a transfer function that we can later apply to the real data. As far as we know, no one came up with such transfer function, usually only a determination of a cross-talk at a certain level is being reported [99]. The effect is the most severe at higher gain.

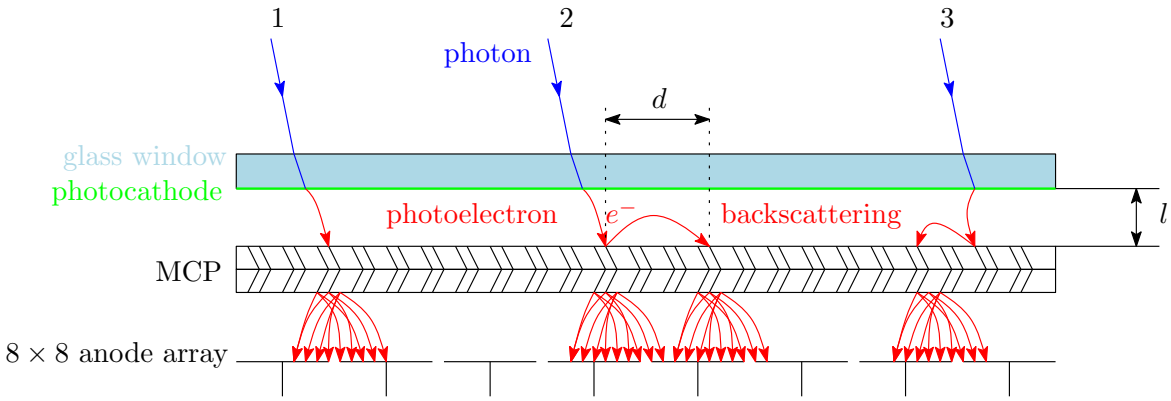

Figure 2.117: MCP-PMT diagram showing three different charge sharing scenarios due to the spread of the electron shower (1), inelastic (2) and elastic (3) e^- backscattering.

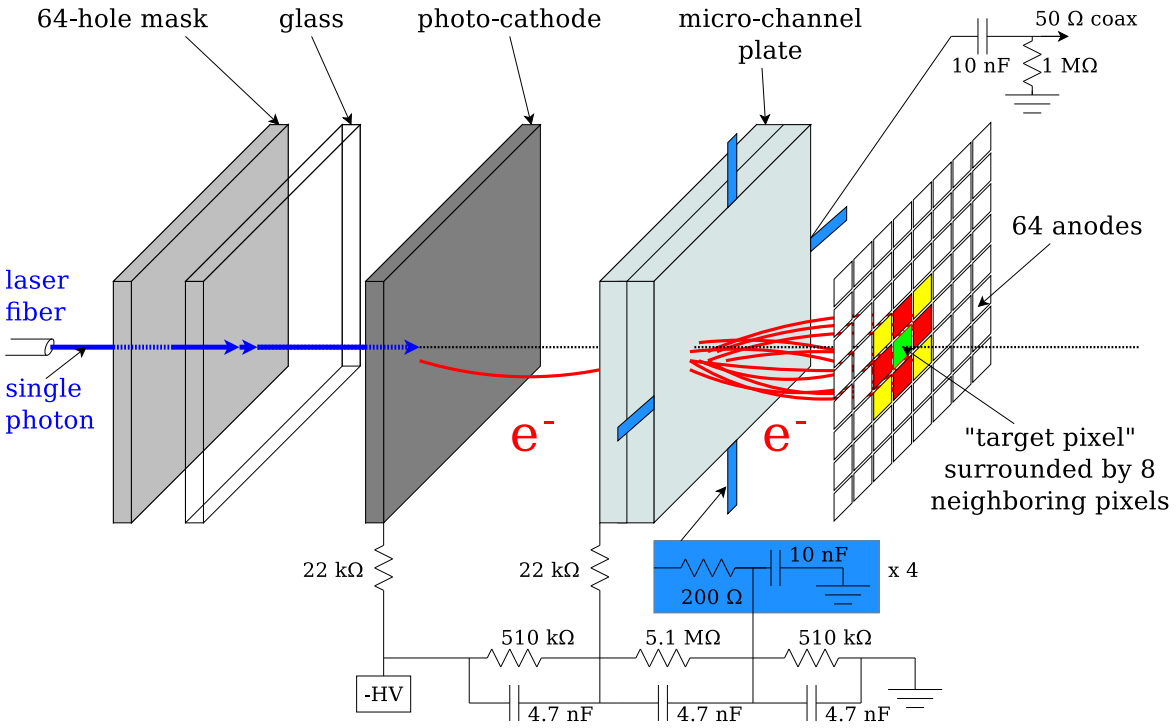

(a) Inside the MCP-PMT, including the voltage divider, and setup for laser fiber tests with a pin-cushion.

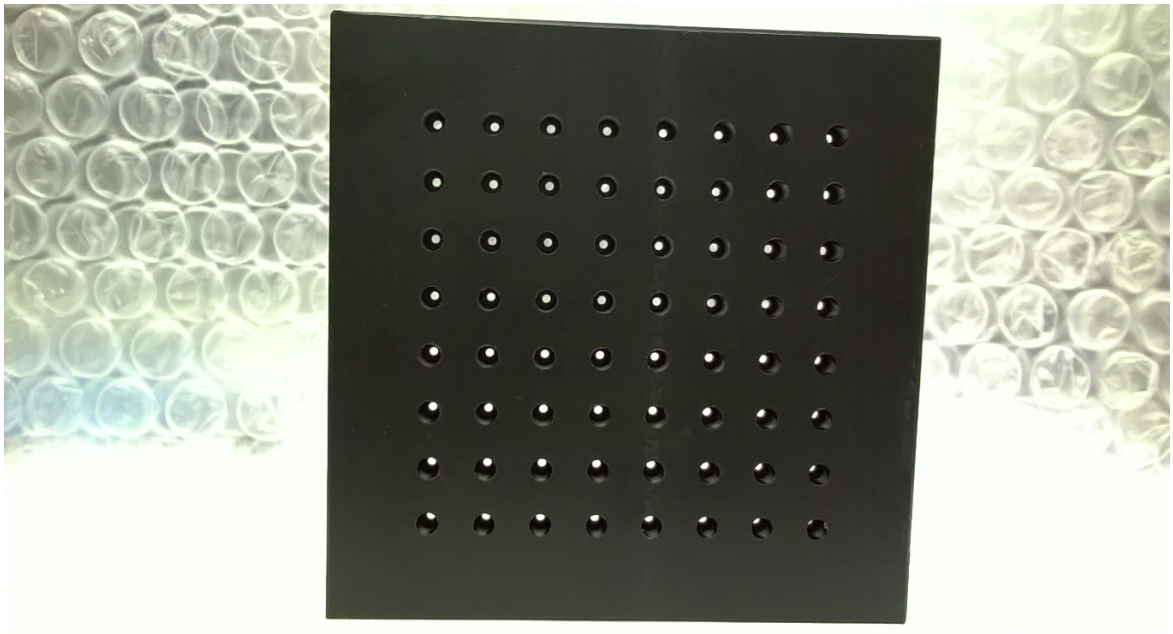

(b) Pincushion — 8×8-hole aperture.

Figure 2.118: Cross-talk nature and the aperture to investigate the cross-talk.

		x	X	x			
		X	T	X			
		x	X	x			

x							
T	x						
x							

				x			
		x	X	X	X	x	
		X	T	X	T	X	
		x	X	X	X	x	
				x			

		x	X	x			
		X	T	X	x		
		x	X	X	X	x	
			x	X	T	X	
				x	X	x	

Table 2.17: A diagram showing 64 pixels of MCP-PMT, describing four different pincushion configurations with one (top) and two (bottom) fibers. T corresponds to a so-called Target pixel where the laser fiber is directed, X — pixels with severe cross-talk, x — smaller cross-talk effect.

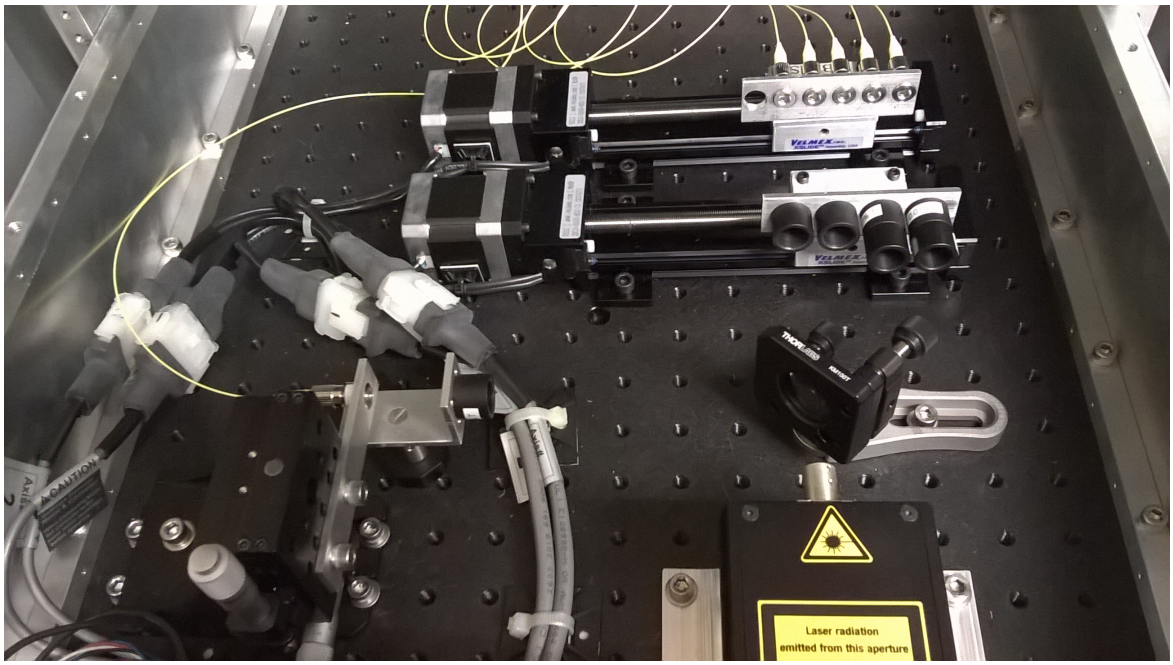

Figure 2.119: Inside of the modified laser box. The laser beam splits into two path down to the fibers.

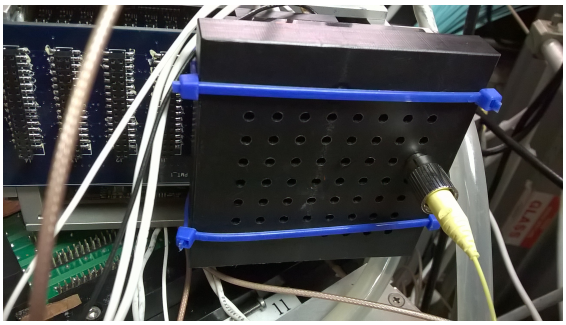

(a) MCP-PMT pincusion test with one fiber illuminating edge pixels.

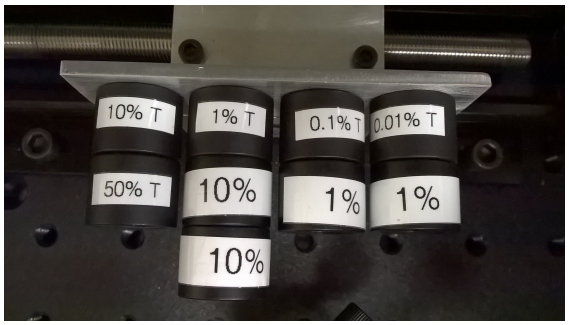

(b) Neutral density filter slide, adjusting light output to single-PE level.

Figure 2.120: Test of cross-talk 2.0 preparations.

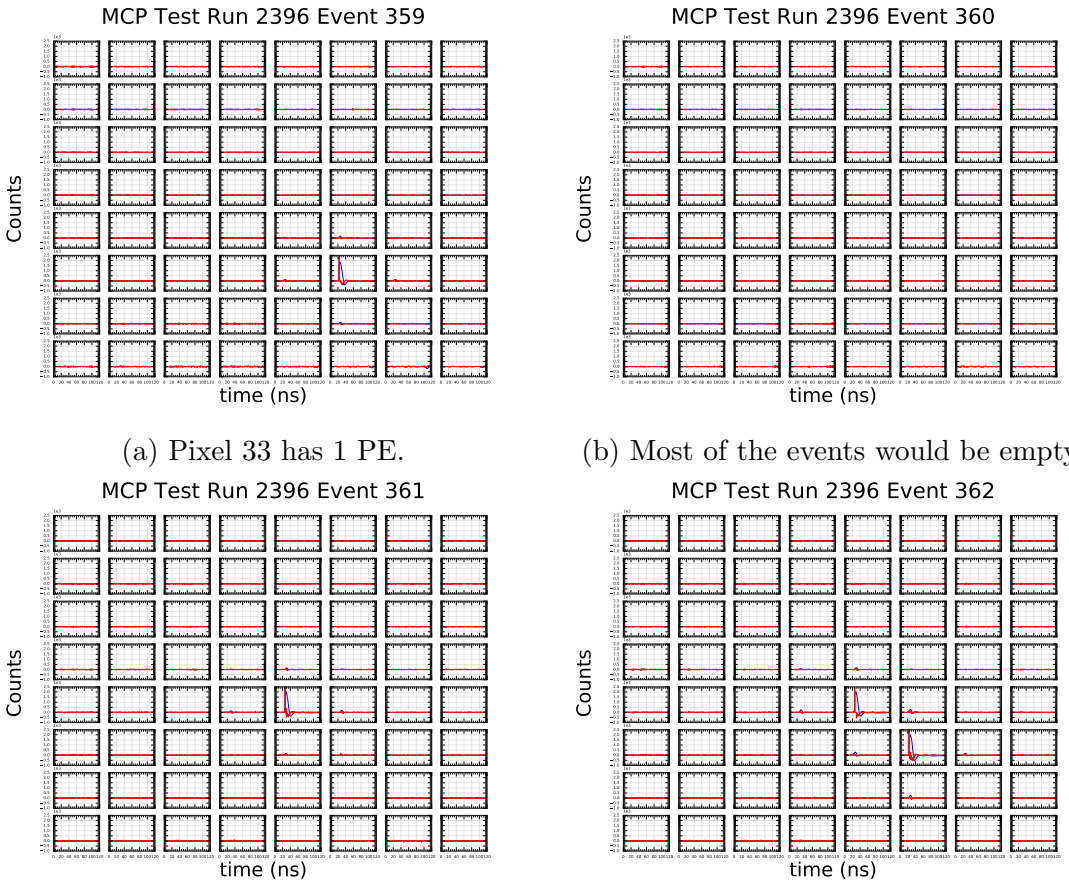

(a) Pixel 33 has 1 PE.

(b) Most of the events would be empty.

(c) Pixel 44 has 1 PE.

(d) Both 33 and 44 has single PE.

Figure 2.121: Typical events in a single-photon two-fiber run. Blue — waveform, red — its derivative. Target pixels — 33 and 44. Pixel 11 is bottom right corner.

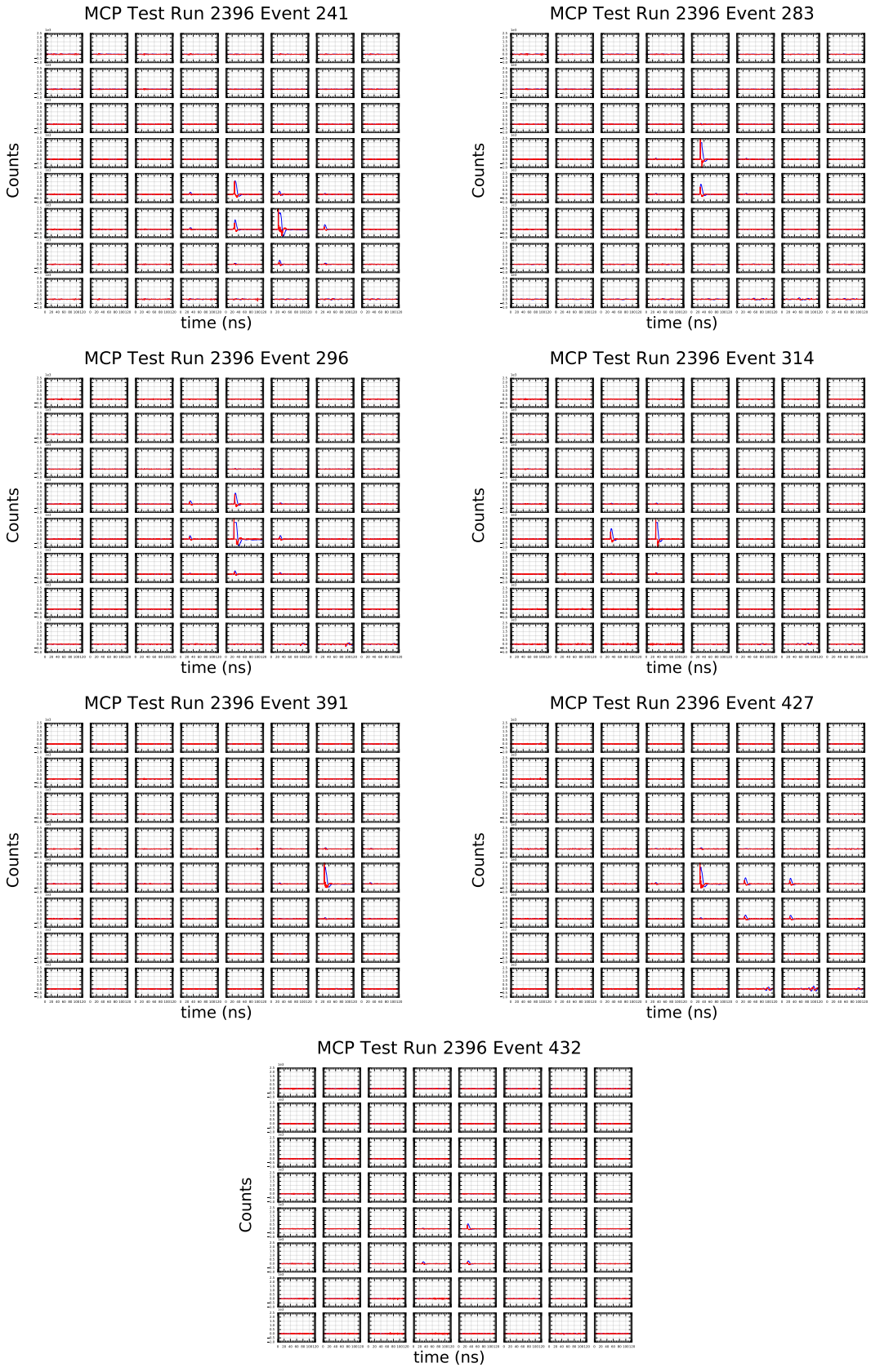

Figure 2.122: Pathological events in a 200-event run. Blue — waveform, red — its derivative. Target pixels — 33 and 44. Pixel 11 is bottom right corner.

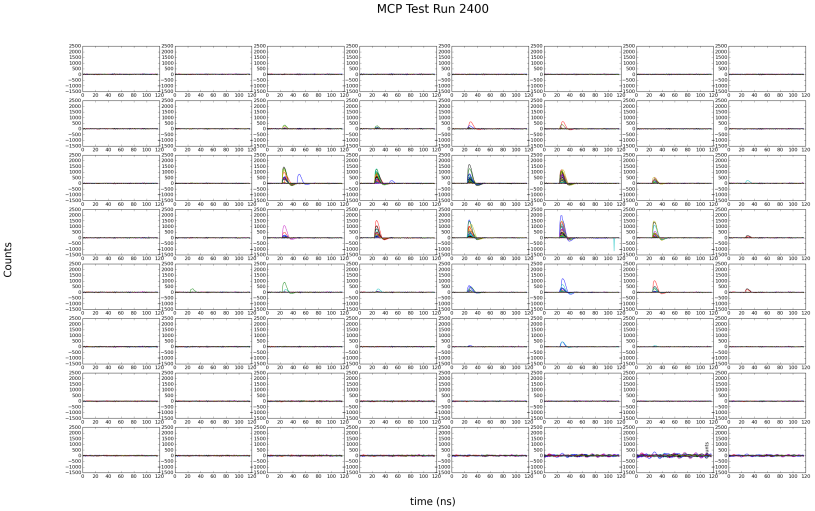

(a) 200.

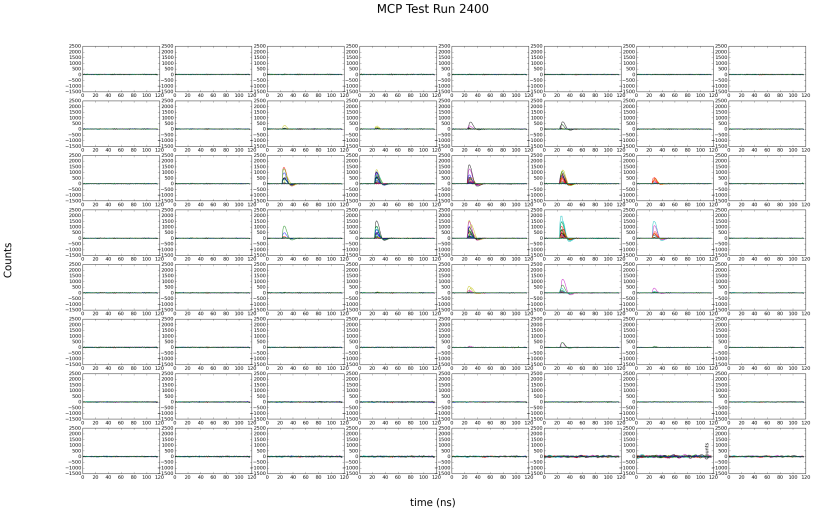

(b) 300.

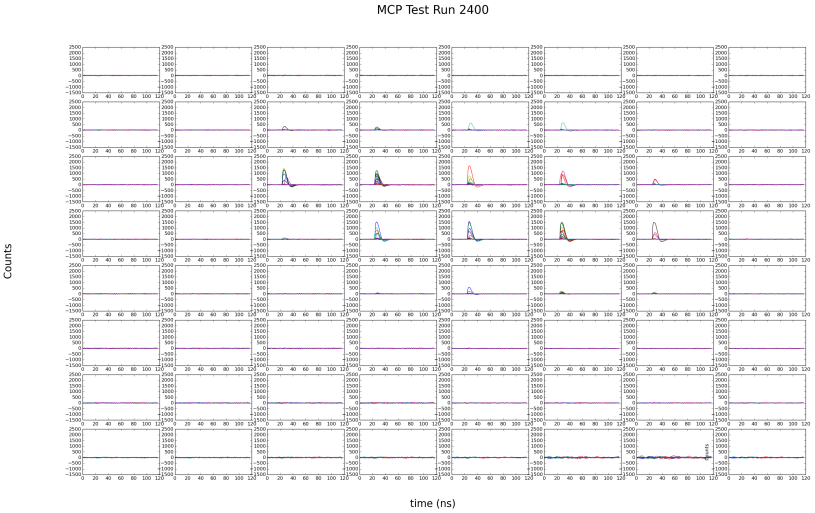

(c) 450.

Figure 2.123: 2-fiber tests, no pincushion. 2400 events in a run, three different threshold level shown. Figures are taken from [116].

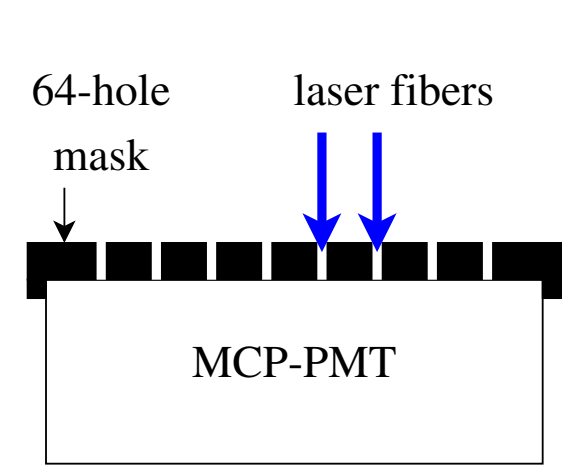

(a) Two fibers with pincushion.

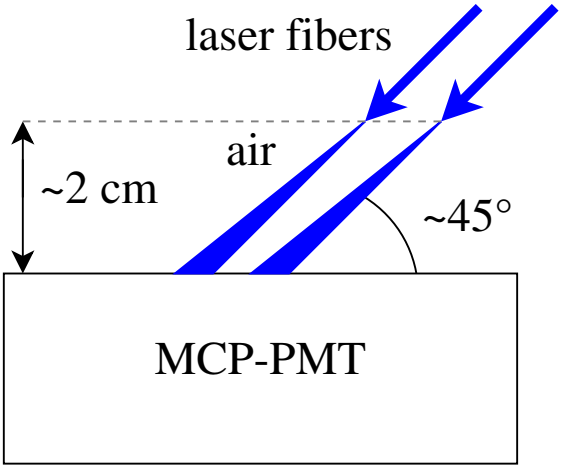

(b) Two fibers, with no pincushion.

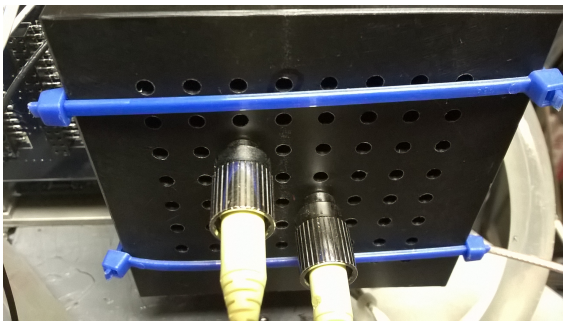

(c) Two fibers with pincushion.

(d) Two fibers, with no pincushion.

Figure 2.124: 2-fiber tests. Photographs and diagrams of the setup.

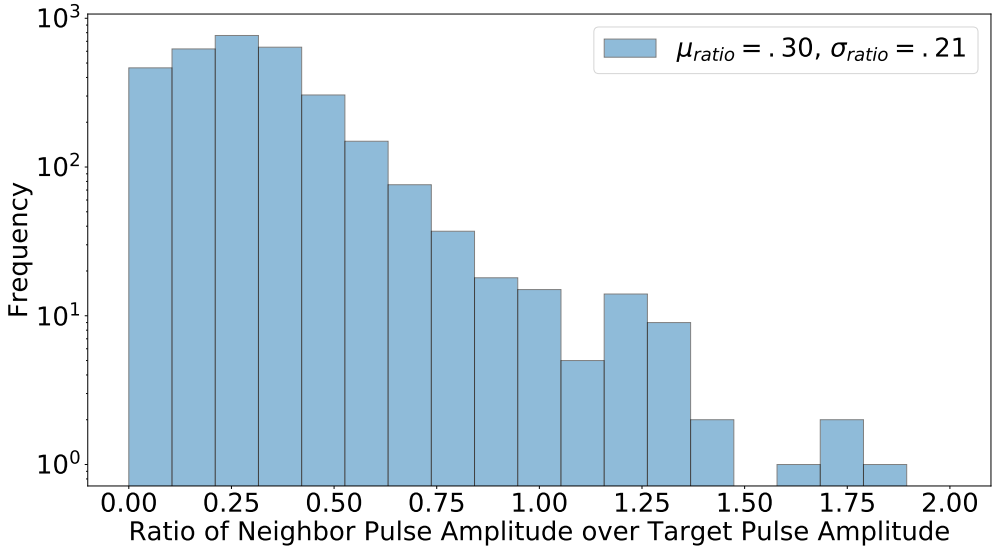

Figure 2.125: Relative amplitude histogram showing the ratio of activated neighbor pulses to the amplitude of the target pulse. We see that this ratio averages at a significant 30%. Figure and caption are taken from [98].

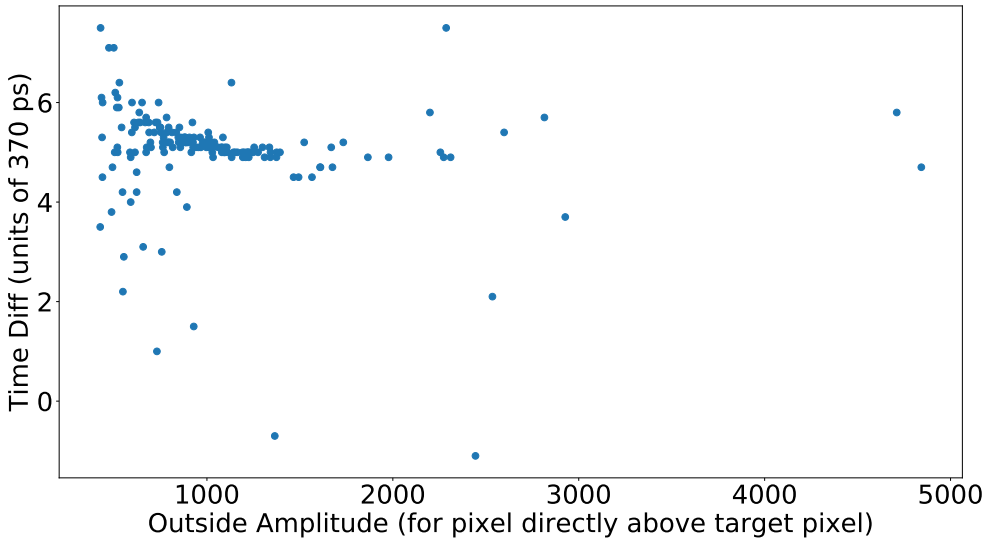

Figure 2.126: The time difference between the neighbor pulses and the target pulses plotted against the amplitude of that neighbor pulse. Any point that lands above zero on the y axis means that the neighbor pulse lagged in time. We see a general tendency for a small lag between the two pulse. The tendency for greater and more consistent lag increases with the amplitude of the neighbor pulse. The average time difference independent of amplitudes is 1.7 ns with a standard deviation of 1.1 ns. Figure and caption are taken from [98].

2.9.1 Ion-feedback

Another feature of MCP-PMTs is that there is always a chance that, along with electrons, there will be some ions produced in the porous MCP structure, shown in Fig 2.127. Those ions, usually having energies in keV region, would propagate in the opposite direction to the electrons in the electric field with a chance of escaping the MCP, and flow back to it, causing a delayed signal being read out on the multi-anode. The delays can vary from a few nanoseconds to a few microseconds. It is relatively hard to cure this problem. The good thing about these delays is that they are not usually correlated among multiple MCP-PMTs or even among multiple groups of pixels within one MCP-PMT.

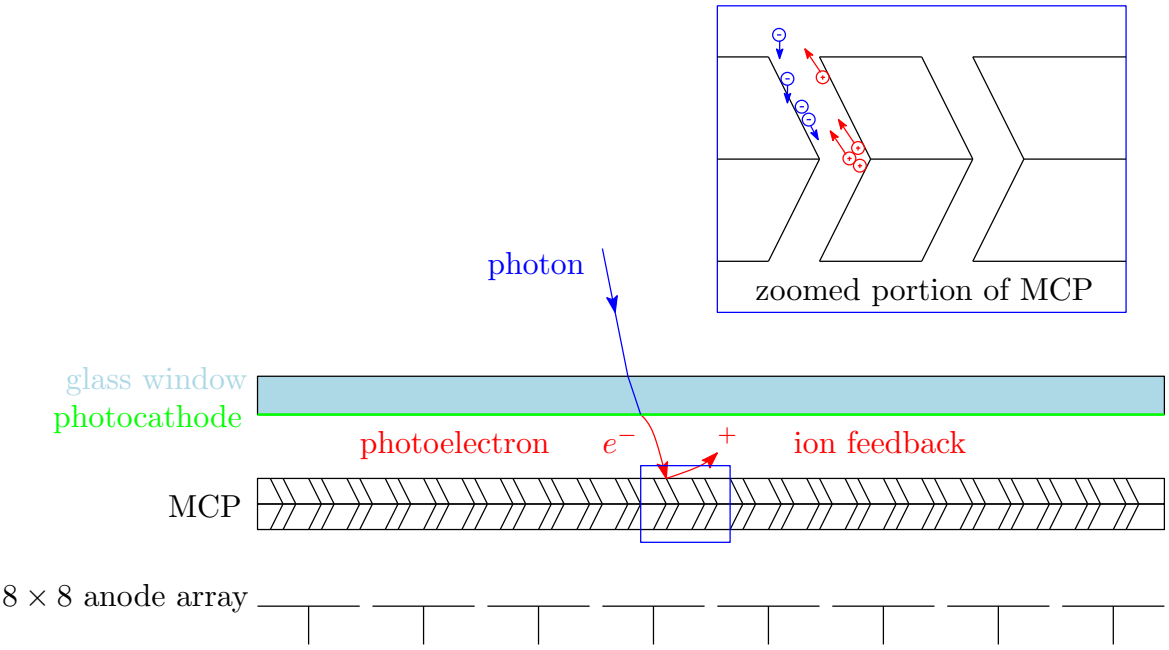

Figure 2.127: MCP-PMT diagram showing ion feedback effect.

2.10 Reactor

After considering other deployment locations, shown in Table 2.18, San-Onofre and a naval reactor, we choose the NIST research reactor [117, 118]. It has a compact split core that usually runs at 20 MW thermal power. There is no electrical power generated. 30 fuel elements, each containing 2 segments of highly-enriched uranium fuel U_3O_8/Al (^{235}U, 93% enrichment), are submerged in heavy water which serves as a moderator and coolant. The upper and lower fuel segments, each 27.9 cm high, are separated by a 17.8 cm unfueled gap which serves as a "flux trap" to minimize the fast-neutron and gamma backgrounds in the neutron beam lines. The overall dimensions of the core are 1.12 m in diameter by 0.74 m in height. The NIST reactor cycle is 38 days on, 10 days for refueling, with the reactor schedule known in advance [119]. Fig. 2.128 shows the spatial power distribution among the 60 fuel segments. The reactor is primarily used to conduct research using neutrons it generates. There are a few neutron guides coming from the reactor, which go to the experiments located in so-called guide hall. Everything is located in building 235 on the NIST campus in Gaithersburg, Maryland.

The reactor fuel is primarily pure ^{235}U (7% ^{238}U). Using a total thermal power of 20 MW_{th}, an average number of 6 $\bar{\nu}_e$ produced per fission, with only ~ 1.5 $\bar{\nu}_e$ (or one in four neutrinos) are above IBD threshold, and with the thermal energies released per fission of ^{235}U and ^{238}U, one can roughly estimate the total number of neutrinos produced at the reactor core to be $\sim 3.7 \times 10^{18}$ $\bar{\nu}_e/s$:

$$N_{235} = 0.93 \times 6\bar{\nu}_e/\text{fission} \times 20 \text{ MW}/(201.7 \text{ MeV/fission}) = 3.45 \times 10^{18} \ \bar{\nu}_e/s \quad (2.17)$$

$$N_{238} = 0.07 \times 6\bar{\nu}_e/\text{fission} \times 20 \text{ MW}/(205.0 \text{ MeV/fission}) = 2.55 \times 10^{17} \ \bar{\nu}_e/s \quad (2.18)$$

This corresponds to a flux of $\sim \ 1.6 \times 10^{12}$ cm^{-2} s^{-1} $\bar{\nu}_e$ at the miniTimeCube location ~ 4.3 m away from the center of the reactor core, Fig. 2.132. It further corresponds to a number of antineutrino interactions with ^{1}H via IBD reaction in the plastic scintillator on the order of a few events per day (see Table 2.18). Total number of antineutrino IBD interactions in the mTC scintillator per day:

$$N_{\bar{\nu}_e} = \frac{1}{4} n_{\text{H}} \ V \ \sigma \ \frac{dN_{\bar{\nu}_e}}{dt} \ \frac{1}{4\pi L^2} \ t_{\text{day}} \quad (2.19)$$

$$N_{\bar{\nu}_e} = \frac{1}{4} \frac{5.16 \times 10^{22}}{\text{cm}^3} \ 13^3\text{cm}^3 \ 5 \times 10^{-43}\text{cm}^2 \ \frac{1.6 \times 10^{12} \ \bar{\nu}_e}{\text{cm}^2 s} \ 86400s = 2 \ \bar{\nu}_e/\text{day} \quad (2.20)$$

Taking into account 40% detector efficiency for the mTC, the number of events is approximately one antineutrino per day:

$$2 \times .40 \approx 1 \ \bar{\nu}_e/\text{day} \quad (2.21)$$

More precisely, the total number of expected antineutrinos from the reactor observed in the detector is given by

$$N^{\text{obs}}_{\bar{\nu}_e} = \frac{N_p}{4\pi L^2} \int \epsilon_{det} P(\bar{\nu}_e \to \bar{\nu}_e) \frac{d\sigma(E_{e^+}, E_{\bar{\nu}_e})}{dE_{e^+}} \times \frac{d^2 N_{\bar{\nu}_e}(E_{\bar{\nu}_e}, t)}{dE_{\bar{\nu}_e} dt} dE_{e^+} dE_{\bar{\nu}_e} dt, \quad (2.22)$$

where N_p is the number of hydrogen atoms in the scintillator ("free protons"); L — the distance between production and detection points of the antineutrino, Fig. 2.130; ϵ_{det} — detector efficiency ~ 40 % based on MC simulations for IBD detection in the mTC; $P(\bar{\nu}_e \to \bar{\nu}_e)$ — survival probability of electron antineutrino [36, 120]; and $\frac{d\sigma(E_{e^+}, E_{\bar{\nu}_e})}{dE_{e^+}}$ — differential cross section of the IBD process as a function of positron energy E_{e^+} and antineutrino energy $E_{\bar{\nu}_e}$ [72].

The antineutrino differential energy distribution in Eq. (2.22) depends primarily on the fuel and on the reactor antineutrino flux model, Eq. (2.23):

$$\frac{d\dot{N}_{\bar{\nu}_e}}{dE_{\bar{\nu}_e}} \cong \sum_i \frac{W_{\text{th}}}{\sum_j f_j(t) E_j} f_i(t) S_i(E_{\bar{\nu}_e}, t) c_i^{\text{oe}} + S_{\text{SNF}}(E_{\bar{\nu}_e}, t) \tag{2.23}$$

where $i = {}^{235}\text{U}$, ${}^{238}\text{U}$, ${}^{239}\text{Pu}$ and ${}^{241}\text{Pu}$ (the four main isotopes), f_i — fission fraction, E_j — thermal energy per fission released, c^{oe} — off-equilibrium corrections [121], and S_{SNF} — spectra of antineutrinos emitted from spent nuclear fuel.

Before installing by the reactor, we had a set of test runs in the guide hall where the shielding cave was first assembled. A special extension panel and a cable tray were installed in order to have a possibility of installing longer cabling, including data and laser calibration fibers, shown in Figs. 2.133 and 2.143.

Parameter	NIST	San-Onofre	NPS
Power, GW_{th}	0.02	3	1.1
⟨Baseline⟩, m	5	25	10
Fuel	HEU	mixed	HEU
Fuel cycle, on/off days	38/10	–	–
Compact core	☑	☐	☑
⟨Event rate⟩, $\bar{\nu}_e$/ day	~ 1	~ 10	~ 20

Table 2.18: mTC at potential deployment sites.

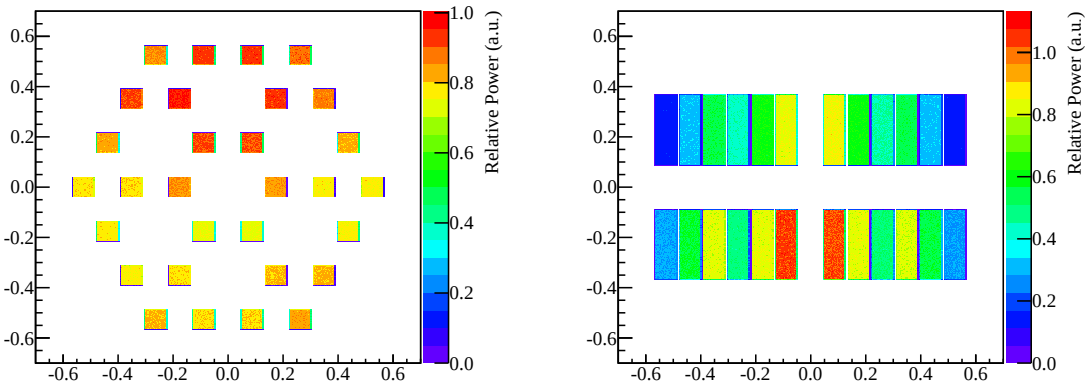

Figure 2.128: Power distribution in the NIST nuclear reactor. Figure is taken from [122].

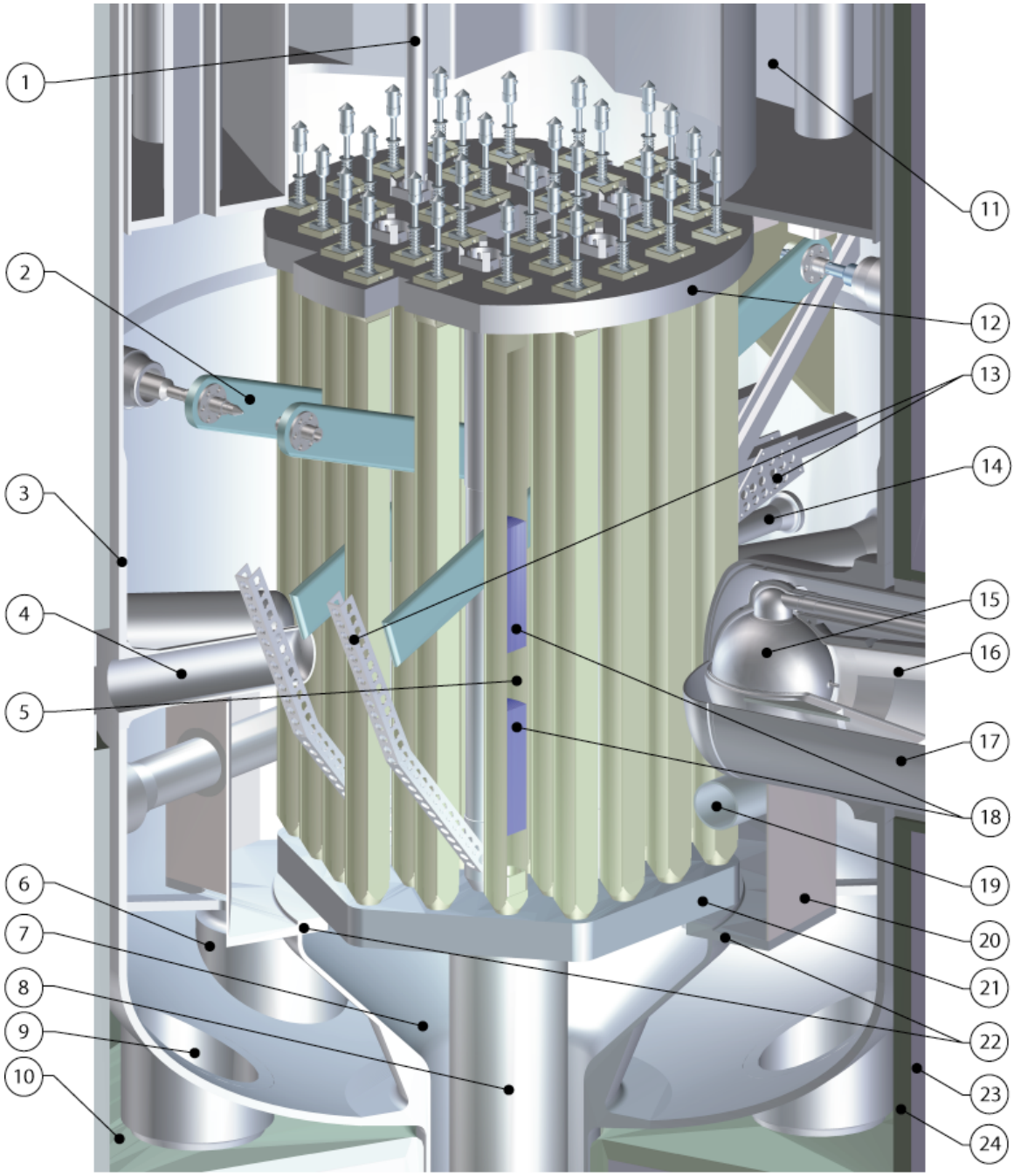

Figure 2.129: CAD snapshot of NIST reactor showing its main components. Courtesy of the NCNR.

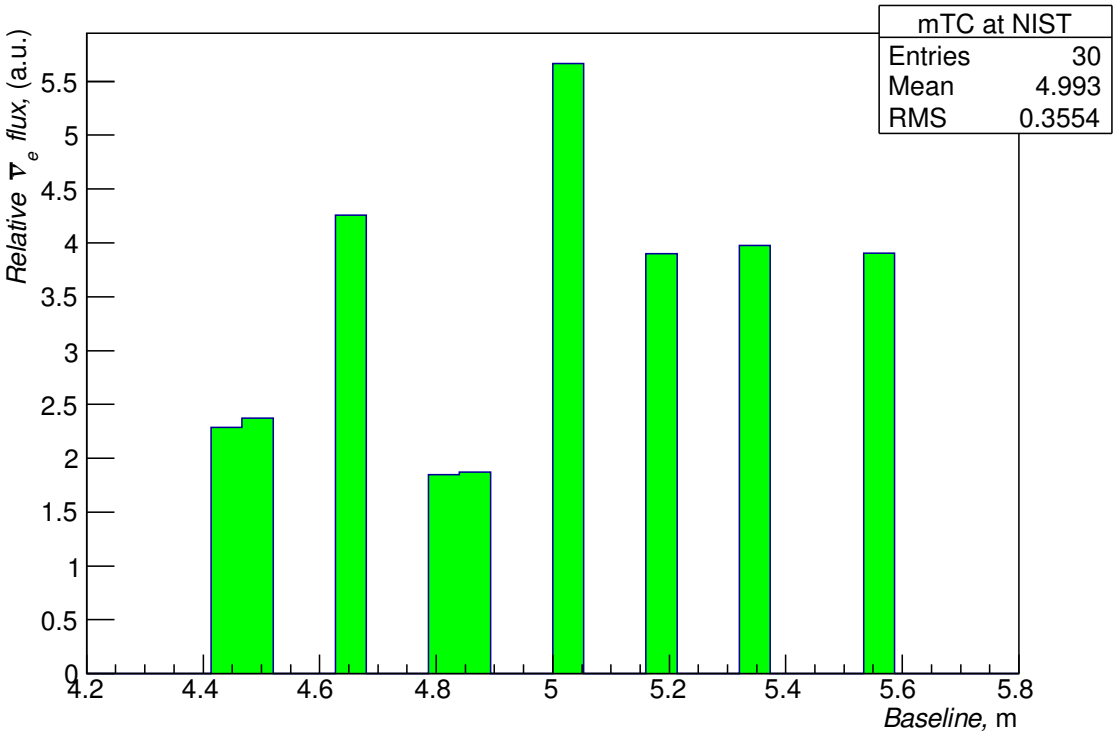

Figure 2.130: Relative electron antineutrino flux vs baseline at an mTC location 5 m away from the center of the NIST reactor core.

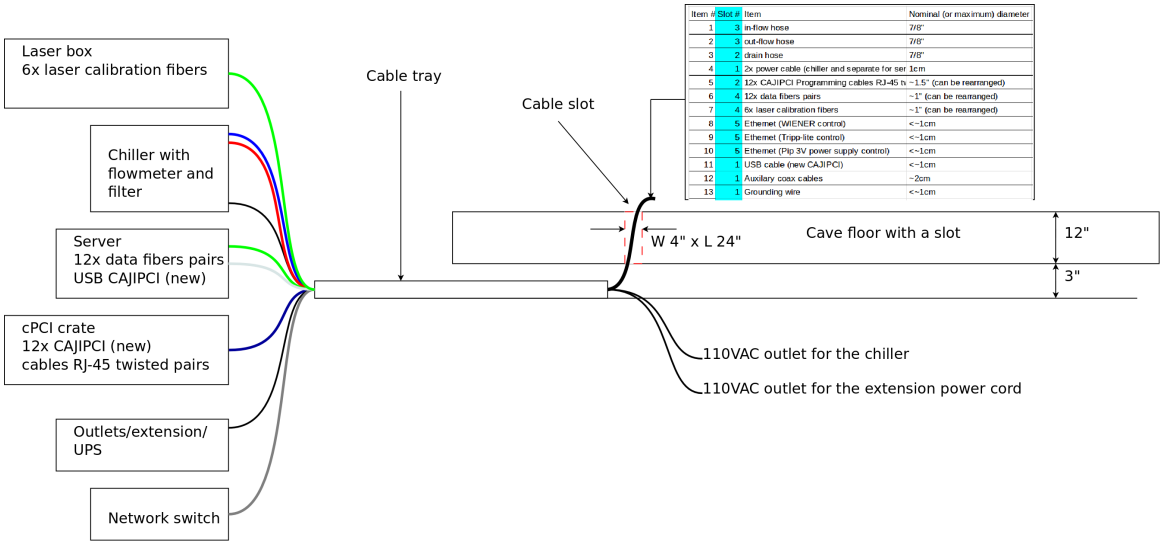

Figure 2.131: Diagram showing different links going into the mTC cave.

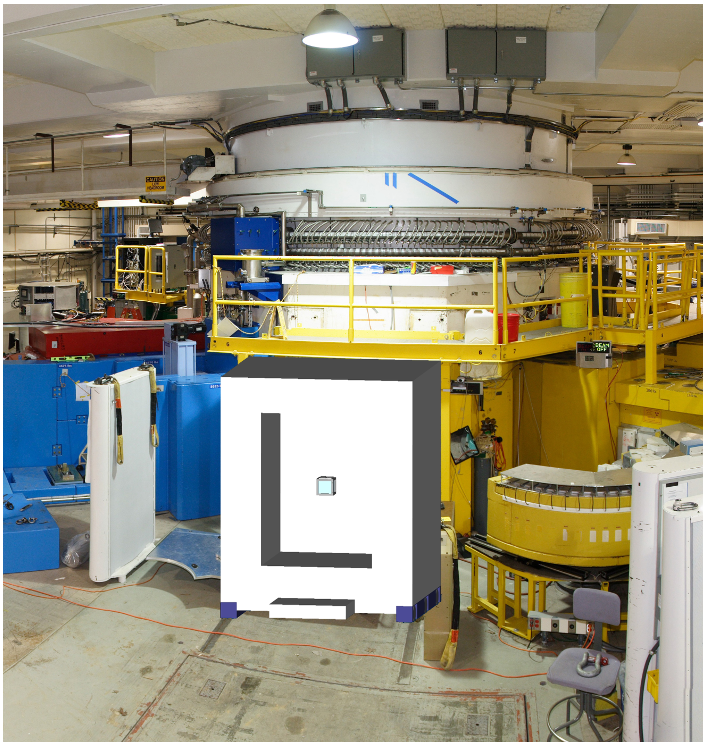

Figure 2.132: Photograph of the location next to the reactor with a diagram of the mTC cave and the scintillator cube added.

Figure 2.133: An extension panel.

2.10.1 Overheating accident before final installation

The absence of a fully functional interlock system allowed the mTC to overheat due to a sudden failure of the refrigeration unit in the chiller system. The accident took place on March 10th 2016. The mTC interlock system is schematically shown in Fig. 2.134. The ASIC temperatures reached temperatures close to 80–100°C, and the sealant on a few MCP-PMTs melted, causing loss of vacuum. We tried to recover some of the tubes.

The dead tubes turned out to be from the batch graded for 50°C maximum operational temperature. In consultation with Photonis, we believe that vacuum seals failed. Some tubes became flashers. On some tubes, the current fluctuations would usually be present, with the current sometimes exceeding the limit set on power supply, which would cause an automatic shutdown of the HV channel. More MCP-PMTs gradually became non-operational, as Fig. 2.136 best illustrates it. If we had known the scale of the problem, we would not have installed the detector by the reactor.

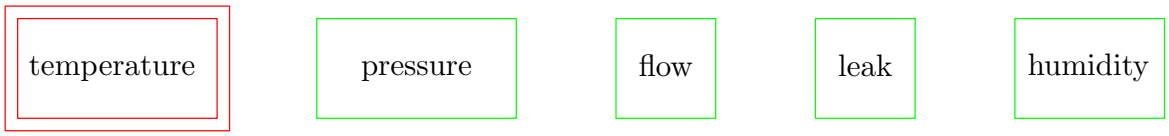

Figure 2.134: Lack of temperature interlocks led to the overheating disaster.

Although we didn't notice deterioration of the system immediately after the second overheating accident, which happened in the middle of summer, it likely also contributed to the overall degradation of the PMTs.

Fig. 2.135 shows only 7 remaining working MCP-PMTs a year after the accident. Bad electronics channels are also shown on those working tubes.

Four MCP-PMTs (# 5, 8, 11, and 13) were produced with an 80°C eutectic vacuum seal. All remaining PMTs were produced after a process change to 120°C material [99]. It is consistent with our observations. Those four tubes were completely dead right after the accident.

Table 2.19 is an excerpt from the e-log dated 3/31/16, when we tried to recover some of the tubes and did measurements of the resistances.

ID	AB	AC	BC	Status
1	∞	∞	40M	OK
2	∞	∞	40M	OK
3	∞	∞	∞	OK
4	∞	∞	∞	Trips, in an unusual way when others are connected
5	44k	50M	50M	Trips, probably vacuum leak
6	∞	∞	50M	OK
7	∞	∞	32M	OK
8	44k	22k	22k	Trips, probably vacuum leak
9	∞	∞	50M	OK
10	∞	∞	52M	OK
11	44k	10M-50M	50M	Trips, probably vacuum leak
12	∞	∞	∞	OK
13	45k	35M	45M	Trips, probably vacuum leak
14	∞	∞	28M	Trips
15	∞	∞	42M	Okay, tripped in a run earlier
16	∞	∞	52M	OK
17	∞	∞	∞	Trips
18	∞	∞	∞	OK
19	∞	∞	40M	OK
20	∞	∞	47M	OK
21	∞	∞	∞	OK
22	∞	∞	54M	OK
23	∞	∞	∞	Trips
24	∞	∞	32M	Tripped before, but now seemed recovered

Table 2.19: Resistance measurements and status of the tubes, as of March 31st 2016. A — cathode, B — MCP in, and C — MCP out.

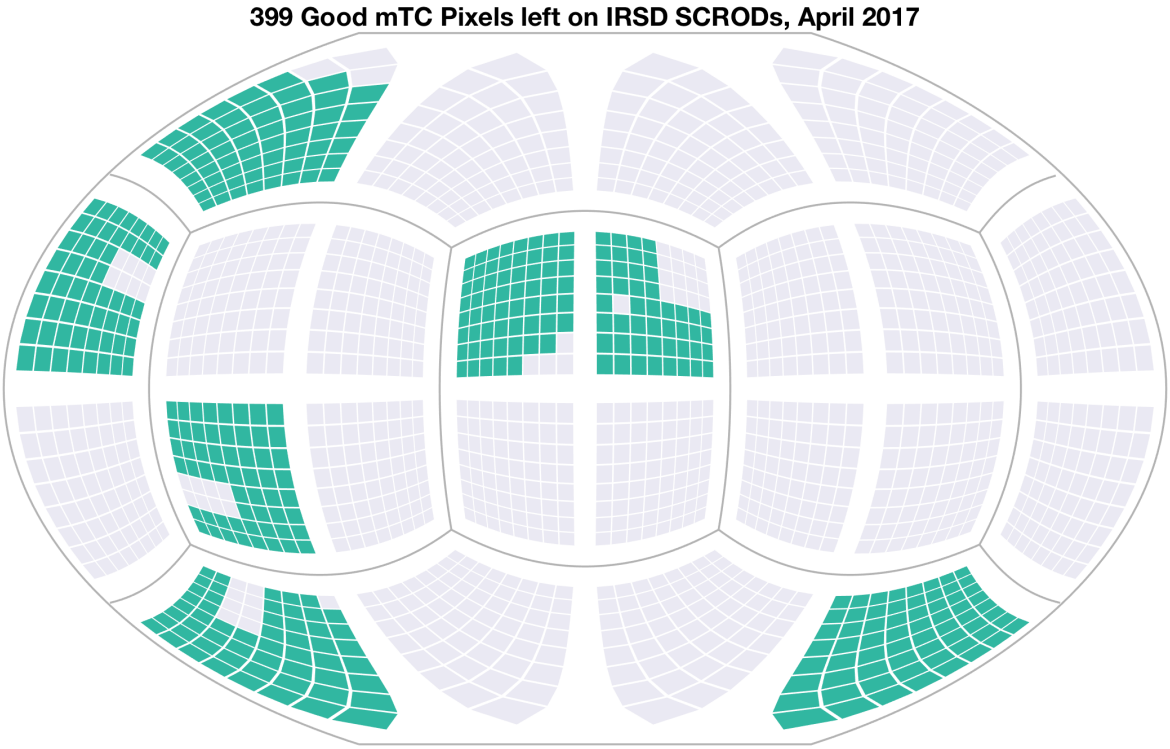

Figure 2.135: Remaining working channels. Figure is taken from [88].

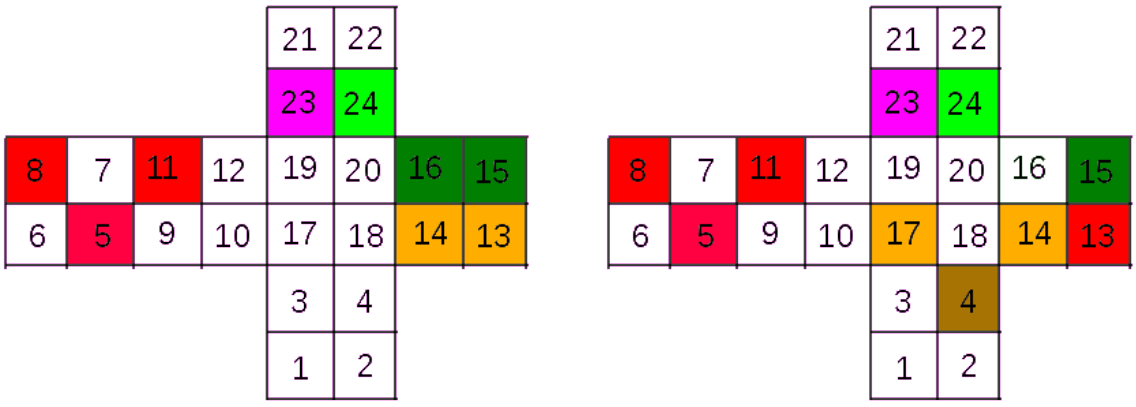

(a) March 24 2016. (b) March 31 2016.

Figure 2.136: Open-cube diagram showing the status of the tubes, one week apart. Color represents the severity: red being most severe, pink — trips with no apparent reason, brown and orange — current fluctuations, green — possibly recoverable tube (note tube 16).

2.10.2 Remote operations and high trigger rates

For slow control, we transitioned from a bash script to an improved GUI interface, shown in Fig. 2.137. Behind the GUI buttons, relatively complex routines are hidden. Every ten seconds, vital information about the instrument is dumped into a log file. A new log file initiates automatically every day and at system start-up. An example of a log file can be found in Appendix (Section A.6). In addition to real time monitoring systems, we also had a logger installed inside the cave to record environmental conditions, shown in Fig. 2.146.

During the first few days of running the mTC by the reactor, it became apparent that something was not well-understood about either our detector, the environment, or both. The trigger rates were extremely high and irregular, as shown in Fig. 2.139, along the detector's live time.

It turned out that it was not due to our detector's misbehaving but due to a neighboring experiment performing spectral scans at various positions. It is likely that those are primarily gammas, Fig. 2.150a. To lower the backgrounds, we installed additional layers of lead (to attenuate gammas) and put borated polyethylene pellets (to capture more background neutrons) into the cave slot. That had little effect on the rates.

The trigger rates were way far above the expected rates in the cave [85]. Even if we had had full working photocoverage and excellent timing, we would not have been be able to reconstruct IBD events.

Fig. 2.150a shows the gamma rate, averaged over 10 minutes, in a gamma detector GammaTracer (GF1414), which was placed between the location of the shielding cave and the MACS instrument at the approximate neutron beam height. Uranium and thorium decay chains in concrete with the exception of the 1115-keV gamma from ^{65}Zn (which has a 244 day half-life and thus persists through reactor refueling cycles) are primary gamma backgrounds during reactor off cycles, as shown in Fig. 2.149a. The cave suppresses the thermal neutron background by a factor of $\sim 40,000$. Table 2.21 represents the thermal neutron flux data collected using the Radpack-GC detector (Sensor Technology Engineering Inc.) inside and outside the cave during reactor on/off periods. It also shows that *inside* the cave there is a difference by a factor of 2–5 between reactor on/off periods. Both experiments, MACS and BT-1, adjacent to the mTC, cause large fluctuations in background rates at the mTC location inside the cave [123].

Dominant backgrounds were gamma and neutrons generated by the neighboring experiments. The cosmogenic muon-generated ^{8}Li and ^{9}B isotopes that could mimic IBD events were almost negligible according to our simulations, as shown in Figs. 2.152.

Fig. 2.154 shows power of the NIST reactor and AB trigger rates as a function of time during the deployment period. There were a few "quiet" periods with reactor ON when the rates were low. Overall, the signal to noise ratio for neutrino detection was $\sim 10^{-6}$.

Run	Operator	Date (ET)	Trigger	L0	$A_{\min}$	$A_{\max}$	$B_{\min}$	$B_{\max}$	$C_{\min}$	$C_{\max}$	PS	Reactor	CAT	Comments
695	Slava	7/21/2016	Laser	100	-	-	-	-				ON	8	Fiber 1.
696	Slava	7/21/2016	Laser	100	-	-	-	-				ON	8	Fiber 2.
697	Slava	7/21/2016	Laser	100	-	-	-	-				ON	8	Fiber 3.
701	Slava	7/21/2016	Ped	100	-	-	-	-				ON	7	Ped, 5V off, HV ON
861	Mark	7/26/2016	AB+C	100	200	768	15	60	650	768		ON	2	Continuing.
862	Mark	7/26/2016	AB+C	100	200	768	15	60	650	768		ON	2	Continuing.
863	Mark	7/26/2016	AB+C	100	200	768	15	60	650	768		ON	2	Continuing.
864	Mark	7/26/2016	AB+C	100	200	768	15	60	650	768		ON	2	Continuing.
865	Slava	7/27/2016	AB+C	100	200	768	15	60	650	768		ON	2	Continuing.
866	Slava	7/27/2016	AB+C	100	200	768	15	60	650	768		ON	2	Continuing.
867	Slava	7/27/2016	AB+C	100	200	768	15	60	650	768		ON	2	Continuing.
868	Slava	7/27/2016	AB+C	100	200	768	15	60	650	768		ON	2	Continuing.
869	Slava	7/27/2016	AB+C	100	200	768	15	60	650	768		ON	2	Continuing.
870	Slava	7/27/2016	AB+C	100	200	768	15	60	650	768		ON	2	Continuing.
871	Ryan	7/27/2016	AB+C	100	200	768	15	60	650	768		ON	2	Continuing.
872	Ryan	7/27/2016	AB+C	100	200	768	15	60	650	768		ON	2	Continuing.
873	Ryan	7/27/2016	AB+C	100	200	768	15	60	650	768		ON	2	Continuing.
943	Kurtis	7/29/2016	AB+C	100	200	768	15	60	650	768		OFF	6	Continuing
944	Kurtis	7/29/2016	AB+C	100	200	768	15	60	650	768		OFF	6	Continuing
945	Kurtis	7/29/2016	AB+C	100	200	768	15	60	650	768		OFF	6	Continuing
2203	Kurtis	10/2/2016	AB+C	100	200	768	15	60	15	768		OFF	9	Run with ^{137}Cs
2204	Kurtis	10/2/2016	AB+C	100	200	768	15	60	15	768		OFF	9	Run with ^{137}Cs
2205	Kurtis	10/2/2016	AB+C	100	200	768	15	60	15	768		OFF	9	Run with ^{137}Cs
2570	Slava	5/2/2017	C	350					40	150	10		17	^{252}Cf with lead

Table 2.20: Excerpt from a run description log which has a couple of thousand different runs. Each run is on the order of a gigabyte in data on average (when running by the reactor). PS is a prescaler value (when the rates are too high we can set it to 10 or so). CAT is a category of runs for analysis purposes.

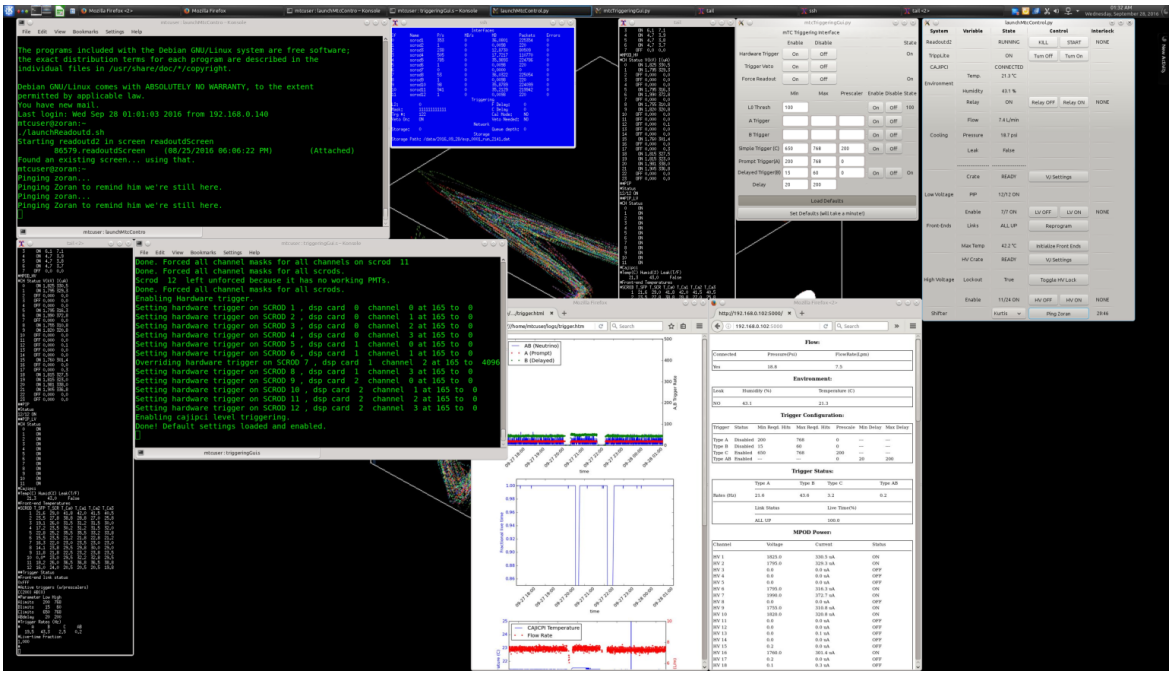

Figure 2.137: Operator desktop connected to the remote mTC control machine.

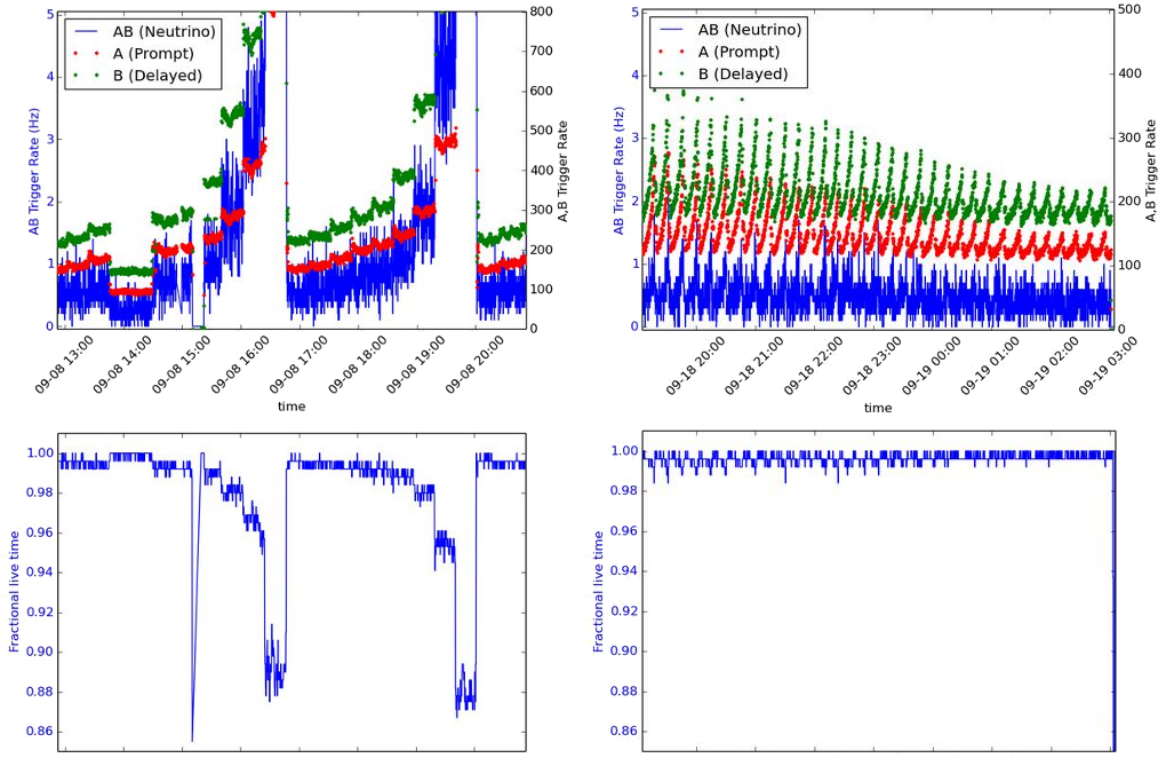

Figure 2.138: Examples of mTC rates by the NIST reactor. Top left: Irregular rates due to MACS, a neighboring spectroscopy experiment. Top right: Extremely high rates causing the detector live time to decrease by 10 %. Bottom row: corresponding detector live time.

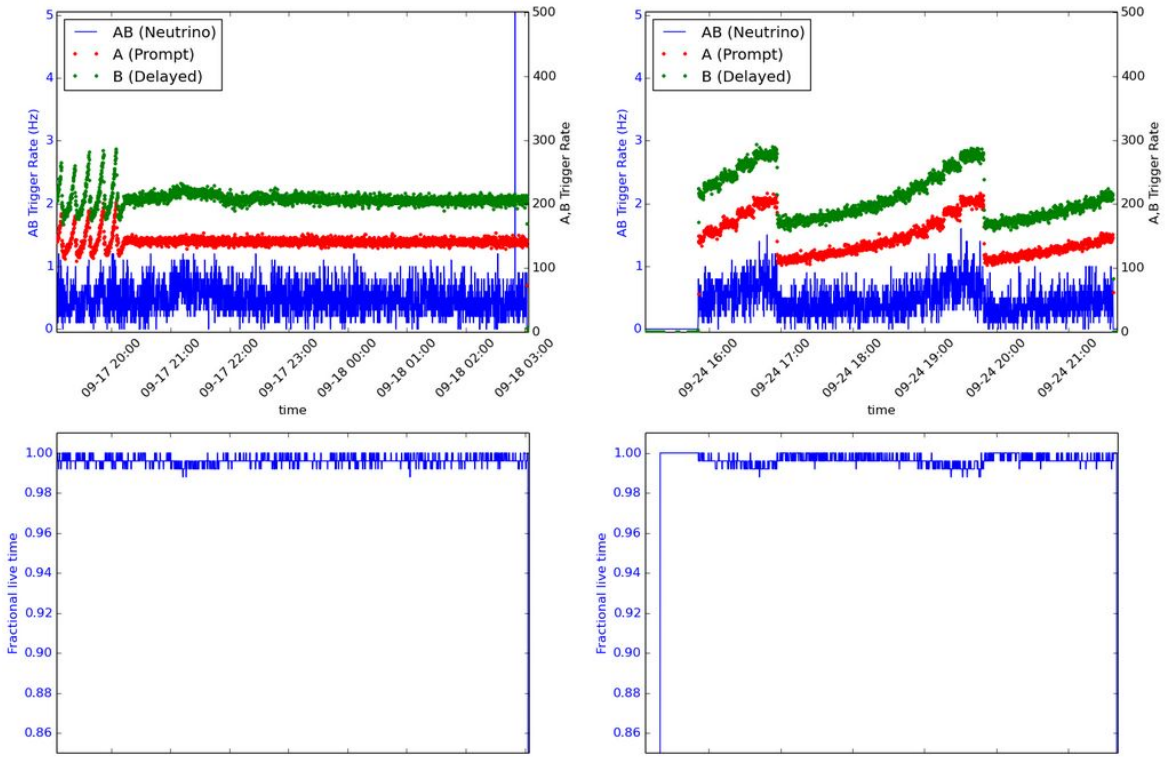

Figure 2.139: Top row: irregular rates (mTC start-up is on the right plot). Bottom row: corresponding detector live time.

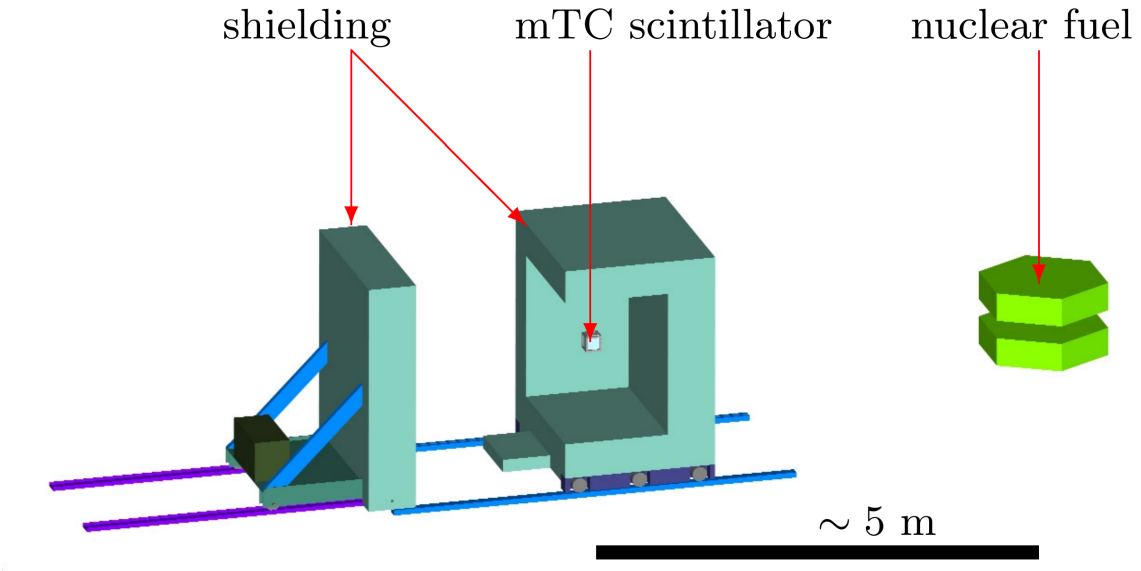

Figure 2.140: CAD snapshot of the cave (front side removed from the CAD for clarity) relative to the reactor core (4.3±0.1 m).

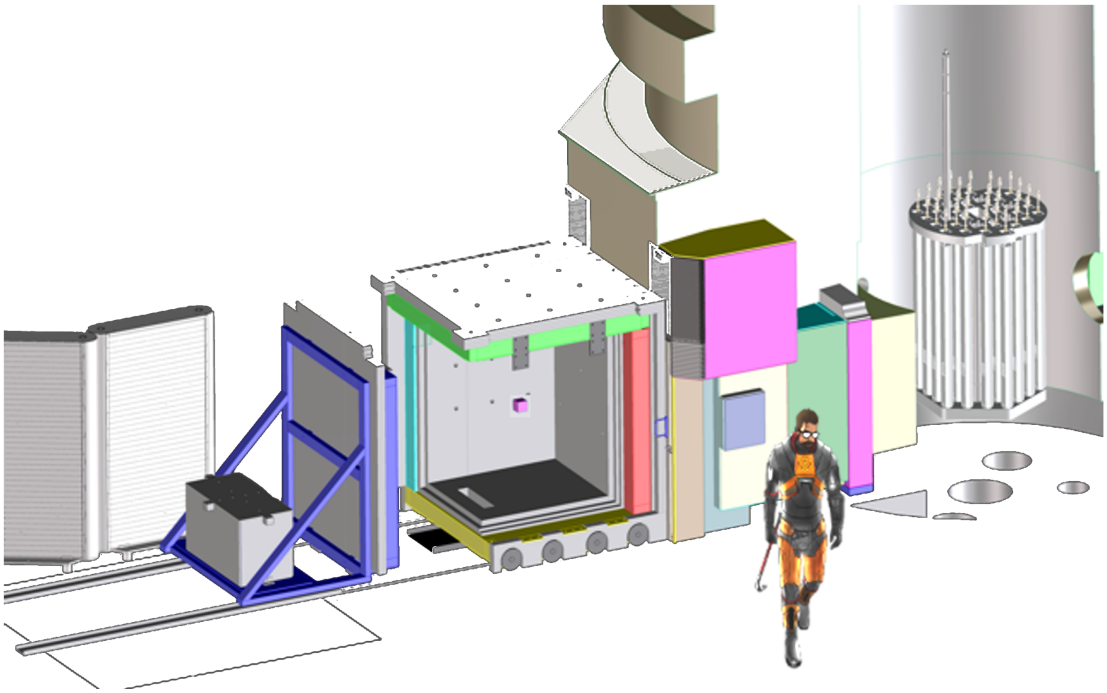

Figure 2.141: Detailed CAD snapshot of the mTC shielding cave and reactor surroundings, the pink cube in the center is the mTC scintillator.

Figure 2.142: Shielding cave after being installed by the reactor.

(a) The mTC main crate on its way to the shielding cave.

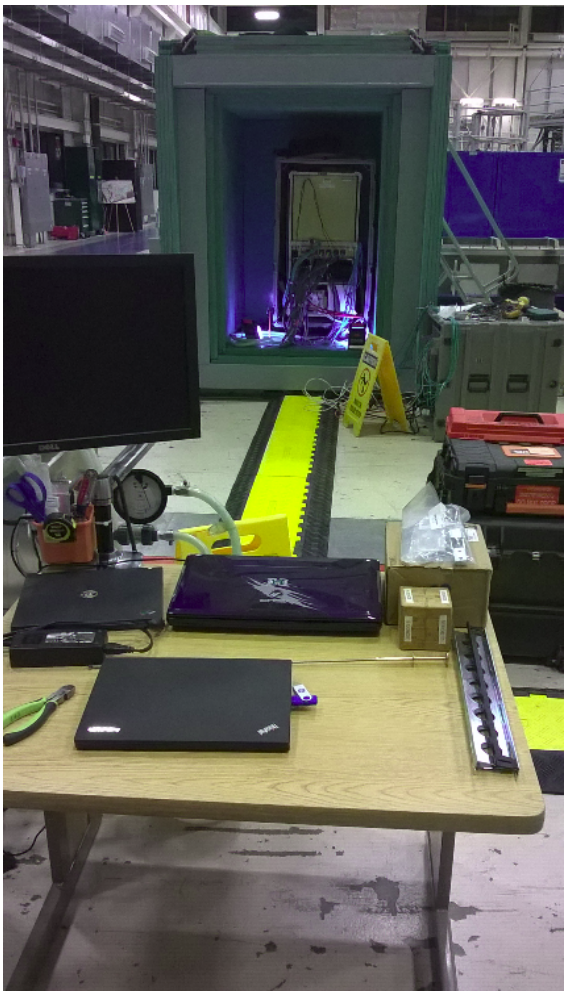

(b) mTC at the NIST guide hall. The yellow part is the cable tray.

Figure 2.143: mTC at NIST.

Figure 2.144: Modified shielding by the reactor, added lead and borated poly pellets.

(a) A special platform to slide the mTC.

(b) Cave closed.

Figure 2.145: mTC at NIST reactor.

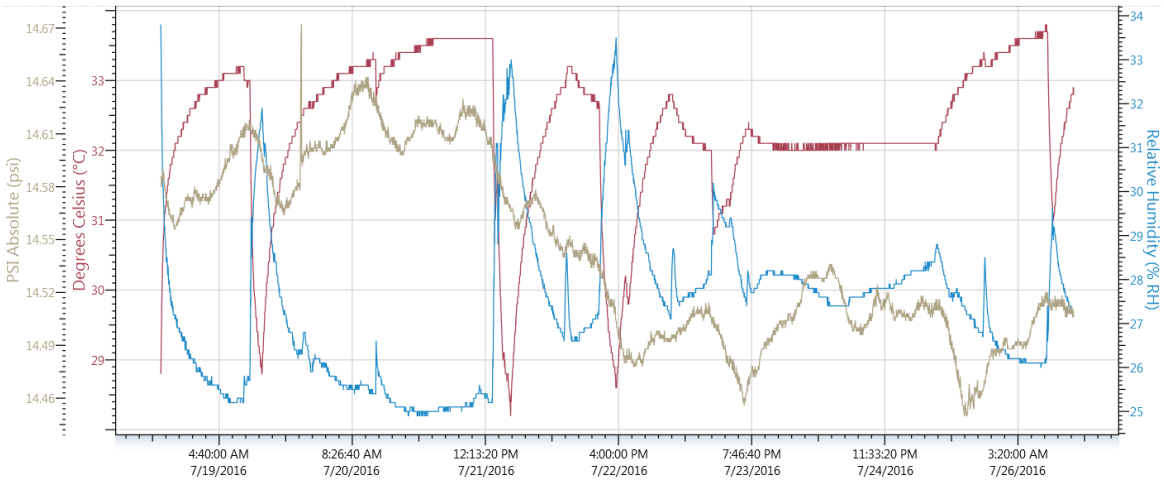

Figure 2.146: Logger installed in the cave reports air temperature, atmospheric pressure, humidity in the mTC shielding cave. Large drops are associated with cave door open. Day/night modulation is also visible.

Figure 2.147: mTC installed in the cave.

Reactor State	Measurement Location	Acquisition Length (s)	Measured Rate (s^{-1})	Flux ($n/cm^2/s$)
Off	Outside Cave	1800	1.03(2)	$3.64(8) \times 10^{-3}$
Off	Inside Cave	3600	0.031(3)	$3.8(4) \times 10^{-5}$
Off	NCNR break area	1800	3.26(4)	$1.15(2) \times 10^{-2}$
On	Outside Cave	600	5870(3)	7.082(4)
On	Inside Cave	3600	0.16(1)	$1.9(1) \times 10^{-4}$
On	Inside Cave	1845	0.13(1)	$1.6(1) \times 10^{-4}$

Table 2.21: The measured count rates using the Radpack-GC thermal neutron detector and the associated calculated neutron fluxes. Table is taken from [123].

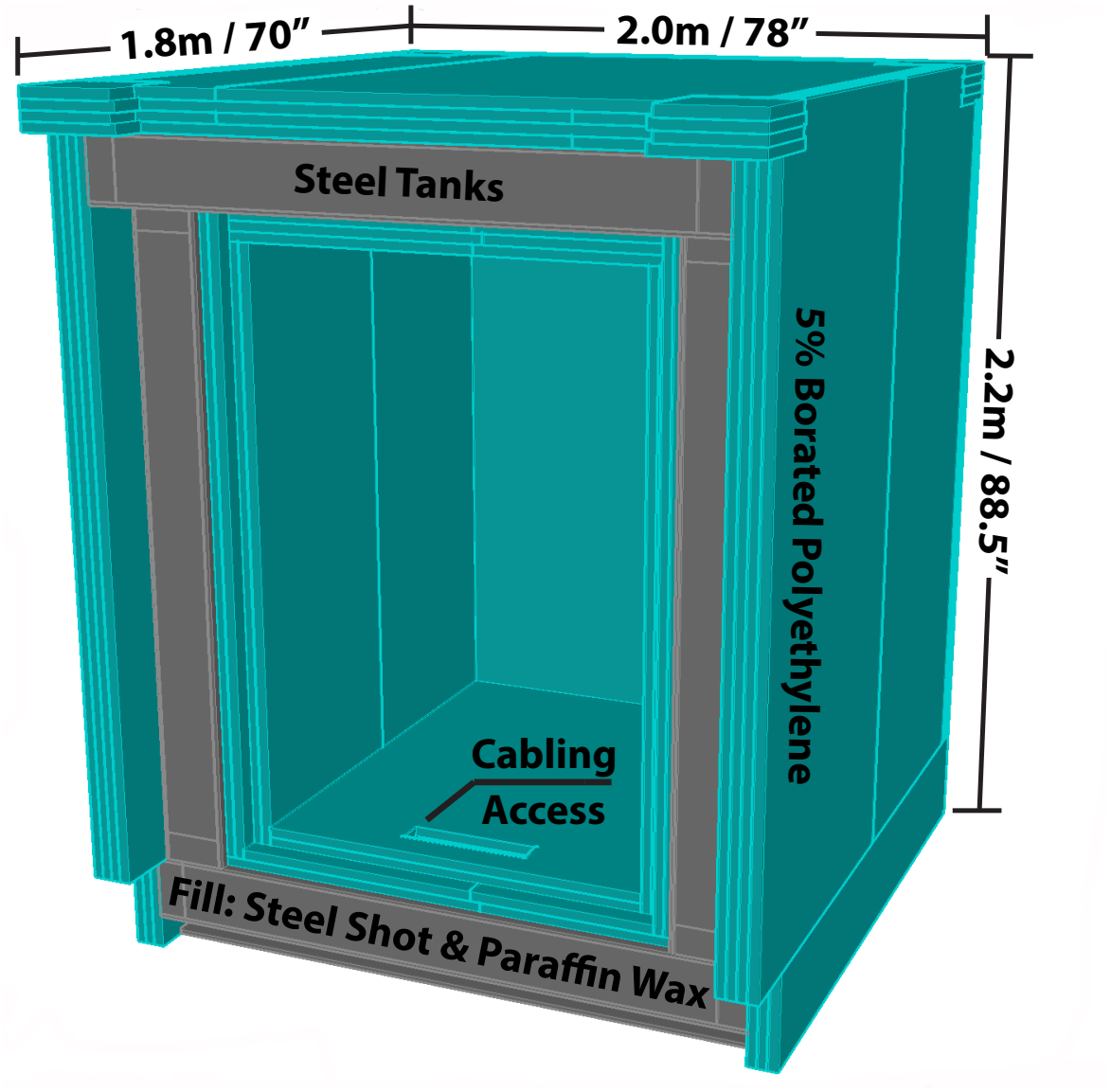

Figure 2.148: CAD snapshot of the cave. Layers labeled. Figure is taken from [123].

	Material	Dimension (cm)
1	Borated polyethylene	10
2	A36 steel	1
3	Steel shot & paraffin wax	15
4	A36 steel	1
5	Borated polyethylene	10

Table 2.22: From exterior to interior, composition and dimension of Cave layers. Polyethylene layer used is doped with 5% boron. Steel layer and steel shot is A36 steel. Steel shot & paraffin wax mixture comprised of 75% steel, 25% wax. Table is taken from [123].

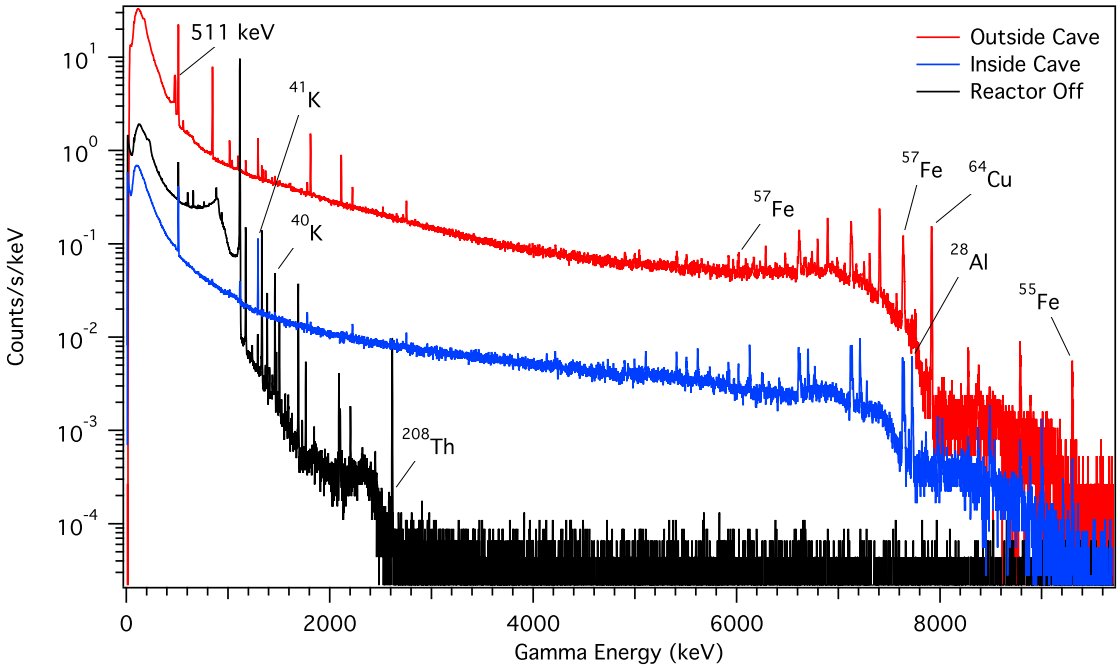

(a) Raw gamma spectrum acquired using a Canberra high-purity germanium detector model CPHA7.5-372000S.

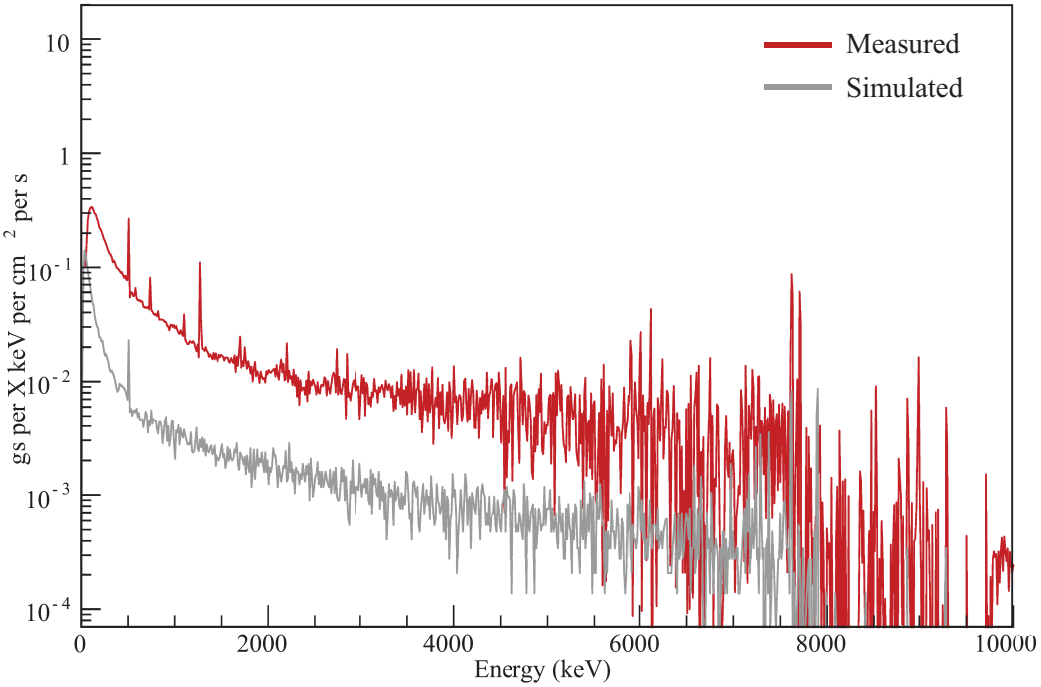

(b) Comparison of unfolded measured and simulated gamma spectra inside the shielding cave.

Figure 2.149: Gamma spectrum survey and simulations. Figures are taken from [123].

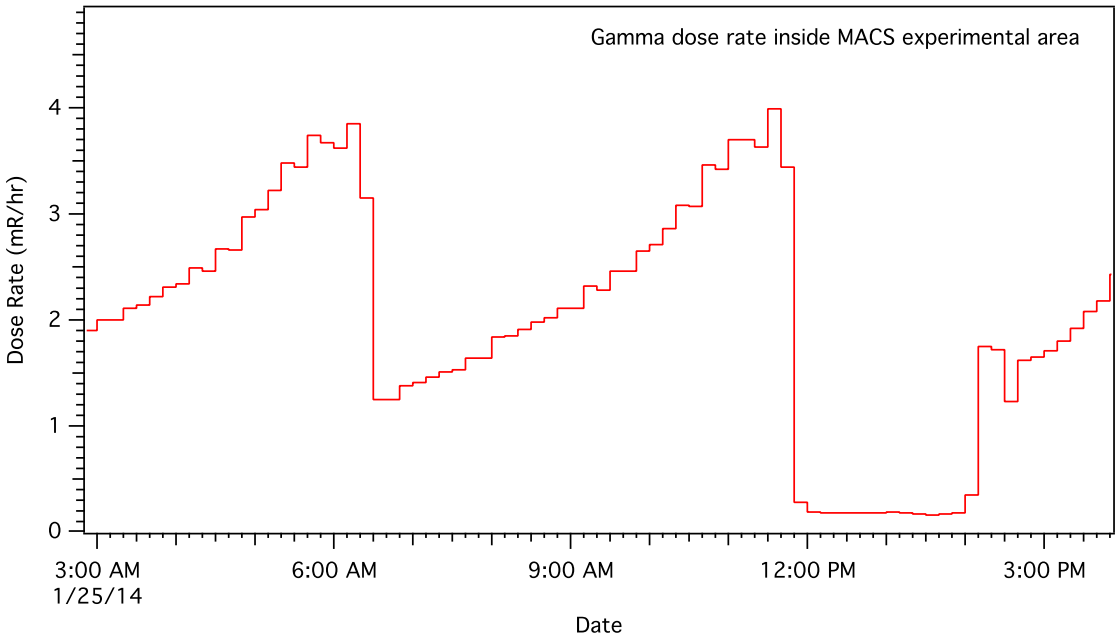

(a) Gamma rate vs time, fluctuations are due to sample position changes in the adjacent MACS spectrometer. Figure is taken from [123].

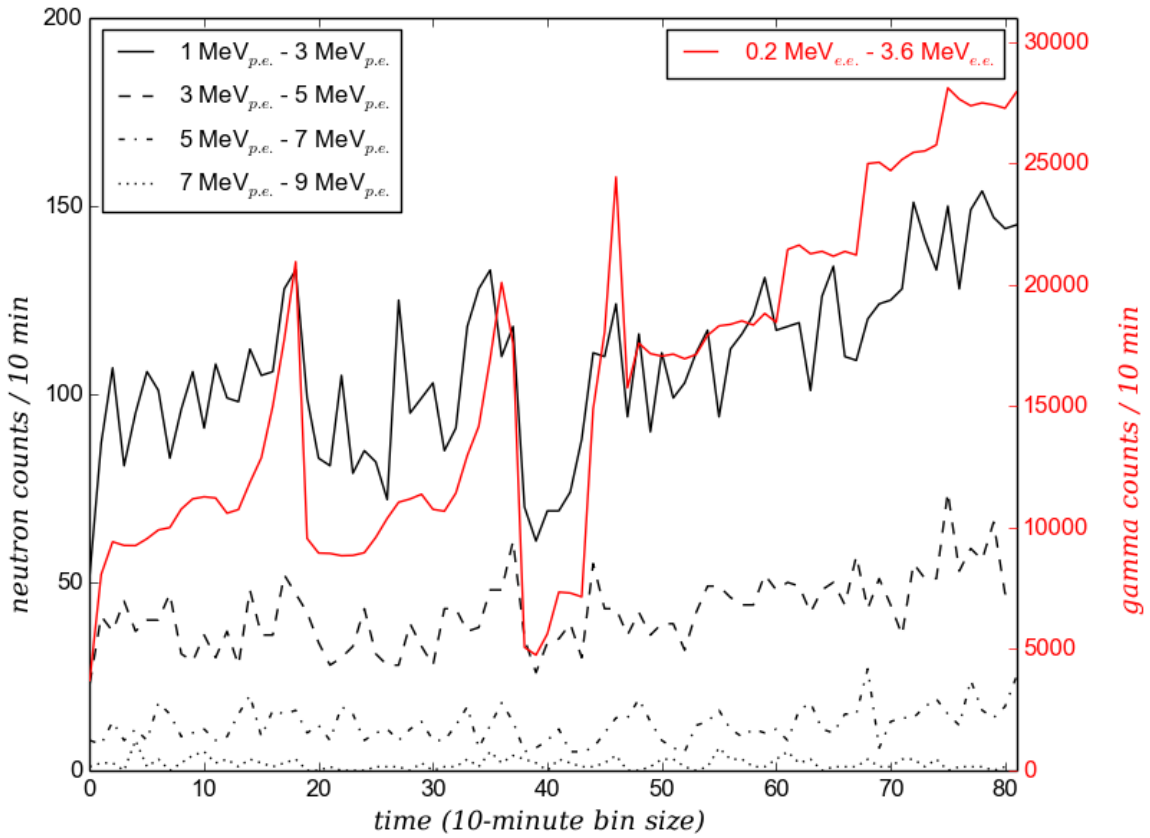

(b) Gamma and neutron count rates measured by a EJ-301 liquid scintillator detector (⊘ 20.32 cm × 20.32 cm) located in the cave during an "on" reactor state. Figure is taken from [123].

Figure 2.150: Gamma and neutron background rates as functions of time. Figures are taken from [123].

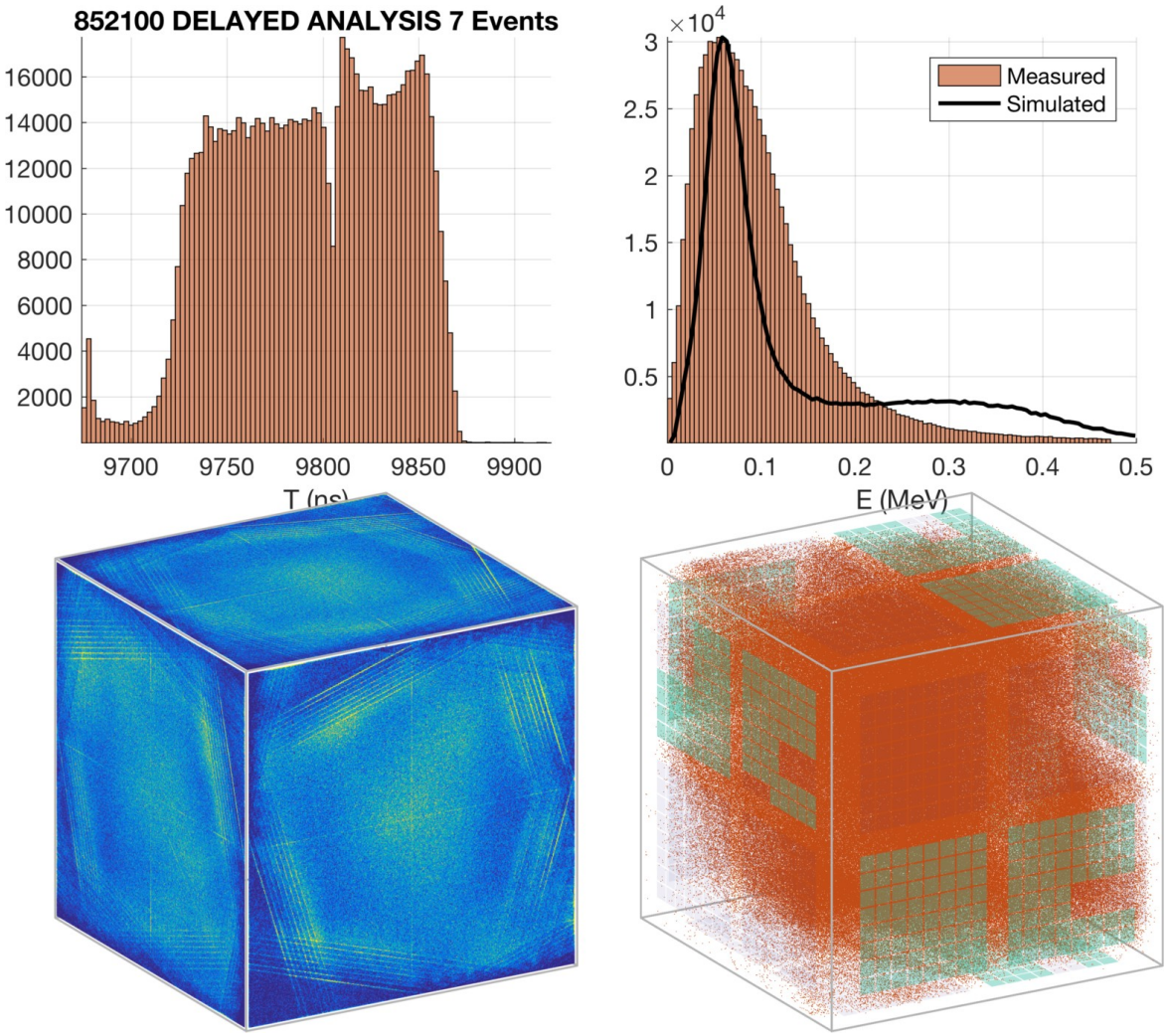

Figure 2.151: IBD and high noise.

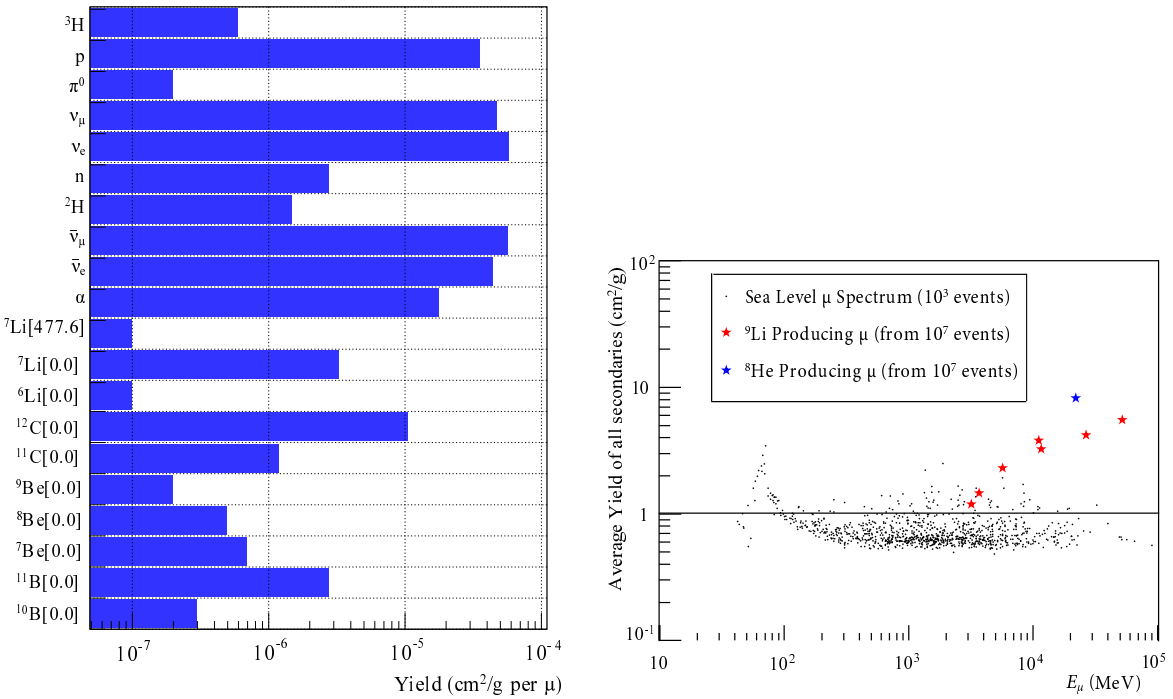

(a) Isotope yield using muon flux at sea level.

(b) Secondary yield vs energy.

Figure 2.152: Simulations of cosmogenic backgrounds that can mimic IBD event. Figures are taken from [85].

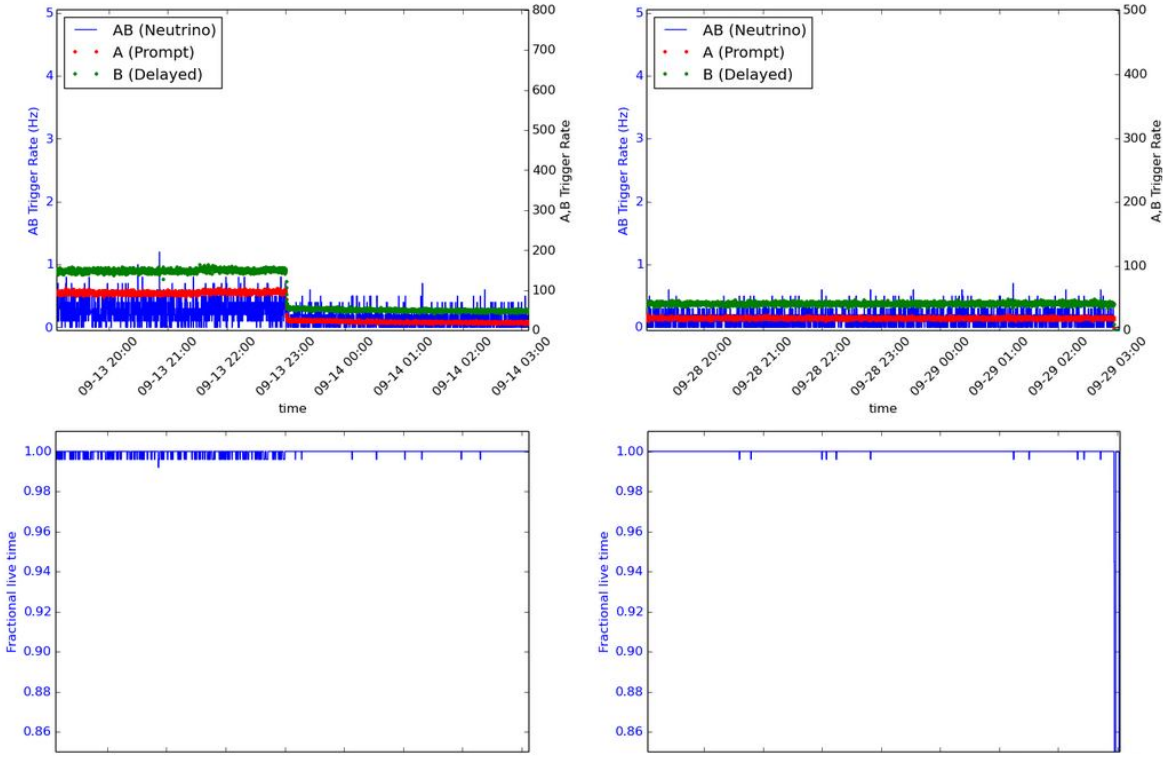

Figure 2.153: Stable rates, on a few occasions. *Top left*: right before the shutdown (drop in rates), and live time of the mTC. *Top right*: reactor was off, and so were neighboring experiments. Bottom set of plots show corresponding live time of the detector.

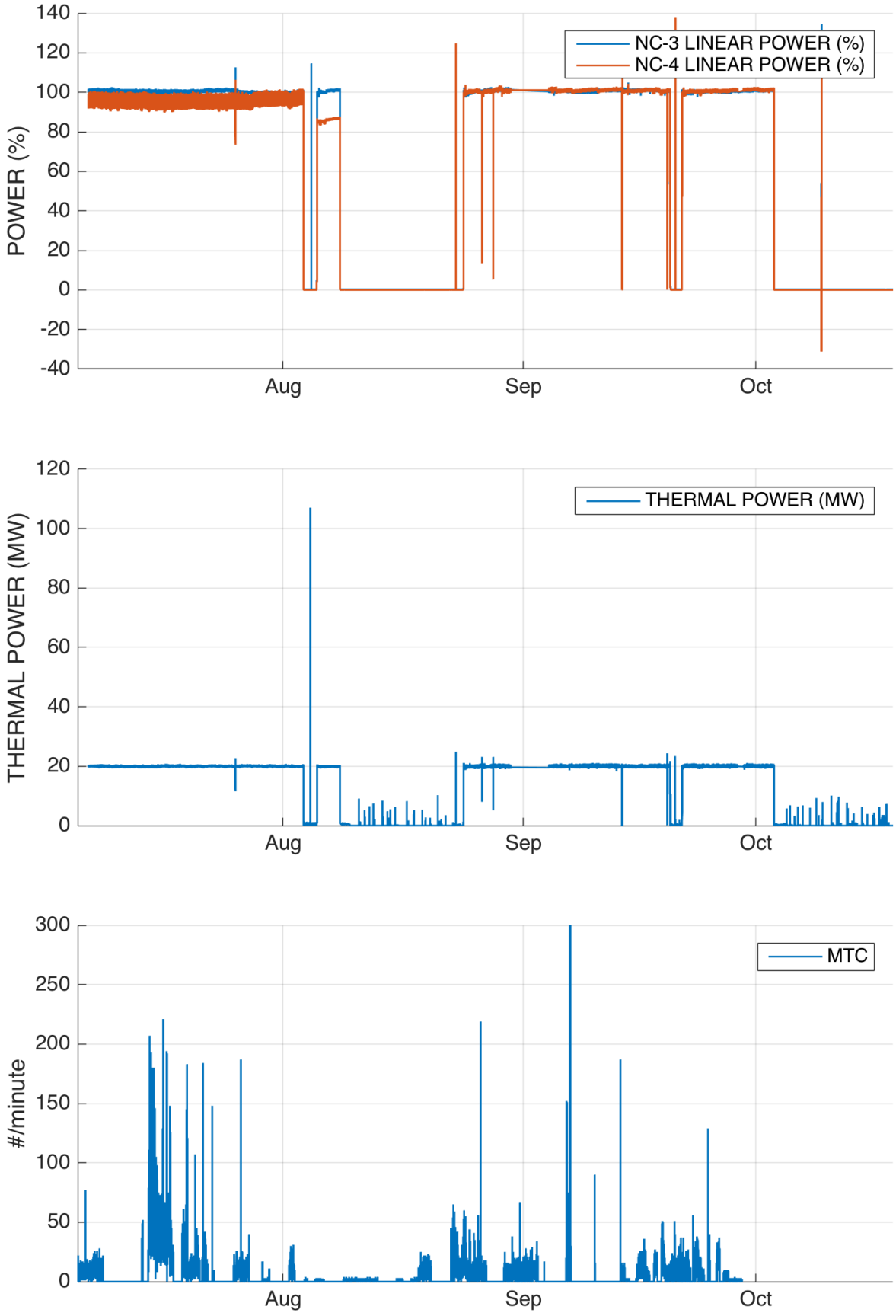

Figure 2.154: Reactor power and AB trigger rates as a function of time. The mTC was collecting data by the reactor July 13th – September 28th.

2.11 Summary

The miniTimeCube was built as a prototype. It is a monolithic scintillator small-volume movable detector that uses a novel technique of first photon arrival times, which was done through the fast-timing electronics and the geometry of many pixels. The temporal resolution and photo-coverage are unprecedented in such a small volume.

The mTC is a low-power and fully integrated multipurpose particle detector. The high density of channels of waveform photon detector on neutrino target (1536 total, ~ 5 mm square pixels) was achieved with the first-time use of compact PMT-mounted electronics for a neutrino experiment, without a huge bundle of cables and bulky electronics racks. It also is a first-time use of boron-doped plastic scintillator in a neutrino detector.

Although the mTC neutrino directional detection model was left unsubstantiated, vast knowledge and experience was gathered to incubate future small-volume detectors. One of the major outcomes of the mTC has been its ability to push existing technological bounds in neutrino detection. A wide range of components have been evaluated. We achieved reliable automated operations and swiftly activated remote operation capability.

The detector compactness and movable shielding is a crucial step forward in understanding neutrino oscillations at very short baselines. This dissertation presents an overview of the process, indicating the achievements and shortcomings in the pursuit of the original goal of detecting neutrinos and directional resolution. Manuscripts describing MCP-PMT performance, neutron tests, and backgrounds are in progress.

The mTC shielding and the electronics can be reused in future detectors, and we are already pursuing some projects built upon our experience.

2.11.1 Shortcomings

Although we haven't reached the ultimate goal of detecting antineutrinos from the NIST nuclear reactor, the miniTimeCube detector proved to be a good prototype detector. The major shortcomings were due to the inability to reach sub-100 ps regime, the loss of more than half the MCP-PMTs, and the unexpectedly-high background rates.

Despite these problems, the mTC is a good multipurpose prototype to study neutrons, gammas, and muons interacting in a small volume, as well as to perform laser calibrations of an array of MCP-PMTs.

2.11.2 Contributions

My personal contributions to the development of the mTC have a broad scope. I made significant improvements to the detector, building and upgrading the laser calibration system; discovering the cause, designing and fabricating copper frames to suppress the MCP-PMT cross-talk (first-time observed); performing neutron and gamma tests; and making MCP-PMT calibrations. My other significant contributions were multiple mechanical (dis)-assemblies of the detector at different locations, machining parts, building and maintaining the cooling system, performing MCP-PMT studies, and doing everyday maintenance of the detector — ranging from mechanical and electrical, data taking and processing, to software and network topics.

All of my experience, along with the experience as a group, will help us shape the next generation of compact detectors which are on the way.

2.11.3 Impact on future compact detectors

The mTC is the direct predecessor for NuLat and NeutronTimeCube (NTC) projects. Both, currently under construction, are using mTC electronics. The main difference from the monolithic mTC is that both detectors are segmented. Although the mTC electronics didn't have the timing performance desired for the mTC purposes, it shouldn't undermine the main goals in these experiments since they are both larger than the mTC.

NuLat is essentially a stack of ∼2.5-inch cubes. The NuLat prototype has $5 \times 5 \times 5$ cubes viewed by 150 2-inch conventional PMTs. The main scientific goals are a search for sterile neutrinos and a study of neutrino oscillations at very short distances. One of the potential deployment sites is at the NIST nuclear reactor, using the mTC shielding. NuLat is a merger between UH mTC and Virginia Tech LENS collaborations.

NTC is essentially a bundle of scintillating fibers viewed by SiPM arrays on each end. The main objective is a homeland security application to identify neutrons from special nuclear materials, with potential interesting physics being done. NTC is solely a University of Hawai‘i project, though we are now going with Sandia/NNSA for a larger effort.

Appendix A

Appendix

A.1 Reactor schedule

Period	Status
January 10 – February 19	operating
February 19 – March 1	shutdown
March 2 – April 11	operating
April 12 – April 26	shutdown
April 27 – June 6	operating
June 7 – June 21	shutdown
June 22 – August 2	operating
August 3 – August 17	shutdown
August 18 – September 26	operating
September 27 – October 17	shutdown
October 18 – November 25	operating
November 26 – December 8	shutdown
December 9 – December 21	operating
December 22 – January 3	shutdown

Table A.1: Reactor schedule for 2016 calendar year. miniTimeCube had a first test run at the reactor July 13, and final reactor data was taken September 28.

A.2 Overview of the schedule

The miniTimeCube detector was primarily constructed at the University of Hawai'i. It was then shipped to NIST in Maryland. The shielding cave was then built.

2011	Scintillator casting. Aluminum light tight enclosure. Rack. Most of ideas are settled.
2012	MCP-PMT tests. High voltage tests. Power supply tests. Mounting MCP-PMTs onto the scintillation cube.
2013	Electronics is finally, after several delays, ready. Calibrations.
2014	Shipping mTC to NIST. Assembling at NCNR lab. Neutron tests at CNIF NIST facility.
2015	Laser calibration system. New better clock board. New fiber optic Ethernet data acquisition system.
Spring 2016	Major ASIC upgrade from IRS3B to IRS3D
2016	Tests at the NIST guide hall. Cave is ready. *Deployment by the NIST nuclear reactor.* Taking shifts, collecting data. Shipping mTC back to UH.
2017	Neutron tests at UH lab. Reusing mTC electronics modules for NeutronTimeCube and NuLat project.

Table A.2: mTC milestones.

Figure A.1: mTC and tools, arrival at UH. October 11 2016.

A.3 Glossary

IBD	inverse beta decay
SCROD	Standard Control and Read-Out of Data
IRS	Ice Radio Sampler – ASIC family developed at (UH IDL)
SCROD	Standard Control and Read-Out of Data
ROI	Region Of Interest
ASIC	application-specific integrated circuit
FPGA	field-programmable gate array
GSa/s	giga-samples per second
PMT	photo-multiplier tube
SiPM	Silicon photo-multiplier
MCP-PMT	micro-channel plate photo-multiplier tube
LAPPD	Large Area Picosecond PhotoDetector
TTS	Transit Time Spread
CFD	Constant Fraction Discriminator
CAJIPCI	Clock And J-tag In PCI
PCI	Peripheral Component Interconnect (local computer bus)
cPCI	compact PCI
PiLas	pico-second laser
DSP	digital signal processing
TTL	transistor-transistor logic
DAQ	data acquisition system
RF	radio frequency
GUI	graphical user interface
RAID	Redundant Array of Independent Disks
SWORD	Software for the Optimization of Radiation Detectors
CRY	Cosmic-ray shower generator
GEANT4	GEometry ANd Tracking v.4
MCNP	general-purpose Monte Carlo N-Particle code for neutron/photon/electron transport
TDC	Time to Digital Converter
ADC	Analog to Digital Converter
FFT	Fast Fourier Transform
SNR	Signal-to-Noise Ratio
SBR	Signal-to-Background Ratio
PCB	Printed Circuit Board
QE	Quantum Efficiency
PE	photo electron
MC	Monte Carlo
SCRAM	“safety control rod axe man” emergency shutdown of nuclear reactor
CAD	Computer-Aided Design

Table A.4: Some terminology, acronyms, and abbreviations to help a reader navigate through the text.

A.4 Electronics channel to spacial conversion

```
file: mtc-software/trunk/configuration/pmtPixTable_new.txt
# conversion table from scrod-carrier-chip-channel
#                   to   <pmt #><raw #><col #>
#    (( column length of this file should be < 63 ))
#  scrod # 1-12, carr # 0-3, chip # 0-3, channel # 0-7
#  pmt # 1-24, raw # (col #) 1-8
# -- PixMap master list ---
224  214  223  213  222  212  221  211  # scr-0-0-0->7
228  218  227  217  226  216  225  215  # scr-0-1
114  124  113  123  112  122  111  121  # scr-0-2
118  128  117  127  116  126  115  125  # scr-0-3
234  244  233  243  232  242  231  241  # scr-1-0
238  248  237  247  236  246  235  245  # scr-1-1
144  134  143  133  142  132  141  131  # scr-1-2
148  138  147  137  146  136  145  135  # scr-1-3
254  264  253  263  252  262  251  261  # scr-2-0
258  268  257  267  256  266  255  265  # scr-2-1
164  154  163  153  162  152  161  151  # scr-2-2
168  158  167  157  166  156  165  155  # scr-2-3
274  284  273  283  272  282  271  281  # scr-3-0
278  288  277  287  276  286  275  285  # scr-3-1
184  174  183  173  182  172  181  171  # scr-3-2
188  178  187  177  186  176  185  175  # scr-3-3
# scrod # assignments "# Scrod: <scrod#> <pmt1#> <pmt2#>"
# -- Top (#6) ---
# Scrod: 12 23 24
# Scrod: 11 22 21
# -- Botom (#1)
# Scrod: 1  1  2
# Scrod: 2  4  3
# -- Side #3
# Scrod: 5  9 10
# Scrod: 6 12 11
# -- Side #2
# Scrod: 3  6  5
# Scrod: 4  7  8
# -- Side #5
# Scrod: 9 17 18
# Scrod: 10 20 19
# -- Side #4
# Scrod: 7 14 13
# Scrod: 8 15 16
output generated via
mtc-software/trunk/configuration$ g++ read_pmtPixTable.C `root-config
--cflags --glibs` -o read_pmtPixTable.o
mtc-software/trunk/configuration$ ./read_pmtPixTable.o
```

```
2424 2414 2423 2413 2422 2412 2421 2411 12
2428 2418 2427 2417 2426 2416 2425 2415 12
2314 2324 2313 2323 2312 2322 2311 2321 12
2318 2328 2317 2327 2316 2326 2315 2325 12
2434 2444 2433 2443 2432 2442 2431 2441 12
2438 2448 2437 2447 2436 2446 2435 2445 12
2344 2334 2343 2333 2342 2332 2341 2331 12
2348 2338 2347 2337 2346 2336 2345 2335 12
2454 2464 2453 2463 2452 2462 2451 2461 12
2458 2468 2457 2467 2456 2466 2455 2465 12
2364 2354 2363 2353 2362 2352 2361 2351 12
2368 2358 2367 2357 2366 2356 2365 2355 12
2474 2484 2473 2483 2472 2482 2471 2481 12
2478 2488 2477 2487 2476 2486 2475 2485 12
2384 2374 2383 2373 2382 2372 2381 2371 12
2388 2378 2387 2377 2386 2376 2385 2375 12
2124 2114 2123 2113 2122 2112 2121 2111 11
2128 2118 2127 2117 2126 2116 2125 2115 11
2214 2224 2213 2223 2212 2222 2211 2221 11
2218 2228 2217 2227 2216 2226 2215 2225 11
2134 2144 2133 2143 2132 2142 2131 2141 11
2138 2148 2137 2147 2136 2146 2135 2145 11
2244 2234 2243 2233 2242 2232 2241 2231 11
2248 2238 2247 2237 2246 2236 2245 2235 11
2154 2164 2153 2163 2152 2162 2151 2161 11
2158 2168 2157 2167 2156 2166 2155 2165 11
2264 2254 2263 2253 2262 2252 2261 2251 11
2268 2258 2267 2257 2266 2256 2265 2255 11
2174 2184 2173 2183 2172 2182 2171 2181 11
2178 2188 2177 2187 2176 2186 2175 2185 11
2284 2274 2283 2273 2282 2272 2281 2271 11
2288 2278 2287 2277 2286 2276 2285 2275 11
224 214 223 213 222 212 221 211 1
228 218 227 217 226 216 225 215 1
114 124 113 123 112 122 111 121 1
118 128 117 127 116 126 115 125 1
234 244 233 243 232 242 231 241 1
238 248 237 247 236 246 235 245 1
144 134 143 133 142 132 141 131 1
148 138 147 137 146 136 145 135 1
254 264 253 263 252 262 251 261 1
258 268 257 267 256 266 255 265 1
164 154 163 153 162 152 161 151 1
168 158 167 157 166 156 165 155 1
274 284 273 283 272 282 271 281 1
278 288 277 287 276 286 275 285 1
184 174 183 173 182 172 181 171 1
188 178 187 177 186 176 185 175 1
```

```
324 314 323 313 322 312 321 311 2
328 318 327 317 326 316 325 315 2
414 424 413 423 412 422 411 421 2
418 428 417 427 416 426 415 425 2
334 344 333 343 332 342 331 341 2
338 348 337 347 336 346 335 345 2
444 434 443 433 442 432 441 431 2
448 438 447 437 446 436 445 435 2
354 364 353 363 352 362 351 361 2
358 368 357 367 356 366 355 365 2
464 454 463 453 462 452 461 451 2
468 458 467 457 466 456 465 455 2
374 384 373 383 372 382 371 381 2
378 388 377 387 376 386 375 385 2
484 474 483 473 482 472 481 471 2
488 478 487 477 486 476 485 475 2
1024 1014 1023 1013 1022 1012 1021 1011 5
1028 1018 1027 1017 1026 1016 1025 1015 5
914 924 913 923 912 922 911 921 5
918 928 917 927 916 926 915 925 5
1034 1044 1033 1043 1032 1042 1031 1041 5
1038 1048 1037 1047 1036 1046 1035 1045 5
944 934 943 933 942 932 941 931 5
948 938 947 937 946 936 945 935 5
1054 1064 1053 1063 1052 1062 1051 1061 5
1058 1068 1057 1067 1056 1066 1055 1065 5
964 954 963 953 962 952 961 951 5
968 958 967 957 966 956 965 955 5
1074 1084 1073 1083 1072 1082 1071 1081 5
1078 1088 1077 1087 1076 1086 1075 1085 5
984 974 983 973 982 972 981 971 5
988 978 987 977 986 976 985 975 5
1124 1114 1123 1113 1122 1112 1121 1111 6
1128 1118 1127 1117 1126 1116 1125 1115 6
1214 1224 1213 1223 1212 1222 1211 1221 6
1218 1228 1217 1227 1216 1226 1215 1225 6
1134 1144 1133 1143 1132 1142 1131 1141 6
1138 1148 1137 1147 1136 1146 1135 1145 6
1244 1234 1243 1233 1242 1232 1241 1231 6
1248 1238 1247 1237 1246 1236 1245 1235 6
1154 1164 1153 1163 1152 1162 1151 1161 6
1158 1168 1157 1167 1156 1166 1155 1165 6
1264 1254 1263 1253 1262 1252 1261 1251 6
1268 1258 1267 1257 1266 1256 1265 1255 6
1174 1184 1173 1183 1172 1182 1171 1181 6
1178 1188 1177 1187 1176 1186 1175 1185 6
1284 1274 1283 1273 1282 1272 1281 1271 6
1288 1278 1287 1277 1286 1276 1285 1275 6
```

```
524 514 523 513 522 512 521 511 3
528 518 527 517 526 516 525 515 3
614 624 613 623 612 622 611 621 3
618 628 617 627 616 626 615 625 3
534 544 533 543 532 542 531 541 3
538 548 537 547 536 546 535 545 3
644 634 643 633 642 632 641 631 3
648 638 647 637 646 636 645 635 3
554 564 553 563 552 562 551 561 3
558 568 557 567 556 566 555 565 3
664 654 663 653 662 652 661 651 3
668 658 667 657 666 656 665 655 3
574 584 573 583 572 582 571 581 3
578 588 577 587 576 586 575 585 3
684 674 683 673 682 672 681 671 3
688 678 687 677 686 676 685 675 3
824 814 823 813 822 812 821 811 4
828 818 827 817 826 816 825 815 4
714 724 713 723 712 722 711 721 4
718 728 717 727 716 726 715 725 4
834 844 833 843 832 842 831 841 4
838 848 837 847 836 846 835 845 4
744 734 743 733 742 732 741 731 4
748 738 747 737 746 736 745 735 4
854 864 853 863 852 862 851 861 4
858 868 857 867 856 866 855 865 4
764 754 763 753 762 752 761 751 4
768 758 767 757 766 756 765 755 4
874 884 873 883 872 882 871 881 4
878 888 877 887 876 886 875 885 4
784 774 783 773 782 772 781 771 4
788 778 787 777 786 776 785 775 4
1824 1814 1823 1813 1822 1812 1821 1811 9
1828 1818 1827 1817 1826 1816 1825 1815 9
1714 1724 1713 1723 1712 1722 1711 1721 9
1718 1728 1717 1727 1716 1726 1715 1725 9
1834 1844 1833 1843 1832 1842 1831 1841 9
1838 1848 1837 1847 1836 1846 1835 1845 9
1744 1734 1743 1733 1742 1732 1741 1731 9
1748 1738 1747 1737 1746 1736 1745 1735 9
1854 1864 1853 1863 1852 1862 1851 1861 9
1858 1868 1857 1867 1856 1866 1855 1865 9
1764 1754 1763 1753 1762 1752 1761 1751 9
1768 1758 1767 1757 1766 1756 1765 1755 9
1874 1884 1873 1883 1872 1882 1871 1881 9
1878 1888 1877 1887 1876 1886 1875 1885 9
1784 1774 1783 1773 1782 1772 1781 1771 9
1788 1778 1787 1777 1786 1776 1785 1775 9
```

1924 1914 1923 1913 1922 1912 1921 1911 10
1928 1918 1927 1917 1926 1916 1925 1915 10
2014 2024 2013 2023 2012 2022 2011 2021 10
2018 2028 2017 2027 2016 2026 2015 2025 10
1934 1944 1933 1943 1932 1942 1931 1941 10
1938 1948 1937 1947 1936 1946 1935 1945 10
2044 2034 2043 2033 2042 2032 2041 2031 10
2048 2038 2047 2037 2046 2036 2045 2035 10
1954 1964 1953 1963 1952 1962 1951 1961 10
1958 1968 1957 1967 1956 1966 1955 1965 10
2064 2054 2063 2053 2062 2052 2061 2051 10
2068 2058 2067 2057 2066 2056 2065 2055 10
1974 1984 1973 1983 1972 1982 1971 1981 10
1978 1988 1977 1987 1976 1986 1975 1985 10
2084 2074 2083 2073 2082 2072 2081 2071 10
2088 2078 2087 2077 2086 2076 2085 2075 10
1324 1314 1323 1313 1322 1312 1321 1311 7
1328 1318 1327 1317 1326 1316 1325 1315 7
1414 1424 1413 1423 1412 1422 1411 1421 7
1418 1428 1417 1427 1416 1426 1415 1425 7
1334 1344 1333 1343 1332 1342 1331 1341 7
1338 1348 1337 1347 1336 1346 1335 1345 7
1444 1434 1443 1433 1442 1432 1441 1431 7
1448 1438 1447 1437 1446 1436 1445 1435 7
1354 1364 1353 1363 1352 1362 1351 1361 7
1358 1368 1357 1367 1356 1366 1355 1365 7
1464 1454 1463 1453 1462 1452 1461 1451 7
1468 1458 1467 1457 1466 1456 1465 1455 7
1374 1384 1373 1383 1372 1382 1371 1381 7
1378 1388 1377 1387 1376 1386 1375 1385 7
1484 1474 1483 1473 1482 1472 1481 1471 7
1488 1478 1487 1477 1486 1476 1485 1475 7
1624 1614 1623 1613 1622 1612 1621 1611 8
1628 1618 1627 1617 1626 1616 1625 1615 8
1514 1524 1513 1523 1512 1522 1511 1521 8
1518 1528 1517 1527 1516 1526 1515 1525 8
1634 1644 1633 1643 1632 1642 1631 1641 8
1638 1648 1637 1647 1636 1646 1635 1645 8
1544 1534 1543 1533 1542 1532 1541 1531 8
1548 1538 1547 1537 1546 1536 1545 1535 8
1654 1664 1653 1663 1652 1662 1651 1661 8
1658 1668 1657 1667 1656 1666 1655 1665 8
1564 1554 1563 1553 1562 1552 1561 1551 8
1568 1558 1567 1557 1566 1556 1565 1555 8
1674 1684 1673 1683 1672 1682 1671 1681 8
1678 1688 1677 1687 1676 1686 1675 1685 8
1584 1574 1583 1573 1582 1572 1581 1571 8
1588 1578 1587 1577 1586 1576 1585 1575 8

A.5 MCP-PMT initial tests

In this sections are result from the initial test when a block of scintillator was sandwiched in between two tubes. Different HV values were applied. The output voltage (average 32 samples) was measured on the common dynode output of the MCP. A laser pulse was sent to the scintillator via a fiber connected to it.

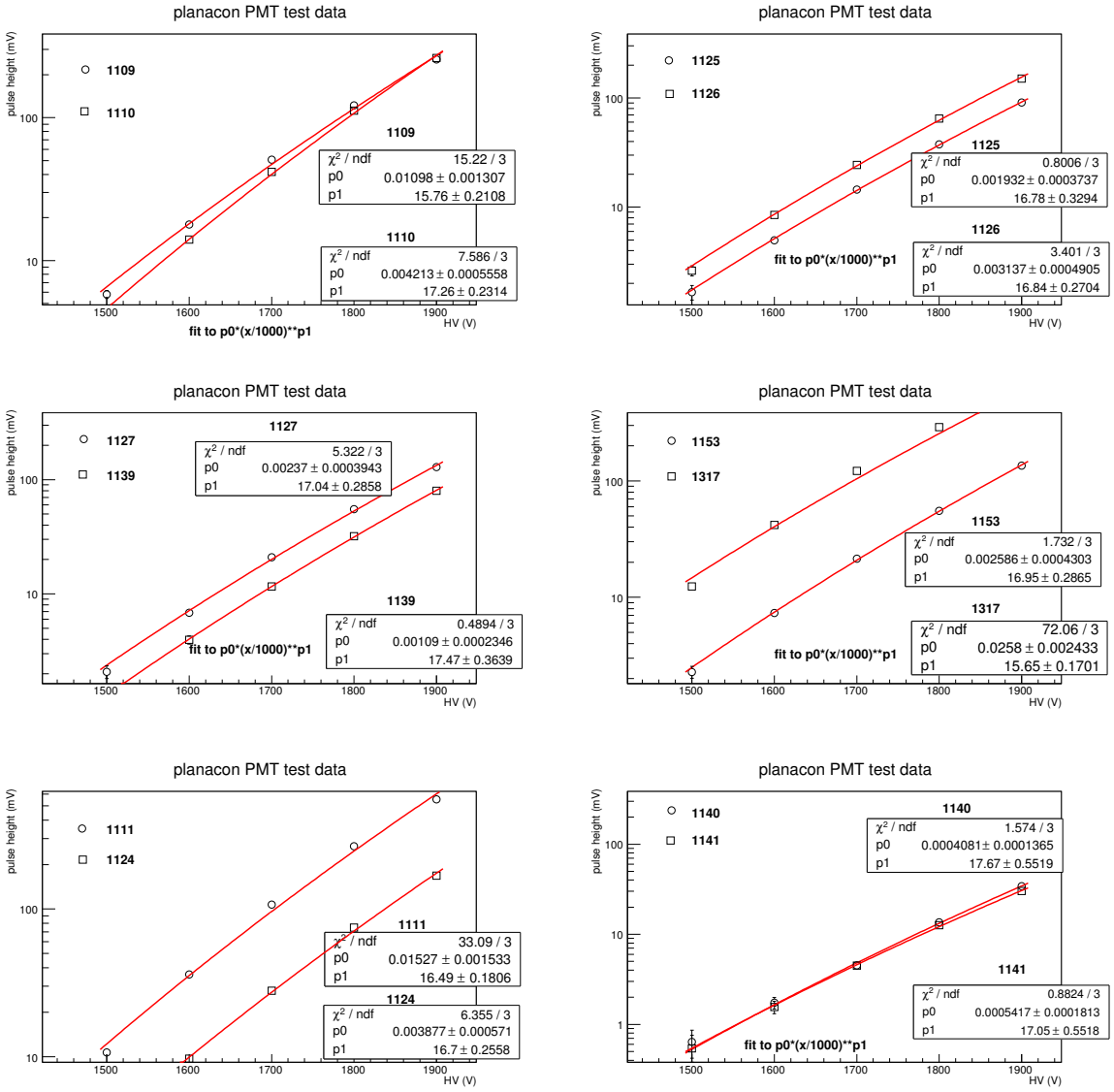

Figure A.2: Initial MCP-PMT gain tests. Figures are taken from [101].

A.6 Log-file example

```
##Time
2016-07-18 16:00:06.588867
##Relay
ON
##Rpi
#Press(psi) Flow(L/min)
       18.9        7.4
##MPOD
#Crate Status
READY
##MPOD_LV
#CH Status V(V) I(A)
  0     ON  6.1  7.0
  1     ON  6.1  7.0
  2     ON  6.1  7.1
  3     ON  6.1  7.1
  4     ON  4.7  3.9
  5     ON  4.7  3.8
  6     ON  4.7  3.7
  7    OFF  0.0  0.0
#MPOD_HV
#CH Status V(kV) I(uA)
  0     ON 1.825 331.3
  1     ON 1.795 330.1
  2    OFF 0.000   0.0
  3    OFF 0.000   0.0
  4    OFF 0.000   0.0
  5     ON 1.795 317.0
  6     ON 1.990 373.9
  7    OFF 0.000   0.0
  8     ON 1.755 311.6
  9     ON 1.820 321.8
 10    OFF 0.000   0.0
 11    OFF 0.000   0.0
 12    OFF 0.000   0.0
 13    OFF 0.000   0.0
 14     ON 1.795 319.5
 15     ON 1.760 302.5
 16    OFF 0.000   0.0
 17    OFF 0.000   0.2
 18     ON 1.815 328.6
 19     ON 1.815 324.0
 20     ON 1.975 337.5
 21     ON 1.905 337.3
 22    OFF 0.000   0.0
 23    OFF 0.000   0.0
```

```
##PIP
#Status
12/12 ON
##PIP_LV
#CH Status
  0     ON
  1     ON
  2     ON
  3     ON
  4     ON
  5     ON
  6     ON
  7     ON
  8     ON
  9     ON
 10     ON
 11     ON
#Cajipci
#Temp(C) Humid(%) Leak(T/F)
    21.2     40.2     False
#Front-end Temperatures
#SCROD T_SFP T_SCR T_Ca0 T_Ca1 T_Ca2 T_Ca3
     1  22.5  30.0  42.8  43.2  42.5  41.5
     2  24.4  28.8  39.5  29.5  27.8  26.5
     3  20.0  27.0  32.5  32.2  32.5  31.0
     4  18.1  24.5  31.2  32.2  32.5  33.0
     5  25.0  26.8  37.5  37.5  35.5  35.8
     6  17.0  25.2  23.0  23.2  24.2  22.8
     7  17.2  23.0  24.0  24.5  24.0  24.0
     8  15.0  24.8  31.0  31.2  31.2  30.2
     9  12.9  22.8  23.2  24.0  24.5  24.2
    10  0.0*  24.2  30.5  33.2  33.8  30.5
    11  19.1  27.0  37.5  37.8  37.5  39.5
    12  16.9  24.8  21.5  21.5  21.5  20.8
##Trigger Status
#Front-end link status
0xfff
#Active triggers (w/prescalers)
AB(0)
#Parameter Low High
Alimits    200  768
Blimits     15   60
Climits      0 65535
ABdelay     20  200
#Trigger Rates (Hz)      A      B      C     AB
  150.0  261.5    0.0    0.4
#Live-time Fraction
1.000
```

A.7 mTC waveforms

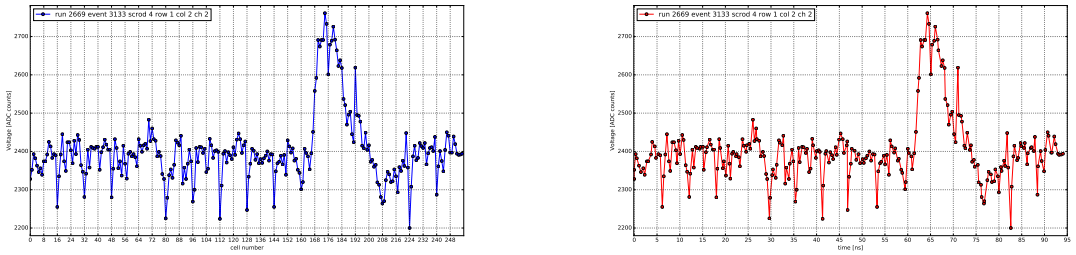

(a) (b)

Figure A.3: Raw data (laser) from one of the channels, corresponding to ~ 1 PE.

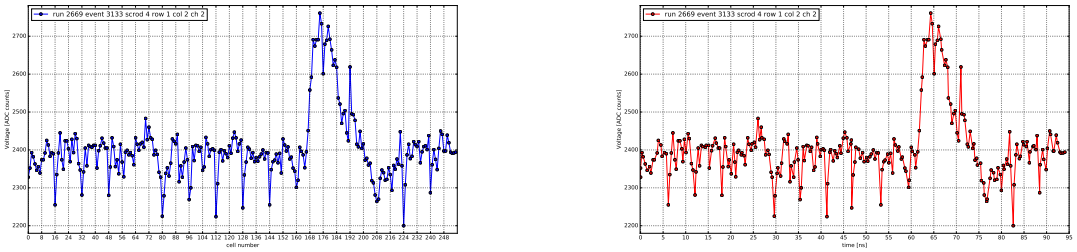

(a) (b)

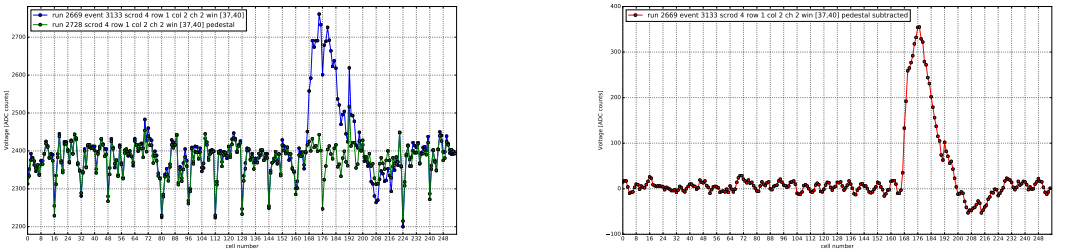

(c) (d)

Figure A.4: Same waveform. Cell-to-time conversion and pedestal subtraction.

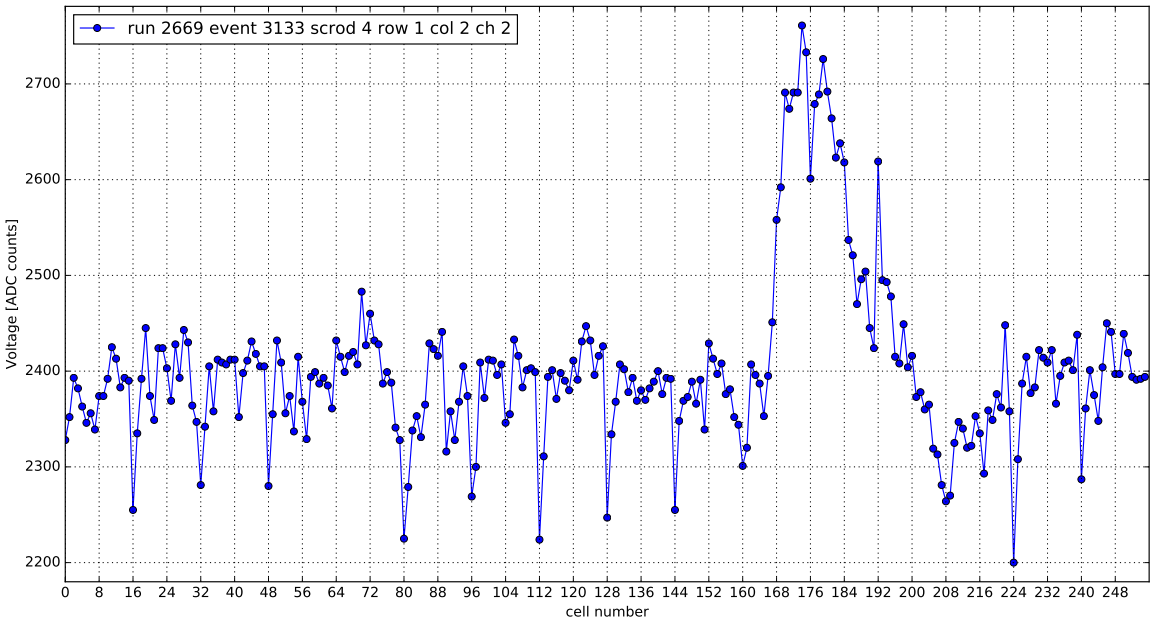

Figure A.5: Raw data (laser) from one of the channels, corresponding to about 1 photo-electron.

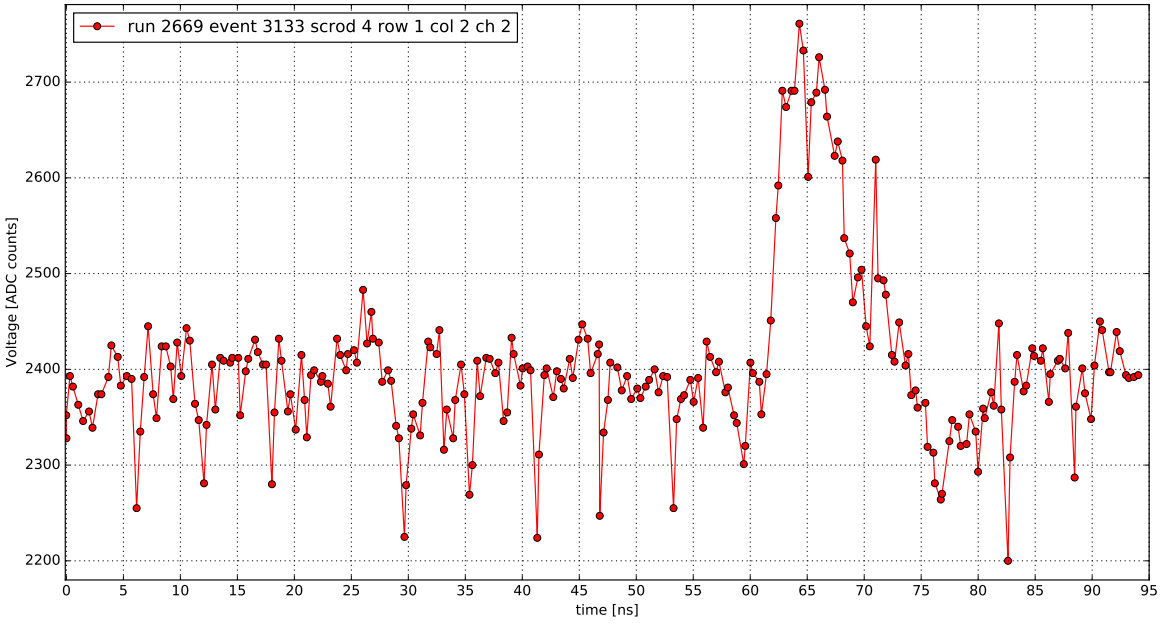

Figure A.6: Same raw single-pe laser calibration data as on the previous plot after adjusting the time.

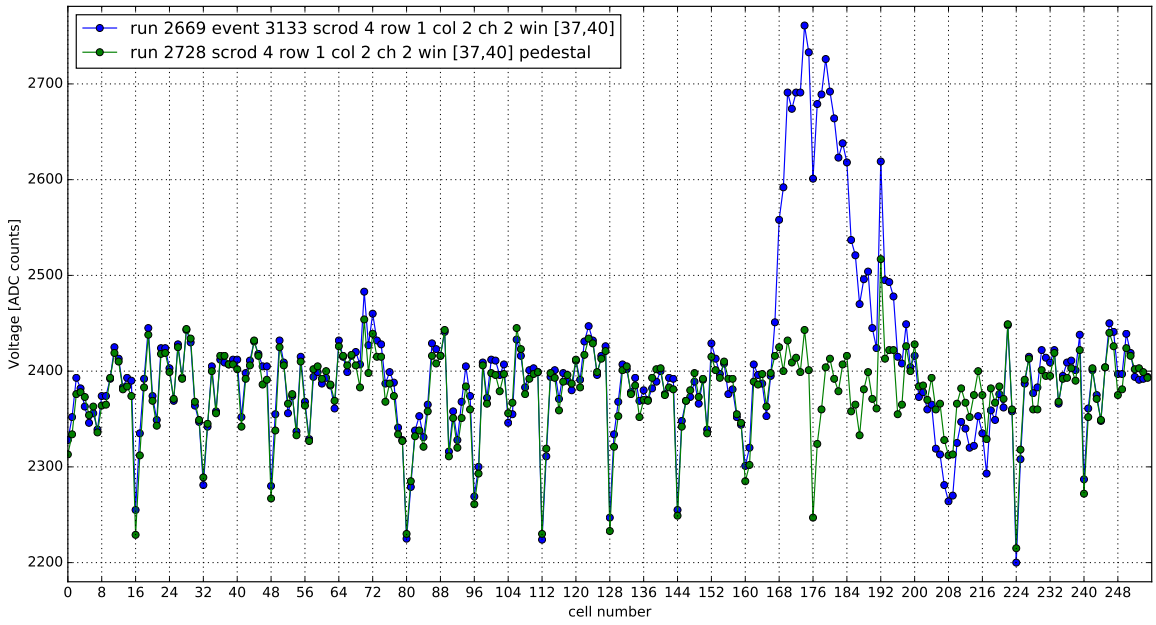

Figure A.7: Raw data (laser) from one of the channels, corresponding to ~ 1 PE, and pedestal.

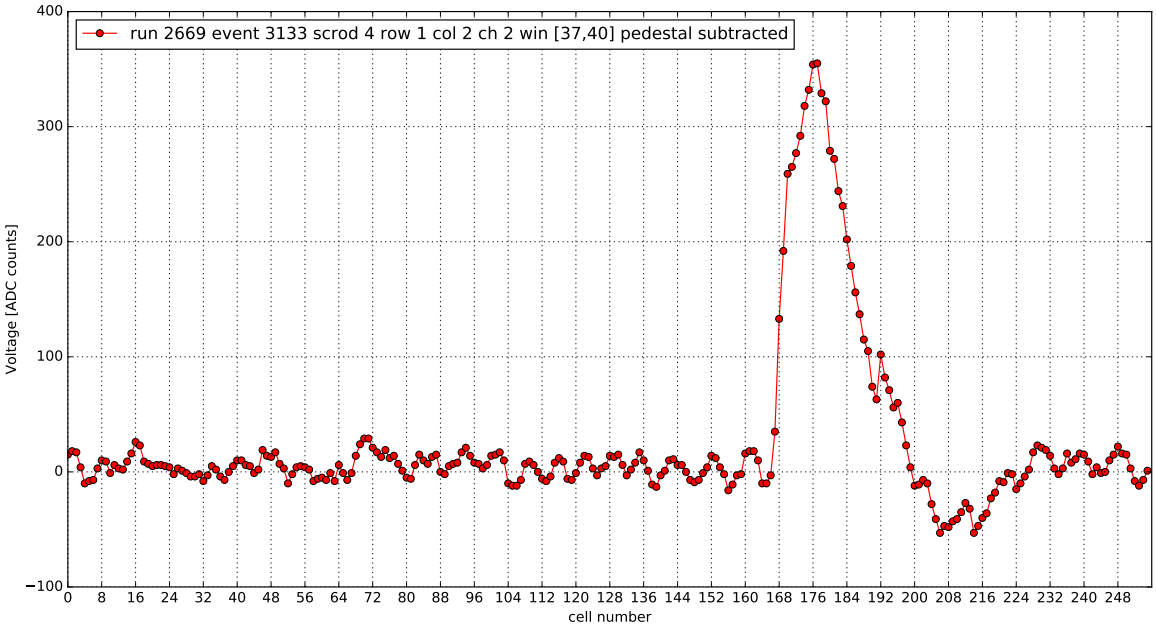

Figure A.8: Raw data (laser) from one of the channels, corresponding to ~ 1 PE, after pedestal subtraction.

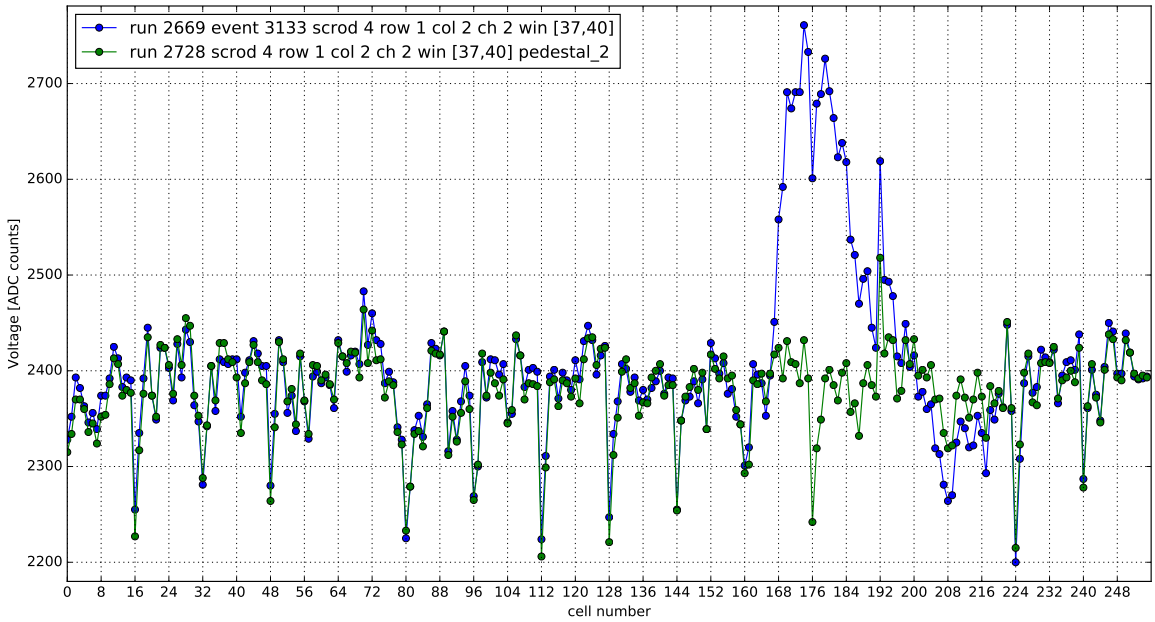

Figure A.9: Raw data (laser) from one of the channels, corresponding to ~ 1 PE, and another pedestal.

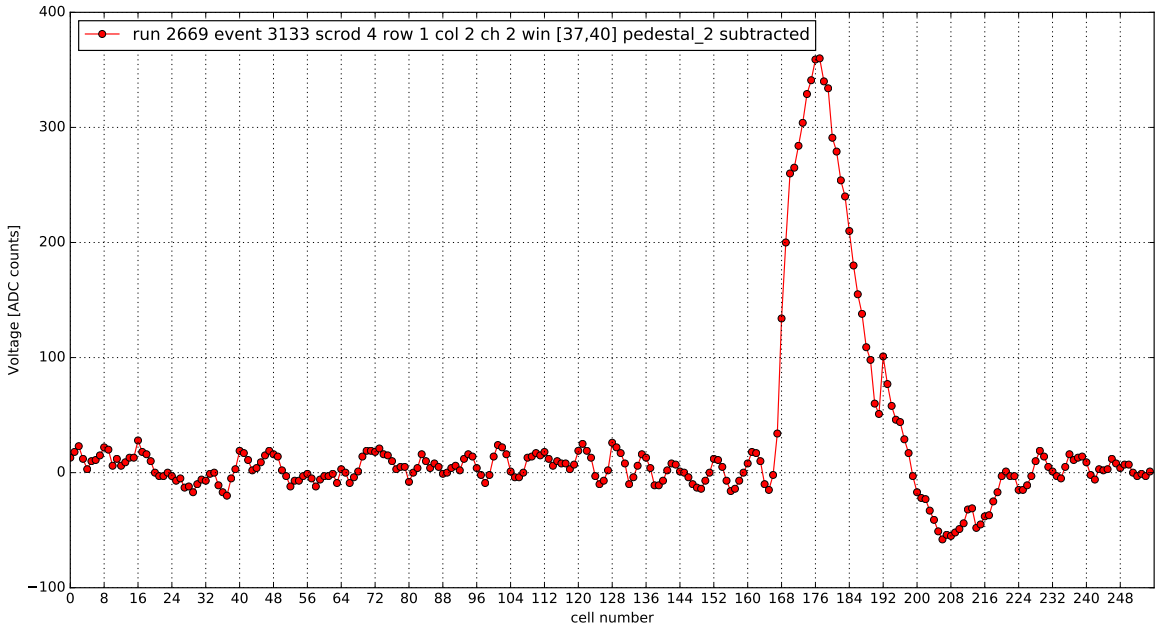

Figure A.10: Raw data (laser) from one of the channels, corresponding to ~ 1 PE, after pedestal subtraction (using another pedestal, from the previous figure).

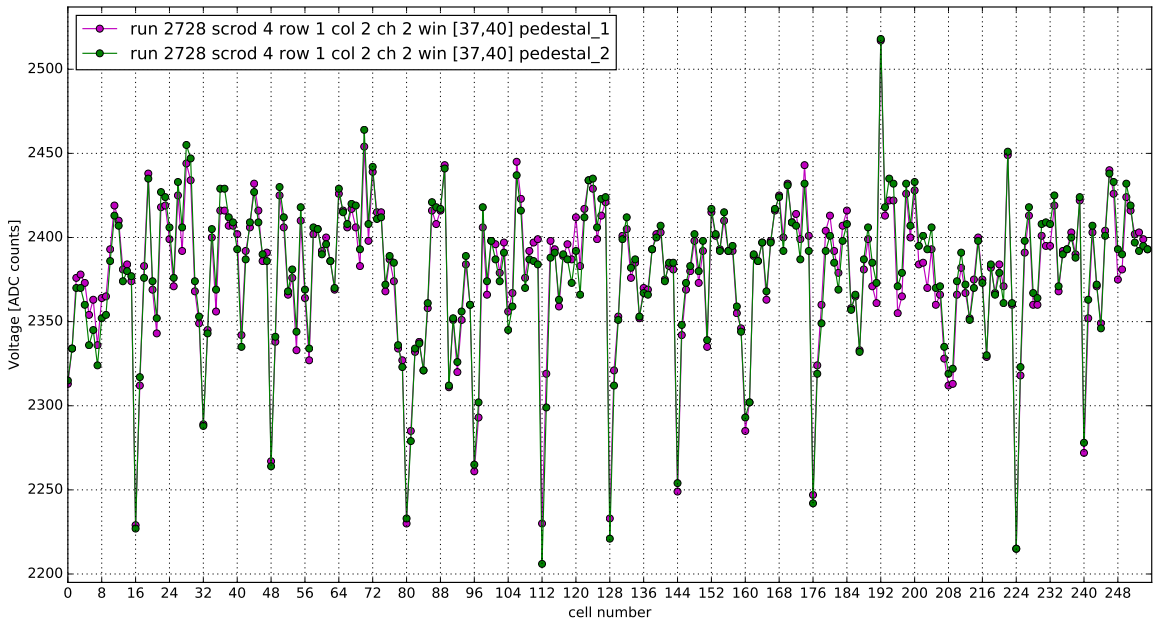

Figure A.11: Procedure of subtracting pedestal. Two different pedestal waveforms.

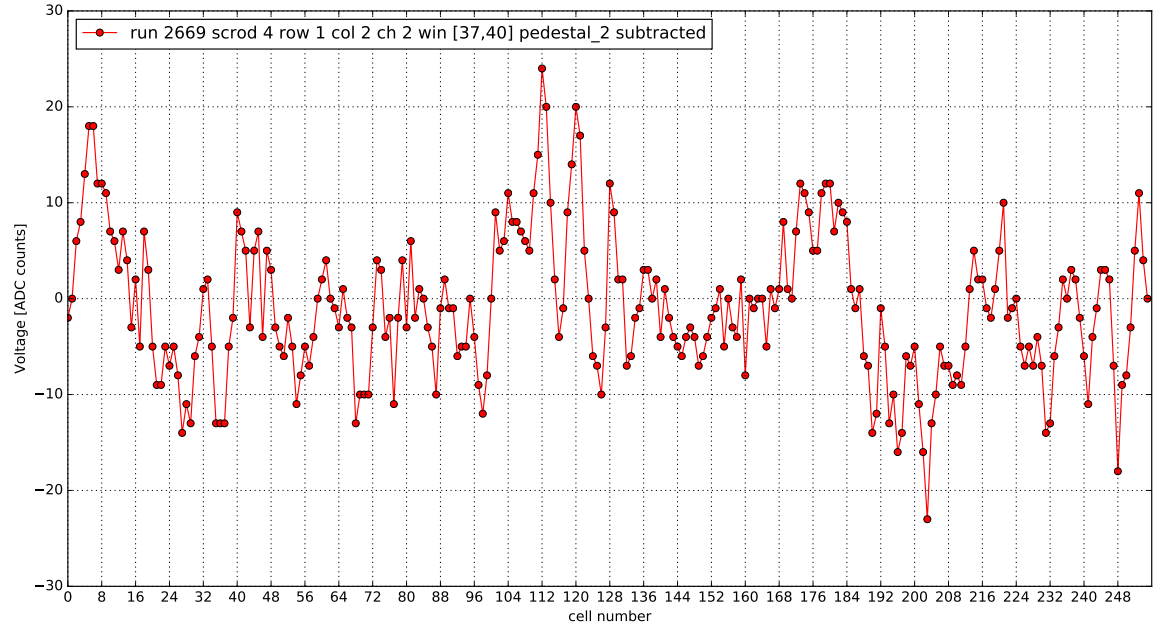

Figure A.12: Pedestal fluctuation within one channel. Two values of pedestal subtracted for each cell.

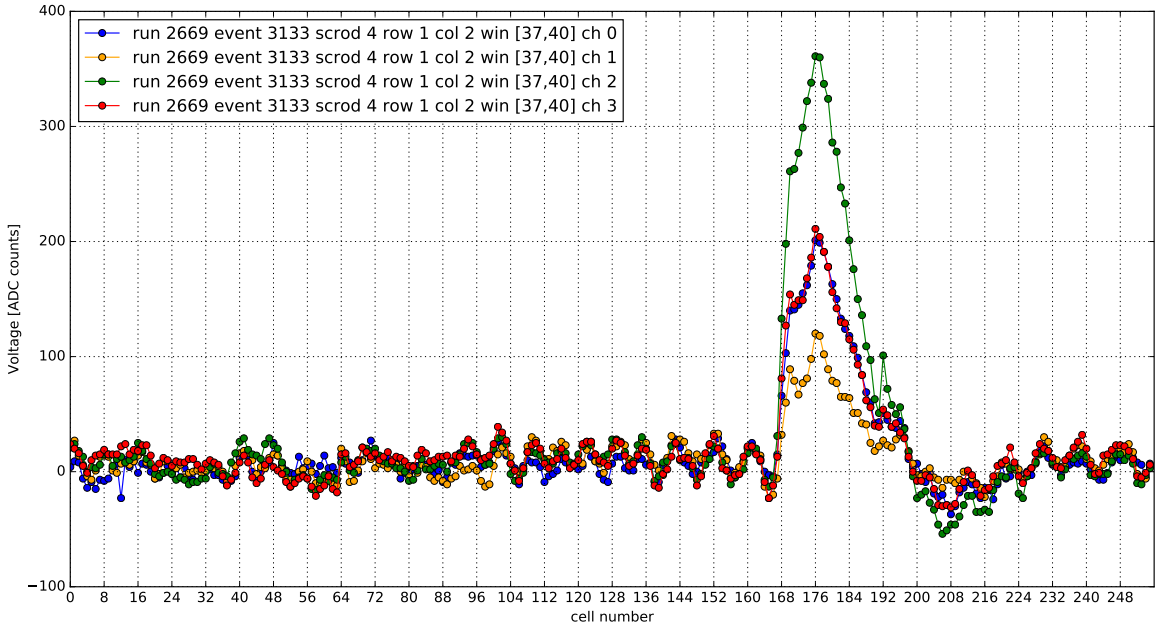

Figure A.13: Raw data from 4 channels within one ASIC, 4 windows of 64 values each. Pedestal subtracted.

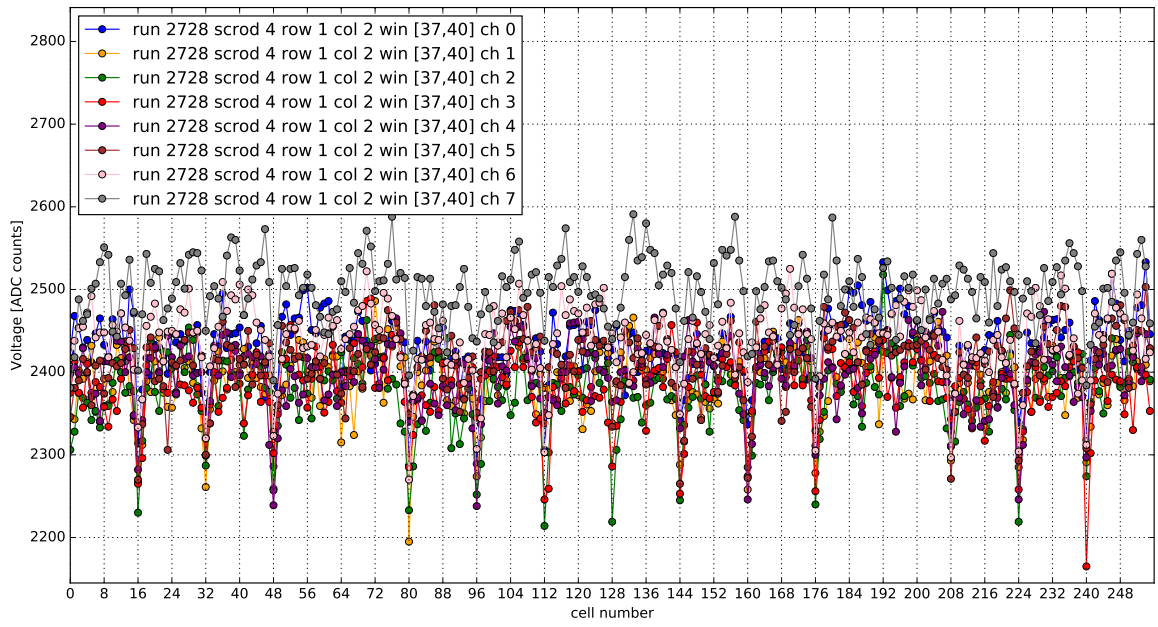

Figure A.14: Raw data from all 8 channels within one ASIC, 4 windows of 64 values each.

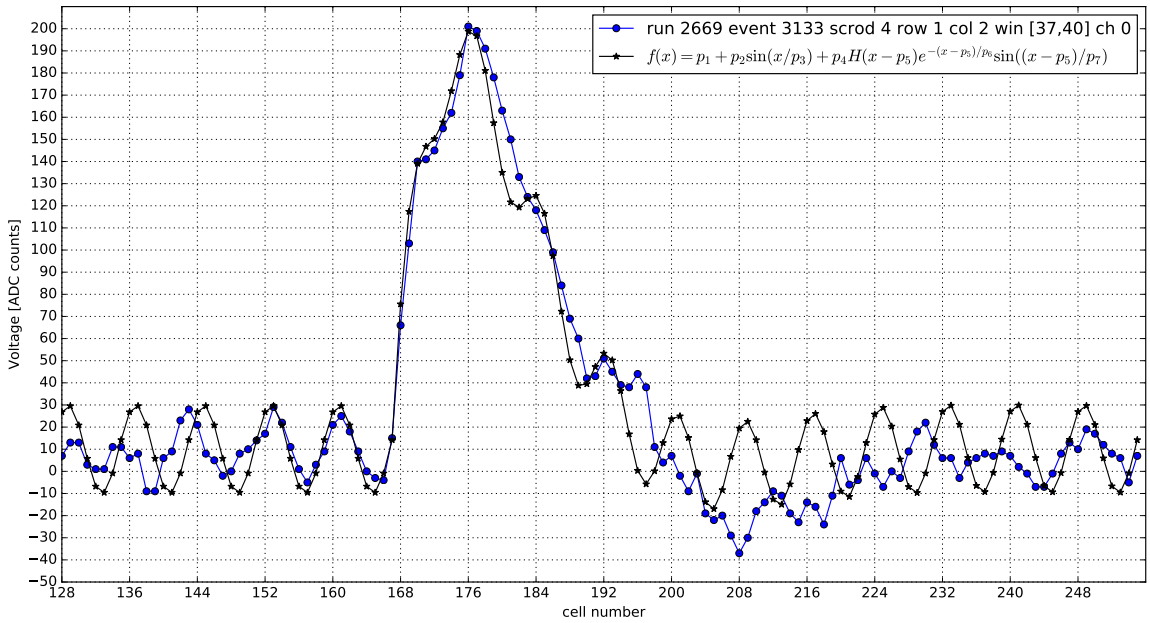

Figure A.15: Fit test function.

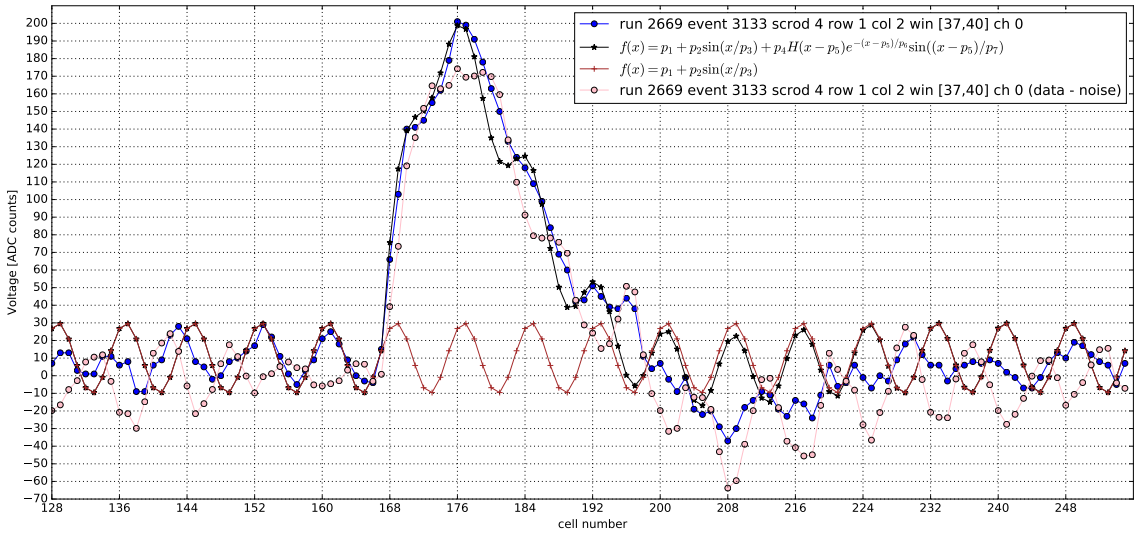

Figure A.16: Fit test function, and example of noise subtracted waveform.

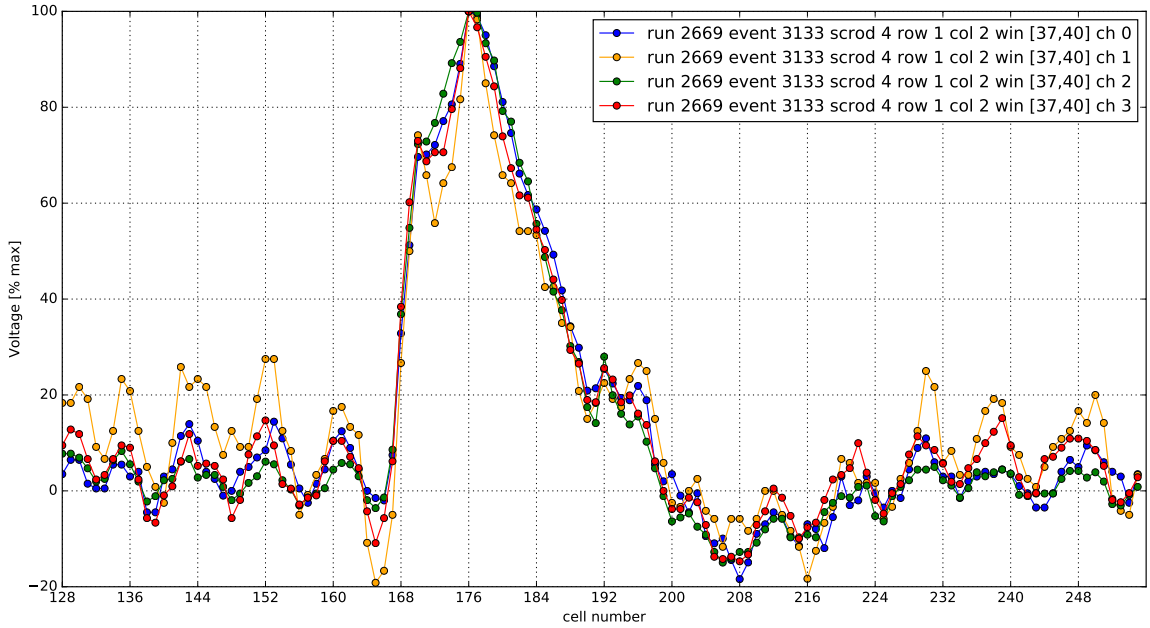

Figure A.17: Pedestal-subtracted normalized data four reporting channels from one ASIC.

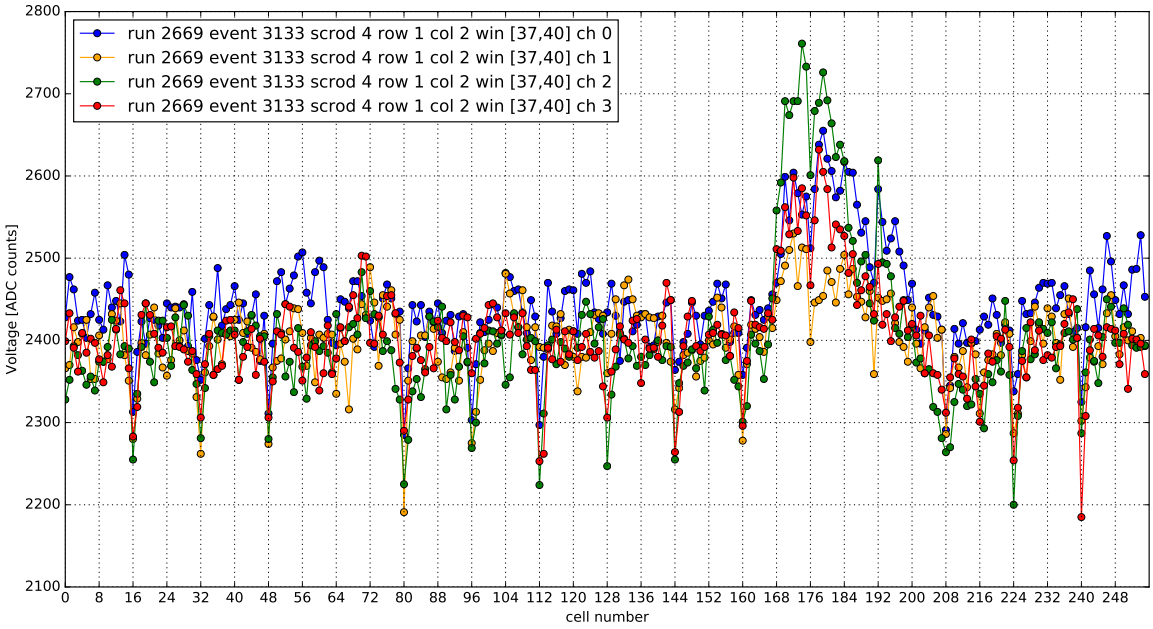

Figure A.18: Raw data from 4 channels within one ASIC, 4 windows of 64 values each. No pedestal subtracted.

A.8 DRS4 ASIC

Here for illustrative purposes of what's available for fast timing on the market, we also present time intervals for DRS4 chip, [106], which is manufactured in PSI, Switzerland. We used it for our other lab tests that require fast timing. Figs. A.19 show DRS4 and IRS3D sampling time intervals.

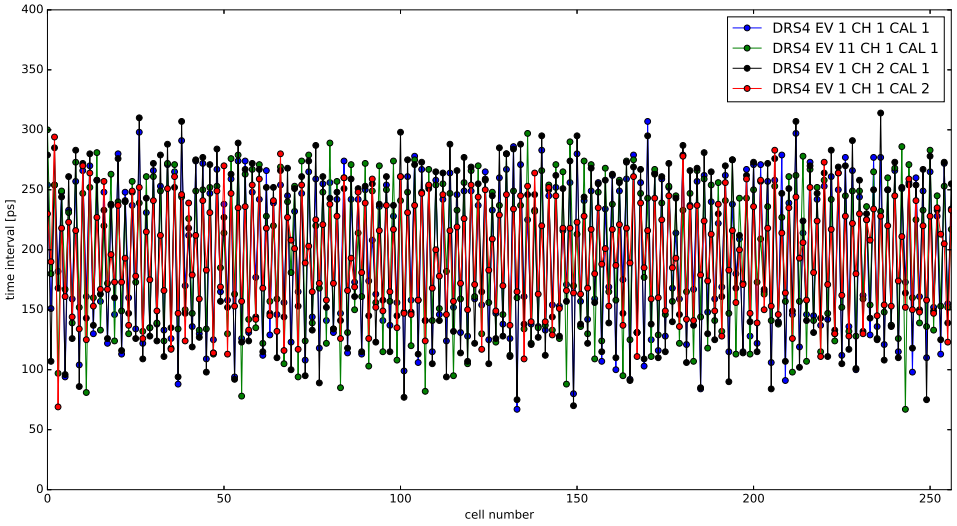

(a) DRS4 ASIC, depending on calibration, event, channel, on same chip. First 256 cells plotted, total number of cells is 1024 in the DRS4 storage array.

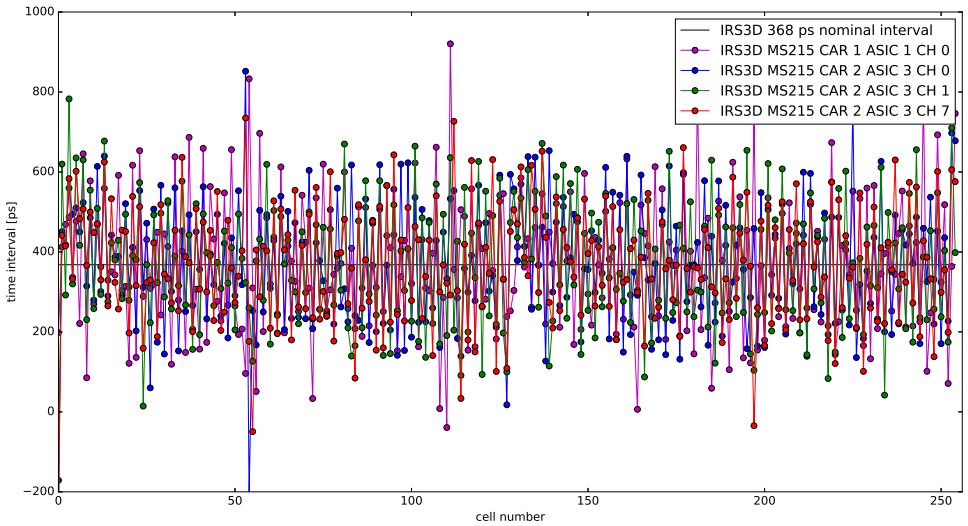

(b) IRS3D, after performing production test.

Figure A.19: Time intervals.

A.9 Math on how to get the event rate in QFT

These are the detailed derivations on how to get the event rate in quantum field theory, taking into account virtual neutrinos and wave packets. It was originally published in my diploma thesis [41].

Let's define the following objects C which will contain spinor products $v^+(p)v^-(p)$,

$$\bar{\mathsf{C}}^p_{s,\,d} = \bar{\mathsf{C}}^p_{s,\,d}(\{k\}_{s,\,d},\ \{p\}_{s,\,d}) \tag{A.1}$$

$$\langle\{p\}_s|\ \mathsf{C}_s(x)\ |\{k\}_s\rangle \equiv \langle 0|\ \mathsf{C}^p_s(\{k\}_s,\ \{p\}_s)\ e^{i\,\{k\}_s\,x}\ e^{i\,\{p\}_s\,x}\ |0\rangle \tag{A.2}$$

index p in C^p shows that there is a dependence on momenta, not on coordinates as for C.

$$\begin{aligned}
&\langle \mathbf{p}_1\mathbf{p}_2\ldots|(S-1)|\mathbf{k}_1\mathbf{k}_2\ldots\rangle = \\
&= \int dxdy\,\langle \mathbf{p}_1\mathbf{p}_2\ldots|\,\mathrm{T}\left[\bar{\mathsf{C}}_s(x)\,\nu_\alpha(x)\overline{\nu}_\beta(y)\mathsf{C}_d(y) + \mathsf{C}_s(x)\,\overline{\nu}_\alpha(x)\nu_\beta(y)\bar{\mathsf{C}}_d(y)\right]\,|\mathbf{k}_1\mathbf{k}_2\ldots\rangle = \\
&\quad = \int dxdy\Big[\bar{\mathsf{C}}^p_s\,e^{-i\,\{k_s\}\,x}e^{+i\,\{p_s\}\,x}\,\left(\int\frac{d^4q}{(2\pi)^4}\tilde{S}_{\alpha\beta}(q)e^{iq(x-y)}\right)\mathsf{C}^p_d\,e^{-i\,\{k_d\}\,y}e^{+i\,\{p_d\}\,y} + \\
&\quad + \tilde{\mathsf{C}}^p_s\,e^{-i\,\{k_s\}\,y}e^{+i\,\{p_s\}\,y}\,\left((-1)\int\frac{d^4q}{(2\pi)^4}\tilde{S}_{\beta\alpha}(q)e^{-iq(x-y)}\right)\bar{\mathsf{C}}^p_d\,e^{-i\,\{k_d\}\,x}e^{+i\,\{p_d\}\,x}\Big]
\end{aligned} \tag{A.3}$$

Sign (-1) is due to neutrino spinor permutation.

$$\langle 0|\mathbf{T}\left[\nu_1(x)\overline{\nu}_1(y)\right]|0\rangle = (-1)\langle 0|\mathbf{T}\left[\overline{\nu}_1(y)\nu_1(x)\right]|0\rangle = i\int\frac{dq}{(4\pi)^4}\frac{\hat{q}+m_1}{q^2-m_1^2}\,e^{+iq(x-y)} \tag{A.4}$$

$$\begin{aligned}
&\langle 0|\mathbf{T}\left[\nu_\alpha(x)\overline{\nu}_\beta(y)\right]|0\rangle = \sum_i\sum_j V_{\alpha i}V^*_{\beta j}\delta_{ij}i\int\frac{dq}{(4\pi)^4}\frac{\hat{q}+m_i}{q^2-m_i^2}\,e^{+iq(x-y)} = \\
&\quad = i\int\frac{dq}{(4\pi)^4}\left(\sum_i V_{\alpha i}V^*_{\beta i}\frac{\hat{q}+m_i}{q^2-m_i^2}\right)e^{+iq(x-y)} \equiv \left(i\int\frac{d^4q}{(2\pi)^4}\tilde{S}_{\alpha\beta}(q)e^{iq(x-y)}\right)
\end{aligned} \tag{A.5}$$

$\tilde{S}_{\alpha\beta}$ — contains three propagators of neutrinos.

Considering the first term in Eq. (A.3), which is relevant for neutrino (but not for $\bar{\nu}$), and substituting Eq. (A.3) in Eq. (1.91), we get

$$\begin{aligned}
&\mathscr{A}_\nu = \left(\prod_{j=1}\int\frac{d^3p_j}{(2\pi)^3\,\sqrt{2\,E_{\mathbf{p}_j}}}\,\varphi_j(p_j)\right)\left(\prod_{i=1}\int\frac{d^3k_i}{(2\pi)^3\,\sqrt{2\,E_{\mathbf{k}_i}}}\,\phi_i(k_i)\right)\cdot \\
&\cdot\int dxdy\int\frac{dq}{(2\pi)^4}\,e^{-i\,\{k_s\}\,x}e^{+i\,\{p_s\}\,x}\,\left(e^{iq(x-y)}\right)e^{-i\,\{k_d\}\,y}e^{+i\,\{p_d\}\,y}\,\mathscr{M}_\nu(\{k\},\,\{p\};\,q)
\end{aligned} \tag{A.6}$$

where $\mathscr{M}_\nu(\{k\},\,\{p\};\,q)$ is the matrix element,

$$\mathscr{M}_\nu(\{k\},\,\{p\};\,q) = \bar{\mathsf{C}}^p_s\tilde{S}_{\alpha\beta}(q)C^p_d \tag{A.7}$$

Introducing functions $\Psi_i(\mathbf{x})$ which are Fourier transforms of $a_i(\mathbf{k}_i)$ (and not of $a_i(\mathbf{k}_i - \bar{\mathbf{k}}_i)$, as it is done in [124]), in the following manner

$$\Psi_i(\mathbf{x}) = \int \frac{d\mathbf{k}_i}{(2\pi)^3}\, a_i(\mathbf{k}_i) e^{+i\mathbf{k}_i\mathbf{x}} = \int \frac{d\mathbf{k}_i}{(2\pi)^3}\, a_i(\mathbf{k}_i - \bar{\mathbf{k}}_i) e^{+i(\mathbf{k}_i - \bar{\mathbf{k}}_i)\mathbf{x}} \tag{A.8}$$

$$\tilde{\Psi}_j(\mathbf{x}) = \int \frac{d\mathbf{p}_j}{(2\pi)^3}\, \tilde{a}_j(\mathbf{p}_j) e^{-i\mathbf{p}_j\mathbf{x}} = \int \frac{d\mathbf{p}_j}{(2\pi)^3}\, \tilde{a}_j(\mathbf{p}_j - \bar{\mathbf{p}}_j) e^{-i(\mathbf{p}_j - \bar{\mathbf{p}}_j)\mathbf{x}} \tag{A.9}$$

Using the expansion in Eq. (1.92), we consider an intergral in Eq. (A.6). For example, for *outgoing* particles inside the *source*, it would mean that the variable of integration would be p_j and the exponent would contain $+ip_jx$),

$$\left(\int \frac{d^3p_j}{(2\pi)^3\, \sqrt{2\, E_{\mathbf{p}_j}}}\, \tilde{a}(\mathbf{p}_j - \bar{\mathbf{p}}_j) e^{-ip_jx_s} \right) e^{+ip_jx} \mathscr{M}_\nu(\dots p_j \dots) =$$
$$= \int \frac{d^3p_j}{(2\pi)^3\, \sqrt{2\, E_{\mathbf{p}_j}}}\, \tilde{a}(\mathbf{p}_j - \bar{\mathbf{p}}_j) e^{+i\mathbf{p}_j(\mathbf{x}_s - \mathbf{x})}\, e^{-iE_{\mathbf{p}_j}(t_s - t)} \mathscr{M}_\nu(\dots p_j \dots) \tag{A.10}$$

Expanding $E_{\mathbf{p}_j}$, in fast-changing exponent $e^{-iE_{\mathbf{p}_j}(t_s - t)}$, in vicinity $\mathbf{p}_j = \bar{\mathbf{p}}_j$, and keep only the linear term for $\mathbf{p}_j$

$$E_{\mathbf{p}_j} = E_{\bar{\mathbf{p}}_j} + \frac{\bar{\mathbf{p}}_j}{E_{\bar{\mathbf{p}}_j}} (\mathbf{p}_j - \bar{\mathbf{p}}_j) + \dots \tag{A.11}$$

Group velocity of j-th wave packet

$$\bar{\mathbf{v}} = \left. \frac{dE_{\mathbf{p}_j}}{d\mathbf{p}_j} \right|_{\mathbf{p}_j = \bar{\mathbf{p}}_j} = \frac{\bar{\mathbf{p}}_j}{E_{\bar{\mathbf{p}}_j}} \tag{A.12}$$

Thus,

$$\begin{aligned} p(x - x_s) = p^0(x^0 - x_s^0) - \mathbf{p}(\mathbf{x} - \mathbf{x}_s) \approx \bar{p}^0(x^0 - x_s^0) + \bar{\mathbf{v}}(\mathbf{p} - \bar{\mathbf{p}})(x^0 - x_s^0) - \mathbf{p}(\mathbf{x} - \mathbf{x}_s) \equiv \\ \equiv \bar{p}^0(x^0 - x_s^0) + \bar{\mathbf{v}}(\mathbf{p} - \bar{\mathbf{p}})(x^0 - x_s^0) - (\bar{\mathbf{p}}(\mathbf{x} - \mathbf{x}_s) + (\mathbf{p} - \bar{\mathbf{p}})(\mathbf{x} - \mathbf{x}_s)) = \\ = \bar{p}(x - x_s) + (\mathbf{p} - \bar{\mathbf{p}})(\bar{\mathbf{v}}(x^0 - x_s^0) - (\mathbf{x} - \mathbf{x}_s)) \end{aligned} \tag{A.13}$$

$$e^{-ip_j(x_s - x)} = e^{+i\bar{p}_j(x - x_s)}\, e^{+i(\mathbf{p}_j - \bar{\mathbf{p}}_j)(\bar{\mathbf{v}}_j(x^0 - x_s^0) - (\mathbf{x} - \mathbf{x}_s))}. \tag{A.14}$$

We'll get the following result

$$\left(\int \frac{d^3p_j}{(2\pi)^3\, \sqrt{2\, E_{\mathbf{p}_j}}}\, \tilde{a}(\mathbf{p}_j - \bar{\mathbf{p}}_j) e^{-ip_jx_s} \right) e^{+ip_jx} \mathscr{M}_\nu(\dots p_j \dots) =$$
$$= \left[\int \frac{d^3p_j}{(2\pi)^3}\, \tilde{a}(\mathbf{p}_j - \bar{\mathbf{p}}_j) e^{-i(\mathbf{p}_j - \bar{\mathbf{p}}_j)(-\bar{\mathbf{v}}_j(x^0 + x_s^0) - (\mathbf{x} - \mathbf{x}_s))} \right] e^{-i\bar{p}_j(x_s - x)} \frac{1}{\sqrt{2\, E_{\mathbf{p}_j}}} \mathscr{M}_\nu(\dots p_j \dots) =$$
$$= \left[\tilde{\Psi}_j(-\bar{\mathbf{v}}_j(x^0 - x_s^0) + (\mathbf{x} - \mathbf{x}_s)) \right] \frac{1}{\sqrt{2\, E_{\bar{\mathbf{p}}_j}}} e^{-i\bar{p}_j(x_s - x)} \mathscr{M}_\nu(\dots \bar{p}_j \dots) \tag{A.15}$$

Amplitude can be written as follows:

$$\mathscr{A}_\nu = \int dxdy \prod_{j=1}^{F_s} \tilde{\Psi}_j(-\bar{\mathbf{v}}_j(x^0 - x_s^0) + (\mathbf{x} - \mathbf{x}_s)) \frac{1}{\sqrt{2\,E_{\bar{\mathbf{p}}_j}}} e^{+i\bar{p}_j(x-x_s)} \cdot$$
$$\cdot \prod_{j=F-F_s}^{F} \tilde{\Psi}_j(-\bar{\mathbf{v}}_j(y^0 - y_d^0) + (\mathbf{y} - \mathbf{y}_d)) \frac{1}{\sqrt{2\,E_{\bar{\mathbf{p}}_j}}} e^{+i\bar{p}_j(y-y_d)} \cdot$$
$$\cdot \prod_{i=1}^{I_s} \Psi_i(+\bar{\mathbf{v}}_i(x^0 - x_s^0) - (\mathbf{x} - \mathbf{x}_s)) \frac{1}{\sqrt{2\,E_{\bar{\mathbf{k}}_i}}} e^{-i\bar{k}_i(x-x_s)} \cdot$$
$$\cdot \prod_{i=I-I_s}^{I} \Psi_i(+\bar{\mathbf{v}}_i(y^0 - y_d^0) - (\mathbf{y} - \mathbf{y}_d)) \frac{1}{\sqrt{2\,E_{\bar{\mathbf{k}}_i}}} e^{-i\bar{k}_i(y-y_d)} \cdot \int \frac{dq}{(2\pi)^4}\, e^{iq(x-y)}\, \mathscr{M}_\nu(\{\bar{k}\},\, \{\bar{p}\};\, q) \tag{A.16}$$

where I is the total number of *initial* states/particles (both in the source and the detector), F — the total number of *final* states/particles (both in the source and the detector), I_s — the total number of *initial* states/particles in the *source*, F_s — the total number of *final* states/particles in the *source*, $I - I_s$ — the total number of *initial* states/particles in the detector, $F - F_s$ — the total number of *final* states/particles in the detector.

Introducing new notations $\Psi_s,\ \Psi_d,\ E_s(x - x_s),$ and $E_d(y - y_d)$ as follows:

$$\Psi_s = \prod_{j=1}^{F_s} \frac{\tilde{\Psi}_j(0)}{\sqrt{2\,E_{\bar{\mathbf{p}}_j}}} \prod_{i=1}^{I_s} \frac{\Psi_i(0)}{\sqrt{2\,E_{\bar{\mathbf{k}}_i}}}, \qquad \Psi_d = \prod_{j=F-F_s}^{F} \frac{\tilde{\Psi}_j(0)}{\sqrt{2\,E_{\bar{\mathbf{p}}_j}}} \prod_{i=I-I_s}^{I} \frac{\Psi_i(0)}{\sqrt{2\,E_{\bar{\mathbf{k}}_i}}} \tag{A.17}$$

$$E_s(x - x_s) = \prod_{j=1}^{F_s} \frac{\tilde{\Psi}_j(-\bar{\mathbf{v}}_j(x^0 - x_s^0) + (\mathbf{x} - \mathbf{x}_s))}{\tilde{\Psi}_j(0)} \prod_{i=1}^{I_s} \frac{\Psi_i(+\bar{\mathbf{v}}_i(x^0 - x_s^0) - (\mathbf{x} - \mathbf{x}_s))}{\Psi_i(0)} \tag{A.18}$$

$$E_d(y - y_d) = \prod_{j=F-F_s}^{F} \frac{\tilde{\Psi}_j(-\bar{\mathbf{v}}_j(y^0 - y_d^0) + (\mathbf{y} - \mathbf{y}_d))}{\tilde{\Psi}_j(0)} \prod_{i=I-I_s}^{I} \frac{\Psi_i(+\bar{\mathbf{v}}_i(y^0 - y_d^0) - (\mathbf{y} - \mathbf{y}_d))}{\Psi_i(0)} \tag{A.19}$$

We can re-write Eq. (A.6) in the following form:

$$\mathscr{A}_\nu = \Psi_s \Psi_d \int dx\, dy\, e^{-i\,(\bar{k}_s - \bar{p}_s)\,(x-x_s)} e^{-i\,(\bar{k}_d - \bar{p}_d)\,(y-y_d)}\, E_s(x - x_s) E_d(y - y_d) \cdot$$
$$\cdot \int \frac{dq}{(2\pi)^4}\, e^{iq(x-y)} \mathscr{M}_\nu(\{\bar{k}\},\, \{\bar{p}\};\, q) \tag{A.20}$$

$\bar{k}_s,\ \bar{p}_s,\ \bar{k}_d,\ \bar{p}_d$ are sums of the momenta:

$$\bar{k}_s = \sum_{i=1}^{I_s} \bar{k}_i, \qquad \bar{p}_s = \sum_{j=1}^{F_s} \bar{p}_j, \qquad \bar{k}_d = \sum_{i=I-I_s}^{I} \bar{k}_i, \qquad \bar{p}_d = \sum_{j=F-F_s}^{F} \bar{p}_j. \tag{A.21}$$

Keep expanding $E_s(x-x_s)$ as a series up to second order of x in the vicinity of $x=x_s$, and keeping in mind that functions $E_s(x-x_s),\ E_d(y-y_d)$ have extrema at $x=x_s,\ y=y_d$ respectively,

$$\left.\frac{\partial E_s(x-x_s)}{\partial x^\mu}\right|_{x=x_s}(x-x_s)^\mu=0, \qquad \left.\frac{\partial E_d(y-y_d)}{\partial y^\mu}\right|_{y=y_d}(y-y_d)^\mu=0. \tag{A.22}$$

$$E_s(x-x_s)\approx 1+\frac{1}{2}\left.\frac{\partial^2 E_s(x-x_s)}{\partial x^\mu\partial x^\nu}\right|_{x=x_s}(x-x_s)^\mu(x-x_s)^\nu \tag{A.23}$$

$$(W_s)_{\mu\nu}\equiv-\left.\frac{\partial^2 E_s(x-x_s)}{\partial x^\mu\partial x^\nu}\right|_{x=x_s} \tag{A.24}$$

Analogous for function $E_d(y-y_d)$

$$E_d(y-y_d)\approx 1-\frac{1}{2}(W_d)_{\mu\nu}(y-y_d)^\mu(y-y_d)^\nu \tag{A.25}$$

$$(W_d)_{\mu\nu}\equiv-\left.\frac{\partial^2 E_d(y-y_d)}{\partial y^\mu\partial y^\nu}\right|_{y=y_d} \tag{A.26}$$

Considering the following object in the amplitude ($\ln(1+\varepsilon)\approx\varepsilon,\quad \varepsilon\to 0$)

$$\begin{aligned}\int dx\ e^{-i\,(\bar{k}_s-\bar{p}_s)\,(x-x_s)}\ e^{iqx}\ E_s(x-x_s)&=e^{+iqx_s}\int dx\ e^{-i\,(\bar{k}_s-\bar{p}_s-q)\,(x-x_s)}E_s(x-x_s)\approx\\ &\approx e^{+iqx_s}\int dx\ e^{-i\,(\bar{k}_s-\bar{p}_s-q)\,(x-x_s)}e^{-\frac{1}{2}(W_s)_{\mu\nu}(x-x_s)^\mu(x-x_s)^\nu}=\\ &=e^{+iqx_s}\frac{\pi^2}{\sqrt{\det(W_s/2)}}\exp\left[-(\frac{1}{2}W_s^{-1})_{\mu\nu}(\bar{k}_s-\bar{p}_s-q)^\mu(\bar{k}_s-\bar{p}_s-q)^\nu\frac{1}{4}\right].\end{aligned} \tag{A.27}$$

$$\begin{aligned}\int dy\ e^{-i\,(\bar{k}_d-\bar{p}_d)\,(y-y_d)}e^{-iqy}E_d(y-y_d)&\approx e^{-iqy_d}\int dy\ e^{-i\,(\bar{k}_d-\bar{p}_d+q)\,(y-y_d)}e^{-\frac{1}{2}(W_d)_{\mu\nu}(y-y_d)^\mu(y-y_d)^\nu}\\ &=e^{-iqy_d}\frac{\pi^2}{\sqrt{\det(W_d/2)}}\exp\left[-(\frac{1}{2}W_d^{-1})_{\mu\nu}(\bar{k}_d-\bar{p}_d+q)^\mu(\bar{k}_d-\bar{p}_d+q)^\nu\frac{1}{4}\right]\end{aligned} \tag{A.28}$$

We used the following here to integrate a generalized Gaussian — if A is a real matrix $n\times n$ ($n=4$ in our case) with positive eigenvalues and has an inverse A^{-1} matrix, then

$$\int dx\ e^{-A_{\mu\nu}x^\mu x^\nu-ik_\mu x^\mu}=\frac{\pi^{n/2}}{\sqrt{\det A}}e^{-(A^{-1})_{\mu\nu}\frac{k^\mu k^\nu}{4}} \tag{A.29}$$

The following property of determinants was also used, $\det(AB)=\det A\det B$, and if $A=cI$, where c is a number, and I is a unit matrix, then $\det A=c^n$.

Let's define four-dimensional volumes

$$V_s=\int dx\ \left[E_s(x-x_s)\right]^2\approx\int dx\ e^{2\left[-\frac{1}{2}(W_s)_{\mu\nu}(x-x_s)^\mu(x-x_s)^\nu\right]}=\frac{\pi^2}{\sqrt{\det W_s}} \tag{A.30}$$

$$V_d=\int dy\ \left[E_d(y-y_d)\right]^2\approx\int dy\ e^{2\left[-\frac{1}{2}(W_d)_{\mu\nu}(y-y_d)^\mu(y-y_d)^\nu\right]}=\frac{\pi^2}{\sqrt{\det W_d}} \tag{A.31}$$

$$\mathscr{A}_\nu = \Psi_s\Psi_d 4V_s 4V_d \int \frac{dq}{(2\pi)^4}\, e^{+iqx_s} \exp\left[-\frac{1}{2}(W_s^{-1})_{\mu\nu}(\bar{k}_s - \bar{p}_s - q)^\mu(\bar{k}_s - \bar{p}_s - q)^\nu\right]\cdot$$
$$\cdot\, e^{-iqy_d} \exp\left[-\frac{1}{2}(W_d^{-1})_{\mu\nu}(\bar{k}_d - \bar{p}_d + q)^\mu(\bar{k}_d - \bar{p}_d + q)^\nu\right] \mathscr{M}_\nu(\{\bar{k}\},\, \{\bar{p}\};\, q)$$

$$D(q) = \frac{1}{2}(W_s^{-1})_{\mu\nu}(\bar{k}_s - \bar{p}_s - q)^\mu(\bar{k}_s - \bar{p}_s - q)^\nu + \frac{1}{2}(W_d^{-1})_{\mu\nu}(\bar{k}_d - \bar{p}_d + q)^\mu(\bar{k}_d - \bar{p}_d + q)^\nu \tag{A.32}$$

Amplitude has form:

$$\mathscr{A}_\nu = \Psi_s\Psi_d 4V_s 4V_d \int \frac{dq}{(2\pi)^4}\, e^{+iqx_s} e^{-iqy_d} e^{-D(q)} \mathscr{M}_\nu(\{\bar{k}\},\, \{\bar{p}\};\, q) \tag{A.33}$$

$$-iq(y_d - x_s) = -iq^0(y_d^0 - x_s^0) + i\mathbf{q}\,\mathbf{L}, \qquad \mathbf{L} = \mathbf{y}_d - \mathbf{x}_s \tag{A.34}$$

There exists a theorem [125], developed for integrating such constructions (neutrino gets into mass-shell)

$$\int d\mathbf{q} e^{-i\mathbf{q}\,\mathbf{L}} \frac{F(\mathbf{q})}{A - \mathbf{q}^2 + i\varepsilon} = -\frac{2\pi^2}{L} F(-\frac{\sqrt{A}\mathbf{L}}{L}) e^{i\sqrt{A}L} + O(L^{-\frac{2}{3}}) \tag{A.35}$$

Applying for our case

$$\mathscr{M} \sim \frac{\hat{q} + m_i}{-\mathbf{q}^2 + q_0^2 - m_i^2 + i\varepsilon} \tag{A.36}$$

$$A = q_0^2 - m_i^2, \qquad F(\mathbf{q}) = (\hat{q} + m_i)\cdot e^{-D(q)} \tag{A.37}$$

Integrating over $\mathbf{q}$ using Eq. (A.35):

$$\mathscr{A}_\nu = \Psi_s\Psi_d 4V_s 4V_d \int \frac{dq^0}{(2\pi)^4}\, e^{+iq^0(x_s^0 - y_d^0)} (-\frac{2\pi^2}{L} e^{i\sqrt{q_0^2 - m_i^2}L} e^{-D(q)} \tilde{\mathscr{M}}_\nu(\{\bar{k}\},\, \{\bar{p}\};\, q)(\hat{q}+m_i)) \tag{A.38}$$

Going back to three neutrino propagators in Eq. (A.5), and Eq. (A.7) from matrix element becomes:

$$\mathscr{M}_\nu(\{\bar{k}\},\, \{\bar{p}\};\, q) = \bar{\mathsf{C}}_s^p(\{\bar{k}\},\, \{\bar{p}\}) \left(\sum_i V_{\alpha i} V_{\beta i}^* \frac{\hat{q} + m_i}{q^2 - m_i^2}\right) \mathsf{C}_d^p(\{\bar{k}\},\, \{\bar{p}\}) \tag{A.39}$$

Then the amplitude is

$$\mathscr{A}_\nu = \Psi_s\Psi_d 4V_s 4V_d \int \frac{dq^0}{(2\pi)^4}\, (-\frac{2\pi^2}{L}) e^{+iq^0(x_s^0 - y_d^0)} e^{i\sqrt{q_0^2 - m_i^2}L} e^{-D(q^0, -\frac{\sqrt{q_0^2 - m_i^2}\mathbf{L}}{L})}\cdot$$
$$\cdot\, \bar{\mathsf{C}}_s^p(\{\bar{k}\},\, \{\bar{p}\}) \left(\sum_i V_{\alpha i} V_{\beta i}^* (\hat{q} + m_i)\right) \mathsf{C}_d^p(\{\bar{k}\},\, \{\bar{p}\}) + O(L^{-\frac{2}{3}}) \tag{A.40}$$

$$\mathbf{q} = -\frac{\sqrt{q_0^2 - m_i^2}\mathbf{L}}{L} \tag{A.41}$$

The most of the integral comes from the vicinity of $\lambda_i = (\bar{q}_0)_i$. Amplitude has its maximum when function $D(q)$ is at its minimum,

$$\left.\frac{dD_i(q)}{dq^0}\right|_{q^0=\lambda_i} = 0 \tag{A.42}$$

Consider the exponent

$$e^{+iq^0(x_s^0-y_d^0)} \cdot e^{i\sqrt{q_0^2-m_i^2}L} \cdot e^{-D(q)}, \qquad D_i(q) = D(q^0,\ -\frac{\sqrt{q_0^2-m_i^2}\mathbf{L}}{L}), \tag{A.43}$$

and the series up to second non-zero terms:

$$D_i(q) = D_i(\lambda_i) + \underbrace{\left.\frac{d^2D_i}{dq^0}\right|_{q^0=\lambda_i}}_{\sigma_i^2}(q^0-\lambda_i)^2 + \dots \tag{A.44}$$

$$\sqrt{q_0^2-m_i^2} = \sqrt{\lambda_i^2-m_i^2} + \underbrace{\frac{\lambda_i}{\sqrt{\lambda_i^2-m_i^2}}}_{v_i^{-1}}(q^0-\lambda_i) + \dots \tag{A.45}$$

$$q^0(x_s^0-y_d^0) = \lambda_i(x_s^0-y_d^0) + (x_s^0-y_d^0)(q^0-\lambda_i) \tag{A.46}$$

$$\begin{aligned}\mathscr{A}_\nu = \Psi_s\Psi_d 4V_s 4V_d \int \frac{dq^0}{(2\pi)^4}\,(-\frac{2\pi^2}{L})\cdot \\ \cdot\exp\left[+i\lambda_i(x_s^0-y_d^0) - D_i(\lambda_i) - \sigma_i^2(q^0-\lambda_i)^2 + i\sqrt{\lambda_i^2-m_i^2}L + i(x_s^0-y_d^0+\frac{L}{v_i})(q^0-\lambda_i)\right]\cdot \\ \cdot \bar{\mathsf{C}}_s^p(\{\bar{k}\},\,\{\bar{p}\})\left(\sum_i V_{\alpha i}V_{\beta i}^*(\hat{q}+m_i)\right)\mathsf{C}_d^p(\{\bar{k}\},\,\{\bar{p}\})\end{aligned} \tag{A.47}$$

Sum over i in Eq. (A.47) is *external*. Integrating over q^0, and using the theorem discussed above on how to integrate generalized Gaussian functions

$$\int dq^0 \exp\left[-\sigma_i^2(q^0-\lambda_i)^2 - i(x_s^0-y_d^0+\frac{L}{v_i})(q^0-\lambda_i)\right] = \frac{\sqrt{\pi}}{\sigma_i}\exp\left[-\frac{1}{\sigma_i^2}(x_s^0-y_d^0+\frac{L}{v_i})^2\frac{1}{4}\right] \tag{A.48}$$

$$\begin{aligned}\mathscr{A}_\nu = \Psi_s\Psi_d 4V_s 4V_d \frac{1}{(2\pi)^4}\,(-\frac{2\pi^2}{L})\frac{\sqrt{\pi}}{\sigma_i}\cdot\exp\left[-\frac{1}{4\sigma_i^2}(x_s^0-y_d^0+\frac{L}{v_i})^2\right]\cdot \\ \cdot\exp\left[+i\lambda_i(x_s^0-y_d^0) - D_i(\lambda_i) + i\sqrt{\lambda_i^2-m_i^2}L\right]\cdot\bar{\mathsf{C}}_s^p\left(\sum_i V_{\alpha i}V_{\beta i}^*(\hat{q}+m_i)\right)\mathsf{C}_d^p\end{aligned} \tag{A.49}$$

Reminding, now we have

$$\hat{q} = \gamma^0\lambda_i - \boldsymbol{\gamma}(-\sqrt{\lambda_i^2-m_i^2}\frac{\mathbf{L}}{L}) \tag{A.50}$$

Let us now proceed to calculating the module square of the amplitude and probability of neutrino oscillations.

$$|\mathscr{A}_\nu|^2 = |\Psi_s|^2|\Psi_d|^2\ V_s^2V_d^2\frac{4}{\pi^3L^2}\ \cdot$$
$$\cdot\left|\sum_i \frac{1}{\sigma_i}V_{\alpha i}V^*_{\beta i}\ e^{-\frac{1}{4\sigma_i^2}(x_s^0-y_d^0+\frac{L}{v_i})^2}e^{+i\lambda_i(x_s^0-y_d^0)-D_i(\lambda_i)+i\sqrt{\lambda_i^2-m_i^2}L}\left[\bar{\mathsf{C}}_s^p(\hat{q}+m_i)\ \mathsf{C}_d^p\right]\right|^2 \quad \text{(A.51)}$$

Number of events in the plane-wave approach has the following form [126]:

$$dN = |A|^2\prod_f\frac{d^3\bar{p}_f}{(2\pi)^3} \quad \text{(A.52)}$$

in our case of wave packets $|\mathscr{A}|^2$ is a dimensionless quantity (that's how we defined and normalized wave packets), the number of events, the differential are inside $|\mathscr{A}|^2$

$$dN = |\mathscr{A}|^2 \quad \text{(A.53)}$$

4–volumes' differentials from Eq. (A.30) for source and detector

$$V_s \to dx_s^0 d\mathbf{x}_s, \qquad V_d \to dy_d^0 d\mathbf{y}_d. \quad \text{(A.54)}$$

Using definitions of $\Psi_{s,\ d}$, from Eq. (A.17)

$$|\Psi_s|^2 = \left|\prod_{j=1}^{F_s}\frac{\tilde{\Psi}_j(0)}{\sqrt{2\,E_{\bar{\mathbf{p}}_j}}}\prod_{i=1}^{I_s}\frac{\Psi_i(0)}{\sqrt{2\,E_{\bar{\mathbf{k}}_i}}}\right|^2 \to \prod_{j=1}^{F_s}\frac{d^3\bar{p}_j}{(2\pi)^3 2E_{\bar{\mathbf{p}}_j}}\prod_{i=1}^{I_s}\frac{f_i(\bar{\mathbf{k}}_i,\ \mathbf{x}_s,\ x_s^0,\ \sigma_i)d^3\bar{k}_i}{(2\pi)^3 2E_{\bar{\mathbf{k}}_i}} \quad \text{(A.55)}$$

$$|\Psi_d|^2 = \left|\prod_{j=F-F_s}^{F}\frac{\tilde{\Psi}_j(0)}{\sqrt{2\,E_{\bar{\mathbf{p}}_j}}}\prod_{i=I-I_s}^{I}\frac{\Psi_i(0)}{\sqrt{2\,E_{\bar{\mathbf{k}}_i}}}\right|^2 \to \prod_{j=F-F_s}^{F}\frac{d^3\bar{p}_j}{(2\pi)^3 2E_{\bar{\mathbf{p}}_j}}\prod_{i=I-I_s}^{I}\frac{f_i(\bar{\mathbf{k}}_i,\ \mathbf{y}_d,\ y_d^0,\ \sigma_i)d^3\bar{k}_i}{(2\pi)^3 2E_{\bar{\mathbf{k}}_i}} \quad \text{(A.56)}$$

$f_i(\bar{\mathbf{k}}_i,\ \mathbf{x}_s,\ x_s^0,\ \sigma_i)$ — distribution function i-th incoming particle (whether in source or in detector) in a phase space [127], σ_i — spin index of this particle.

Later, when we take the average over spins of incoming and outgoing particles, we won't write index σ_i for f_i.

Thus, formula for event number becomes

$$dN = \prod_{j=1}^{F_s}\frac{d^3\bar{p}_j}{(2\pi)^3 2E_{\bar{\mathbf{p}}_j}}\prod_{i=1}^{I_s}\frac{f_i(\bar{\mathbf{k}}_i,\ \mathbf{x}_s,\ x_s^0)d^3\bar{k}_i}{(2\pi)^3 2E_{\bar{\mathbf{k}}_i}}\prod_{j=F-F_s}^{F}\frac{d^3\bar{p}_j}{(2\pi)^3 2E_{\bar{\mathbf{p}}_j}}\prod_{i=I-I_s}^{I}\frac{f_i(\bar{\mathbf{k}}_i,\ \mathbf{y}_d,\ y_d^0)d^3\bar{k}_i}{(2\pi)^3 2E_{\bar{\mathbf{k}}_i}}\cdot$$
$$\cdot\, dx_s^0 d\mathbf{x}_s dy_d^0 d\mathbf{y}_d V_s V_d\frac{4}{\pi^3L^2}\ \cdot$$
$$\cdot\left|\sum_i \frac{1}{\sigma_i}V_{\alpha i}V^*_{\beta i}\ e^{-\frac{1}{4\sigma_i^2}(x_s^0-y_d^0+\frac{L}{v_i})^2}e^{+i\lambda_i(x_s^0-y_d^0)-D_i(\lambda_i)+i\sqrt{\lambda_i^2-m_i^2}L}\left[\bar{\mathsf{C}}_s^p(\hat{q}+m_i)\ \mathsf{C}_d^p\right]\right|^2 \quad \text{(A.57)}$$

After opening the square module we get the following expression:

$$e^{-\frac{1}{4\sigma_i^2}(x_s^0-y_d^0+\frac{L}{v_i})^2-\frac{1}{4\sigma_j^2}(x_s^0-y_d^0+\frac{L}{v_j})^2}\cdot e^{+i(\lambda_i-\lambda_j)(x_s^0-y_d^0)}\cdot e^{i(\sqrt{\lambda_i^2-m_i^2}-\sqrt{\lambda_j^2-m_j^2})L}\cdot e^{-D_i(\lambda_i)-D_j(\lambda_j)} \quad \text{(A.58)}$$

The first exponent in this important Eq. (A.58) is due to a new non-trivial object which quantum mechanic treatment doesn't have (compare with Eq. (1.31)); the second exponent factor in ultra relativistic limit is equal to 1; third exponent — is basically an oscillation factor, which we had in QM derivation; fourth — is a consequence of momentum conservation law.

Consider the integral over dx_s^0 (neutrino emission time), such integral becomes full in the region where this exponent is at its maximum

$$e^{-\frac{1}{4\sigma_i^2}(x_s^0-y_d^0+\frac{L}{v_i})^2}\cdot e^{-\frac{1}{4\sigma_j^2}(x_s^0-y_d^0+\frac{L}{v_j})^2} \tag{A.59}$$

Finding the maximum of the exponent:

$$\frac{1}{4\sigma_i^2}(x_s^0-y_d^0+\frac{L}{v_i})^2+\frac{1}{4\sigma_j^2}(x_s^0-y_d^0+\frac{L}{v_j})^2 \tag{A.60}$$

$$\frac{d}{dx_s^0}\ :\qquad \frac{1}{2\sigma_i^2}(x_s^0-y_d^0+\frac{L}{v_i})+\frac{1}{2\sigma_i^2}(x_s^0-y_d^0+\frac{L}{v_i})=0 \tag{A.61}$$

$$x_s^0=y_d^0-L\frac{\sigma_i^2v_i+\sigma_j^2v_j}{\sigma_i^2+\sigma_j^2}\frac{1}{v_iv_j},\qquad v_{ij}^{-1}\equiv\frac{\sigma_i^2v_i+\sigma_j^2v_j}{\sigma_i^2+\sigma_j^2}\frac{1}{v_iv_j} \tag{A.62}$$

If we have eqaulity $\sigma_i\approx\sigma_j$, the we can write

$$(x_s^0)_{\min}=(x_s^0)_{ij}=y_d^0-L\frac{v_i+v_j}{2v_iv_j}, \tag{A.63}$$

and second derivative is

$$\frac{d^2}{d(x_s^0)^2}\ :\qquad \frac{1}{2}\left(\frac{1}{\sigma_i^2}+\frac{1}{\sigma_i^2}\right)\approx\frac{1}{\sigma^2} \tag{A.64}$$

In the ultra-relativistic limit $\lambda_i\gg m_i$, (reminding that $\lambda_i\sim E_i$ average) : $v_i\approx v_j\approx v_{ij}\approx 1$, $\lambda_i\approx\lambda$

$$\left|\left[\bar{\mathsf{C}}_s^p(\hat{q}+m_i)\ \mathsf{C}_d^p\right]\right|^2\to\left|\left[\bar{\mathsf{C}}_s^p\sum_{s_\nu}\nu\bar{\nu}\mathsf{C}_d^p\right]\right|^2\to\left|\sum_{s_\nu}\mathscr{M}_s\mathscr{M}_d\right|^2=\sum_{s_\nu}|\mathscr{M}_s|^2\,|\mathscr{M}_d|^2 \tag{A.65}$$

In Eq. (A.65) we use that neutrino in the ultra-relativistic limit has only one spin state (helicity is "almost" conserved), therefore writing sum over the spin can be omitted.

Expanding exponent in Eq. (A.60) until the second order in the vicinity of its minimum $(x_s^0)_{ij}$

$$\begin{aligned}&\frac{1}{4\sigma_i^2}(x_s^0-y_d^0+\frac{L}{v_i})^2+\frac{1}{4\sigma_j^2}(x_s^0-y_d^0+\frac{L}{v_j})^2\approx\\&\frac{1}{4\sigma^2}\left[\left(\left(-\frac{v_i+v_j}{2v_iv_j}+\frac{1}{v_i}\right)^2+\left(-\frac{v_i+v_j}{2v_iv_j}+\frac{1}{v_j}\right)^2\right)L^2+\frac{1}{2!}2\left(\left(x_s^0-(x_s^0)_{ij}\right)^2+\left(x_s^0-(x_s^0)_{ij}\right)^2\right)\right]\\&=\frac{1}{4\sigma^2}\left[2\left(\frac{v_i-v_j}{2v_iv_j}\right)^2L^2+2\left(x_s^0-y_d^0+L\frac{v_i+v_j}{2v_iv_j}\right)^2\right]\equiv\frac{1}{2\sigma^2}\left[\left(\frac{v_i-v_j}{2v_iv_j}\right)^2L^2+z^2\right]\end{aligned} \tag{A.66}$$

$$x_s^0 - y_d^0 \equiv \left(x_s^0 - y_d^0 + L\frac{v_i + v_j}{2v_i v_j} \right) - L\frac{v_i + v_j}{2v_i v_j} \equiv z - L\frac{v_i + v_j}{2v_i v_j} \tag{A.67}$$

where the new variable z is defined as follows: $\int dx_s^0 f(x_s^0) = \int dz f(x_s^0)$.

$$\left(\frac{v_i - v_j}{2v_i v_j} \right)^2 \approx \frac{1}{4} \left(\frac{\sqrt{\lambda_i^2 - m_i^2}}{\lambda_i} - \frac{\sqrt{\lambda_j^2 - m_j^2}}{\lambda_j} \right)^2 \approx \frac{1}{4} \left(m_i^2 - m_j^2 \right)^2 \frac{1}{4\lambda^4} \tag{A.68}$$

Momentum conservation [124] is inside the following function which becomes δ–function in a 'non-wavepacket' treatment:

$$\sqrt{\frac{2\pi}{\sigma^2}} e^{-D_i(\lambda_i)} e^{-D_i(\lambda_i)} \to 2\sqrt{\frac{\pi}{2\sigma^2}} e^{-2D(\lambda)} = 2e^{-2D(\lambda)} \int\limits_0^{+\infty} dE_{\mathbf{q}} e^{-2\sigma^2 (E_{\mathbf{q}} - \lambda)^2} =$$

$$= 2 \int\limits_0^{+\infty} dE_{\mathbf{q}} e^{-2D(E_{\mathbf{q}})} \to 2\frac{\pi^8}{V_s V_d} \delta^4(\bar{p}_s - \bar{k}_s + q(\lambda)) \delta^4(\bar{p}_d - \bar{k}_d - q(\lambda)) \tag{A.69}$$

$$dN = \prod_{j=1}^{F_s} \frac{d^3\bar{p}_j}{(2\pi)^3 2E_{\bar{\mathbf{p}}_j}} \prod_{i=1}^{I_s} \frac{f_i(\bar{\mathbf{k}}_i,\ \mathbf{x}_s,\ x_s^0) d^3\bar{k}_i}{(2\pi)^3 2E_{\bar{\mathbf{k}}_i}} \prod_{j=F-F_s}^{F} \frac{d^3\bar{p}_j}{(2\pi)^3 2E_{\bar{\mathbf{p}}_j}} \prod_{i=I-I_s}^{I} \frac{f_i(\bar{\mathbf{k}}_i,\ \mathbf{y}_d,\ y_d^0) d^3\bar{k}_i}{(2\pi)^3 2E_{\bar{\mathbf{k}}_i}} \cdot$$

$$\cdot d\mathbf{x}_s dy_d^0 d\mathbf{y}_d \sqrt{2\pi\sigma^2} \frac{4}{\pi^3 L^2}\ 2 \left(\sqrt{\frac{\pi}{2\sigma^2}} \right)^{-1} \cdot$$

$$\cdot (\pi)^8 \frac{1}{\sigma^2} \left(\sum_{i,\,j} V_{\alpha i}^* V_{\beta i} V_{\alpha j} V_{\beta j}^*\ e^{-\frac{1}{2\sigma^2} \frac{1}{4} \left(m_i^2 - m_j^2 \right)^2 \frac{1}{4\lambda^4} L^2} e^{-i\frac{1}{2\lambda}\left(m_i^2 - m_j^2 \right) L} \right) \cdot$$

$$\cdot \delta^4(\bar{p}_s - \bar{k}_s + q(\lambda)) \delta^4(\bar{p}_d - \bar{k}_d - q(\lambda)) \sum_{\text{spins}} |\mathscr{M}_s|^2 \sum_{\text{spins}} |\mathscr{M}_d|^2 \tag{A.70}$$

$$|\mathscr{M}_d|^2 = |\bar{\mathsf{C}}_d^p \nu|^2 = |\bar{\mathsf{C}}_d^p(\{\bar{k}_i\}_d,\ \{\bar{p}_j\}_d) \nu(q)|^2 \tag{A.71}$$

$$|\mathscr{M}_s|^2 = |\bar{\nu} \mathsf{C}_s^p|^2 = |\bar{\nu}(q) \mathsf{C}_s^p(\{\bar{k}_i\}_s,\ \{\bar{p}_j\}_s)|^2 \tag{A.72}$$

$$d\Gamma = \frac{dN}{dy_d^0} = \int \prod_{j=1}^{F_s} \frac{d^3\bar{p}_j}{(2\pi)^3 2E_{\bar{\mathbf{p}}_j}} \int \prod_{i=1}^{I_s} \frac{f_i(\bar{\mathbf{k}}_i,\ \mathbf{x}_s,\ x_s^0) d^3\bar{k}_i}{(2\pi)^3 2E_{\bar{\mathbf{k}}_i}} \prod_{j=F-F_s}^{F} \frac{d^3\bar{p}_j}{(2\pi)^3 2E_{\bar{\mathbf{p}}_j}} \cdot$$

$$\cdot \int \prod_{i=I-I_s}^{I} \frac{f_i(\bar{\mathbf{k}}_i,\ \mathbf{y}_d,\ y_d^0) d^3\bar{k}_i}{(2\pi)^3 2E_{\bar{\mathbf{k}}_i}} \int d\mathbf{x}_s \int d\mathbf{y}_d \frac{4}{\pi^3 L^2}\ 4 \cdot$$

$$\cdot (\pi)^8 \mathscr{P}_{\text{mix}}(\sigma(\lambda),\ L) \delta^4(\bar{p}_s - \bar{k}_s + q(\lambda)) \delta^4(\bar{p}_d - \bar{k}_d - q(\lambda)) \cdot \sum_{\text{spins}} |\mathscr{M}_s|^2 \sum_{\text{spins}} |\mathscr{M}_d|^2 \tag{A.73}$$

Mixing probability (compare with Eq. (1.31) which was found using non-relativistic quantum mechanics)

$$\boxed{\mathscr{P}_{\rm mix}(\sigma(\lambda),\ L) = \sum_{i,\,j} V^*_{\alpha i} V_{\beta i} V_{\alpha j} V^*_{\beta j}\ e^{-\frac{1}{2\sigma^2}\frac{1}{4}\left(m_i^2-m_j^2\right)^2 \frac{1}{4\lambda^4} L^2} e^{-i\frac{1}{2\lambda}\left(m_i^2-m_j^2\right)L}} \tag{A.74}$$

Taking into account that neutrino three-momentum is equal to $\mathbf{q} = \mathbf{q}(\lambda,\ L)$, equation (A.41), $q^0 = \lambda = \lambda(\{\bar{k}_i\}_s,\ \{\bar{p}_j\}_s,\ \{\bar{k}_i\}_d,\ \{\bar{p}_j\}_d)$, equations (A.42), and (A.32), in case there is only one incoming particle inside the detector $|\text{in(detector)}\rangle$ we can introduce the quantity of differential cross-section [124])

$$d\sigma = \frac{1}{2\lambda 2E_{\bar{\mathbf{k}}_{1\,d}}} \prod_{j=F-F_s}^{F} \frac{d^3\bar{p}_j}{(2\pi)^3 2E_{\bar{\mathbf{p}}_j}} (2\pi)^4 \delta^4(\bar{p}_d - \bar{k}_{1\,d} - q(\lambda)) \sum_{\rm spins} |\mathscr{M}_d|^2 \tag{A.75}$$

$4\sqrt{(qk_{1\,d})^2 - m_\nu^2 m_{1\,d}^2} = 4\lambda E_{\bar{\mathbf{k}}_{1\,d}}$ $(m_\nu \ll \lambda)$.

$$\begin{aligned} d\Gamma = \left[d\sigma 2\lambda \int \frac{f_{1\,d}(\bar{\mathbf{k}}_{1\,d},\ \mathbf{y}_d,\ y_d^0) d^3\bar{k}_{1\,d}}{(2\pi)^3 2E_{\bar{\mathbf{k}}_{1\,d}}}\right] \int \prod_{j=1}^{F_s} \frac{d^3\bar{p}_j}{(2\pi)^3 2E_{\bar{\mathbf{p}}_j}} \int \prod_{i=1}^{I_s} \frac{f_i(\bar{\mathbf{k}}_i,\ \mathbf{x}_s,\ x_s^0) d^3\bar{k}_i}{(2\pi)^3 2E_{\bar{\mathbf{k}}_i}} \cdot \\ \cdot \int d\mathbf{x}_s \int d\mathbf{y}_d \frac{4}{\pi^3 L^2}\ 4 \cdot \\ \cdot (\pi)^4 \mathscr{P}_{\rm mix}(\sigma(\lambda),\ L) \delta^4(\bar{p}_s - \bar{k}_s + q(\lambda)) \sum_{\rm spins} |\mathscr{M}_s|^2 \end{aligned} \tag{A.76}$$

where $d\Gamma$ is a differential event rate, with integration variable $\lambda \to E_{\mathbf{q}}$,

$$\begin{aligned} d\Gamma(\{\bar{k}\},\ \{\bar{p}\},\ L) = \Big[\int_0^{+\infty} \frac{1}{L^2} \frac{E_{\mathbf{q}}^2 dE_{\mathbf{q}}}{(2\pi)^3 2E_{\mathbf{q}}} \left[\prod_{i=1}^{I_s} \frac{1}{2E_{\bar{\mathbf{k}}_i}}\right] \left[\int \prod_{j=1}^{F_s} \frac{d^3\bar{p}_j}{(2\pi)^3 2E_{\bar{\mathbf{p}}_j}}\right] \cdot \\ \cdot \sum_{\rm spins} |\mathscr{M}_s|^2 (2\pi)^4 \delta^4(\bar{p}_s - \bar{k}_s + q(E_{\mathbf{q}}))\Big] \mathscr{P}_{\rm mix}(\sigma(\lambda),\ L) d\sigma(\{\bar{p}\}_d,\ \bar{k}_{1\,d},\ E_{\mathbf{q}}) \end{aligned} \tag{A.77}$$

Finally, the event rate is

$$\begin{aligned} \Gamma = \int \frac{f_{1\,d}(\bar{\mathbf{k}}_{1\,d},\ \mathbf{y}_d,\ y_d^0) d^3\bar{k}_{1\,d}}{(2\pi)^3} \int \prod_{i=1}^{I_s} \frac{f_i(\bar{\mathbf{k}}_i,\ \mathbf{x}_s,\ x_s^0) d^3\bar{k}_i}{(2\pi)^3} \cdot \\ \cdot \int d\mathbf{x}_s \int d\mathbf{y}_d d\Gamma(\{\bar{k}\},\ \{\bar{p}\},\ L) \end{aligned} \tag{A.78}$$

A.10 Reactor antineutrino experiments

Ultimately, our detector did not succeed; however, even if it had succeeded, there would still be a further challenge in getting the observed vs. predicted antineutrino flux ratio right. Significantly, in this field of study, only a handful of experiments are successful. "Success" here means being able to put a data point on the baseline plot, shown in Fig. A.20. In addition to issues with the detectors themselves, getting these very projects approved by nuclear reactor facilities is also an issue. In this section, we briefly discuss the main components of these and other milestone reactor antineutrino experiments.

Nuclear reactors are complicated facilities, with a number of different isotopes produced in the core. As a result, the exact spectrum and neutrino event rates are not perfectly understood. For example, consider the recent observations of the $\sim$ 5-MeV "bump" in the neutrino spectrum (DayaBay [128], RENO [129], DoubleChooz [130], and NEOS [131]). There have been several attempts to explain these observations by recalculating the neutrino spectrum [132]; however, there is one most-recent consistent explanation [133] that attributes the bump to $^{12}C^*$ de-excitation yielding 4.4 MeV gamma, which then travels a relatively long distance (also, explaining why the segmented DANSS doesn't see the bump due to its trigger scheme).

An mTC-like detector with sufficient statistics may make a significant contribution to sorting out these ambiguities.

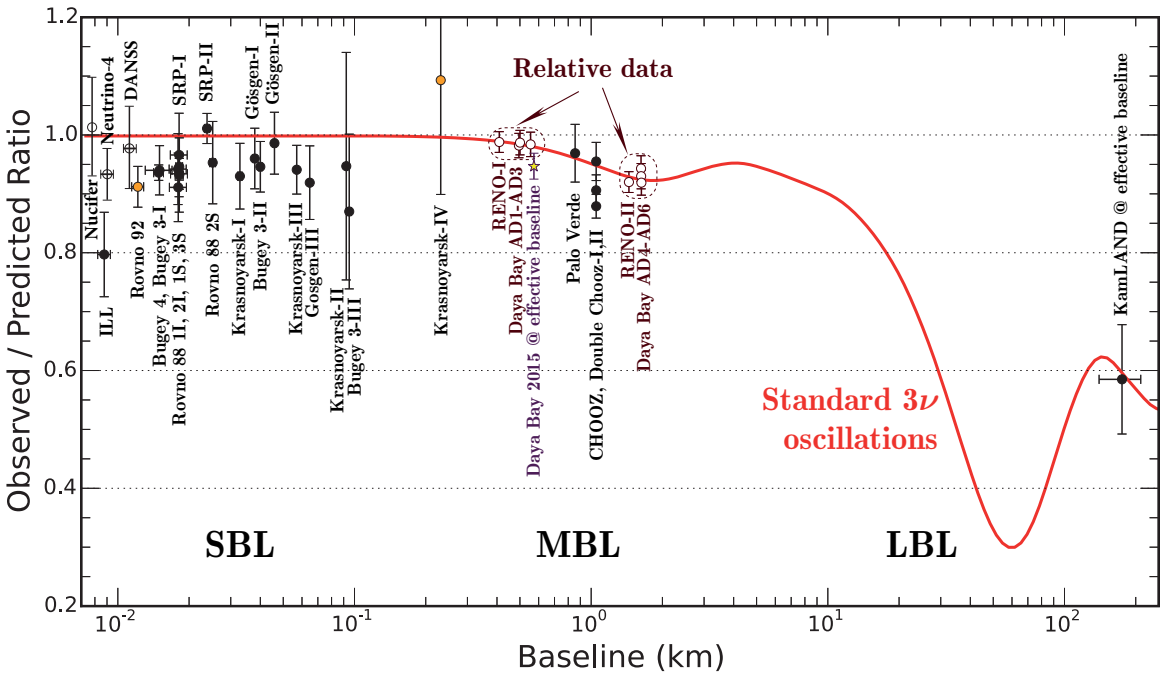

Figure A.20: Most of the reactor antineutrino experiments. Figure is adapted from [134] and [49].

A.10.1 Hanford. First attempt to detect reactor antineutrinos.

The detector had 90 2″ PMTs mounted on the wall of the cylinder tank, 75 cm in diameter, filled with 300 liters of liquid scintillator [135]. It was named unofficially "Herr Auge" (German for Mr. Eye).

Advantages: later used to measure natural human radioactivity – full body counter. Sensitive to ^{40}K.

Disadvantage: High background, and electronics noise.

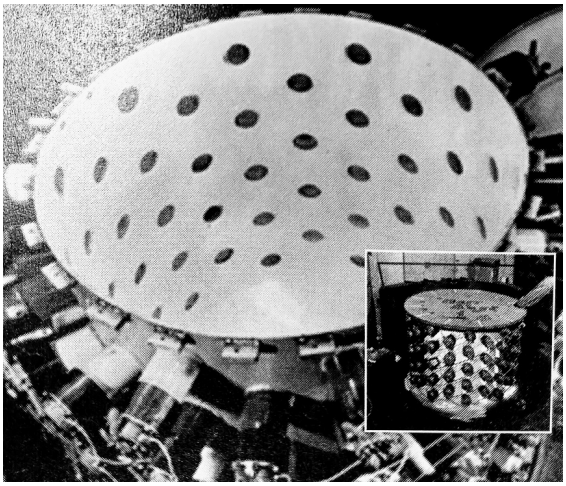

(a) Photograph of the opened detector before liquid scintillator was poured. The inset is a side view.

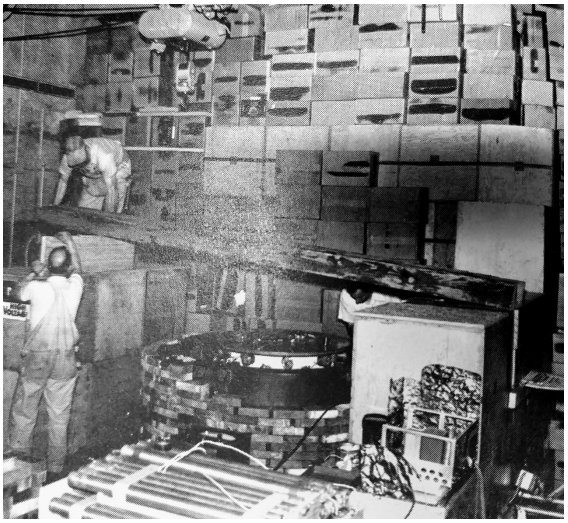

(b) Detector by the reactor. Shielding is being assembled.

Figure A.21: Hanford detector. Figures are taken from [136].

A.10.2 Savannah River experiment. First observation of neutrinos. 1956.

Baseline: 11 meters from the reactor center.

Detector was located 12 meters underground in a massive building, contained two tanks of water with cadmium salts diluted in the water, and three large tanks of liquid scintillator, each tanks was viewed by 110 PMTs.

Shielding: poly and lead bricks.

Disadvantage: toluene (part of the liquid scintillation mixture) is toxic and inflammable, and Cadmium salts are highly toxic.

Advantage: relatively pure ^{235}U fuel.

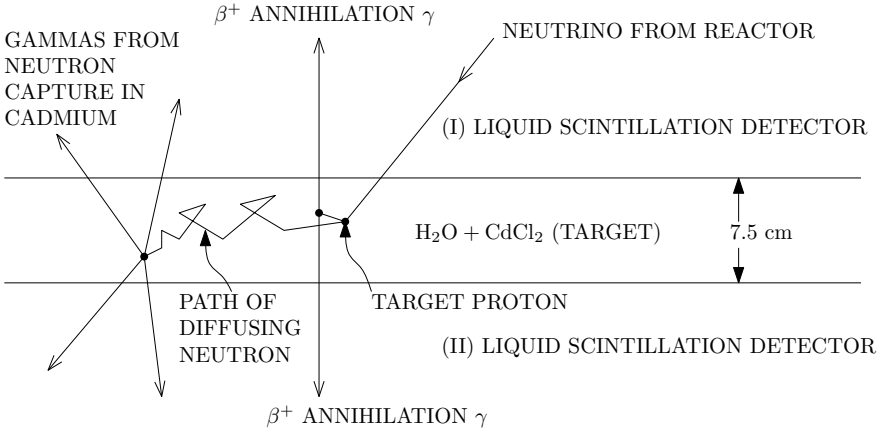

(a) Detection mechanism, an adaptation from [65].

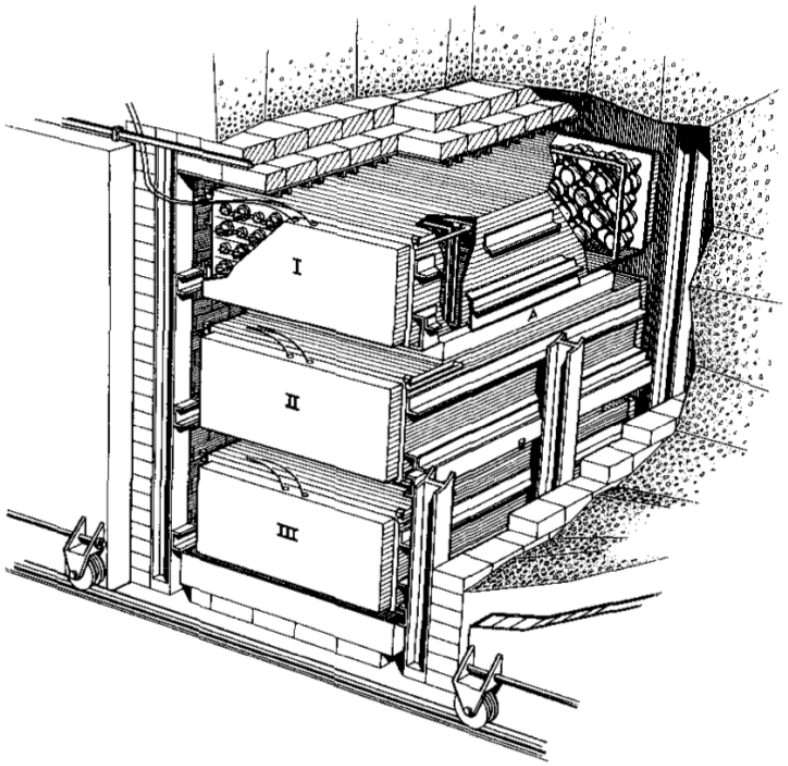

(b) The detector's 3 tanks of liquid scintillator, and 2 tanks of water in between them [137].

Figure A.22: Savannah River experiment.

A.10.3 KamLAND

Perhaps, the most famous and challenging detector of reactor antineutrinos, which were coming from $\sim$ 50 Japanese reactors (when they were in operation), and a few Korean reactors, at very different baselines.

Distance: 180 km (flux-averaged).

Advantages: high detector volume, and low backgrounds. KamLAND uses unique digitization scheme, with three different amplification regimes (20x, 4x, .5x) which makes a large dynamic range 1–1000 p.e. from PMT.

Results: first observation of a disappearance of reactor antineutrinos due to neutrino oscillations [69] and first observation of geo-neutrinos [60].

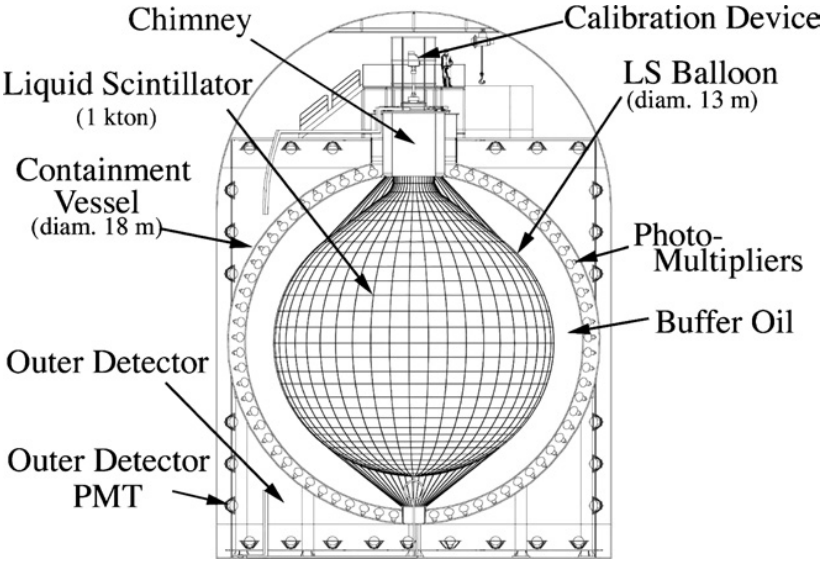

(a) Detector [69].

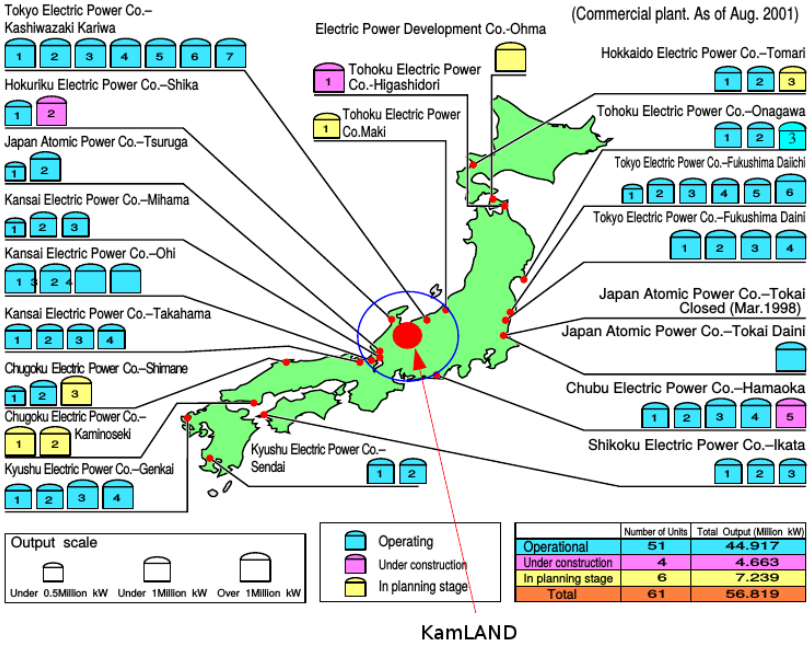

(b) Location of KamLAND and Japanese reactors [84].

Figure A.23: The KamLAND experiment.

A.10.4 SRP-II. Savannah river two-position experiment. 1996.

Baseline: the detector was placed at two different positions — 18 m and 24 m.

Reactor: 2000 MW_{th}. Neutrino flux: $\sim 10^{13}$ $\bar{\nu}_e s^{-1} cm^2$ at 20 m from the core.

Advantages: relatively pure ^{235}U fuel, with ^{239}Pu fissions constituted less than 8%, ^{238}U less than 4 %. For neutrino energies 2-8 MeV the difference from pure ^{235}U was less than 1.5%. Reactor cycles composes of several short reactor-on periods with even shorter reactor-off periods which yields approximately constant neutrino spectrum.

Detector: 21 5" EMI hemispherical PMTs viewing a stainless steel cylindrical tank containing 275 l of xylene-based 0.5 % Gd-loaded liquid scintillator with PSD capabilities. That tank (target) is situated in another steel tank (blanket) containing 1100 l of a mineral oil based scintillator, optically divided into uppper and lower portions each viewed by 30 5" flat faced PMTs. The larger tank is surrounded by 2" low-background lead – a shield against gamma and charged particles. Then there is an active shield made of a 3"-thick plastic scintillator – operating in an anticoincidence mode to ignore cosmic muon events. Finally, a 8"-thick layer of lead completely surrounds the active shielding layer in order to reduce very large flux of gammas coming from gammas from the heat exchangers of the reactor. Total shield weight ∼50 tons.

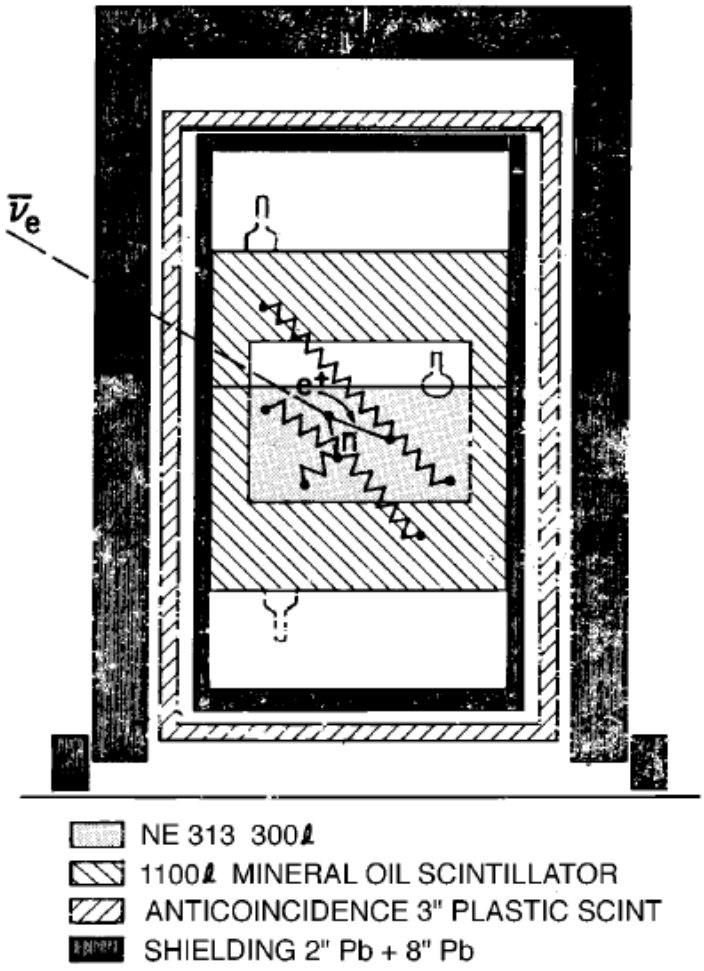

Figure A.24: Savannah River Project, mobile detector [138]

A.10.5 ILL

Baseline: 8.76 m.

Detector: 30 target cells (9cm x 20 cm x 88 cm, outside dimensions, 6 mm thick walls made of lucite) filled a 'mineral-oil–based proton-rich" liquid scintillator NE235C, PSD capable. Total volume of scintillator 377 l – 2.39 $\times 10^2 8$ protons. 4 large ^{3}He wire chambers are sandwiched in between the 5 groups of 6 target cells. PMTs: 60, each cell is viewed by two optically coupled 3″ PMTs – high gain, fast timing, low-dark-current tube (as of 1980s).

Main reaction: inverse-beta decay. antineutrino from a reactor is captured on proton in a liquid scintillator producing positron and neutron. Positron slows down by ionization – prompt signal, before stopping and annihilating with an electron producing two 511-keV gammas. Most of annihilation gammas escape target cell (absorption length 14 cm). The neutron (few keV) thermalizes in a target cell and diffuses into ^{3}He chamber (mean diffusion time 150 μs), before being captured on ^{3}He:

$$n + {}^3\mathrm{He} \rightarrow p + {}^3\mathrm{H} + 765\mathrm{keV} \qquad \text{(cross section 5550 b for thermal neutron)} \quad \text{(A.79)}$$

Advantage: potentially capable of directionality, very short baseline, PSD capabilities.

Disadvantage: usage of ^{3}He which is hard to get these days.

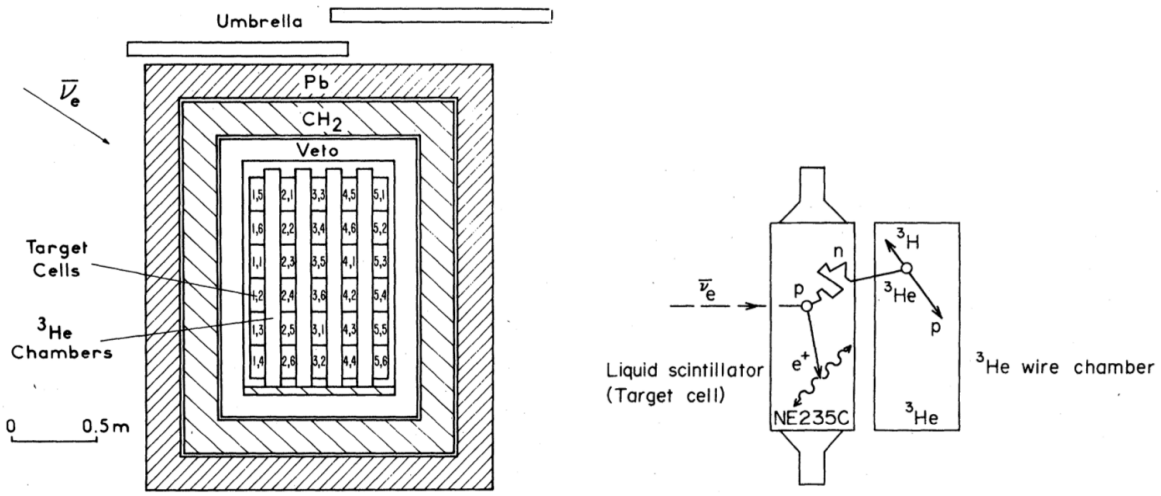

(a) Detector diagram [139]. (b) Main reaction [139].

Figure A.25: Institut Laue Langevin (ILL) experiment. Figures are taken from [139]

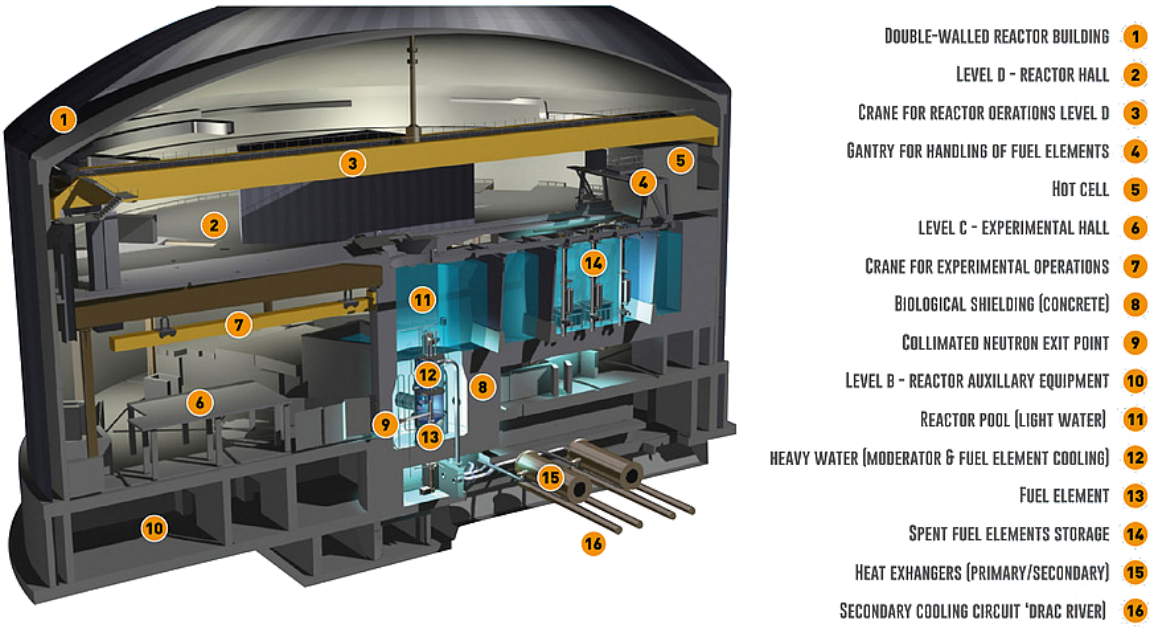

Figure A.26: ILL reactor. Figure is from public domain.

A.10.6 Bugey

Distance: 15, 40, and 95 m.

Reactor: 2800 MW thermal power, Bugey (France) nuclear power plant.

Detector: similar to the ILL experiment — 5 planes of 6 target cells, each filled with liquid scintillator (with PSD capabilities), total volume 321 l. 4 PMTs per cell (to reduce dark counts). Thermalized neutrons from IBD reaction captured in ^{3}He chambers.

Typical energy resolution: 20% FWHM at 1 MeV positron energy. Neutron detection efficiency ∼26%.

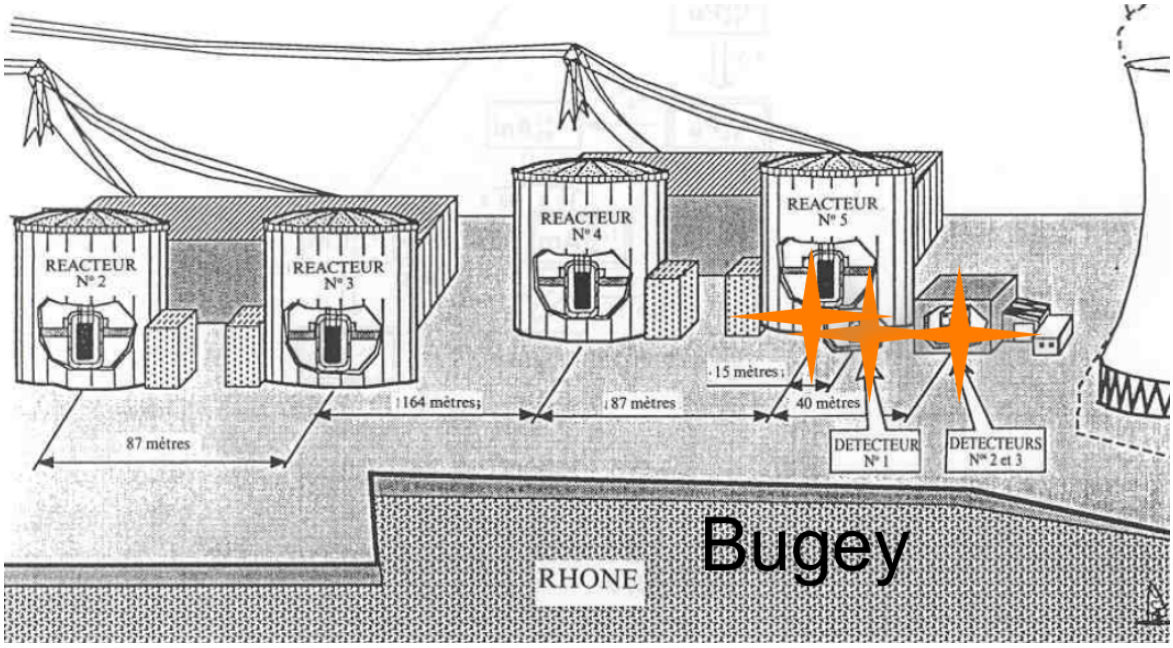

Figure A.27: Bugey power plant and three detector locations [140].

A.10.7 Gösgen

The detector is essentially the same, as in the ILL experiment. The difference is the new reactor, and three different positions of the detector.

Reactor: 2800 MW thermal power, Gösgen, Switzerland. $5 \times 10^20\ \bar{\nu}_e/s$.

Results: neutrino energy spectrum was measured at three different positions of the detector. The result is consistent with ILL. New limits on the neutrino mixing parameters were obtained.

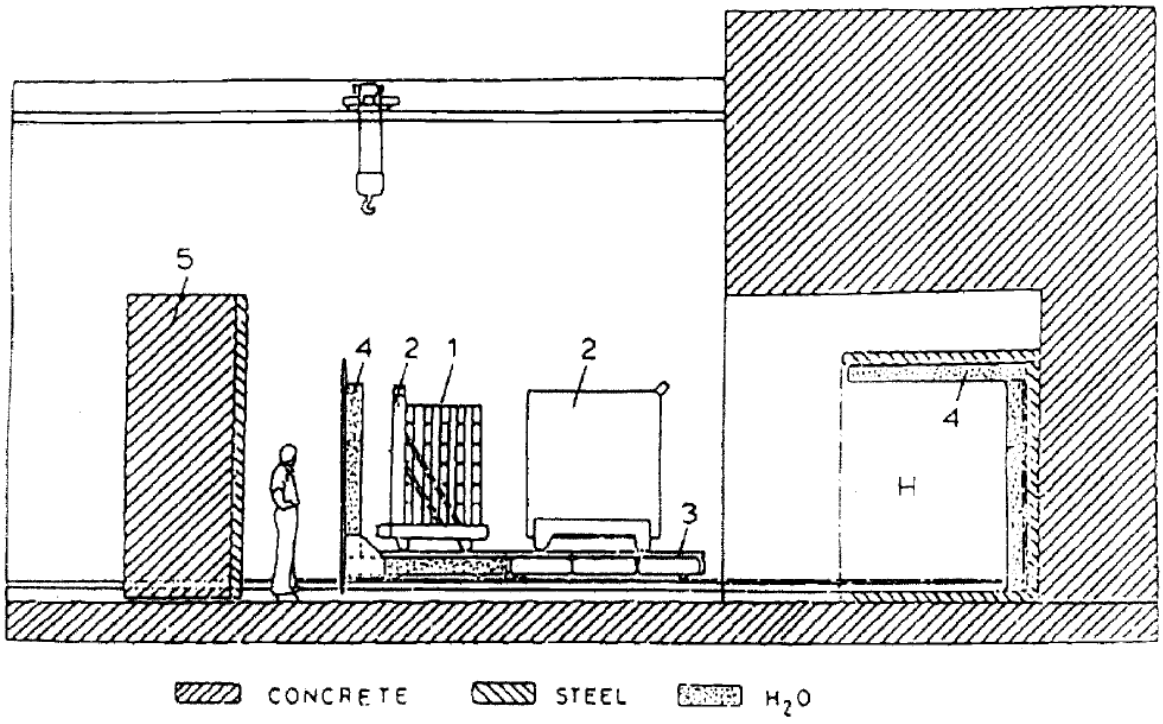

Figure A.28: Gösgen (ILL) detector main parts including shielding [141]. 1 — central detector unit, 2 — tanks of active veto, 3 — rails on which various parts move, 4 — water tanks, and 5 — movable concrete door.

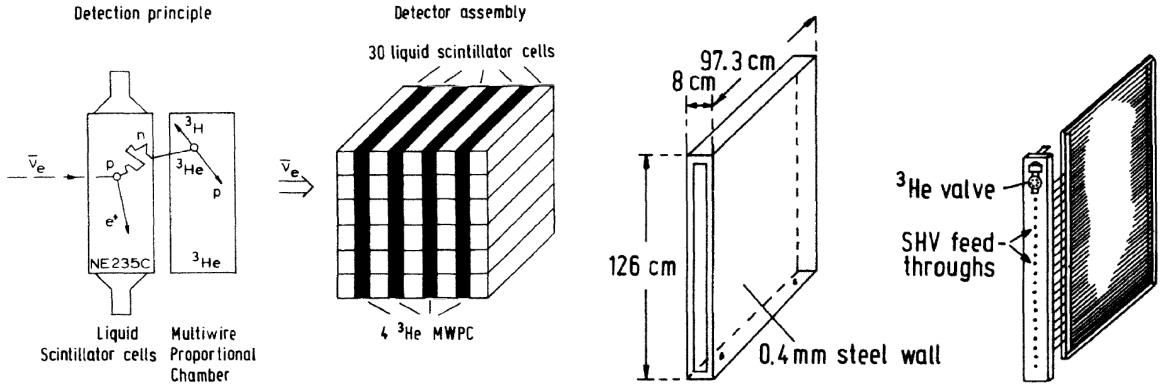

(a) Detection mechanism (same as in ILL). (b) ^{3}He counter chamber.

Figure A.29: Gösgen detectors. Figures are taken from [141].

A.10.8 RENO

RENO was the first experiment to utilize two identical near and far detectors.

Reactor: 6 pressurized-water reactors (2 x 2.775 GWth, 4 x 2.815 GWth), Hanbit Nuclear Power Plant, Korea.

Detector: 2 identical 16-ton Gd-doped liquid scintillators. The reactor flux-weighted baseline is 410.6 m for the near detector and 1445.7 m for the far detector.

Results: determining mixing angle θ_{13} (along with DayaBay and Double Chooz), neutrino mass square difference, and confirmed 5 MeV bump in neutrino spectrum (along with DayaBay). RENO-50 will be a bigger version at a much larger baseline (47 km).

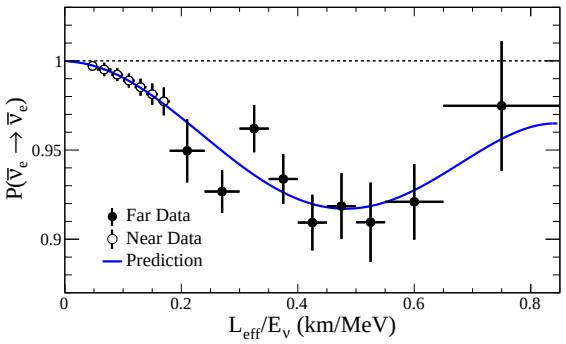

(a) RENO observed oscillation pattern.

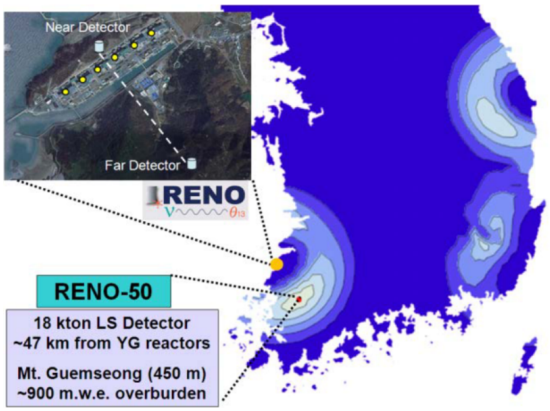

(b) RENO and RENO-50 locations with respect to the power reactors.

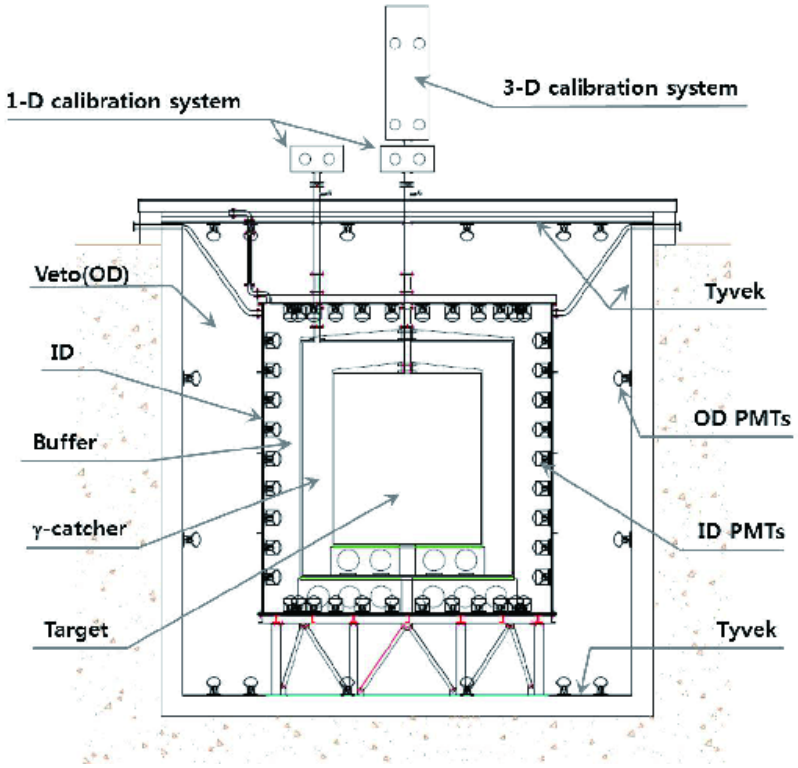

(c) One of the detector.

Figure A.30: The RENO experiment. Figures are taken from [129].

A.10.9 Palo Verde

Distance: 750m,2 x 890m. First long baseline experiment.

Reactors: three identical pressurized water high-purity reactors. Palo Verde Power Generating station in Arizona, total thermal power 11.6 GW.

Detector: 32 m.w.e. overburden (5x muon flux reduction), triple coincidence for both signals prompt and delayed.

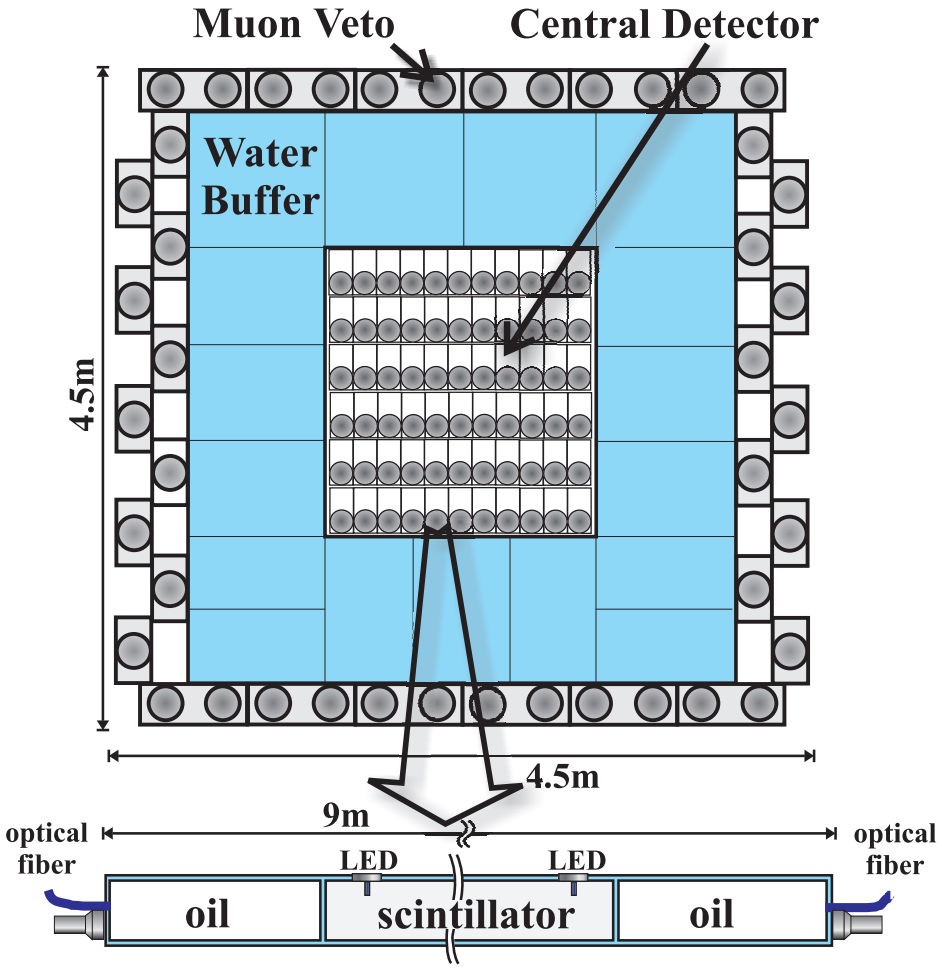

Figure A.31: Palo Verde detector [142].

A.10.10 CHOOZ

Detector: the target 5-ton 0.09 % Gd-loaded liquid scintillator in a transparent acrylic container was suspended in an intermediate 70-cm thick region filled with 17-ton undoped high flash point liquid scintillator surrounded by 192 8" PMTs (15 % surface coverage, 150 pe/MeV). Such separation is chosen to protect the target from PMT radioactivity and to distinguish gamma rays from neutron capture.

The cylindrical steel tank (5.5 m diameter and 5.5 m height) painted with high reflectivity paint on the inside filled with the same scintillator as an intermediate volume and optically (8mm-thick acrylic layer) separated from it was surrounded by 2 rings of 24 8" PMTs.

Distance: 1 km. Distance between two reactors 116.7 m.

Result: the best limit on Δm^2 parameter at that time. First detector with neutrino directionality capabilities.

Advantages: high purity reactor, high overburden.

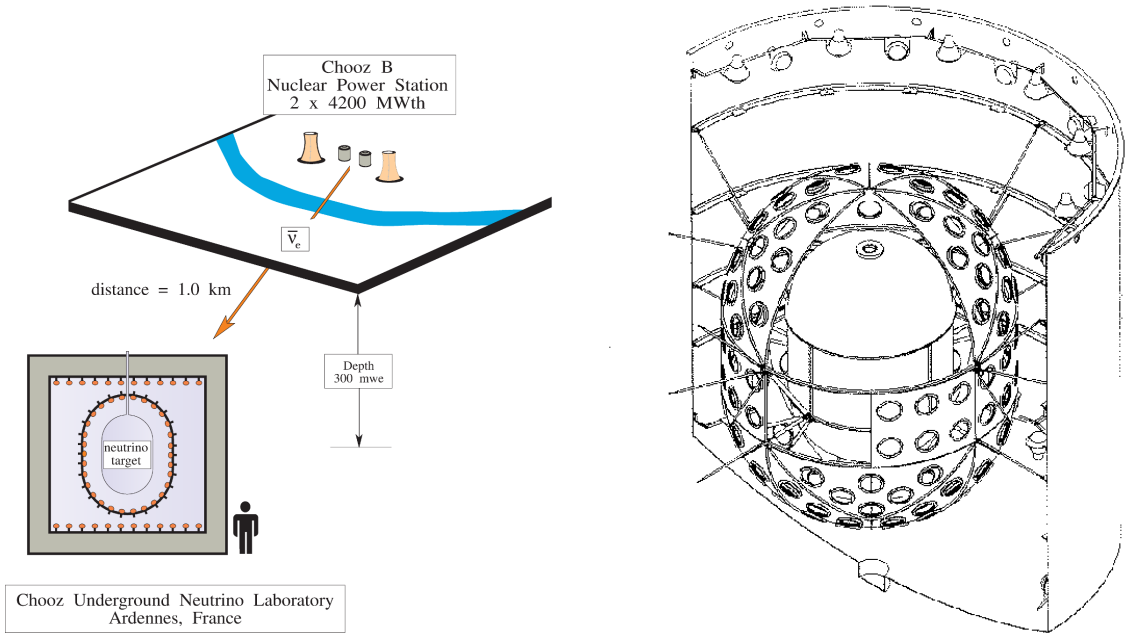

(a) Detector location. (b) Detector diagram.

Figure A.32: CHOOZ experiment. Figures are taken from [143].

A.10.11 Double CHOOZ

Optical instability of the Gd-loaded scintillator in CHOOZ lead to an upgrade.
Result: first measurement of θ_{13} from delayed neutron capture on hydrogen.

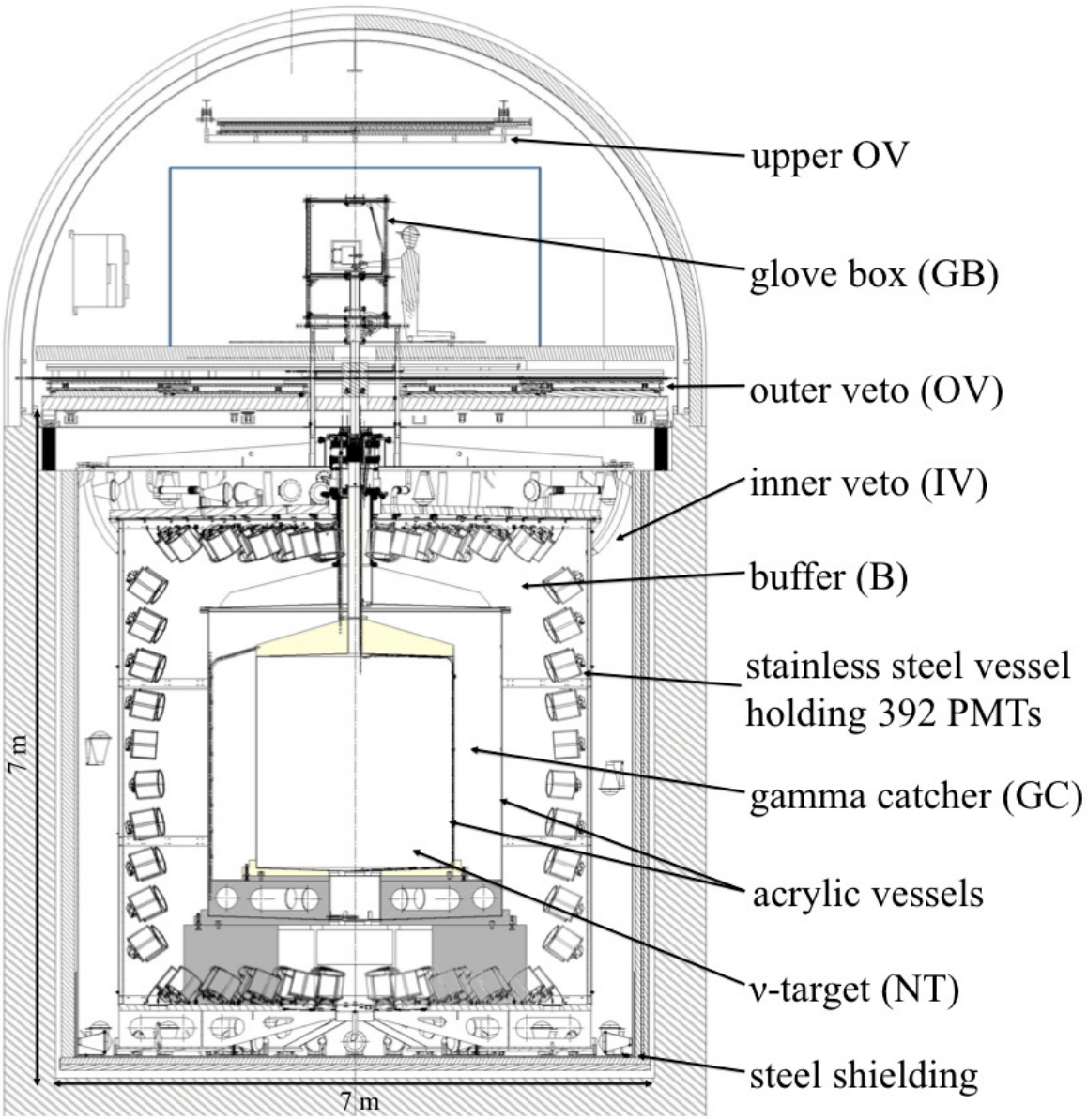

Figure A.33: Schematic diagram [144].

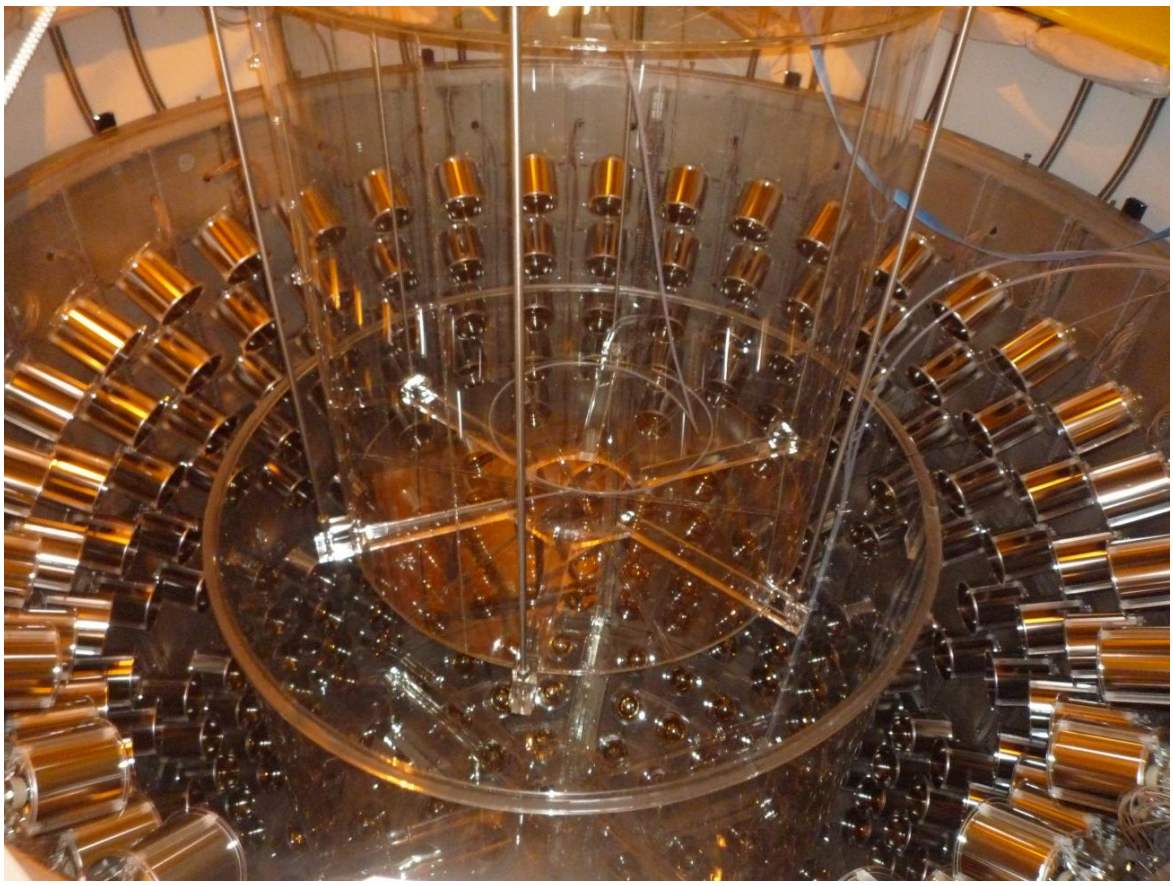

Figure A.34: Interior of the Double CHOOZ detector (photo credit Th. Lasserre, CEA/Imagin'In IRFU).

A.10.12 Rovno

Target: pure water (no positron tagging), ^{3}He proportional counters in the water to detect neutron IBD neutrons.

Baseline: 12 m.

Power: 1375 MW thermal.

Detector: stainless-steel tank filled with 1300 liters of distilled water, surrounded by 140 neutron ^{3}He counters. Hydrogen in the water is the neutrino target and neutron moderator, number of protons — 2.53×10^{28} protons.

Result: $\sim 3 \times 10^4$ $\bar{\nu}_e$ were detected. One of the first very precise measurements of the number of antineutrinos emitted in the nuclear reactor. Analyzing antineutrino spectrum it was shown accumulation of ^{239}Pu (part of the IAEA program for non-proliferation). Precision measurement of energy production at the water-cooled water moderated reactor (VVER-440).

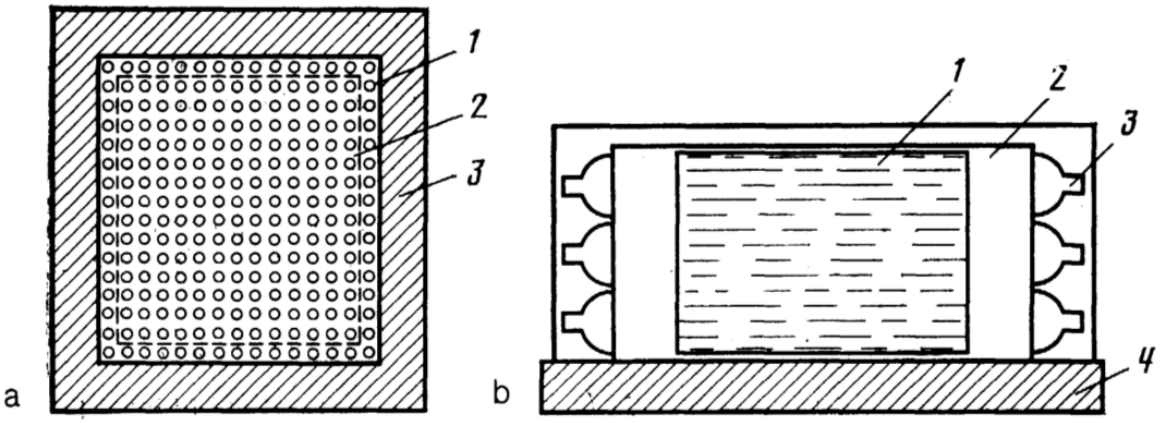

Figure A.35: Rovno two detectors. Left (a) the integrating detector: 1 — proportional counter filled with ^{3}He, 2 — polyethylene, 3 — borated polyethylene. Right (b) the scintillation-counter spectrometer: 1 — liquid scintillator, 2 — lightguide, 3 — PMT, 4 — borated polyethylene. Figures and captions are taken from [145].

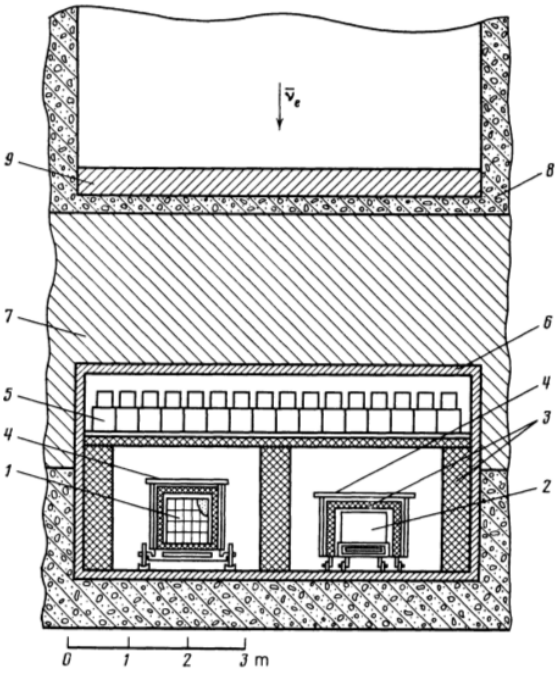

(a) Schematic diagram of the experimental setup: 1 — integrating detector, 2 — scintillation-counter spectrometer, 3 — polyethylene, 4 — scintillators of the anticoincidence shield, 5 — tanks containing the liquid scintillator (anticoincidence "hood"), 6 — steel, 7 — heavy concrete, 8 — concrete, 9 — additional shielding.

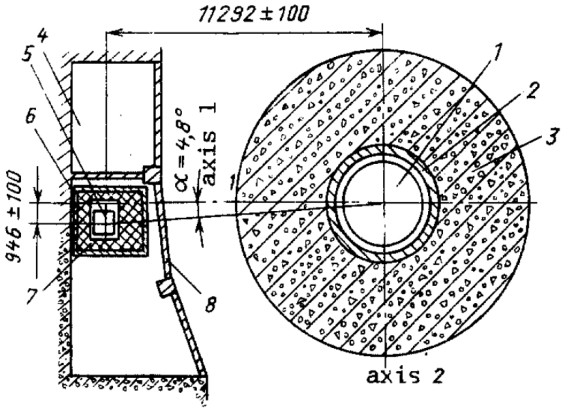

(b) Location of ionization chambers: 1 — reactor core, 2 — reactor vessel, 3 — concrete radiation shield, 4 — room for electronic apparatus of neutrino detector, 5 — neutrino detector, 6 — iron castle, 7 — polyethylene, 8 — brick wall.

Figure A.36: ROVNO detector locations relative to the reactor. Figures and captions are taken from [145].

A.10.13 Krasnoyarsk

Detection method: IBD.

Detector: 105 ^{3}He neutron counters are inserted into the plexiglass solid $80 \times 80 \times 97$ cm, total number of protons (hydrogen nuclei) 2.78×10^{28}, which also serves as a neutron moderator.

Reactor: $\sim 100\%$ ^{235}U, 7–9 days off periods, in every 50 days, located underground (excellent shielding from cosmogenic backgrounds).

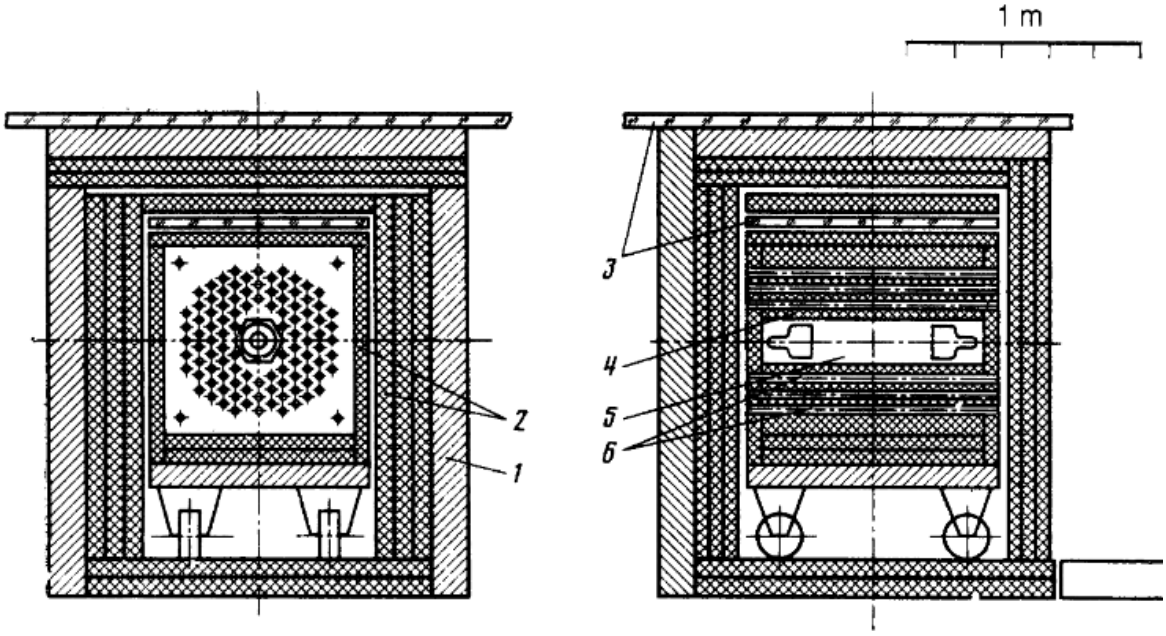

Figure A.37: Diagram of the Krasnoyarsk detector [146]. 1 — copper (gamma shielding), 2 — borated polyethylene (neutron shielding), 3 — active shielding, 4 — plexiglass (moderator/target), 5 — scintillator, 6 — ^{3}He neutron counters.

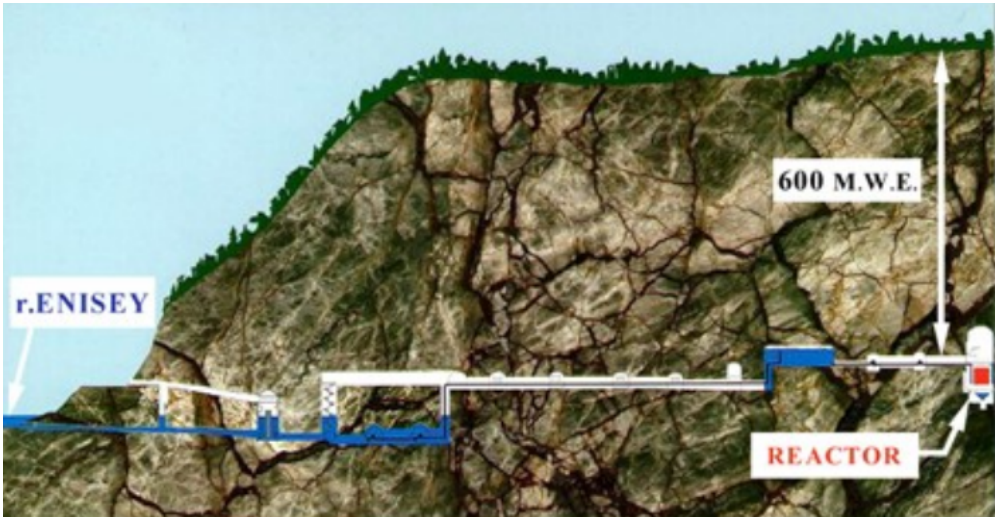

Figure A.38: Reactor's relative location in the Krasnoyarsk experiment. Different baselines were accessible [140].

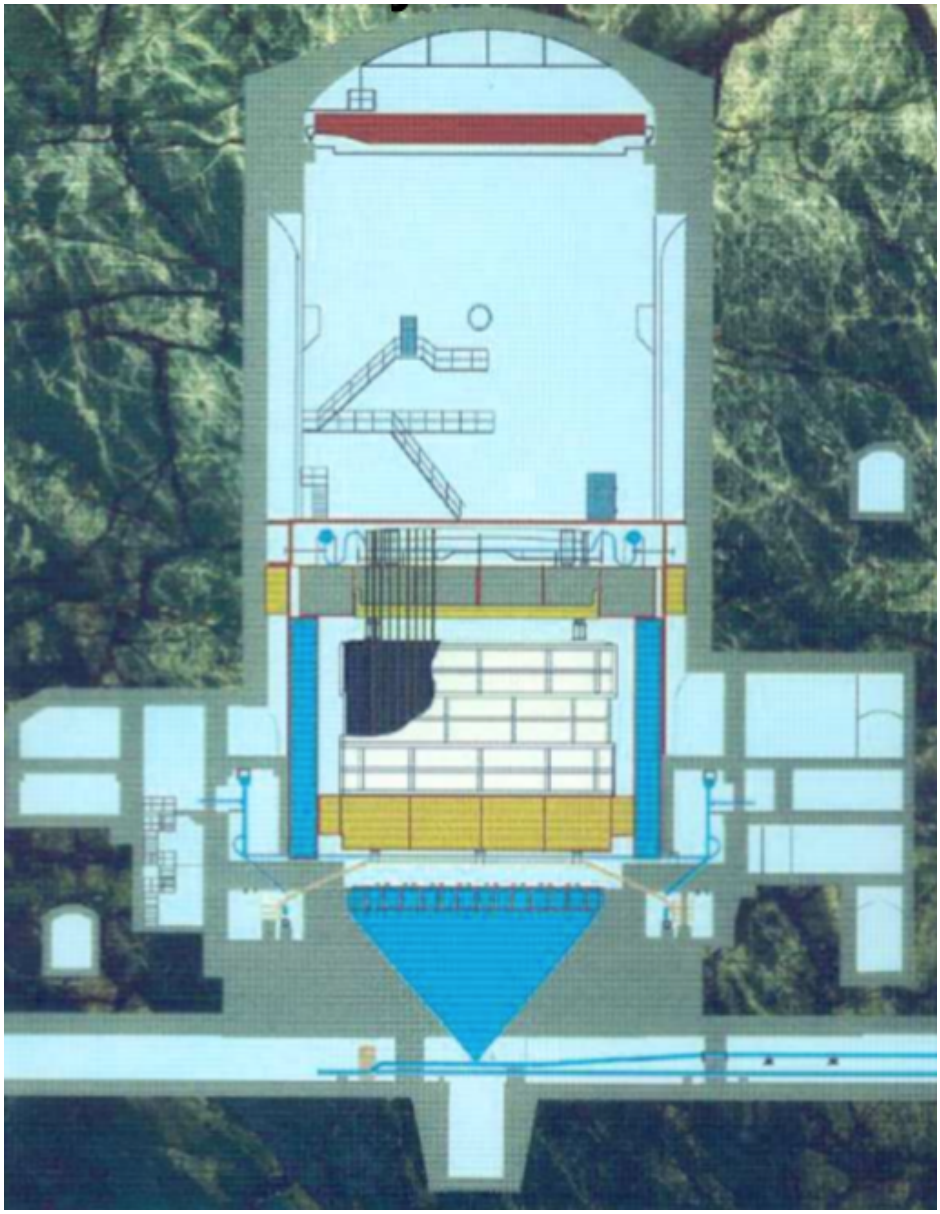

Figure A.39: Underground reactor in the Krasnoyark experiment. Figure is taken from [140].

A.10.14 Daya Bay

Results: first measurement of θ_{13}.

Detector: 6 identical antineutrino detectors (AD) placed at different baselines.

From the DayaBay article [147]: "Each AD consists of a cylindrical, 5-m diameter stainless steel vessel (SSV) that houses two nested, UV-transparent acrylic cylindrical vessels. A 3.1-m diameter inner acrylic vessel (IAV) holds 20 t of Gd-LS (target). It is surrounded by a region with 20 t of liquid scintillator (LS) inside a 4-m diameter outer acrylic vessel (OAV). Between the SSV and OAV, 37 t of mineral oil (MO) shields the LS and Gd-LS from radioactivity. IBD interactions are detected by 192 Hamamatsu R5912 PMTs. A black radial shield and specular reflectors are installed on the vertical detector walls and above and below the LS volume, respectively. Gd-LS and LS are prepared and filled into ADs systematically to ensure all ADs are functionally identical."

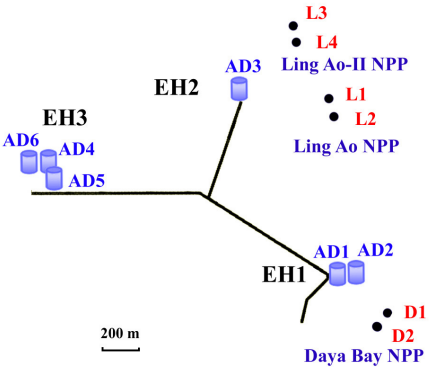

(a) Location of Daya Bay reactors (D1, D2, L1–L4) and detectors (AD1–AD6).

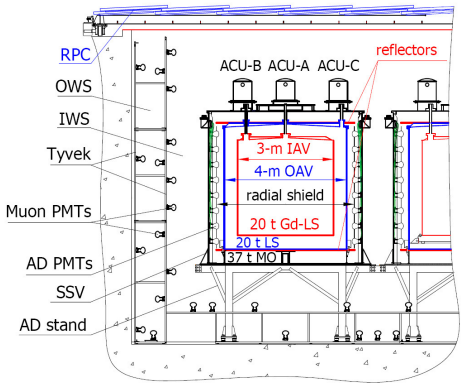

(b) Detector assembly.

Figure A.40: DayaBay experiment. Figures are taken from [147]. IWS and OWS — inner and outer water shields.

Besides having a range of different baselines and advantages for calibrations, having identical detectors is also greatly affecting the sensitivity of the instrument.

As demonstrated in the DayaBay technical design proposal [50], the method of swapping in case of two detectors with "desired" rates N and F for near and far locations respectively reduces systematic uncertainties by approximately a factor of a hundred. Having detector 1 with efficiency ϵ_1 in the near location and detector 2 with efficiency ϵ_2 in the far location, the rate ratio would be

$$\frac{N_1}{F_2} = \frac{\epsilon_1}{\epsilon_2}\frac{N}{F} \tag{A.80}$$

After swapping the detectors

$$\frac{N_2}{F_1} = \frac{\epsilon_2}{\epsilon_1}\frac{N}{F} \tag{A.81}$$

Combining two equations above the value for N/F is given by (to first order)

$$\frac{N}{F} = \frac{1}{2}\left(\frac{N_1}{F_2} + \frac{N_2}{F_1}\right)\left(1 + \frac{\delta^2}{2}\right)^{-1} \tag{A.82}$$

where $\delta\epsilon_1 - 1$. As noted in the DayaBay report [50], even for efficiencies different by as much as 1% the value of N/F to be determined to a fractional precision better than 10^{-4}.

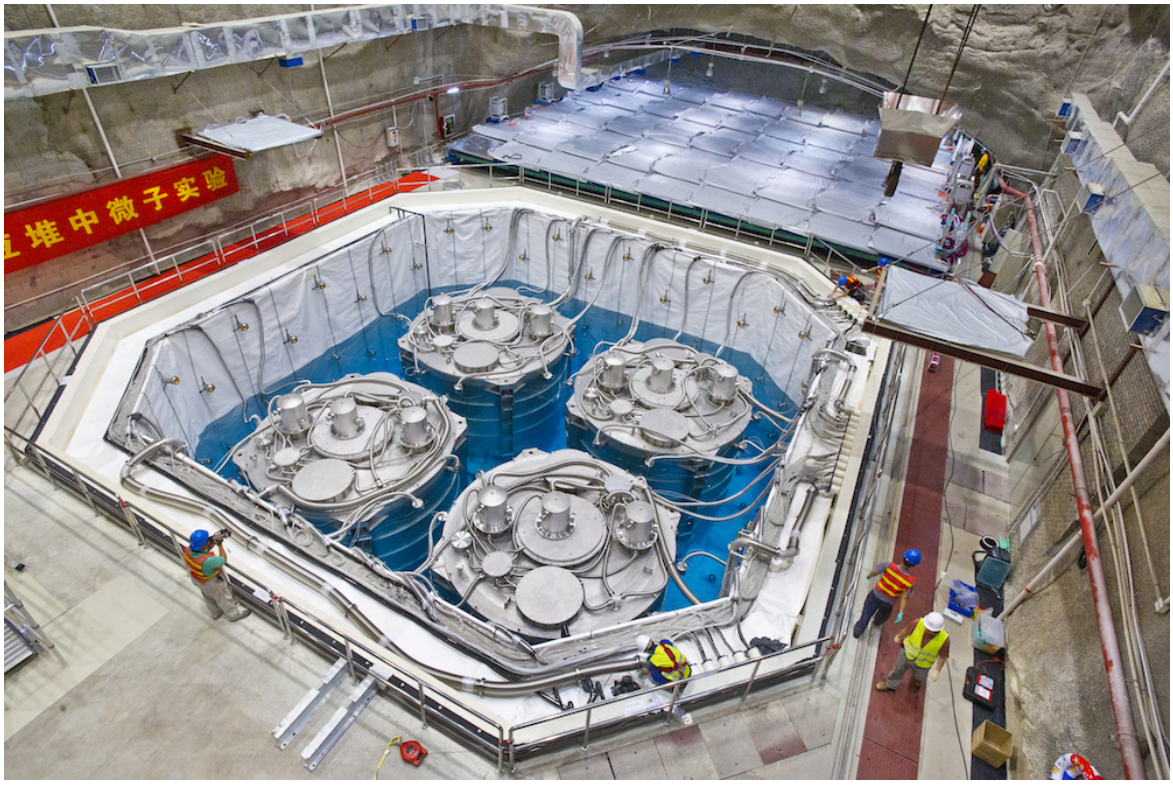

(a) One pool is being filled.

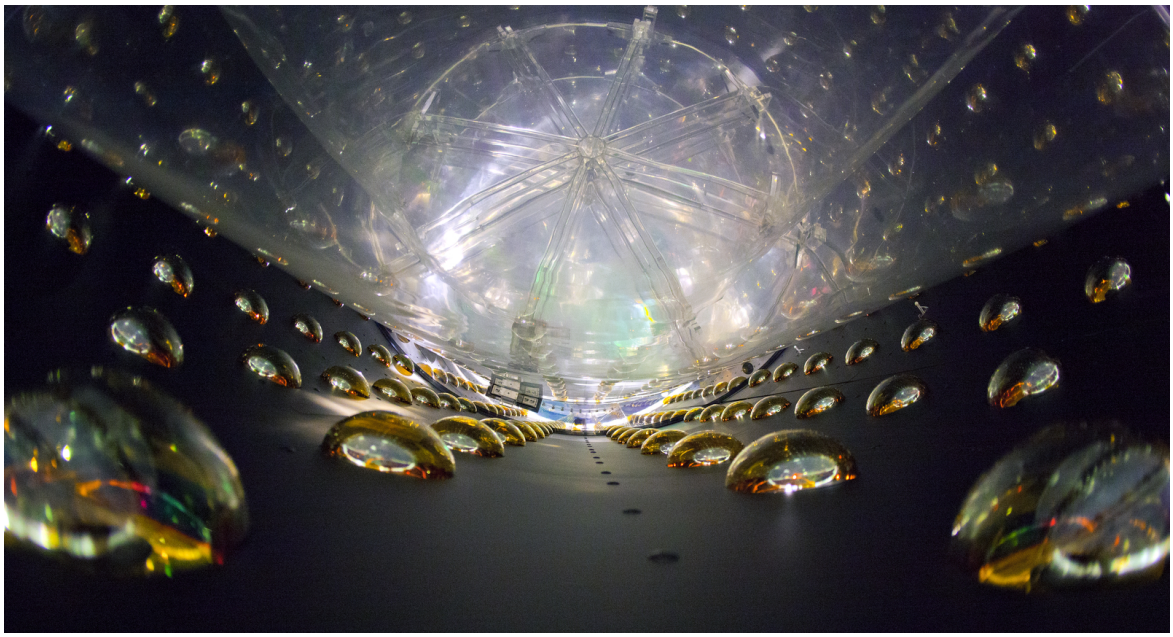

(b) PMTs.

Figure A.41: DayaBay experiment (photo by Roy Kaltschmidt / Berkeley Lab).

A.10.15 Nucifer

Result: a total of 40,760 $\bar{\nu}_e$ were detected in the Nucifer detector deployed ~ 7 m from the 70 MW_{th} compact $57 \times 57 \times 60$ cm^3 research Osiris reactor core [148]. The rate was ~ 281 observed antineutrino interactions per day. A study was performed how a Nucifer-like detector can be used to monitor a disposition of weapon-grade plutonium in nuclear reactors.

Detector: ~ 847 liters of 0.17% Gd-doped liquid scintillator inside a cylindrical stainless steel vessel $\varnothing 1.25$ m $\times \sim 1.4$ m, the inside of which is coated with reflective white Teflon. The volume is viewed by 16 8″ PMTs, located at the top. The overall dimensions with the shielding is $3 \times 3 \times 2.4$ m^3. Additionally, two 10-cm thick and one 4-cm thick lead walls were built to further suppress reactor-induced gammas. Muon veto consists of 32 plastic scintillator bars ~ 1.6 m $\times 25$ cm $\times 5$ cm. It is worth noting that the muon veto thickness (5 cm) was optimized to discriminate between cosmic muons and high-energy gammas. Muon energy deposition passing through the scintillator of the veto is 10 MeV, the same as the highest gamma energy (gamma from neutron capture on metal or concrete surroundings of the detector). Muon detection efficiency is 97% [148].

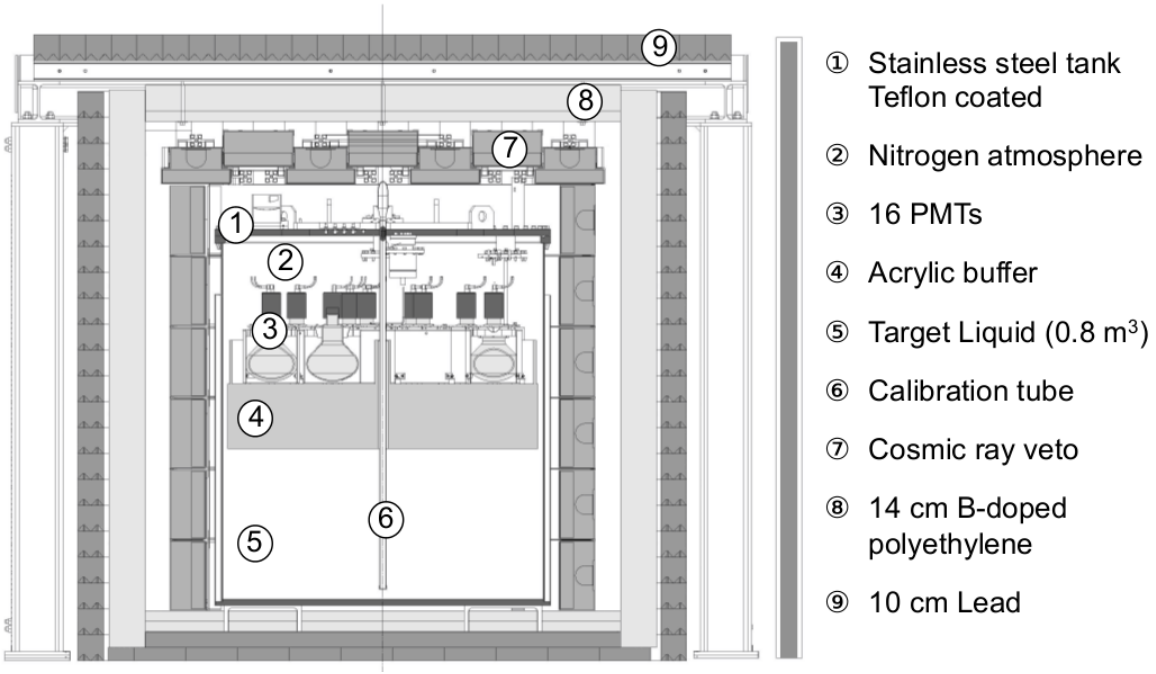

Figure A.42: Nucifer detector main parts [148].

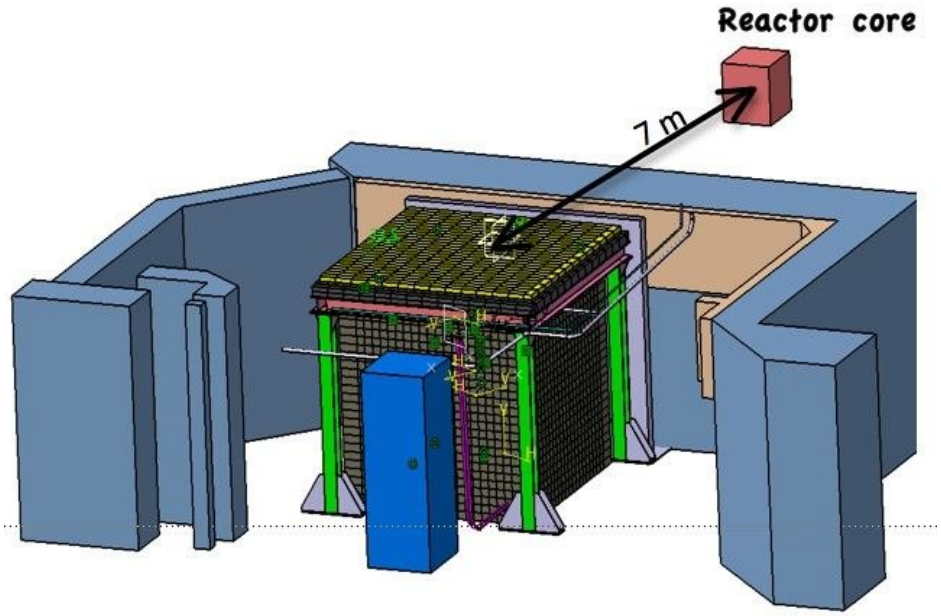

Figure A.43: Nucifer detector location [149].

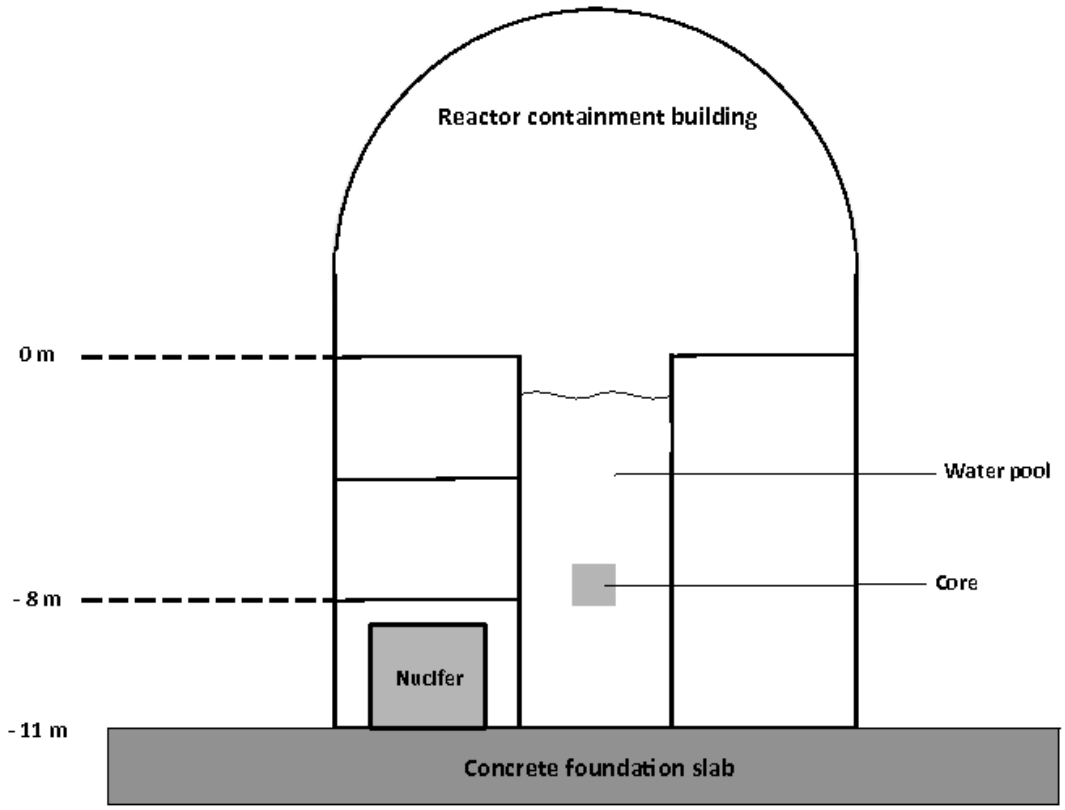

Figure A.44: Nucifer experimental layout [148].

A.10.16 Neutrino-4

Advantage: very short baseline, movable detector (6-12 m), low backgrounds due to absence of any other experiments nearby.

Preliminary results [49] indicate that the antineutrino flux does not follow $1/L^2$. Their next plan is to have two detectors at different baselines.

Reactor: 100 MW_{th} in Dimitrovgrad. Compact core: $35 \times 42 \times 42$ cm^3.

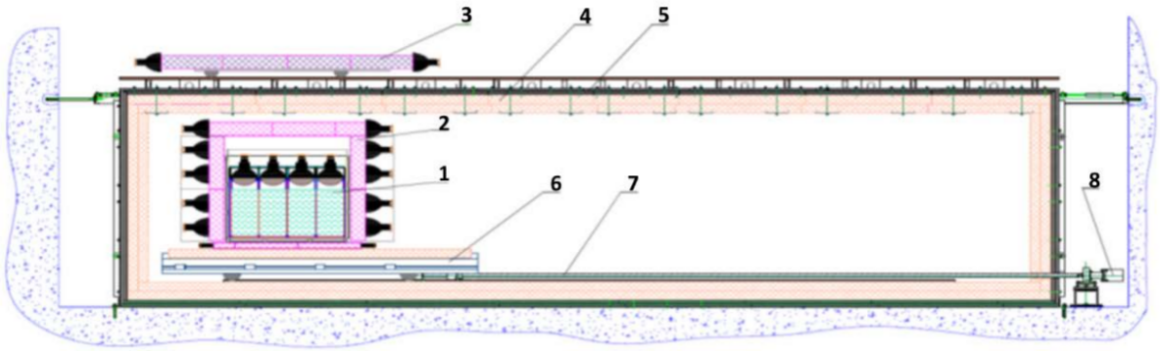

(a) First iteration. 1 — $90 \times 90 \times 50$ cm^3 (∼400 liters) liquid 0.1% Gd-doped scintillator segmented in 16 sections $22.5 \times 22.5 \times 50$ cm^3.

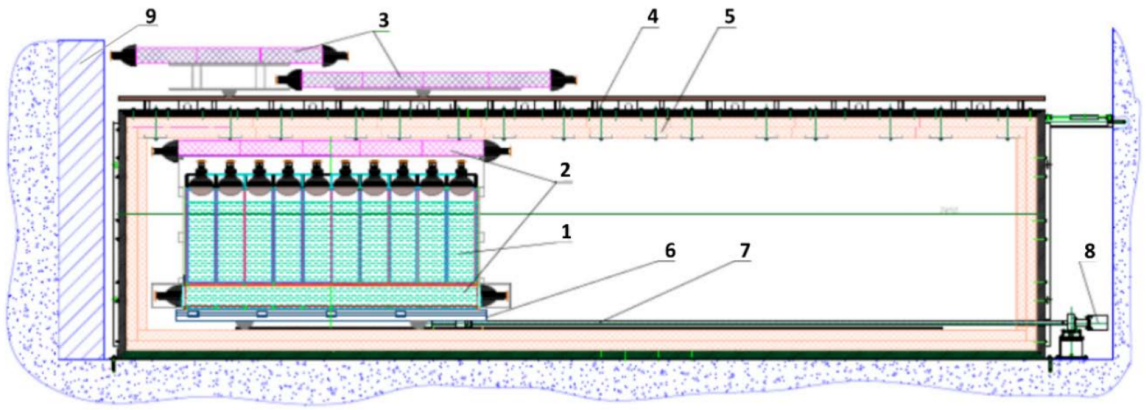

(b) Full detector setup [49]. 1 — total liquid scintillator volume is 3 m^3, segmented in 50 sections. 9 — iron shot (shielding against fast neutrons).

Figure A.45: Neutrino-4 detector [49]. 2 — internal active shielding; 3 — external active shielding; 4 — borated polyethylene (passive shielding); 5 — steel and lead (passive shielding); 6 — movable platform; 7 — feed screw; 8 — step motor.

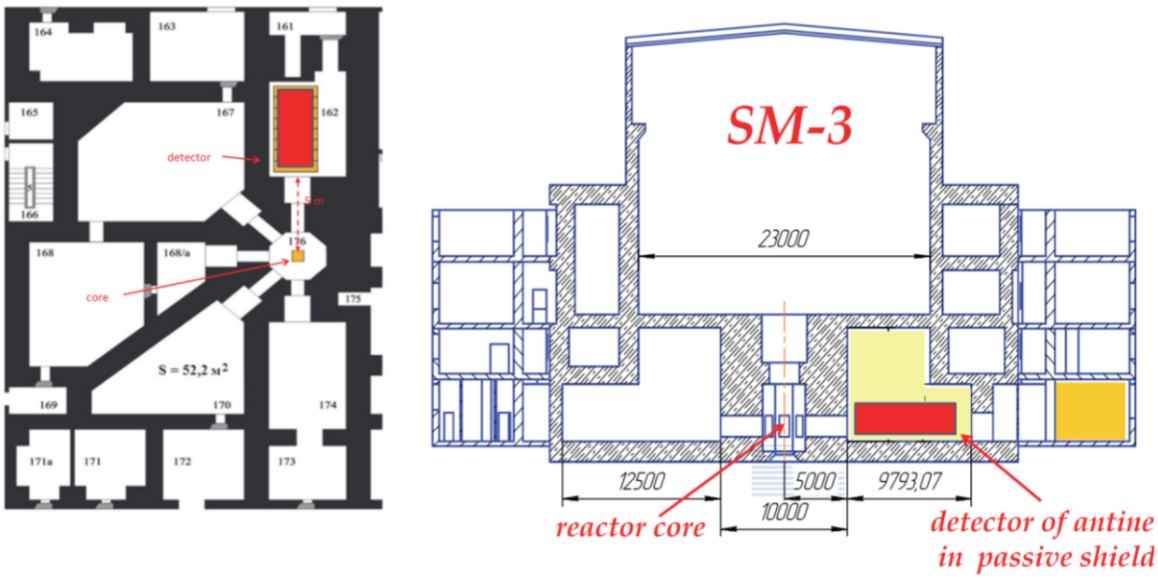

Figure A.46: Neutrino-4 relative location of the detector to the reactor [49].

Figure A.47: Neutrino-4 first iteration [49].

A.10.17 DANSS

Segmented 1-m^3 detector of the reactor AntiNeutrino based on Solid Scintillator is deployed under a 3-GW$_{th}$ power reactor [150].

The whole assembly weights 15 t and is located on a four-post truck lifting mechanism, which can move the detector up to 2.5 m high.

Advantage: high power reactor, short adjustable baseline. Unique geometry — detector is right underneath the reactor core.

DANSS uses both PMTs and SiPMs (MPPC) in their setup. Each 1 m × 4 cm × 1 cm scintillator strip, coated with Gd-doped coating (1.6 mg/cm^2 Gd-density), has an MPPC attached to a wavelength-shifting fiber embedded in the strip.

$$50 \text{ strips} \times (5X + 5Y) \text{ modules} \times 5Z \text{ levels} = 6,250 \text{ strips}$$

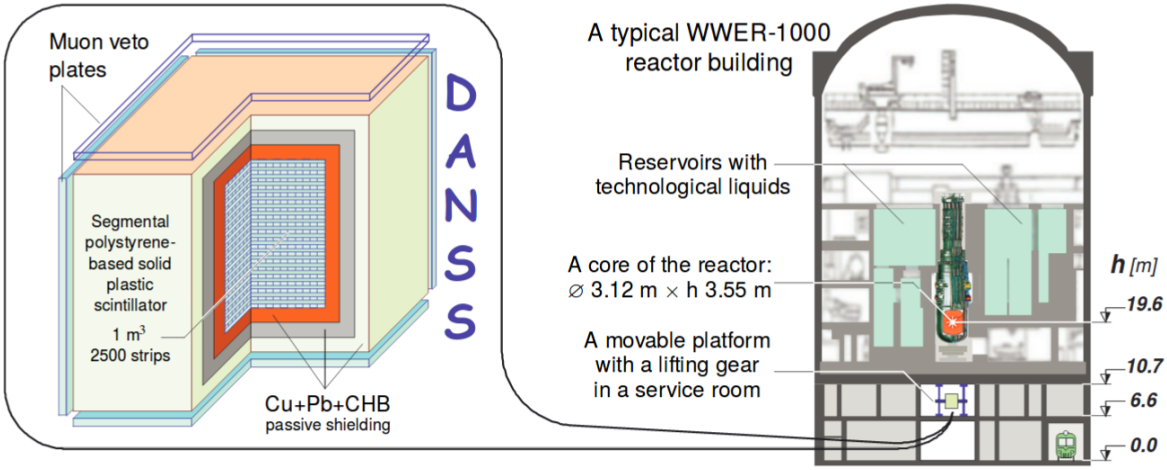

Figure A.48: DANSS reactor and detector [151].

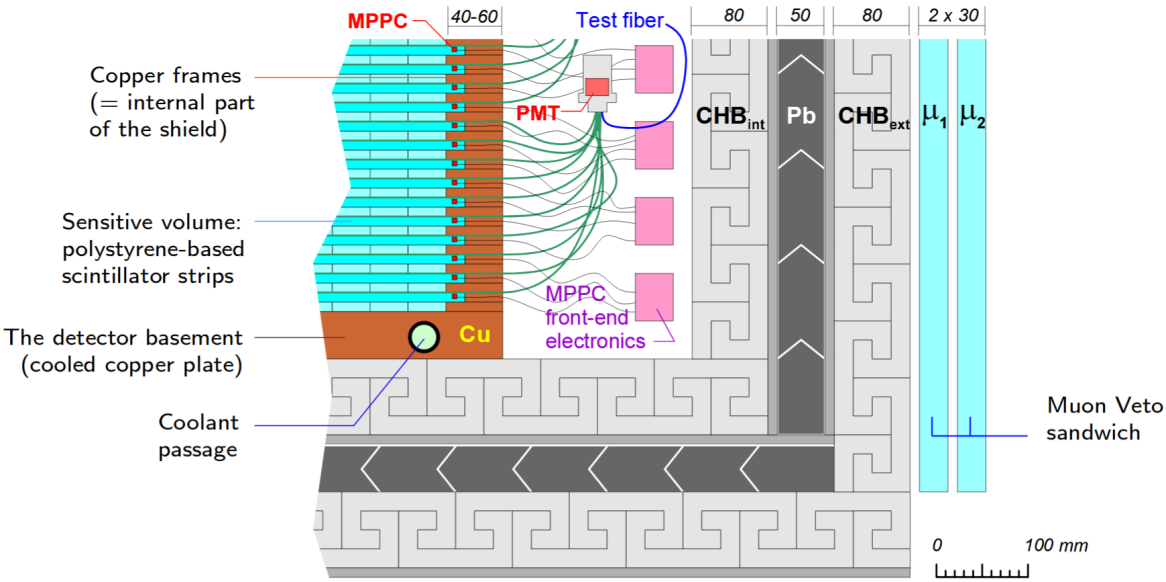

Figure A.49: DANSS shielding layers [150], lead layer is in between two borated polyethylene (CHB) layers.

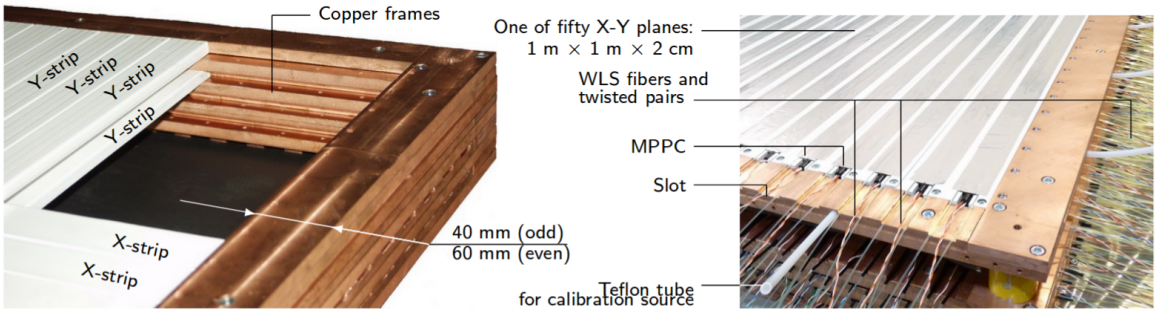

(a) Modules assembly and copper frames.

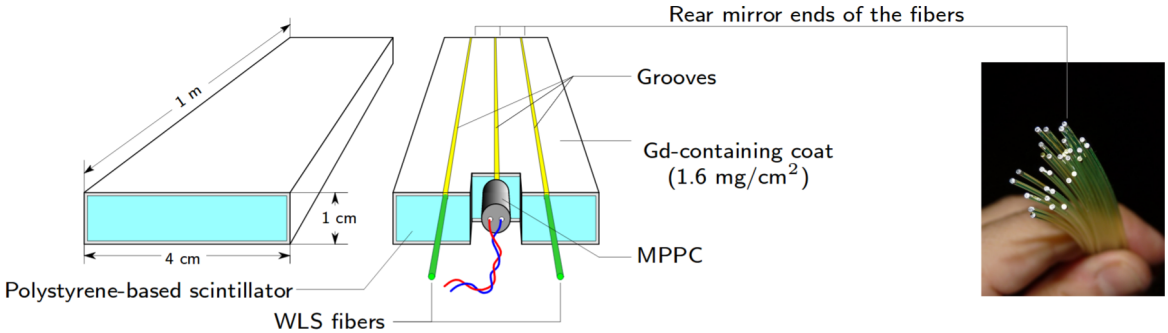

(b) Plastic scintillator strip with three WLS fibers — one goes to an MPPC and two others create a bundle of a 100 (from 50 other strips) and go to a PMT.

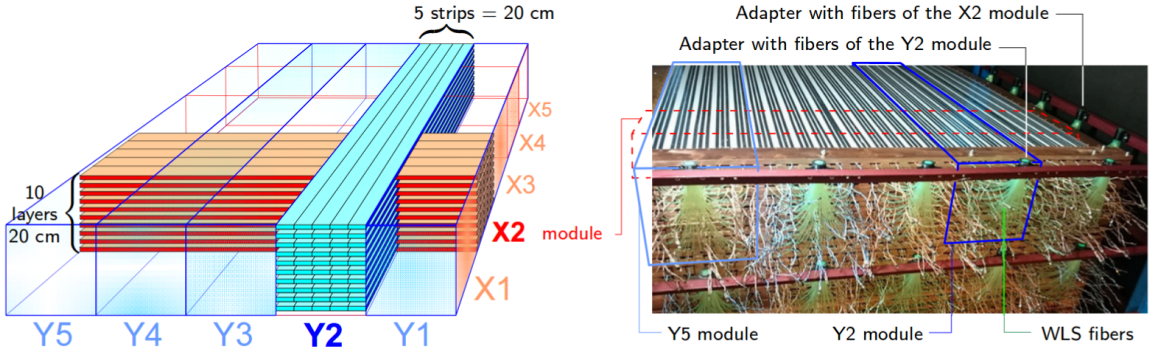

(c) CAD and assembly of one of ten layers.

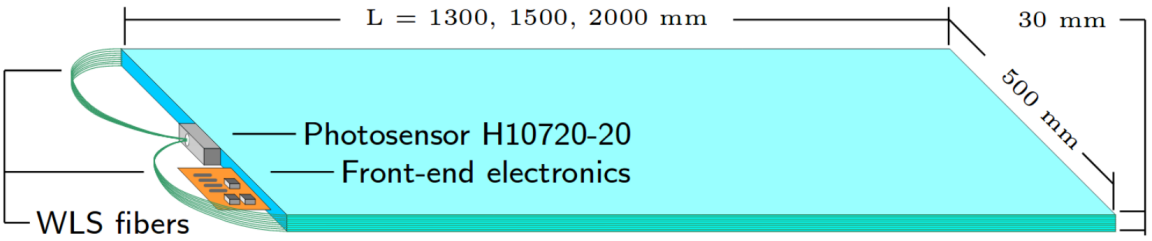

(d) Muon veto.

Figure A.50: DANSS main parts [150].

A.10.18 PANDA

PANDA is a robust and relatively simple detector to operate/model. It is an array of consist of square 10 cm × 10 cm 100-cm long plastic scintillator pieces wrapped in Gd-coated sheets. PANDA stands for Plastic Anti-Neutrino Detector Array.

PANDA collaboration has been expanding their segmented neutrino detector from their first version of 4 × 4 in 2009 to 10 × 10 version in 2016.

Unfortunately, due to the most Japanese reactor remaining shut-down, the tests are limited; only 6 × 6 prototype was deployed at Ohi power station for preliminary tests.

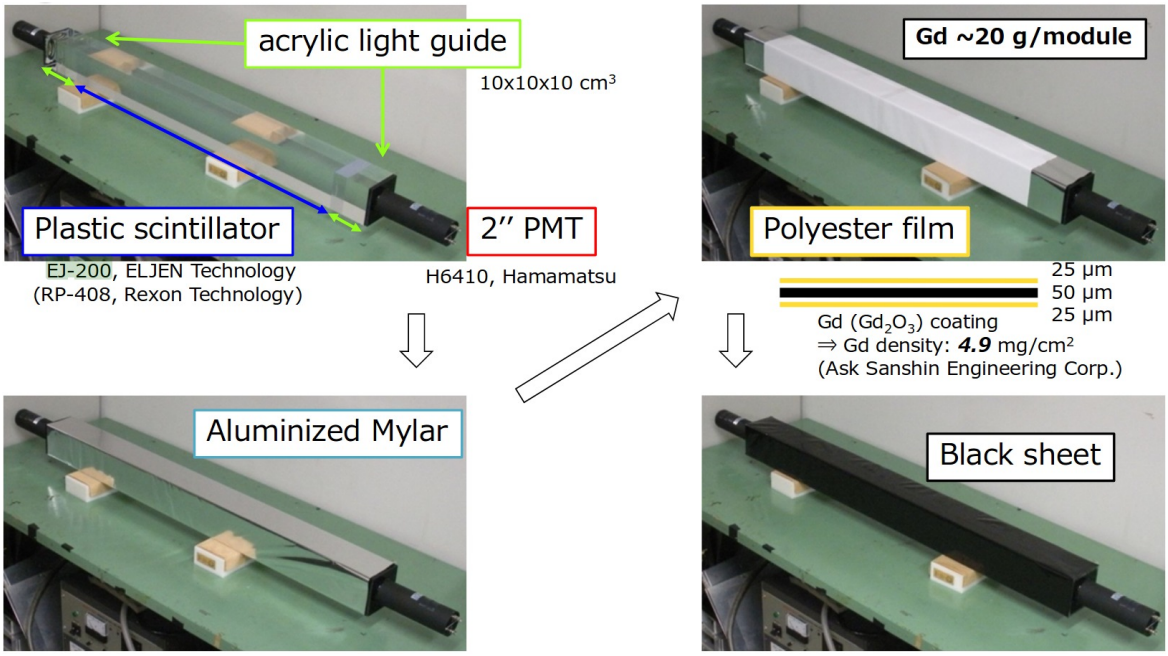

Figure A.51: PANDA module [152].

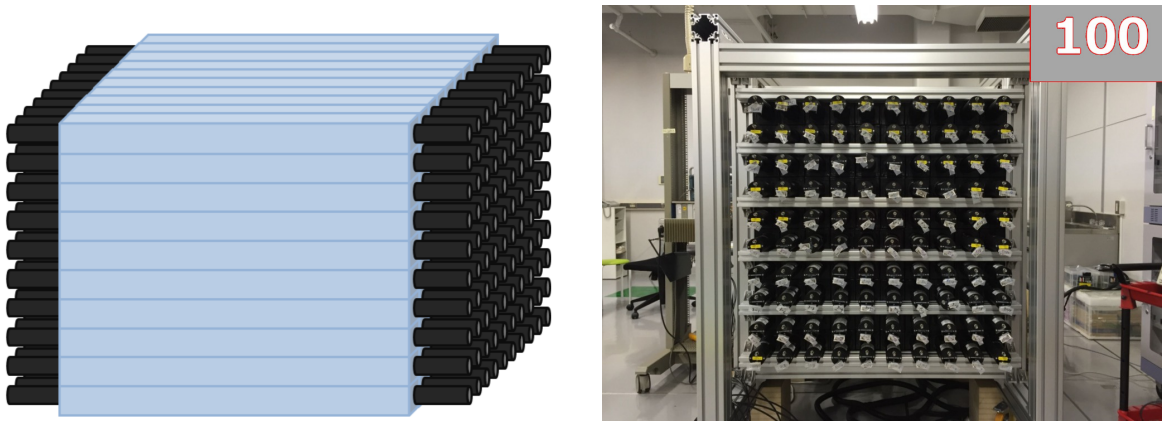

Figure A.52: PANDA100. Blocks of scintillator and PMTs without shielding, cabling, and electronics racks [152].

A.10.19 SONGS

Baseline: ~ 24 m.

Reactor: 2×1.127 GW_{th}, San Onofre Nuclear Generating Station.

Disadvantage: trouble with estimating fiducial volume (i.e. target protons) leading to big systematic uncertainties.

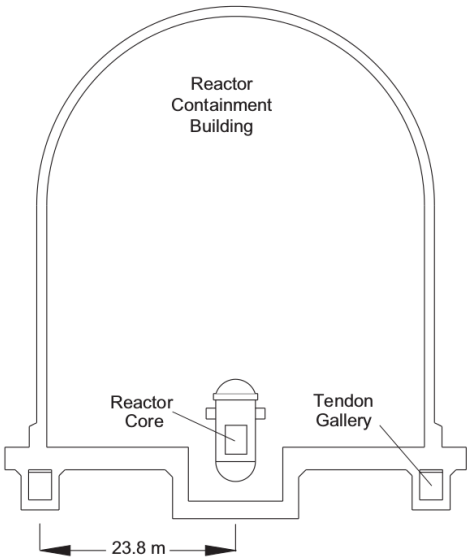

(a) Detector position relative to the reactor core.

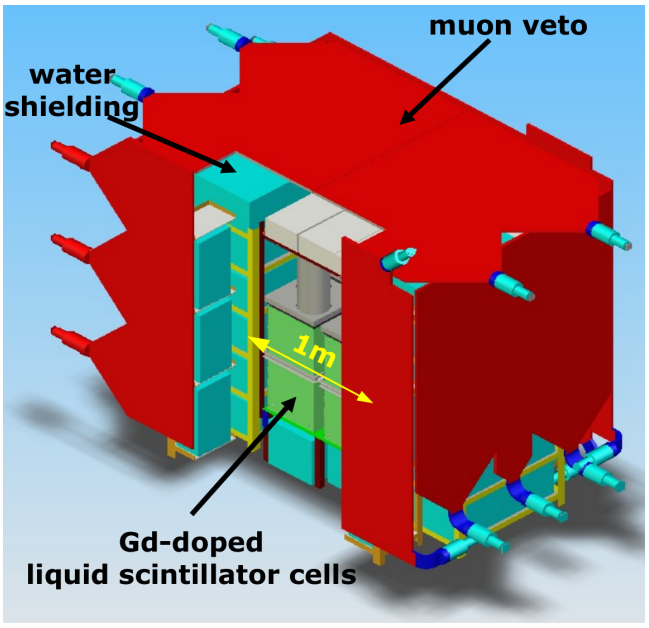

(b) Detector's main assembly.

Figure A.53: SONGS experiment. Figures are taken from [153].

A.10.20 NEOS

Similar to SONGS, although the detector was capable of detecting reactor antineutrinos and measure the spectrum, including the 5 MeV bump [131], the collaboration was unable to estimate the ratio of observed vs predicted antineutrino flux.

Reactor: 2.8 GW_{th} (Hanbit Nuclear Power Plant in Yeonggwang).

Detector: 1 ton of Gd-loaded liquid scintillator. Distance: $\sim$ 24 m.

Measured $\bar{\nu}_e$ rate: 1976 per day with a signal to background ratio of $\sim$ 22.

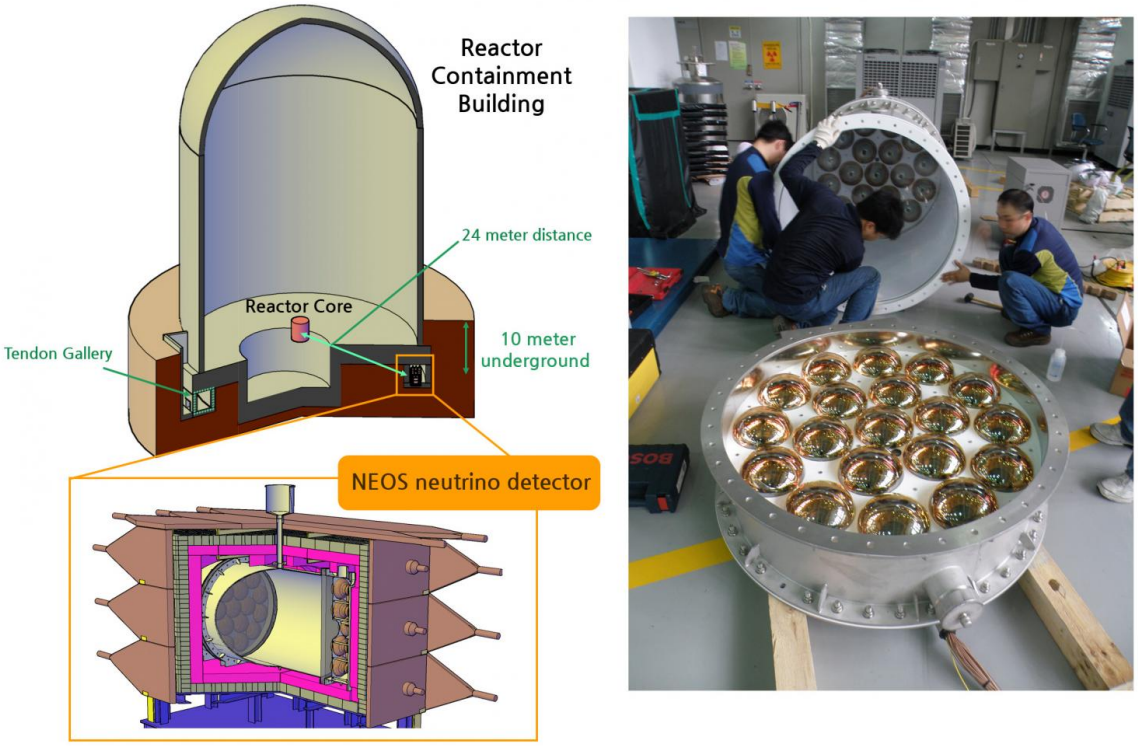

Figure A.54: NEOS experiment in Korea [131].

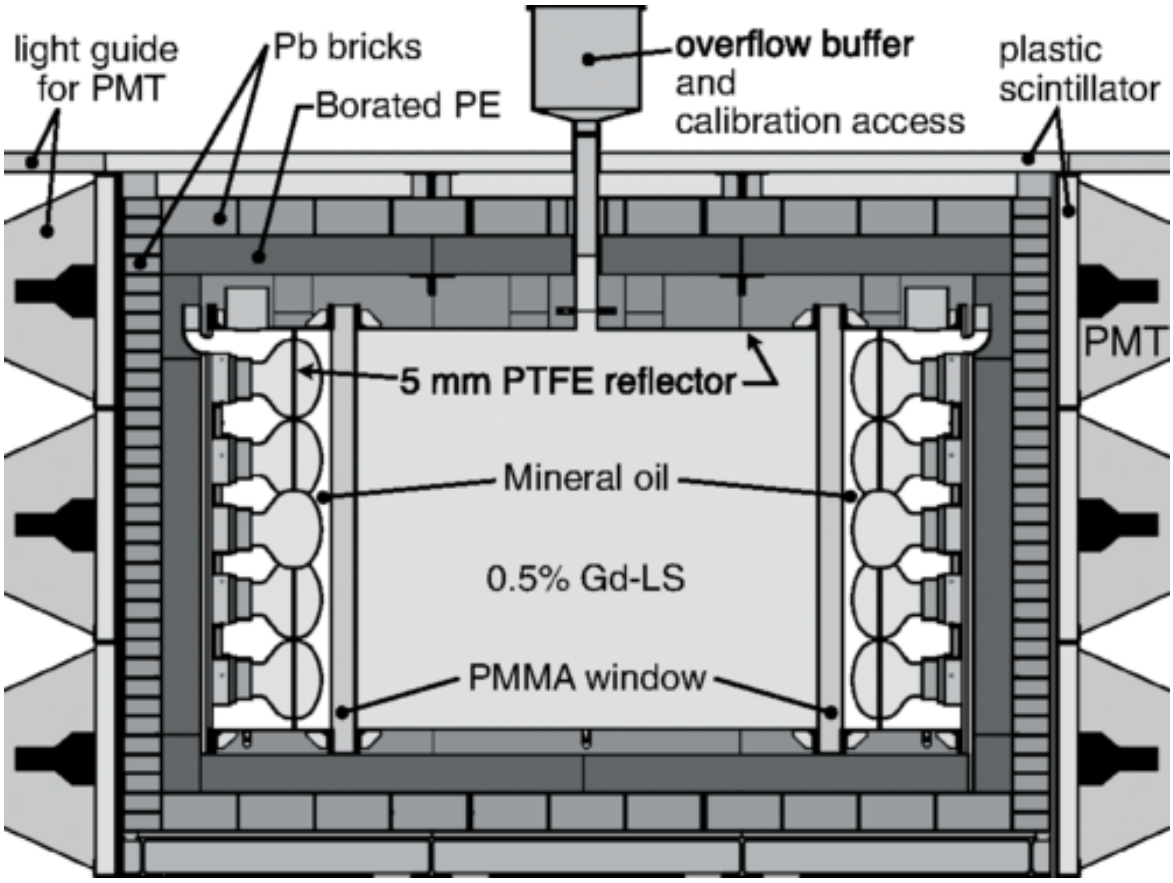

Figure A.55: NEOS detector [131].

A.10.21 Savannah river 1976

Another experiment was performed at the Savannah river nuclear power plant led by Reines [154]. The experiment successfully measured the cross section of elastic $\bar{\nu}_e e^- \to \bar{\nu}_e e^-$ scattering (primary detection reaction). The detector was also capable of detecting reactor antineutrinos via IBD reaction.

Detector: 15.9 kg plastic scintillator

Reactor: 1800 MW_{th}, providing $\bar{\nu}_e$ flux $2.2{\times}10^{13}$ cm^{-2} s^{-1} at the detector's location.

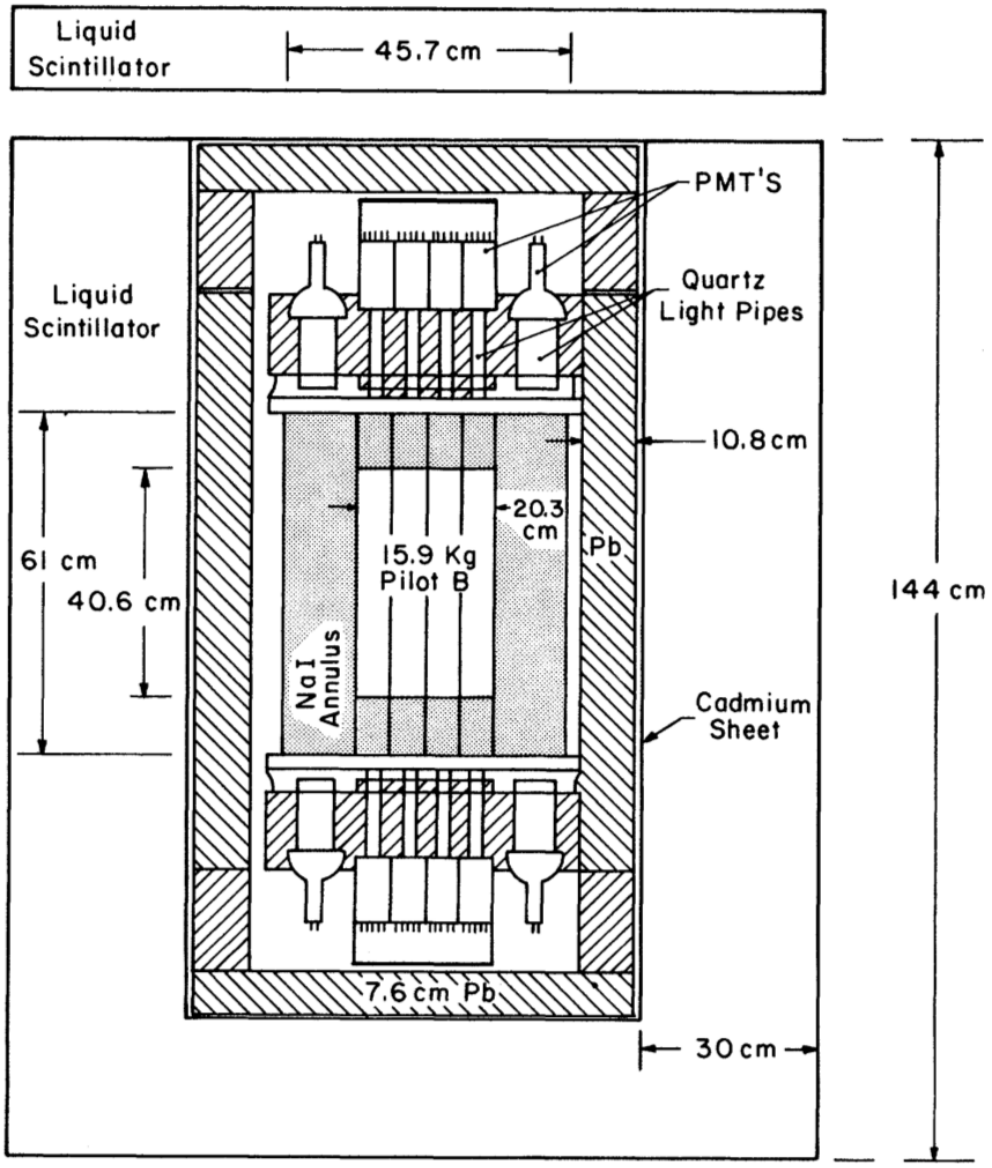

Figure A.56: Reines' $\bar{\nu}_e e^- \to \bar{\nu}_e e^-$ detector [154]. The 15.9-kg plastic scintillator target, is at the center, segmented in 16 optically-isolated elements and totally-enclosed by 300-kg NaI scintillation light pipes and annulus anticoincidence enclosed in lead, cadmium absorber, and 2200-liter liquid scintillation anticoincidence detector.

A.10.22 Rovno elastic

Another experiment at the Rovno power plant neutrino laboratory was performed to study elastic $\bar{\nu}_e e^-$ scattering cross section, to measure neutrino magnetic moment, and to search for potential neutrino decay modes [155].

Detector: multi-detector consisted of 600 cylindrical Si(Li) modules ⌀ 3 cm × 12.5 cm tightly packed and enclosed in a cylindrical shielding ⌀ 36 cm × 39 cm. That assembly was in a vacuum chamber 64 cm in diameter, cooled to liquid-nitrogen temperature.

The signals were read out from p-type contacts via 20 μm lead and were fed to charge-sensitive preamplifiers $\sim$ 1 m from the detector; n^+ lithium contacts were grounded and connected to each other.

Passive shielding to suppress gamma had a 8-cm thick layer of mercury and a 15-cm thick layer of copper.

To reduce contribution from IBD events there was a neutron moderator, which had 50-cm thick layer of graphite surrounded by a cadmium absorber.

Active shielding had 120 plastic scintillator $2.5 \times 2.5 \times 2$ m^3 modules.

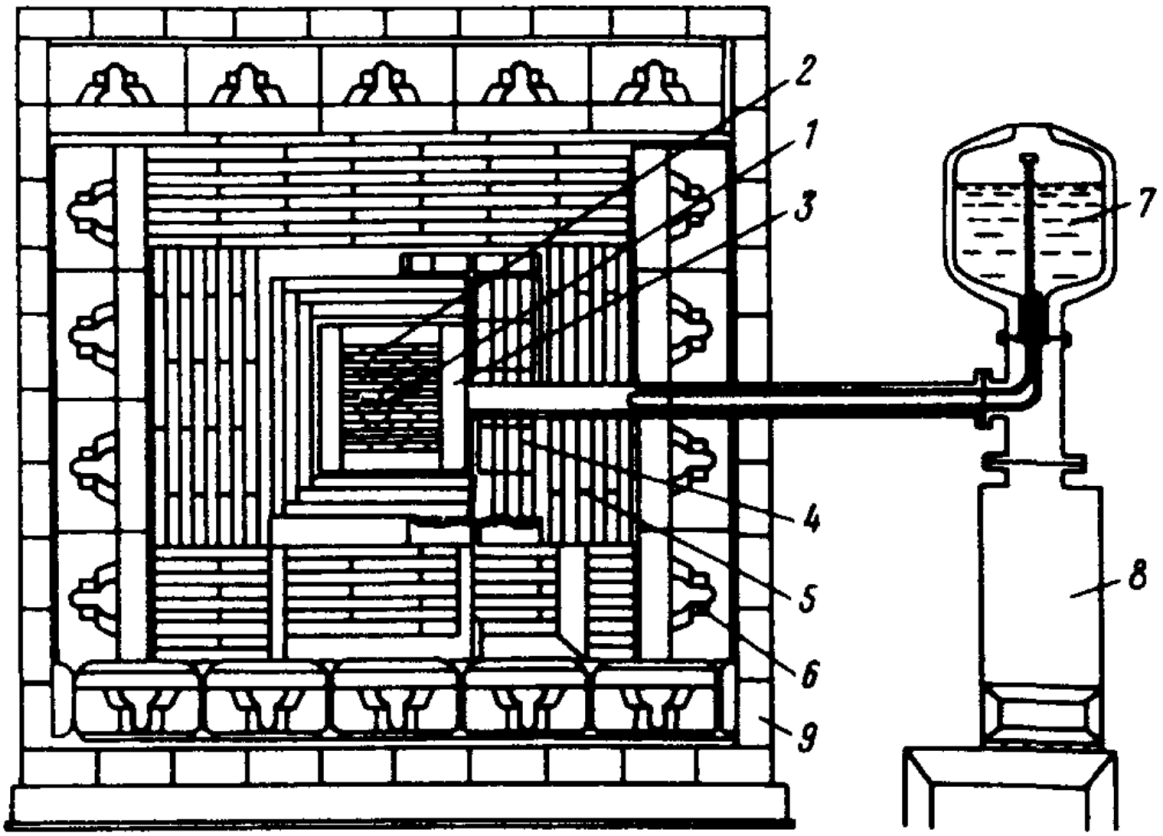

Figure A.57: Rovno $\bar{\nu}_e e^-$ elastic scattering detector [155]. 1 — high-purity Germanium detector; 2 — 600 Si(Li) detectors; 3 — mercury cavity; 4 — copper shielding; 5 — graphite shielding; 6 — active scintillation shielding; 7 — apparatus for cooling the cryostat with liquid nitrogen; 8 — getter-ion pump; 9 — cast-iron housing (mass 85 t, wall thickness 15 cm, dimensions $4 \times 4 \times 3.5$ m^3), the center is 15 m away from the center of the reactor core.

A.10.23 MUNU

Result: estimation of the upper limit of neutrino magnetic moment in a reactor experiment [156].

Reactor: Bugey 2750 MW_{th}.

Detector: TPC for detecting an electron from $\bar{\nu}_e e^- \to \bar{\nu}_e e^-$ scattering. Installed 18 m from the reactor core.

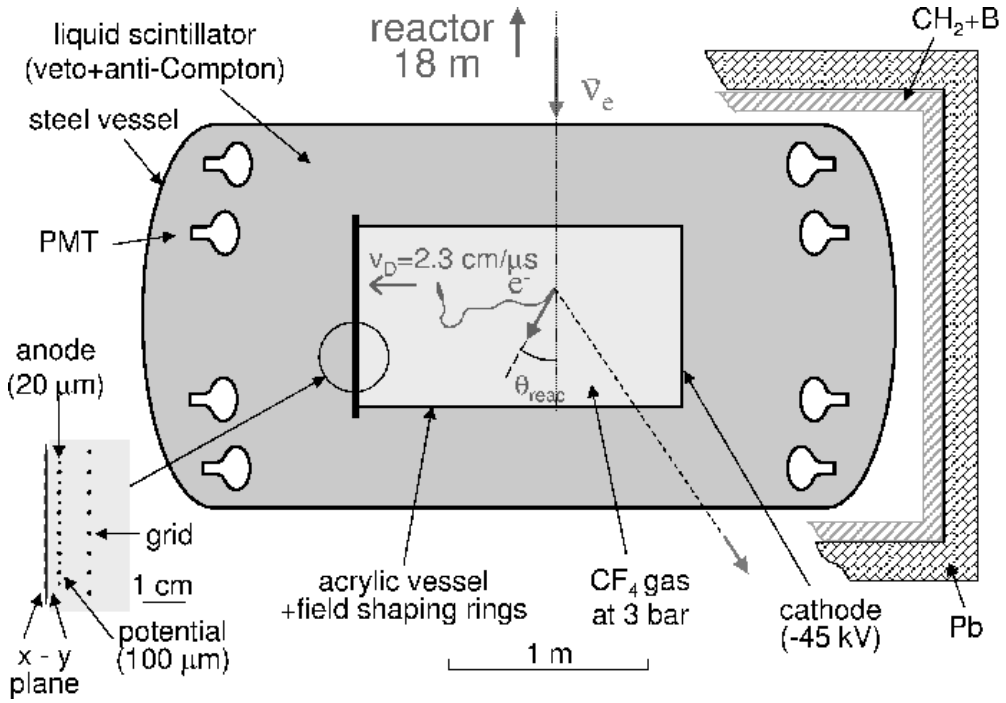

Figure A.58: MUNU $\bar{\nu}_e e^- \to \bar{\nu}_e e^-$ detector [156]. Central TPC surrounded by liquid scintillator (veto) and layers of passive shielding.

A.10.24 TEXONO

Detection reaction: elastic $\bar{\nu}_e e^- \rightarrow \bar{\nu}_e e^-$ scattering.

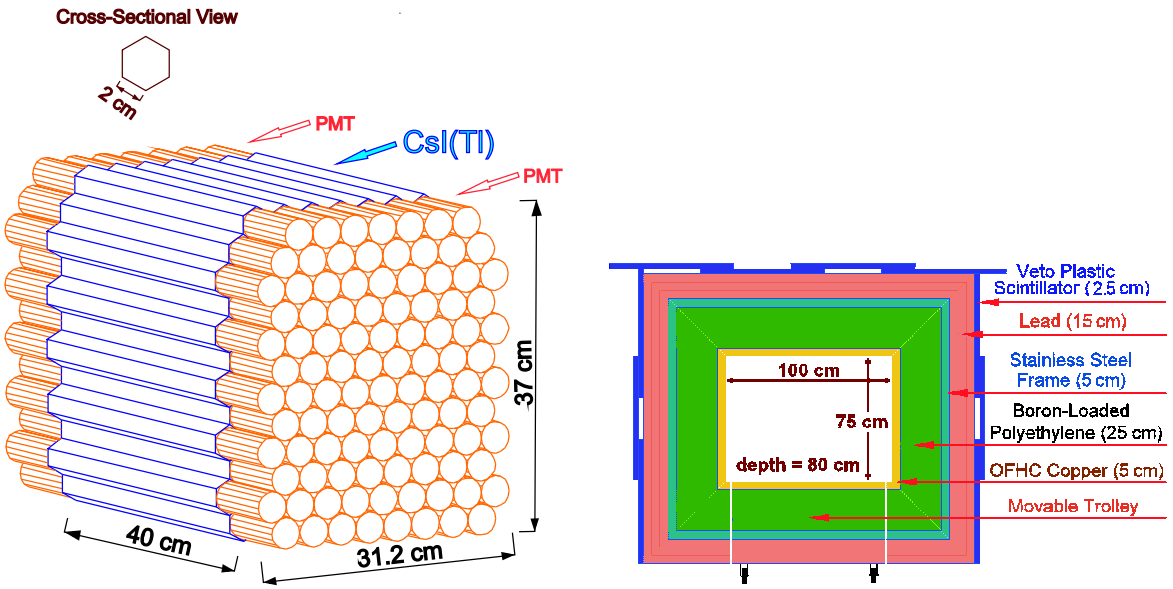

(a) Scintillation fiber array. (b) Shielding.

Figure A.59: TEXONO experiment. Figures are taken from [157].

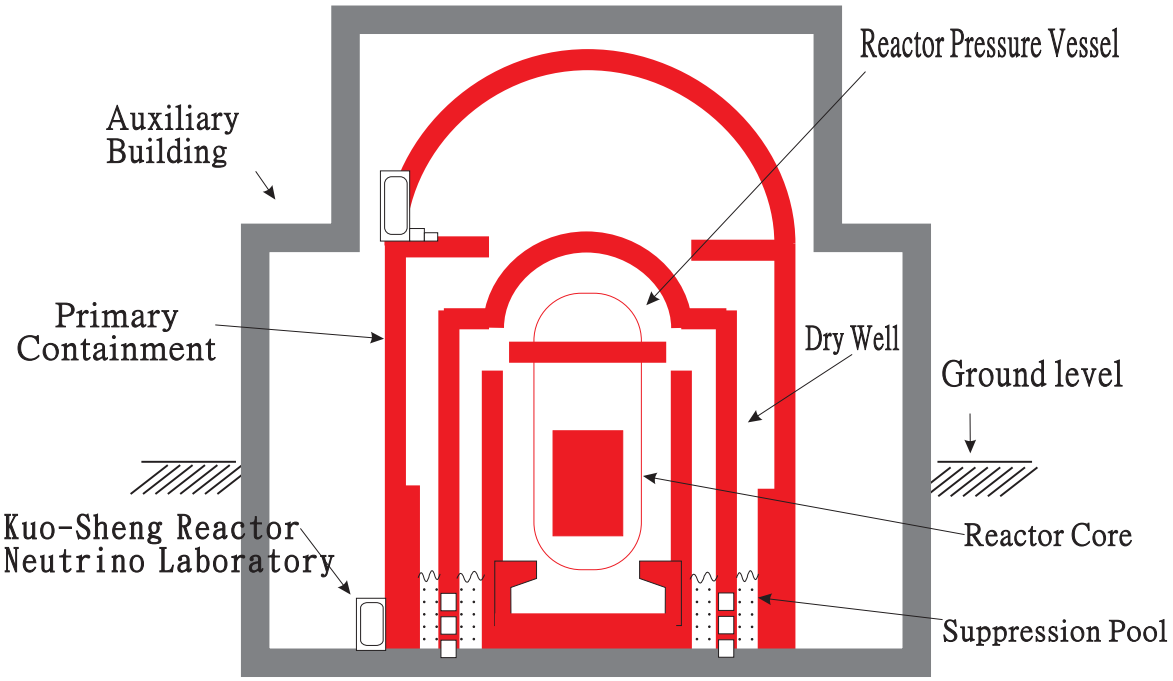

Figure A.60: Reactor building. Texono laboratory at the Kuo-Sheng nuclear power station in Taiwan [157].

A.10.25 SOLID

Proposed project. A lattice of scintillator blocks with wavelength-shifting fibers, in some ways similar to DANSS concept.

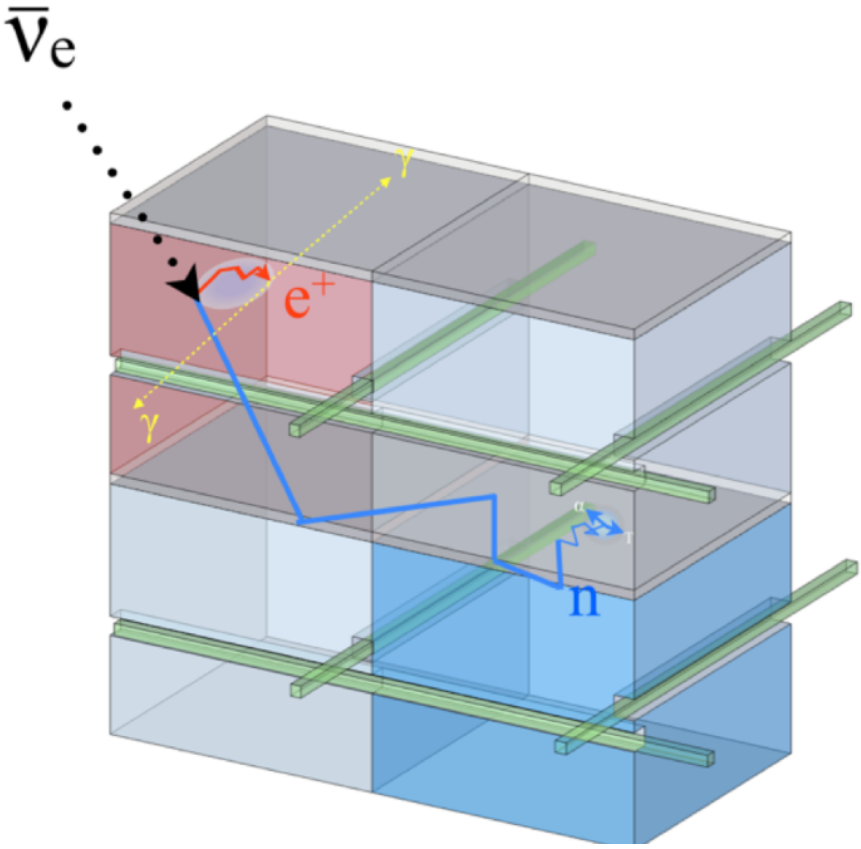

Figure A.61: SOLID detection technique [158].

A.10.26 NuLat

Project is under construction. $15 \times 15 \times 15$ (3375) Raghavan Optical Lattice of $2''$ scintillation cubes with ^{10}B and ^{6}Li dopings. Currently we are building a $5 \times 5 \times 5$ (125-cube) prototype with 150 $2''$ Hamamatsu PMTs, which will potentially be deployed at the same location at NIST, as the mTC detector.

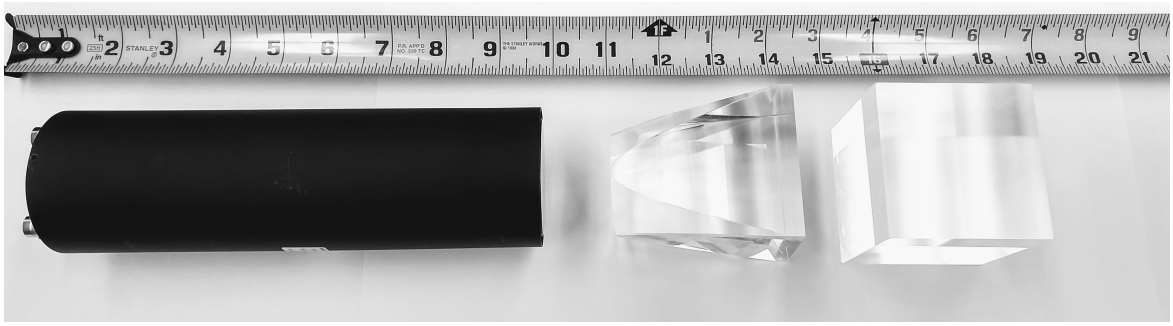

Figure A.62: Single cube, light guide, and PMT.

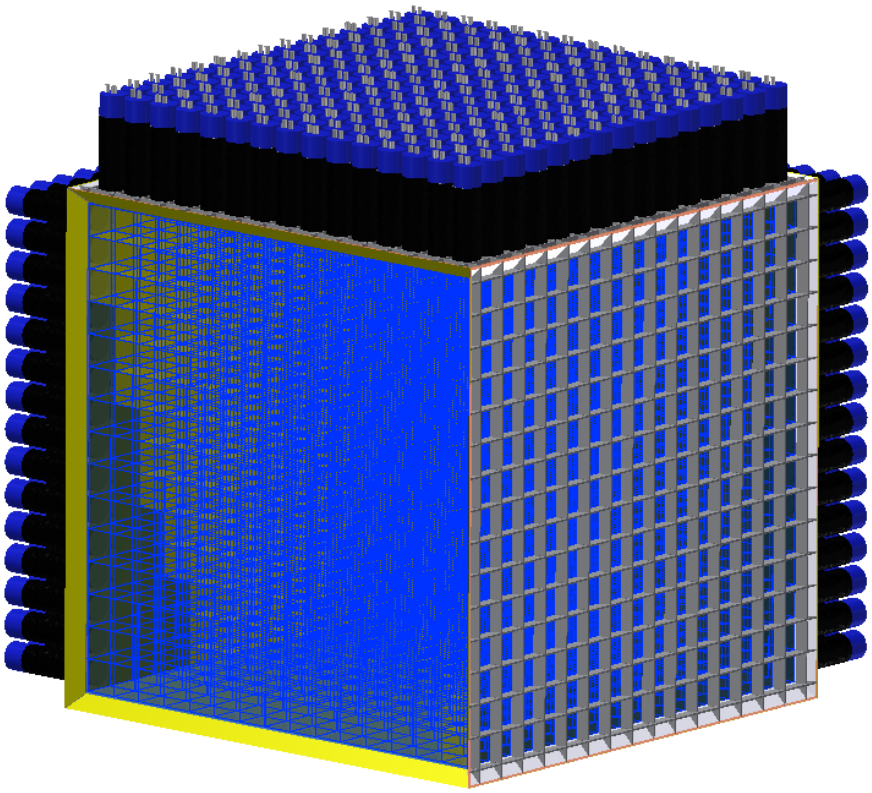

Figure A.63: CAD of the full NuLat [36]. $15 \times 15 \times 15$ (3375) plastic scintillator $2.5''$ cubes placed in a lattice spaced $0.01''$ apart. The lattice is viewed by $6 \times 15 \times 15$ (1350) $2''$ PMTs.

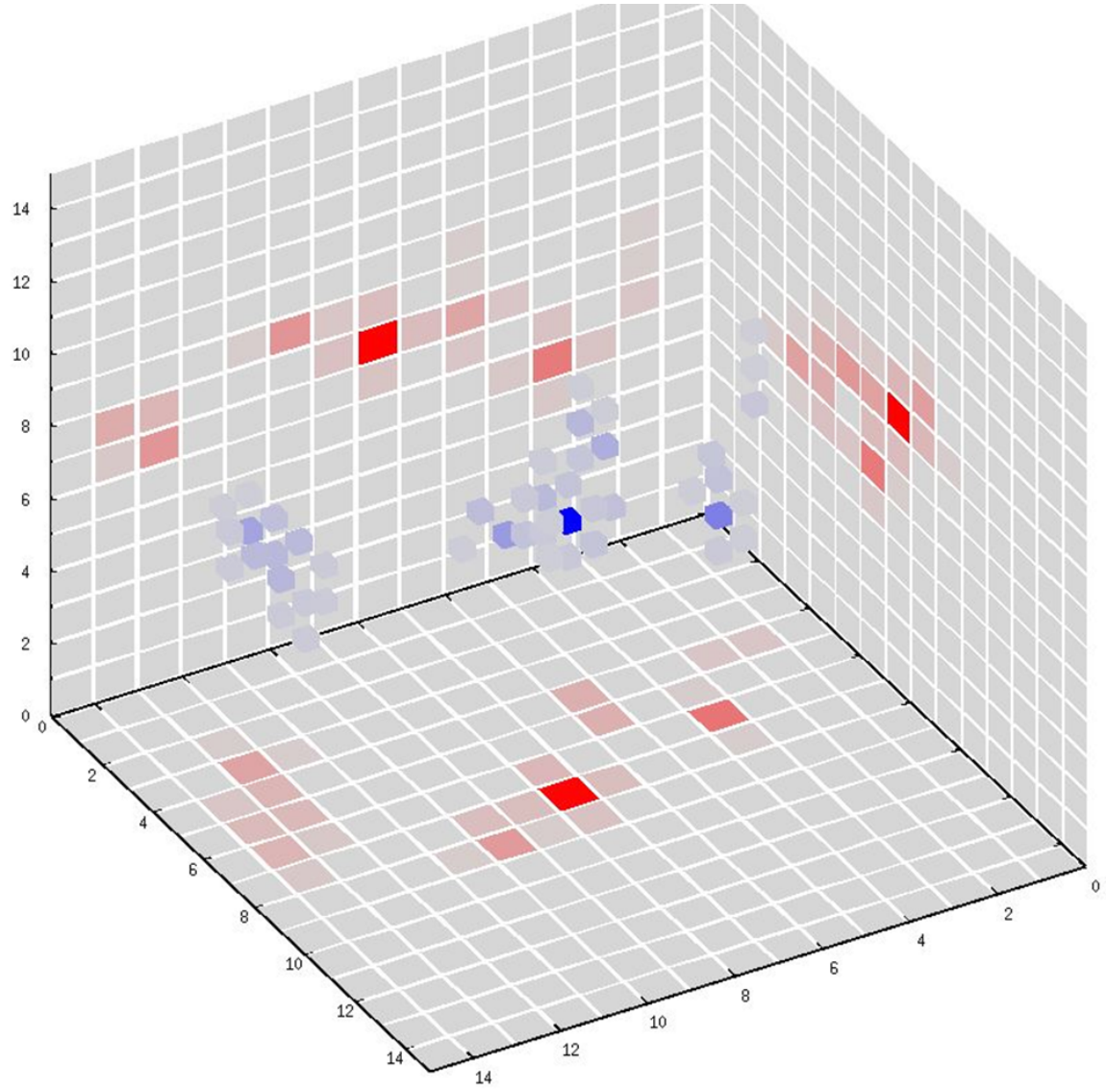

Figure A.64: Simulated IBD event [36]. Prompt event — 2-MeV positron. Red indicated the charge collected via PMTs, blue — energy deposited in the individual cells. One large energy deposited cloud where e^+e^- annihilation takes place. Two smaller ones indicate annihilation gammas. Numbers on the plot indicate cube ID.

(a) Assembly.

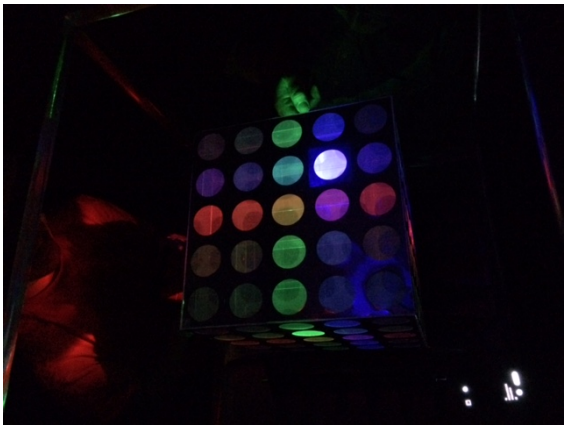

(b) Laser test.

(c) Color addition.

(d) Light guide.

Figure A.65: NuLat $5 \times 5 \times 5$ prototype. Figure courtesy of NuLat collaboration.

Bibliography

[1] W. Pauli. Dear radioactive ladies and gentlemen. *Phys. Today*, 31N9:27, 1978.

[2] Enrico Fermi. Tentativo di una teoria dell'emissione dei raggi beta. *Ric. Sci.*, 4:491–495, 1933.

[3] T. Adam et al. Measurement of the neutrino velocity with the OPERA detector in the CNGS beam. *JHEP*, 10:093, 2012, 1109.4897.

[4] A. Yu. Smirnov. Solar neutrinos: Oscillations or No-oscillations? 2016, 1609.02386.

[5] Arthur B. McDonald. Nobel Lecture: The Sudbury Neutrino Observatory: Observation of flavor change for solar neutrinos. *Rev. Mod. Phys.*, 88(3):030502, 2016.

[6] R. Davis. Nobel Lecture: A half-century with solar neutrinos. *Rev. Mod. Phys.*, 75:985–994, 2003.

[7] Masatoshi Koshiba. Nobel lecture: Birth of neutrino astrophysics. *Rev. Mod. Phys.*, 75:1011–1020, Aug 2003.

[8] Carlo Giunti and Chung W. Kim. *Fundamentals of Neutrino Physics and Astrophysics*. 2007.

[9] M. Fukugita and T. Yanagida. *Physics of neutrinos and applications to astrophysics*. 2003.

[10] John N. Bahcall. *Neutrino Astrophysics*. 1989.

[11] C. Patrignani et al. Review of Particle Physics. *Chin. Phys.*, C40(10):100001, 2016.

[12] S. Pakvasa. Do neutrinos decay? *AIP Conf. Proc.*, 542(1):99–112, 2000, hep-ph/0004077.

[13] John F. Beacom and Nicole F. Bell. Do solar neutrinos decay? *Phys. Rev.*, D65:113009, 2002, hep-ph/0204111.

[14] Ettore Majorana. Teoria simmetrica dell'elettrone e del positrone. *Nuovo Cim.*, 14:171–184, 1937.

[15] B. Pontecorvo. Mesonium and anti-mesonium. *Sov. Phys. JETP*, 6:429, 1957. [Zh. Eksp. Teor. Fiz.33,549(1957)].

[16] Ziro Maki, Masami Nakagawa, and Shoichi Sakata. Remarks on the unified model of elementary particles. *Prog. Theor. Phys.*, 28:870–880, 1962.

[17] B. W. Lee, S. Pakvasa, R. E. Shrock, and H. Sugawara. Muon and Electron Number Nonconservation in a V-A Six Quark Model. *Phys. Rev. Lett.*, 38:937, 1977. [Erratum: Phys. Rev. Lett.38,1230(1977)].

[18] Tsutomu Yanagida. Horizontal Symmetry and Masses of Neutrinos. *Prog. Theor. Phys.*, 64:1103, 1980.

[19] C.L. Cowan, F. Reines, F.B. Harrison, H.W. Kruse, and A.D. McGuire. Detection of the free neutrino: A Confirmation. *Science*, 124:103–104, 1956.

[20] X. Qian and P. Vogel. Neutrino Mass Hierarchy. *Prog. Part. Nucl. Phys.*, 83:1–30, 2015, 1505.01891.

[21] Raymond Davis, Jr., Don S. Harmer, and Kenneth C. Hoffman. Search for neutrinos from the sun. *Phys. Rev. Lett.*, 20:1205–1209, 1968.

[22] S. Fukuda et al. Solar B-8 and hep neutrino measurements from 1258 days of Super-Kamiokande data. *Phys. Rev. Lett.*, 86:5651–5655, 2001, hep-ex/0103032.

[23] K. S. Hirata et al. Experimental Study of the Atmospheric Neutrino Flux. *Phys. Lett.*, B205:416, 1988. [,447(1988)].

[24] W. W. M. Allison et al. Measurement of the atmospheric neutrino flavor composition in Soudan-2. *Phys. Lett.*, B391:491–500, 1997, hep-ex/9611007.

[25] Y. Fukuda et al. Atmospheric muon-neutrino / electron-neutrino ratio in the multiGeV energy range. *Phys. Lett.*, B335:237–245, 1994.

[26] Y. Fukuda et al. Evidence for oscillation of atmospheric neutrinos. *Phys. Rev. Lett.*, 81:1562–1567, 1998, hep-ex/9807003.

[27] Takaaki Kajita. Atmospheric neutrino results from Super-Kamiokande and Kamiokande: Evidence for neutrino(mu) oscillations. *Nucl. Phys. Proc. Suppl.*, 77:123–132, 1999, hep-ex/9810001.

[28] M. Ambrosio et al. Measurement of the atmospheric neutrino induced upgoing muon flux using MACRO. *Phys. Lett.*, B434:451–457, 1998, hep-ex/9807005.

[29] Y. Ashie et al. Evidence for an oscillatory signature in atmospheric neutrino oscillation. *Phys. Rev. Lett.*, 93:101801, 2004, hep-ex/0404034.

[30] R. Becker-Szendy et al. The Electron-neutrino and muon-neutrino content of the atmospheric flux. *Phys. Rev.*, D46:3720–3724, 1992.

[31] R. Becker-Szendy et al. A Search for muon-neutrino oscillations with the IMB detector. *Phys. Rev. Lett.*, 69:1010–1013, 1992.

[32] C. Athanassopoulos et al. Evidence for nu(mu) – nu(e) neutrino oscillations from LSND. *Phys. Rev. Lett.*, 81:1774–1777, 1998, nucl-ex/9709006.

[33] Yu. A. Litvinov et al. Observation of Non-Exponential Orbital Electron Capture Decays of Hydrogen-Like ^{140}Pr and ^{142}Pm Ions. *Phys. Lett.*, B664:162–168, 2008, 0801.2079.

[34] G. Mention, M. Fechner, Th. Lasserre, Th.A. Mueller, D. Lhuillier, et al. The Reactor Antineutrino Anomaly. *Phys.Rev.*, D83:073006, 2011, 1101.2755.

[35] F. P. An et al. Evolution of the Reactor Antineutrino Flux and Spectrum at Daya Bay. *Phys. Rev. Lett.*, 118(25):251801, 2017, 1704.01082.

[36] C. Lane, S.M. Usman, J. Blackmon, C. Rasco, H.P. Mumm, et al. A new type of Neutrino Detector for Sterile Neutrino Search at Nuclear Reactors and Nuclear Nonproliferation Applications. 2015, 1501.06935.

[37] S. P. Mikheev and A. Yu. Smirnov. Resonance Oscillations of Neutrinos in Matter. *Sov. Phys. Usp.*, 30:759–790, 1987. [Usp. Fiz. Nauk153,3(1987)].

[38] S. P. Mikheev and A. Yu. Smirnov. Resonant amplification of neutrino oscillations in matter and solar neutrino spectroscopy. *Nuovo Cim.*, C9:17–26, 1986.

[39] S. P. Mikheev and A. Yu. Smirnov. Resonance Amplification of Oscillations in Matter and Spectroscopy of Solar Neutrinos. *Sov. J. Nucl. Phys.*, 42:913–917, 1985. [Yad. Fiz.42,1441(1985)].

[40] L. Wolfenstein. Neutrino Oscillations in Matter. *Phys. Rev.*, D17:2369–2374, 1978.

[41] Viacheslav Li. Neutrino Oscillations in the Quantum Field Theory approach (in Russian, copy available upon request), 2008.

[42] N. N. Bogolyubov and D. V. Shirkov. Introduction to the theory of quantized fields. *Intersci. Monogr. Phys. Astron.*, 3:1–720, 1959.

[43] D. A. Kirzhnits. Nonlocal quantum field theory. *Sov. Phys. Usp.*, 9:692–700, 1967. [Usp. Fiz. Nauk90,129(1966)].

[44] Michael E. Peskin and Daniel V. Schroeder. *An Introduction to quantum field theory*. 1995.

[45] Steven Weinberg. *The Quantum theory of fields. Vol. 1: Foundations*. Cambridge University Press, 2005.

[46] E. C. G. Sudarshan and R. E. Marshak. Chirality invariance and the universal Fermi interaction. *Phys. Rev.*, 109:1860–1860, 1958.

[47] R. P. Feynman and Murray Gell-Mann. Theory of Fermi interaction. *Phys. Rev.*, 109:193–198, 1958.

[48] Murray Gell-Mann and M Levy. The axial vector current in beta decay. *Nuovo Cim.*, 16:705, 1960.

[49] A.P. Serebrov et al. Experiment Neutrino-4 on search for sterile neutrino at SM-3 reactor. 2017, 1708.00421.

[50] Xinheng Guo et al. A Precision measurement of the neutrino mixing angle θ_{13} using reactor antineutrinos at Daya-Bay. 2007, hep-ex/0701029.

[51] Sandip Pakvasa and John Learned. Lecture notes in neutrino physics and astrophysics, 2009.

[52] Lawrence M. Krauss, Sheldon L. Glashow, and David N. Schramm. Antineutrinos Astronomy and Geophysics. *Nature*, 310:191–198, 1984.

[53] J. A. Formaggio and G. P. Zeller. From eV to EeV: Neutrino Cross Sections Across Energy Scales. *Rev. Mod. Phys.*, 84:1307–1341, 2012, 1305.7513.

[54] R. M. Bionta et al. Observation of a Neutrino Burst in Coincidence with Supernova SN 1987a in the Large Magellanic Cloud. *Phys. Rev. Lett.*, 58:1494, 1987.

[55] K. Hirata et al. Observation of a Neutrino Burst from the Supernova SN 1987a. *Phys. Rev. Lett.*, 58:1490–1493, 1987. [,727(1987)].

[56] E. N. Alekseev, L. N. Alekseeva, I. V. Krivosheina, and V. I. Volchenko. Detection of the Neutrino Signal From SN1987A in the LMC Using the Inr Baksan Underground Scintillation Telescope. *Phys. Lett.*, B205:209–214, 1988.

[57] K. Bays et al. Supernova Relic Neutrino Search at Super-Kamiokande. *Phys. Rev.*, D85:052007, 2012, 1111.5031.

[58] John F. Beacom and Mark R. Vagins. GADZOOKS! Anti-neutrino spectroscopy with large water Cherenkov detectors. *Phys. Rev. Lett.*, 93:171101, 2004, hep-ph/0309300.

[59] John G. Learned, Stephen T. Dye, and Sandip Pakvasa. Hanohano: A Deep ocean anti-neutrino detector for unique neutrino physics and geophysics studies. pages 235–269, 2007, 0810.4975.

[60] T. Araki et al. Experimental investigation of geologically produced antineutrinos with KamLAND. *Nature*, 436:499–503, 2005.

[61] M. Agostini et al. Spectroscopy of geoneutrinos from 2056 days of Borexino data. *Phys. Rev.*, D92(3):031101, 2015, 1506.04610.

[62] M. Antonello et al. Study of Pion Production in nu(mu) CC Interactions on O-16 Using Different MC Generators. *Acta Phys. Polon.*, B40:2519–2535, 2009, 0912.0538.

[63] Lise Meitner and Otto Robert Frisch. Disintegration of Uranium by Neutrons: a New Type of Nuclear Reaction. *Nature*, 143(3615):239–240, 1939.

[64] E. Fermi, E. Amaldi, O. D'Agostino, F. Rasetti, and E. Segre. Artificial radioactivity produced by neutron bombardment. *Proceedings of the Royal Society of London A: Mathematical, Physical and Engineering Sciences*, 146(857):483–500, 1934, http://rspa.royalsocietypublishing.org/content/146/857/483.full.pdf.

[65] Frederick Reines and Clyde L. Cowan. The neutrino. *Nature*, 178:446–449, 1956.

[66] Petr Vogel, Liangjian Wen, and Chao Zhang. Neutrino Oscillation Studies with Reactors. *Nature Commun.*, 6:6935, 2015, 1503.01059.

[67] C. Bemporad. Underground neutrino detectors. In *International Workshop on Neutrino Telescopes, 3rd Venice, Italy, February 26-28, 1991*, pages 171–188, 1991.

[68] Alessandro Strumia and Francesco Vissani. Precise quasielastic neutrino/nucleon cross-section. *Phys. Lett.*, B564:42–54, 2003, astro-ph/0302055.

[69] K. Eguchi et al. First results from KamLAND: Evidence for reactor anti-neutrino disappearance. *Phys. Rev. Lett.*, 90:021802, 2003, hep-ex/0212021.

[70] T. Araki et al. Measurement of neutrino oscillation with KamLAND: Evidence of spectral distortion. *Phys. Rev. Lett.*, 94:081801, 2005, hep-ex/0406035.

[71] M. Battaglieri. CORMORAD: COre Reactor MOnitoRing by an Antineutrino Detector. Presented at Workshop on Applied Antineutrino Physics (AAP 2012), Hawaii, 2012.

[72] P. Vogel and John F. Beacom. Angular distribution of neutron in inverse beta decay. *Phys. Rev.*, D60:053003, 1999, hep-ph/9903554.

[73] M. Apollonio et al. Determination of neutrino incoming direction in the CHOOZ experiment and supernova explosion location by scintillator detectors. *Phys. Rev.*, D61:012001, 2000, hep-ex/9906011.

[74] F. Boehm et al. Results from the Palo Verde neutrino oscillation experiment. *Phys. Rev.*, D62:072002, 2000, hep-ex/0003022.

[75] G.F. Knoll. *Radiation Detection and Measurement*. Wiley, 2000.

[76] R. J. de Meijer, F. D. Smit, F. D. Brooks, R. W. Fearick, H. J. Wortche, and F. Mantovani. Towards Earth AntineutRino TomagrapHy (EARTH). In *Neutrino geophysics. Conference Proceedings "Neutrino Sciences 2005"*, pages 193–206, 2005.

[77] Hiroko Watanabe. Toward low energy anti-neutrinos directional measurement; development of Li-loaded liquid scintillator. Presented at Workshop Toward Neutrino Technologies. Trieste – Italy, 2009.

[78] John G. Learned. *KamLAND internal memo*, 2009.

[79] S. Agostinelli et al. GEANT4: A Simulation toolkit. *Nucl.Instrum.Meth.*, A506:250–303, 2003.

[80] John Learned. The miniTimeCube: A Portable Directional Anti-Neutrino Detector. Presented at Workshop AntiNeutrino Technologies (ANT 2011), Philadelphia, 2011.

[81] Photonis Corp. Photon detector XP85012 MCP-PMT data sheet. 2013.

[82] F. J. Lynch. Improved Timing with NaI(Tl). *IEEE Transactions on Nuclear Science*, 13(3):140–147, June 1966.

[83] R. J. de Meijer, F. D. Smit, F. D. Brooks, R. W. Fearick, H. J. Wortche, and F. Mantovani. Towards Earth AntineutRino TomograpHy (EARTH). *Earth Moon Planets*, 2006, physics/0607049. [Earth Moon Planets99,193(2006)].

[84] Toshiyuki Iwamoto. *Measurement of Reactor Anti-Neutrino Disappearance in KamLAND*. PhD thesis, Tohoku U., 2003.

[85] V. A. Li et al. Invited Article: miniTimeCube. *Rev. Sci. Instrum.*, 87(2):021301, 2016, 1602.01405.

[86] ELJEN. EJ-254. *Scintillator EJ-254 data sheet*.

[87] D.M. Drake, W.C. Feldman, and C. Hurlbut. New electronically black neutron detectors. *Nucl. Instrum. Meth.*, A247(3):576 – 582, 1986.

[88] Glenn Jocher. unpublished, private communication.

[89] Mark Duvall. unpublished, private communication.

[90] L. R. Greenwood and N. R. Chellew. Improved B-10 loaded liquid scintillator with pulse-shape discrimination. *Review of Scientific Instruments*, 50(4):466–471, 1979, https://doi.org/10.1063/1.1135853.

[91] J. Vavra. PID techniques: Alternatives to RICH Methods. *Nucl.Instrum.Meth.*, A639:193–201, 2011.

[92] L. Ruckman, G. Varner, and K. Nishimura. Development of an imaging Time-of-Propagation (iTOP) prototype detector. *Nucl. Instrum. Meth.*, A623:365–367, 2010.

[93] Alan Schwartz et al. Performance confirmation of the Belle II imaging Time Of Propogation (iTOP) prototype counter. 2011.

[94] Matthew Barrett. Particle identification with the iTOP detector at Belle-II. In *Meeting of the APS Division of Particles and Fields (DPF 2013)*, 2013, 1310.4542.

[95] Schott glass. 8337b. *Data sheet*.

[96] ELJEN. EJ-550. *Optical grease EJ-550 data sheet*.

[97] V.A. Li. Annual review. *Antineutrino/Neutron Imaging Program Review and Workshop*, 2015.

[98] V. Li et al. Studies of cross-talk in the MCP-PMT. *paper in progress*, 2018.

[99] Jeff DeFazio. unpublished, private communication.

[100] C. Field, T. Hadig, M. Jain, D. W. G. S. Leith, G. Mazaheri, B. N. Ratcliff, J. Schwiening, and J. Va'vra. Novel photon detectors for focusing DIRC prototype. *Nucl. Instrum. Meth.*, A518:565–568, 2004.

[101] Shige Matsuno. unpublished, private communication.

[102] Marc Rosen. unpublished, private communication.

[103] G. S. Varner, L. L. Ruckman, P. W. Gorham, J. W. Nam, R. J. Nichol, J. Cao, and M. Wilcox. The large analog bandwidth recorder and digitizer with ordered readout (LABRADOR) ASIC. *Nucl. Instrum. Meth.*, A583:447–460, 2007, physics/0509023.

[104] Eric Oberla, Jean-Francois Genat, Herve Grabas, Henry Frisch, Kurtis Nishimura, et al. A 15 GSa/s, 1.5 GHz bandwidth waveform digitizing ASIC. *Nucl.Instrum.Meth.*, A735:452–461, 2014, 1309.4397.

[105] Stefan Ritt, Roberto Dinapoli, and Ueli Hartmann. Application of the {DRS} chip for fast waveform digitizing. *Nuclear Instruments and Methods in Physics Research Section A: Accelerators, Spectrometers, Detectors and Associated Equipment*, 623(1):486 – 488, 2010. 1st International Conference on Technology and Instrumentation in Particle Physics.

[106] D. A. Stricker-Shaver, S. Ritt, and B. J. Pichler. Novel Calibration Method for Switched Capacitor Arrays Enables Time Measurements with Sub-Picosecond Resolution. *IEEE Trans. Nucl. Sci.*, 61(6):3607–3617, 2014, 1405.4975.

[107] Kurtis Nishimura. unpublished, private communication.

[108] Sergey Negrashov. unpublished, private communication.

[109] John Learned and Gary Varner. mTC data flow, 2014.

[110] D. Breton, E. Delagnes, J. Maalmi, K. Nishimura, L. L. Ruckman, G. Varner, and J. Va'vra. High resolution photon timing with MCP-PMTs: a comparison of commercial constant fraction discriminator (CFD) with ASIC-based waveform digitizers TARGET and WaveCatcher. *Nucl. Instrum. Meth.*, A629:123–132, 2011.

[111] G. Jocher et al. miniTimeCube: Neutron telescope. *paper in progress*, 2018.

[112] F. Ardellier et al. Double Chooz: A Search for the neutrino mixing angle theta(13). 2006, hep-ex/0606025.

[113] John Koblanski. PhD thesis (UH Manoa), 2018.

[114] K. Inami et al. Cross-talk suppressed multi-anode MCP-PMT. *Nucl. Instrum. Meth.*, A592(3):247 – 253, 2008.

[115] Samo Korpar. Electron backscattering in MCP. Photodetection: Principles, Performance and Limitations (CERN conference EDIT), 2011.

[116] Ryan Dorrill. unpublished, private communication.

[117] L. Cheng, A. Hanson, D. Diamond, J. Xu, J. Carew, and D. Rorer. Physics and Safety Analysis for the NIST Research Reactor. *Technical Report BNL-NIST-0803, Rev. 1*, 2004.

[118] A. Hanson and D. Diamond. Calculation of Design Parameters for an Equilibrium LEU Core in the NBSR. *Technical Report BNL-96386-2011-IR*, 2011.

[119] NCNR. NIST Center for Neutron Research. *Operations Schedule*.

[120] K.A. Olive et al. Review of Particle Physics. *Chin.Phys.*, C38:090001, 2014.

[121] Th.A. Mueller, D. Lhuillier, M. Fallot, A. Letourneau, S. Cormon, et al. Improved Predictions of Reactor Antineutrino Spectra. *Phys.Rev.*, C83:054615, 2011, 1101.2663.

[122] J. Ashenfelter et al. Background Radiation Measurements at High Power Research Reactors. *Nuclear Instruments and Methods in Physics Research Section A: Accelerators, Spectrometers, Detectors and Associated Equipment*, 2015, 1506.03547v1.

[123] K. Engel et al. miniTimeCube: Background Radiation Shielding Enclosure. *paper in progress*, 2018.

[124] Christian Y. Cardall. Coherence of neutrino flavor mixing in quantum field theory. *Phys. Rev.*, D61:073006, 2000, hep-ph/9909332.

[125] W. Grimus and P. Stockinger. Real oscillations of virtual neutrinos. *Phys. Rev.*, D54:3414–3419, 1996, hep-ph/9603430.

[126] A.I. Akhiezer and V.B. Berestetsky. *Quantum electrodynamics (in Russian)*. Nauka, 1981.

[127] L.D. Landau and E.M. Lifshitz. *The Classical Theory of Fields*. Nauka, 1973.

[128] W. Zhong et al. Measurement of the reactor antineutrino flux and spectrum at DayaBay. *37th International Conference on High Energy Physics*, 2014.

[129] Seon-Hee Seo. New Results from RENO and The 5 MeV Excess. 2014, 1410.7987.

[130] Y. Abe et al. Improved measurements of the neutrino mixing angle θ_{13} with the Double Chooz detector. *JHEP*, 1410:086, 2014, 1406.7763.

[131] Y. J. Ko et al. Sterile Neutrino Search at the NEOS Experiment. *Phys. Rev. Lett.*, 118(12):121802, 2017, 1610.05134.

[132] D.A. Dwyer and T.J. Langford. Spectral Structure of Electron Antineutrinos from Nuclear Reactors. *Phys.Rev.Lett.*, 114(1):012502, 2015, 1407.1281.

[133] Jeffrey M. Berryman, Vedran Brdar, and Patrick Huber. Nuclear and Particle Conspiracy Solves Both Reactor Antineutrino Anomalies. 2018, 1803.08506.

[134] D. V. Naumov, V. A. Naumov, and D. S. Shkirmanov. Inverse-square law violation and reactor antineutrino anomaly. *Phys. Part. Nucl.*, 48(1):12–20, 2017, 1507.04573.

[135] F. Reines, C. L. Cowan Jr., F. B. Harrison, and D. S. Carter. Detection of neutrons with a large liquid scintillation counter. *Review of Scientific Instruments*, 25(11):1061–1070, 1954, https://doi.org/10.1063/1.1770939.

[136] N.G. Cooper et al. Celebrating the Neutrino. *Los Alamos Science*, 25, 1997.

[137] Frederick Reines. The neutrino: from poltergeist to particle. Nobel Lecture, 1995.

[138] Z. D. Greenwood et al. Results of a two position reactor neutrino oscillation experiment. *Phys. Rev.*, D53:6054–6064, 1996.

[139] H. Kwon, F. Boehm, A.A. Hahn, H.E. Henrikson, J.L. Vuilleumier, et al. Search for Neutrino Oscillations at a Fission Reactor. *Phys.Rev.*, D24:1097–1111, 1981.

[140] Th. Lasserre. Overview of anti-neutrino detection, challenges. Presented at Workshop on Applied Antineutrino Physics (AAP 2012), Hawaii, 2012.

[141] G. Zacek et al. Neutrino Oscillation Experiments at the Gosgen Nuclear Power Reactor. *Phys. Rev.*, D34:2621–2636, 1986.

[142] F. Boehm et al. Search for neutrino oscillations at the Palo Verde nuclear reactors. *Phys. Rev. Lett.*, 84:3764–3767, 2000, hep-ex/9912050.

[143] M. Apollonio et al. Search for neutrino oscillations on a long baseline at the CHOOZ nuclear power station. *Eur. Phys. J.*, C27:331–374, 2003, hep-ex/0301017.

[144] Y. Abe et al. Reactor electron antineutrino disappearance in the Double Chooz experiment. *Phys. Rev.*, D86:052008, 2012, 1207.6632.

[145] A. I. Afonin, S. N. Ketov, V. I. Kopeikin, L. A. Mikaelyan, M. D. Skorokhvatov, and S. V. Tolokonnikov. A Study of the Reaction $\bar{\nu}_e + P \to e^+ + N$ on a Nuclear Reactor. *Sov. Phys. JETP*, 67:213–221, 1988. [Zh. Eksp. Teor. Fiz.94N2,1(1988)].

[146] G. S. Vidyakin, V. N. Vyrodov, I. I. Gurevich, Yu. V. Kozlov, V. P. Martemyanov, S. V. Sukhotin, V. G. Tarasenkov, and S. Kh. Khakimov. Detection of Anti-neutrinos in the Flux From Two Reactors. *Sov. Phys. JETP*, 66:243–247, 1987. [Zh. Eksp. Teor. Fiz.93,424(1987)].

[147] F. P. An et al. Observation of electron-antineutrino disappearance at Daya Bay. *Phys. Rev. Lett.*, 108:171803, 2012, 1203.1669.

[148] G. Boireau et al. Online Monitoring of the Osiris Reactor with the Nucifer Neutrino Detector. *Phys. Rev.*, D93(11):112006, 2016, 1509.05610.

[149] M. Cribier. Neutrinos for Peace. *J. Phys. Conf. Ser.*, 593(1):012004, 2015.

[150] I. Alekseev et al. DANSS: Detector of the reactor AntiNeutrino based on Solid Scintillator. *JINST*, 11(11):P11011, 2016, 1606.02896.

[151] I. Alekseev, V. Belov, V. Brudanin, M. Danilov, V. Egorov, et al. DANSSino: a pilot version of the DANSS neutrino detector. *Phys.Part.Nucl.Lett.*, 11:473–482, 2014, 1305.3350.

[152] S. Iwata. Development of plastic anti-neutrino detector array (panda) for reactor monitoring. *International School of Nuclear Physics 39th Course at Erice-Sicily, Sep. 16-24, 2017.*

[153] N. S. Bowden et al. Experimental results from an antineutrino detector for cooperative monitoring of nuclear reactors. *Nucl. Instrum. Meth.*, A572:985–998, 2007, physics/0612152.

[154] F. Reines, H. S. Gurr, and H. W. Sobel. Detection of anti-electron-neutrino e Scattering. *Phys. Rev. Lett.*, 37:315–318, 1976.

[155] A. I. Derbin, A. V. Chernyi, L. A. Popeko, V. N. Muratova, G. A. Shishkina, and S. I. Bakhlanov. Experiment on anti-neutrino scattering by electrons at a reactor of the Rovno nuclear power plant. *JETP Lett.*, 57:768–772, 1993. [Pisma Zh. Eksp. Teor. Fiz.57,755(1993)].

[156] Z. Daraktchieva et al. Limits on the neutrino magnetic moment from the MUNU experiment. *Phys. Lett.*, B564:190–198, 2003, hep-ex/0304011.

[157] M. Deniz et al. Measurement of Nu(e)-bar -Electron Scattering Cross-Section with a CsI(Tl) Scintillating Crystal Array at the Kuo-Sheng Nuclear Power Reactor. *Phys. Rev.*, D81:072001, 2010, 0911.1597.

[158] Y. Abreu et al. A novel segmented-scintillator antineutrino detector. *JINST*, 12(04):P04024, 2017, 1703.01683.